The Protective Role of Lipocalin-2 in Kidney Transplantation: Intricate Mechanisms of Renoprotection and Alloimmunity Modulation

Inaugural-Dissertation

to obtain the academic degree

Doctor rerum naturalium (Dr. rer. nat.)

submitted to the Department of Biology, Chemistry, Pharmacy

of Freie Universität Berlin

by

Anna Maria Pfefferkorn

Berlin, 2024

The research presented in this dissertation was conducted at the Charité—Universitätsmedizin Berlin in the Department of Surgery, Experimental Surgery, CCM|CVK (Univ.-Prof. Dr med. Igor M. Sauer) under the supervision of Dr phil. Muhammad Imtiaz Ashraf between August 2019 and December 2023 as part of the Collaborative Research Centre (CRC) 1365 Renoprotection (Project C02).

1st reviewer: Univ.-Prof. Dr. med. Igor Maximilian Sauer

2nd reviewer: Prof. Dr. med. Silke Rickert-Sperling

Date of defence: 11.06.2024

“Life is not easy for any of us. But what of that? We must have perseverance and above all confidence in ourselves. We must believe that we are gifted for something, and that this thing must be attained.”

Marie Curie

ACKNOWLEDGEMENTS

First and foremost, I would like to thank Prof. Dr. Felix Aigner for giving me the opportunity to work in the field of kidney research and for having the faith in me that I will manage whatever comes along the way.

Sincere thanks to Prof. Dr. Igor Sauer for being my doctoral supervisor and my heartfelt thanks for your support in all aspects that matter.

A big thank you to Prof. Dr. Silke Rickert-Sperling for kindly agreeing to review this thesis.

Special thanks to Dr. M. Imtiaz Ashraf, for your supervision and the courage to direct the project into a different, but extremely exciting way together with me. I really do appreciate your support.

To all my colleagues, I do appreciate that you all created a good working atmosphere, that made working in the lab such a joy. I especially want to thank Steffen Lippert, Peter Tang, Anja Schirmeier, and Kirsten Führer for always lending a sympathetic ear and supporting my research.

I would like to express my gratitude to all collaborators, especially Dr. Angelika Kusch, Dr. Rusan Catar, Dr. Aurélie Philippe, Giang Tong, PhD, and Dr. Benedikt Obermayer-Wasserscheid. Your support and contributions have, by all means, elevated the outcome of this project.

To my big brother, my family, and friends, thank you for always being by my side. And to Matthias, thank you, thank you. From the bottom of my heart.

Mom and Dad, you are the strongest people I know, I admire you so much. You both are true heroes. Without you, I would not be where I am now. Without your endless love and support I could not blossom the way I do. Thank you for your unwavering encouragements, for lifting me up, even when most people, even myself, have doubted me. You are my roots, my forever home. My heart beats to your beat. I love you both endlessly.

Love of my life, my darling husband; being allowed living alongside you, is the greatest of gifts. With you I feel safe, come what may. Whatever lies beyond that horizon for us, I know that I can count on you. Thank you for standing by my side, for always making me laugh, and for going above and beyond for me. You are the measure of my dreams, my light in dark places. My heart belongs to you, always.

DECLARATION OF INDEPENDENCE

Herewith I certify that I have written my dissertation entitled

"*The Protective Role of Lipocalin-2 in Kidney Transplantation: Intricate Mechanisms of Renoprotection and Alloimmunity Modulation*".

independently and that I have not used any sources and aids other than those indicated by me.

Intellectual property of other authors has been marked accordingly.

I also declare that I have not applied for an examination procedure at any other institution and that I have not submitted the dissertation in this or any other form to any other faculty as a dissertation.

Anna Maria Pfefferkorn

TABLE OF CONTENTS

ACKNOWLEDGEMENTS I
DECLARATION OF INDEPENDENCE III
TABLE OF CONTENTS V
LIST OF FIGURES VIII
LIST OF SUPPLEMENTARY FIGURES X
LIST OF TABLES XI
LIST OF SUPPLEMENTARY TABLES XI
ABBREVIATIONS XII
SUMMARY 1
ZUSAMMENFASSUNG 2
1 INTRODUCTION 3
1.1 KIDNEY TRANSPLANTATION (KTx) 3
1.2 LIPOCALIN-2 / NGAL 4
1.3 EPITHELIA IN THE NEPHRON 5
1.3.1 PROXIMAL TUBULES 6
1.4 AIM OF THE STUDY 8
2 MATERIALS AND METHODS 9
2.1 EQUIPMENT 9
2.2 CHEMICALS AND REAGENTS 10
2.3 MEDIA, BUFFER, AND SOLUTIONS 15
2.4 READY-TO-USE KITS 17
2.5 LABORATORY DEVICES 17
2.6 SOFTWARE APPLICATIONS 18
2.7 MURINE KIDNEY TRANSPLANTATIONS (mKTx) 19
2.7.1 RECOMBINANT LCN2 20
2.8 IMMUNOPHENOTYPING 20
2.8.1 KIDNEY GRAFT 20
2.8.2 SPLEEN 20
2.8.3 LYMPH NODES 21
2.8.4 BLOOD 21
2.8.5 STAINING OF CELLS WITH ANTIBODIES AFTER ISOLATION FROM SPLEEN, LYMPH NODES, KIDNEY, AND BLOOD 21
2.8.6 *EX VIVO* CELL STIMULATION 22
2.8.7 PAN NK CELL ACTIVATION 23
2.8.8 INDUCTION OF NKG2D ON $CD8^+$ T CELLS (T CELL ACTIVATION) 23
2.8.9 DATA ANALYSIS 24

2.9 ISOLATION, CULTURING AND CHARACTERIZATION OF PRIMARY PROXIMAL TUBULAR EPITHELIAL CELLS (PTEC) 24
2.9.1 BREEDING OF mT/mG*PEPCK-Cre MOUSE LINE 24
2.9.2 KIDNEY PREPARATION 25
2.9.3 CELL ISOLATION PROCEDURE 25
2.9.4 FLUORESCENCE-ACTIVATED CELL SORTING (FACS) 25
2.9.5 ULTRACENTRIFUGATION 26
2.9.6 CELL SORTING WITH MICROBEADS 26
2.9.7 CELL CULTURE 27
2.9.8 HYPOXIA / REOXYGENATION in PTEC 27
2.9.9 MICROSCOPIC PICTURES 27
2.9.10 PROTEIN ISOLATION and PREPARATION OF LYSATES 28
2.9.11 PROTEIN DETERMINATION (BCA ASSAY) 28
2.9.12 MULTIPLEX IMMUNOASSAY 28
2.9.13 RNA ISOLATION AND cDNA SYNTHESIS 29
2.9.14 REAL-TIME QUANTITATIVE PCR 30
2.9.15 IMMUNOHISTOCHEMISTRY OF PTEC 30
2.9.16 RNASCOPE *IN SITU* HYBRIDIZATION 32
2.9.17 IMMUNOHISTOCHEMISTRY COMBINED WITH RNASCOPE *IN SITU* HYBRIDIZATION 33
2.9.18 scRNAseq OF PRIMARY PROMXIMAL EPITHELIAL CELLS (PTEC) 33
2.10 GENE EXPRESSION UNDER VARIOUS KIDNEY TRANSPLANTATION CONDITIONS 35
2.10.1 HISTOPATHOLOGY 35
2.10.2 GRAFT SURVIVAL 35
2.10.3 SINGLE-NUCLEUS-RNA-SEQUENCING 36
2.11 STATISTICS 37
3 RESULTS 38
3.1 COMPREHENSIVE IMMUNOPHENOTYPING 38
3.1.1 TREATMENT WITH rLCN2 SPECIFICALLY ALTERS ADAPTIVE IMMUNE CELL POPULATIONS 38
3.1.2 TREATMENT WITH rLCN2 ALTERS RELATIVE INNATE IMMUNE CELL FREQUENCIES 43
3.1.3 PAN NK CELL POULATIONS ARE NOT ALTERED UPON TREATMENT WITH rLCN2 45
3.1.4 rLCN2-TREATMENT MIGHT HAVE AN INDIRECT EFFECT ON NKG2D^{+} CELLS 48
3.1.5 THE FUNCTIONALITY OF IMMUNE CELLS SIGNIFICANTLY IMPROVES UPON TREATMENT WITH rLCN2 50
3.1.6 IFNγ^{+} CELLS ARE REDUCED IN KIDNEY GRAFTS DUE TO TREATMENT WITH rLCN2 56
3.1.7 TOTAL IMMUNE CELL COUNTS ON POD-3 ARE DISTINCTIVLY AFFECTED BY rLCN2-TREATMENT 62

3.2 TARGETING STRUCTURAL CELLS OF THE KIDNEY: CULTURING OF PRIMARY PROXIMAL TUBULAR EPITHELIAL CELLS (PTEC) 63
3.2.1 STANDARD ISOLATION PROCEDURE ONLY RETIREVES A LIMITED AMOUNT OF PTEC 64
3.2.2 SORTING-BASED ENRICHMENT WITH ANTI-PROMININ-1 LEADS TO THE BEST OUTCOME 66
3.2.3 rLCN2 SIGNIFICANTLY LOWERS THE PHOSPHORYLATION OF THE ERK1/2 PATHWAY 70
3.2.4 rLCN2 DOES NOT AFFECT THE EXPRESSION OF CANDIDATE SIGNALLING MARKER *IN VIVO* 72
3.2.5 ENHANCED LCN2 AND VIMENTIN EXPRESSION AFTER 3 DAYS OF CELL CULTURE 74
3.3 OPTIMIZATION OF CELL ISOLATION PROCEDURE PRIOR TO scRNAseq ANALYSIS 75
3.3.1 scRNAseq ANALYSIS OF CULTURED PRIMARY PTEC DENOTES TRANSDIFFERENTIATION 77
3.3.2 CELLS ON DAY 3 AND DAY 6 OF CULTURE DIFFER EXTENSIVELY COMPARED TO DAY 0 82
3.3.3 TRAJECTORY ANALYSIS REVEALS POSSIBLE FATES OF CULTURED PTEC 85
3.4 EXPRESSION OF ENDOGENOUS LCN2 AND ITS RECEPTORS IN VARIOUS mKTx SETTINGS 92
3.4.1 STRONGEST LCN2 EXPRESSION IN COLLECTING DUCT-PRINCIPAL CELLS 93
3.4.2 WITHIN THE PROXIMAL TUBULE ONLY INJURED PROXIMAL STRAIGHT TUBULES EXPRESS LCN2 98
3.4.3 MOST OF THE ANALYSED IMMUNE CELL TYPES EXPRESS LCN2 102
4 DISCUSSION 109
4.1 rLCN2 MODULATES DISTINCT IMMUNE CELL POPULATIONS AND THEIR FUNCTIONALITY 109
4.2 CELL CULTURE OF PTEC REVEALS DECREASED *LRP2* EXPRESSION AND IMPAIRED rLCN2 UPTAKE IN SORTED PTEC 113
4.3 rLCN2 DOES NOT ALTER SIGNALLING PATHWAYS *IN VIVO* NOR *IN VITRO* 115
4.4 DUAL FATE OF PTEC IN CELL CULTURE 118
4.5 ENDOGENOUS LCN2 IS PRODUCED BY INJURED PROXIMAL STRAIGHT TUBULAR CELLS AND STRESSED INTERMEDIATE DENDRITIC CELLS/MACROPHAGES 121
4.6 CONCLUSIONS 123
5 REFERENCES 124
6 SUPPLEMENT 139
6.1 SUPPLEMENTARY FIGURES 139
6.2 SUPPLEMENTARY TABLES 165

LIST OF FIGURES

Figure 1: Schematic overview of the kidney and its functional unit, the nephron. 5
Figure 2: Schematic overview of the megalin-cubulin complex-mediated uptake of Lcn2/rLcn2 in a proximal tubular epithelial cell. 7
Figure 3: Relative frequencies of distinctive pan T-cell and T-cell subsets change substantially due to treatment with rLcn2. 39
Figure 4: Relative frequencies of distinctive helper T (T_h)-cells and subgroups are significantly affected due to treatment with rLcn2. 41
Figure 5: Altered relative abundances of distinctive T_c-cells and subgroups due to rLcn2-treatment. 42
Figure 6: Perioperative treatment with rLcn2 significantly affects certain innate immune cell populations. 43
Figure 7: Intermediate mature macrophages were significantly reduced in kidney grafts due to treatment with rLcn2 on pod-7. 44
Figure 8: Treatment with rLcn2 significantly alters intermediate mature NK cells from spleen and blood. 46
Figure 9: $CD8^+NKG2D^+$ cells are significantly reduced at pod-7 by rLcn2-treatment in both spleen and blood. 47
Figure 10: NKG2D expression on T_h-cells was significantly induced *in vitro* with CD3/CD28 antibody combination. 48
Figure 11: *Ex vivo* stimulation of NK cells suggests indirect effect of treatment with rLcn2. 49
Figure 12: Treatment with rLcn2 significantly lowers distinctive $CD4^+$ subsets after *ex vivo* activation. 52
Figure 13: *Ex vivo* activated T_h1 cells from kidney grafts are significantly reduced due to treatment with rLcn2. 53
Figure 14: Distinctive subsets of *ex vivo* activated $CD8^+$ cells are significantly reduced after rLcn2-treatment. 54
Figure 15: From *ex vivo* activated subsets of $NKp46^+$ cells, only $CD107a^+$ cells are significantly reduced after treatment with rLcn2. 55
Figure 16: t-SNE analysis reveals enhanced NK cell expression in spleens on pod-3 of rLcn2 treated samples after allogenic mKTx. 58
Figure 17: t-SNE analysis shows significantly reduced expression of subsets from NK^+, $CD4^+$, $CD8^+$ cells at pod-3 in rLcn2-treated kidney grafts after allogenic mKTx. 59
Figure 18: t-SNE analysis reveals distinct profiles of immune cell subsets in post-transplant spleens on pod-7 after mKTx. 60
Figure 19: t-SNE analysis reveals significantly reduced immune cell expression, especially $IFN\gamma^+$ subsets at pod-7 in rLcn2-treated kidney grafts after allogenic mKTx. 61
Figure 20: Cell culture of murine primary proximal tubular epithelial cells. 64
Figure 21: Cell culture of PTEC isolated from mT/mG*PEPCK-Cre mice sorted by Fluorescence-activated-cell-sorting (FACS) compared to unsorted. 65
Figure 22: Anti-prominin-1 sorted PTEC have a higher percentage of GFP+ cells and do not express phenotypic changes compared to unsorted PTEC. 67
Figure 23: Cell culture of GFP-sorted PTEC leads to loss of epithelial cell and certain PTEC markers. 68
Figure 24: Cell culture of RFP-sorted PTEC leads to a significant loss of Cdh1 expression over time. 69
Figure 25: Cell culture of prominin-1 sorted PTEC leads to a significant increase of Acta2 expression. 70

Figure 26: Intracellular signalling pathway analysis *in vitro* after isolation of primary PTEC from C57Bl/6 kidney cortexes followed by anti-prominin-1 microbeads-based MACS sorting. 71
Figure 27: Effect of rLcn2 on stress, inflammation and survival signalling pathways and graft function. 73
Figure 28: Proximal tubular cells express Lcn2 and Megalin in cell culture. 75
Figure 29: Isolation at room temperature using 98b buffer improves cell culture. 76
Figure 30: scRNAseq of anti-prominin-1 sorted and unsorted PTEC on isolation day (day 0). 79
Figure 32: Annotated and summarized cluster of both sorted and unsorted PTEC from isolation day (day 0). 80
Figure 31: Gene expression patterns of representative marker genes on the isolation day of primary proximal tubular epithelial cells. 80
Figure 33: Pathway activities across the day 0 clusters. 81
Figure 34: scRNAseq of anti-prominin-1 sorted and unsorted PTEC on day 3 and 6 of cell culture. 82
Figure 35: Gene expression patterns of representative marker genes on day 3 and day 6 of cultured primary proximal tubular epithelial cells. 83
Figure 36: Pathway activities across day 3 and 6 of cell culture. 84
Figure 37: Trajectory analysis of day 3 and day 6 cultured primary PTEC. 85
Figure 38: Gene expression patterns of representative marker genes on day 3 and day 6 of cultured primary PTEC after trajectory analysis. 86
Figure 39: Branching pattern of cells along pseudotime axis indicates two dedifferentiation paths. 87
Figure 40: Smooth trajectory of gene expression changes over pseudotime. 89
Figure 41: Gene set enrichment analysis (GSEA) on clusters from of smooth gene expression along pseudotime (Figure 40). 91
Figure 42: Histopathological observations and graft function analysis after various syngeneic and allogenic mKTx over time. 93
Figure 43: Single-nucleus RNA-sequencing. 95
Figure 44: Frequencies of summarized cell types after murine kidney transplantation. 96
Figure 45: Violin plots of summarized cell types and injured cell markers. 97
Figure 46: Detailed analysis of the proximal tubule cluster. 98
Figure 47: Proximal tubules (PT) subcluster gene expression. 100
Figure 48: Summarized proximal tubule subclusters. 101
Figure 49: Gene expression in summarized proximal tubules (PT) subclusters. 102
Figure 50: Detailed analysis of the immune cell cluster. 103
Figure 51: Candidate immune cell marker gene expression in immune cell subclusters. 104
Figure 52: Summarized immune cell cluster. 106
Figure 53: Detailed analysis of the immune cell subclusters. 108

LIST OF SUPPLEMENTARY FIGURES

Figure S1: Gating strategy Functional-Panel. 139
Figure S2: Gating strategy for NK-Panel. 140
Figure S3: Gating strategy T-Panel. 141
Figure S4: Gating strategy Innate-Panel. 142
Figure S5: Treatment with rLcn2 significantly lowers total cell counts of central memory T-cells in lymph nodes at pod-3 after allogenic mKTx. 143
Figure S6: Treatment with rLcn2 does not affect total cell counts of T_h-cells at pod-3 after allogenic mKTx. 144
Figure S7: Total cell counts of central memory cytotoxic T-cells were significantly reduced in lymph nodes due to treatment with rLcn2 at pod-3 after allogenic mKTx. 145
Figure S8: rLcn2-treatment significantly reduces the amount of mature dendritic cells in kidney grafts at pod-3 after allogeneic mKTx. 146
Figure S9: Treatment with rLcn2 significantly reduces the amount distinct macrophage populations at pod-3 after allogeneic mKTx. 147
Figure S10: Total cell counts of distinctive NK cell populations in lymph nodes are affected by rLcn2-treatment at pod-3 after allogenic mKTx. 148
Figure S11: No effects of rLcn2 on $CD4^+$ cells from *ex vivo* stimulated T cells. 149
Figure S12: Treatment with rLcn2 had no effect on *ex vivo* stimulated T_h cells. 150
Figure S13: rLcn2-treatment exerted no effects on *ex vivo* stimulated $CD8^+$ cells. 151
Figure S14: Treatment with rLcn2 significantly lowers total cell counts of *ex vivo* stimulated $CD4^+$ immune cells in kidney grafts at pod-3 after allogenic mKTx. 152
Figure S15: rLcn2-treatment-reduced total cell counts of *ex vivo* stimulated $CD8^+$ and $NKp46^+$ immune cells in kidney grafts at pod-3 after allogenic mKTx. 153
Figure S16: Fluorescence activated cell sorting with a BD Aria II Calliope cytometer of primary proximal tubular epithelial cells isolated from mT/mG*PEPCK-Cre. 154
Figure S17: MACSQuant® Tyto® sorted primary PTEC (GFP^+) from mT/mG*PEPCK-Cre do not survive the first 24 h of cell culture. 155
Figure S18: Most isolated proximal tubules from mT/mG*PEPCK-Cre using ultracentrifugation do not attach to the surface. 156
Figure S19: Representative scatter plots measuring isolated primary proximal tubular epithelial cells during flow cytometrical analysis. 157
Figure S20: Overview of growing patterns of primary PTEC over time according to sorting procedures. 158
Figure S21: Intracellular signalling pathway analysis *in vivo* after kidney transplantation. 159
Figure S22: Intracellular signalling pathway analysis *in vitro* after isolation of primary PTEC from C57Bl/6 kidney cortexes followed by anti-prominin-1 microbeads-based MACS sorting. 160
Figure S23: Single-cell RNA-sequencing of isolated PTEC from cell culture. 161
Figure S24: Follow-up analysis of cleaned scRNAseq data from isolated PTEC from cell culture. 162
Figure S25: Initial analysis of snRNAseq data. 163
Figure S26: Gene expression analysis in clusters from initial analysis. 164

LIST OF TABLES

Table 1: List of equipment/laboratory materials used in this study. ... 9
Table 2: List of chemicals and reagents used in this study. ... 10
Table 3: List of fluorescence antibodies for flow cytometrical analysis used in this study. ... 13
Table 4: List of beads used in this study. ... 14
Table 5: List of media, buffer, and solutions used in this study. ... 15
Table 6: List of commercially available ready-to-use kits used in this study. ... 17
Table 7: List of laboratory devices used in this study. ... 17
Table 8: List of software applications used in this study. ... 18
Table 9: Overview of murine kidney transplantations (mKTx) performed in this study. ... 19
Table 10: Panels used for staining of isolated immune cells from spleen, lymph nodes, kidney, and blood. ... 22
Table 11: List of expression assays for RT-qPCR. ... 30
Table 12: List of primary antibodies applied during immunohistochemical analyses. ... 31
Table 13: List of secondary antibodies applied during immunohistochemical analyses. ... 31
Table 14: Probe for RNAScope Assays 2.5 HD Brown and Multiplex Fluorescent V2. ... 33
Table 15: Overview of samples used for scRNAseq analysis. ... 34
Table 16: Overview of validated marker genes for cell type identification during scRNAseq analysis. ... 78

LIST OF SUPPLEMENTARY TABLES

Table S1: Counts of NK^+ cells, $CD4^+$,and $CD8^+$ cells including their subsets calculated with t-SNE analysis using FlowJo. ... 165
Table S2: Relative standard deviations (RSD) of the analytes' mean fluorescence intensities (MFI) in the quality controls after multiplex analysis. ... 166
Table S3: Annotation of the 19 distinct clusters from anti-prominin-1 microbeads-sorted and unsorted primary proximal tubular epithelial cells (PTEC) on isolation day (day 0). ... 167
Table S4: Samples for single-nucleus RNA-sequencing from kidneys of 12-week-old, male mice. ... 168
Table S5: Marker genes to identify cell types in the distinct 27 clusters from initial snRNAseq analysis. ... 168
Table S6: Initial clustering based on marker gene expression. ... 169
Table S7: Initial cluster summarized to broad cell types. ... 170
Table S8: Percent expression of selected genes from the initial clustering in syngeneic and allogeneic murine kidney transplantation groups. ... 170
Table S9: Proximal tubule clustering based on validated marker gene expression. ... 171
Table S10: Proximal tubule cluster summarized to broad cell types. ... 171
Table S11: Percent expression of selected genes from the proximal tubule clustering in syngeneic and allogeneic murine kidney transplantation groups. ... 171
Table S12: Clustering of immune cells based on *Find.Markers* function from the Seurat package. ... 172
Table S13: Immune cell cluster summarized to broad cell types. ... 172
Table S14: Percent expression of selected genes from the immune cells clustering in syngeneic and allogeneic murine kidney transplantation groups. ... 173

ABBREVIATIONS

24p3R	24p3/Lcn2 receptor
ACK	Ammoniumchlorid-Kalium
AKI	Acute Kidney Injury
ANOVA	Analysis of Variance
apo-Lcn2	iron-free form of the Lipocalin-2 protein
AQP	Aquaporin
AR	Acute Rejection
ATP	Adenosine triphosphate
BCA assay	Bicinchoninic acid assay
Bl/6	C57Bl/6 mouse
BSA	Bovine serum albumin
cDNA	complementary DNA
CKD	Chronic Kidney Disease
CLDN	Claudin
Coll IV	Collagenase 4
Cre	cAMP-responsive element
Cre-Recombinase	Enzyme from Bacteriophage P1
DAPI	4',6-Diamidino-2-phenylindol
DCT	Distal convoluted tubule
ddH_2O	Distilled water
DEPC water	Diethyl pyrocarbonate treated (0.1% v/v) water, Rnase-free water
DNA	Deoxyribonucleic acid
dNTP	Nucleoside triphosphate
ECM	Epithelial cell medium
EDTA	Ethylenediaminetetraacetic acid
EGF	Epidermal growth factor
ESRD	End stage renal disease
EtOH	Ethanol
FACS	Fluorescence Activated Cell Sorting
FBS	Fetal bovine serum
FcR	Fc-receptor
FCS file	Flow cytometry standard file
Fe	Iron
GFP	Green-fluorescent protein
h	hours
H	Hypoxic condition
H/R	Hypoxic condition followed by reoxygenation
H/R + rLcn2	Hypoxic condition followed by reoxygenation with addition of rLcn2
HBSS	Hanks' Balanced Salt Solution
IL-2	Interleukin-2
INFγ	Interferon gamma
IRI	Ischemia-Reperfusion Injury of the Kidney
K^+	Potassium
kDa	Kilodalton
KTx	Kidney Transplantation
L/D	Live-Death fluorochrome

Lcn2	Lipocalin-2
Lrp2	Low Density Lipoprotein receptor-related Protein 2, megalin
mAB	monoclonal antibody
MACS	Magnetic Cell Separation
min	minutes
mKTx	Murine Kidney Transplantation
mRNA	Messenger RNA
mT/mG	mouse-tomato/mouse-green-Phosphoenolpyruvat-Carboxykinase-cAMP-responsive element
mTor	Mechanistic/mammalian target of Rapamycin
Na^+	Sodium
NaCl	Sodium chloride
NFκB	nuclear factor 'kappa-light-chain-enhancer' of activated B-cells
NGAL	native Neutrophil gelatinase-associated lipocalin protein, synonym for LCN2
NK cells	Natural killer cells
pAB	Primary Antibody
PALA	Periarterial lymphocytic aggregates
PAS staining	Periodic-Acid-Schiff staining
PBS	Phosphate buffered saline
PCR	Polymerase chain reaction
PCT	Proximal convoluted tubule
PEB	Protein extraction buffer
PEPCK	Phosphoenolpyruvat-Carboxykinase
PermBuffer	Permeabilisation Buffer
PFA	Paraformaldehyde
PI	Propidium Iodide
PMA	Phorbol 12-myristate 13-acetate
pod	Postoperative day
PST	Proximal straight tubule
PT	Proximal tubule
PTEC	Primary proximal tubular epithelial cells
RFP	Red-fluorescent protein
RIPA buffer	Radioimmunoprecipitation assay buffer
rLcn2 or holo-Lcn2	Lcn2:Siderophore:Fe (recombinant Lipocalin-2)
RNA	Ribonucleic acid
ROS	reactive oxygen species
rp	Ribosomal protein
rpm	revolutiona per minute
RT	Reverse Transcription
RT-qPCR/qPCR	Real-time quantitative PCR
sAB	Secondary antibody
sCr	serum creatinine
scRNA-seq	single-cell RNA-sequencing
SD	Standard deviation
SDS	Sodium Dodecyl Sulfate
SGLT	Sodium dependent glucose co-transporter
snRNA-seq	single-nucleus RNA-sequencing

TAL	Thick ascending limb
TBST Buffer	Tris-buffered Saline-Tween 20 buffer
T_c-cells	cytotoxic T-cells ($CD8^+$ cells)
T_h-cells	T-helper cells ($CD4^+$ cells)
Triton™ X-100	2-[4-(2,4,4-trimethylpentan-2-yl)phenoxy]ethanol
TRIzol™	Guanidinium thiocyanate used in guanidinium thiocyanate-phenol-chloroform extraction
t-SNE	t-distributed stochastic neighbor embedding
TST Buffer	Trition-SDS-Tris-Lysisbuffer
UMAP	Uniform Manifold Approximation and Projection for Dimension Reduction
w/o	without
wt	Wild type

SUMMARY

Kidney transplantation (KTx) stands as the sole curative treatment option for individuals afflicted with end-stage renal disease, providing them a renewed opportunity for kidney function. However, the success of KTx is hindered by immune-mediated graft rejection, occurring both in the early postoperative phase and over the long term. These rejections episodes profoundly affect graft function and survival, posing significant challenges to successful transplantation outcomes. Lipocalin-2 (Lcn2), a member of lipocalin family, has received substantial recognition in the field of kidney transplantation due to its pivotal role in diverse physiological processes, such as iron transport, bacterial defence, and regulation of immune responses. Studies have shown that Lcn2 expression is upregulated in renal allografts during acute rejection episodes, suggesting its involvement in the immune response against the graft. Furthermore, preclinical studies have demonstrated the potential of exogenously administered recombinant Lcn2 (rLcn2) in ameliorating kidney injury and promoting graft survival.

The primary objective of this research was to explore the intricate molecular and cellular mechanisms that underlie the renoprotective effects of rLcn2 in a mouse model of kidney transplantation. Treatment with rLcn2 during the perioperative period led to significant alterations in both adaptive and innate immune cell populations, particularly impacting the functionality and degranulation capacities of immune cells within the kidney graft. Moreover, an effective method for isolating and culturing primary proximal tubular epithelial cells (PTEC) was established to investigate their response to treatment with rLcn2. However, the PTEC exhibited diverse gene expression patterns during the culturing process and early on signs of beginning dedifferentiation processes, indicating two possible cellular fates for the cultured cells: a mesenchymal-like and an epithelial-like state. Furthermore, our investigations identified injured proximal straight tubule cells and stressed intermediate state dendritic cells/macrophages as the principal sources of endogenous Lcn2, providing insights into the cellular dynamics involved in Lcn2 production during allograft rejection. By elucidating the effects of rLcn2 on immune cells and uncovering the cellular origins of Lcn2 expression, this study enhances our understanding of how rLcn2 exerts its renoprotective effects in kidney transplantation. These findings contribute to the growing body of knowledge surrounding Lcn2 as a promising therapeutic target for mitigating immune-mediated damage to the kidney grafts and improving their outcomes.

ZUSAMMENFASSUNG

Die Nierentransplantation (NTx) ist derzeit die einzige kurative Behandlungsoption für Menschen mit terminaler Niereninsuffizienz, die ihnen eine neue Chance auf ausreichende Nierenfunktion bietet. Der Erfolg der NTx wird jedoch durch die immunvermittelte Abstoßung des Transplantats beeinträchtigt, die sowohl in der frühen postoperativen Phase als auch langfristig auftreten kann. Diese Abstoßungsereignisse haben erhebliche Auswirkungen auf die Funktion und das Überleben des Transplantats und stellen langfristig eine große Herausforderung dar. Lipocalin-2 (Lcn2), ein Mitglied der Lipocalin-Familie, hat aufgrund seiner zentralen Rolle bei verschiedenen physiologischen Prozessen, wie dem Transport von Eisen, der Abwehr von Bakterien und der Regulation von Immunreaktionen, große Beachtung im Bereich der Nierentransplantation erfahren. Studien haben gezeigt, dass die Expression von Lcn2 in Nierentransplantaten während akuter Abstoßungsreaktionen erhöht ist, was auf eine Beteiligung an der Immunantwort gegen das Transplantat hinweist. Darüber hinaus haben präklinische Studien das Potenzial von exogen verabreichtem rekombinanten Lcn2 (rLcn2) aufgezeigt, Nierenschäden zu vermindern und das Überleben des Transplantats zu fördern.

Der Schwerpunkt dieser Forschungsarbeit lag darauf, die komplexen molekularen und zellulären Mechanismen, die den nephroprotektiven Effekten von rLcn2 zugrunde liegen, in einem Mausmodell der Nierentransplantation zu erforschen. Die perioperative Behandlung mit rLcn2 führte zu signifikanten Veränderungen sowohl bei adaptiven als auch angeborenen Immunzellpopulationen, wodurch insbesondere die Funktionalität und Degranulationsfähigkeit von Immunzellen im Nierentransplantat beeinflusst wurden. Darüber hinaus erfolgte die Etablierung einer effektiven Methode zur Isolierung und Kultivierung primärer proximaler Tubulusepithelzellen, um ihr Ansprechen auf die Behandlung mit rLcn2 zu untersuchen. Im Laufe des Kultivierungsprozesses zeigten die Tubulusepithelzellen sehr diverse Genexpressionsmuster sowie Anzeichen für beginnende Dedifferenzierungsprozesse, wodurch sich zwei mögliche zelluläre Zustände für die kultivierten Zellen ergaben: ein mesenchymähnlicher oder ein epithelähnlicher Zustand. Unsere Untersuchungen zeigten außerdem, dass verletzte proximale Tubuluszellen des *pars recta* und gestresste intermediäre dendritische Zellen/Makrophagen die Hauptquellen für die Bildung von endogenem Lcn2 sind, was Einblicke in die zelluläre Dynamik der Lcn2-Produktion während der Abstoßung von Allotransplantaten ermöglichte. Durch die Aufklärung der Auswirkungen von rLcn2 auf Immunzellen und die Beschreibung der zellulären Ursprünge der Lcn2-Expression verbessert diese Studie unser Verständnis dafür, wie rLcn2 seine nephroprotektiven Effekte bei Nierentransplantationen entfalten könnte. Diese Ergebnisse tragen zum stetig wachsenden Wissen über Lcn2 als potenziell vielversprechendes Therapeutikum bei, mit dem Ziel immunvermittelte Schäden an Nierentransplantaten zu mindern und das Überleben des Transplantats zu verbessern.

1 INTRODUCTION

The kidneys are remarkable organs that perform crucial functions for maintaining the body's overall health and well-being. Through their intricate filtration system, the kidneys help remove waste products, regulate fluid and electrolyte balance, and produce urine [4-6]. However, diseases affecting the kidneys and thus putting their function and integrity at risk, are of increased prevalence. For example, chronic kidney disease (CKD) affects more than 10 % of the global population, ultimately leading to end-stage renal disease (ESRD) and a tremendous demand for renal replacement therapies and transplantation [7,8]. The scarcity of suitable donor organs, coupled with the limitations of dialysis, underscores the urgent need for effective transplantation options to provide life-saving treatment and significantly improve the quality of life for individuals with end-stage renal disease.

1.1 KIDNEY TRANSPLANTATION (KTx)

Despite advancements in kidney transplantation – remaining the most effective treatment option for individuals facing ESRD – certain challenges persist, including host-driven alloimmune responses, antibody- or T-cell-mediated rejections [9], as well as the risk of early allograft dysfunction and long-term graft loss due to various factors, such as ischemia-reperfusion injury (IRI) [10,11].

Early allograft dysfunction refers to impaired kidney function shortly after transplantation, characterized by delayed graft function (DGF) or slow recovery of graft function. DGF can occur due to several factors, including prolonged cold ischemia time, poor donor quality, and the presence of pre-existing antibodies in the recipient that can cause immune-mediated damage to the transplanted kidney. DGF increases the risk of acute rejection (AR), infection, and other complications, sometimes requiring temporary dialysis until the kidney recovers its function [12,13]. Besides, long-term graft loss is also a significant concern in kidney transplantation. Despite improvements in organ preservation and immunosuppressive therapies prolonging short-term survival, the transplanted kidney may still be susceptible to damage over time, leading to chronic rejection or other complications, as long-term graft survival has improved less effectively in the last decade [14,15]. IRI can occur during the transplantation process and sets in motion a cascade of events that contribute to long-term graft loss. This injury can trigger both immediate and long-term complications in the graft through triggering inflammation, oxidative stress, and immune responses that can eventually lead to tissue fibrosis and chronic dysfunction of the transplanted kidney. It is generally recognized that prolonged ischemia times during kidney transplantation can increase the risk of allograft damage and negatively impact graft function [10,11]. The risks associated with early allograft dysfunction and long-term graft loss underline the pressing need for the development of innovative strategies to mitigate these complications and improve transplantation outcomes.

1.2 LIPOCALIN-2 / NGAL

A promising potential therapeutic agent in kidney transplantation is recombinant Lcn2 (rLcn2), which has recently been described to ameliorate graft function and to exert renoprotective effects [16-18].

Lipocalin 2 (Lcn2), also known as neutrophil gelatinase-associated lipocalin (NGAL), is a 25-kDa glycoprotein predominantly expressed and secreted by neutrophils [19-22]. Lcn2 expression is regulated by multiple factors, including pro-inflammatory cytokines, reactive oxygen species (ROS), and nuclear factor-κB (NF-κB) signalling [23-26]. Its essential role lies in antibacterial innate immune responses through iron-siderophore binding and delivery to various organs and sites of inflammation [27,28]. Lcn2 stimulates chemotaxis, promoting a faster migration of white blood cells to the side of an infection, thus stimulating immune response [29]. Furthermore, studies have demonstrated its involvement in the growth, differentiation, and apoptosis of mammalian cells, which significantly relies on the regulation of iron homeostasis within the target cells [30-33]. However, the effects of Lcn2 on targeted cells depend on its nature, specifically whether it is bound to iron, as this determines whether Lcn2 will sequester or deliver iron into cells, resulting in proapoptotic or survival effects, respectively [32,34]. When iron-loaded, Lcn2 delivers iron and prevents apoptosis, whereas in its iron-lacking form, it depletes cellular iron and induces apoptosis. Moreover, Lcn2 plays a role in ameliorating morphological and functional damage by reducing apoptosis of tubular epithelial cells and stimulating their proliferation, which depends on the delivery of sufficient amounts of iron to specific cellular structures [30-33]. Lcn2 levels in blood serum and urine have shown promise as early indicators for acute kidney injury (AKI) and delayed graft function, as well as a potential biomarker for acute renal graft rejection, due to a strong induction in damaged nephron epithelia resulting in a release of Lcn2 into body fluids, and an upregulation in renal transplants [35-37]. While the precise mechanisms of Lcn2 are not yet fully elucidated, studies have revealed its ability to reduce tubular cell death, enhance tubular epithelial cell proliferation, and facilitate the recovery of renal structure and function in models of IRI [17,18,38]. Additionally, during renal allograft rejection, elevated serum levels of Lcn2 were found to mainly originate from the host rather than the graft itself [17]. However, the functional role of Lcn2 during IRI remains controversial. Some studies suggest that Lcn2 exhibits protective properties during AKI and IRI [18,38,39], while others propose that it induces excessive autophagy, cell damage, and cell death [40,41]. In kidney transplantation, Lcn2 has been detected in allograft biopsies using immunohistochemistry. Its presence predicts the degree of AKI, which correlates significantly with postoperative serum creatinine levels and the subsequent need for dialysis [38]. Additionally, urinary Lcn2, at a specific cutoff, accurately distinguishes acute allograft rejection from other causes of AKI in the post-transplant follow-up [42,43]. However, limited data exist regarding the function of endogenously synthesized Lcn2 in kidney allografts and the biological functions and metabolism of exogenously administered recombinant Lcn2:Siderophore:Fe complex (rLcn2) in the recipient.

1.3 EPITHELIA IN THE NEPHRON

Building up as the functional unit of the kidney, the nephron holds responsibility for solute uptake, secretion, and reabsorption [5,6]. Within the intricate microarchitecture of the kidney, the nephron consists of distinct segments that perform specific functions and respond uniquely to injury. Key structural elements within the nephron include the glomerulus, a cluster of permeable capillaries; the Bowman's capsule, a cup-shaped structure that collects ultrafiltrate; and the juxtaglomerular apparatus, housing the macula densa. The proximal tubule, comprising both a convoluted segment in the cortical region and a straight segment in the outer stripe of the outer medulla, primarily handles solute reabsorption. The distal tubule plays a major role in water reabsorption. The Loop of Henle encompasses the descending thin limb (highly permeable to water), ascending thin limb (impermeable to water), and ascending thick limb (responsible for ion reabsorption). Furthermore, the distal convoluted tubule facilitates additional ion reabsorption, while the collecting duct system is responsible for further reabsorbtion of water (**Figure 1**).

These tubular segments, by actively secreting and reabsorbing specific molecules, regulate the urine's composition and serve as a significant site for Lcn2 absorption. Epithelial cells within the nephron

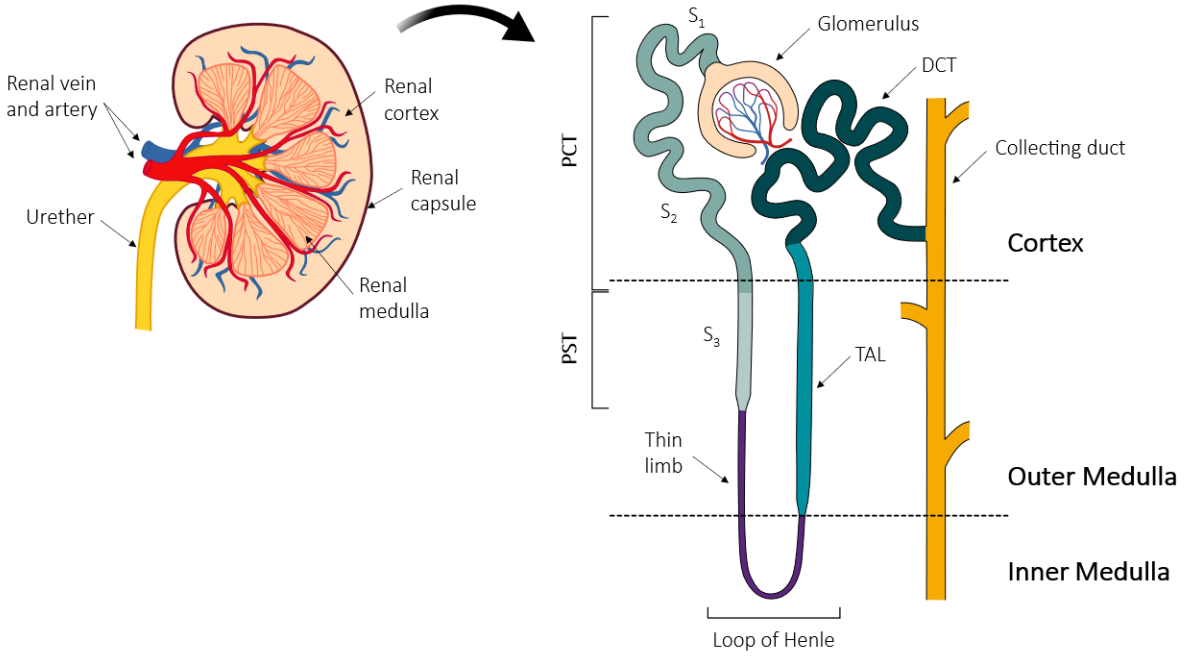

Figure 1: Schematic overview of the kidney and its functional unit, the nephron.
The kidney is comprised of two major compartments: the renal cortex and the renal medulla, which is segmented into outer and inner medulla. The renal capsule surrounds the functional tissue of the kidney and protects it from injury. Stretched through the three segments of the kidney, nephrons build up as the functional units, being responsible for urine filtration, reabsorption, secretion, and maintaining electrolyte and water balance. PCT—proximal convoluted tubule, PST—proximal straight tubule, DCT—distal convoluted tubule, TAL—thick ascending limb. Own illustration based on [1,2].

play a vital role in maintaining kidney homeostasis and responding to injuries, with particular emphasis on the proximal tubules [4-6,44,45].

1.3.1 PROXIMAL TUBULES

Proximal tubules (PT) are crucial structures within the kidneys due to their high metabolic activity and involvement in transport processes. As the major sites for water, electrolyte, nutrient, and especially Lcn2 absorption and delivery of Lcn2 to the sites of inflammation, the proximal tubules bear responsibility for approximately 60-70 % of the comprehensive solute reabsorption from the glomerular filtrate, while the distal tubules account for around 20-25 % of the overall reabsorption [46,47]. However, proximal tubules display strong susceptibility to ischemic and nephrotoxic insults, leading to impaired reabsorption, inflammation, and the release of damage-associated molecular patterns (DAMPs) [48-53]. Consequently, they significantly contribute to the pathogenesis of kidney transplant injury.

PT are broadly segmented into the proximal convoluted tubule (*pars convoluta*) and the proximal straight tubule (*pars recta*). A further division into S_1, S_2, and S_3 segments relates to ultrastructural characteristics, e.g. abundance and height of microvilli [6,54] (**Figure 1**). Depending on the length of the nephron, S_1 segments originate at the urinary pole of the glomerulus, situated in the outer layers of the cortex. They transition gradually into S_2 segments as they traverse through the inner cortex region. Finally, the S_2 segments continue their transformation at various levels within the medullary pyramids. This progression culminates in the S_3 segments, which extend up to the boundary between the outer and the inner stripe. The convoluted part encompasses the subsegment S_1 and the initial portion of S_2, whereas the remaining section of S_2 and S_3 belong to the proximal straight tubule [4,6,45,55].

The luminal surface of the PT is lined by proximal tubular epithelial cells (PTEC), mainly responsible for reabsorbing solutes from the glomerular filtrate, maintaining electrolyte balance, and participating in various metabolic processes, including glucose metabolism and energy production, utilizing energy for nutrient reabsorption and waste secretion [5,6]. Moreover, PTEC have been described as target cells of Lcn2 [18,32]. Upon occurrence of kidney damage, PTEC are mainly affected and can suffer from serious injuries, eventually leading to impaired kidney function.

Due to the expression of pore-forming claudins-2 and 10 in the tight junctions between the PTEC, the proximal tubule epithelium is often referred to as being “leaky” [54,56]. PT demonstrate high transport rates primarily driven by Na^+/K^+ ATPase. This process demands substantial energy, mainly fulfilled through oxidative metabolism [57]. Consequently, the apical membrane of PTEC features numerous microvilli, significantly increasing the surface area available for reabsorption. However, the height and abundance of microvilli notably decreases from the proximal convoluted tubule (PCT) to the proximal straight tubule (PST) [5,6]. Alongside the expression of AQP1 and sodium-glucose dependent transporters such as SGLT1 and SGLT2, the apical membrane of the proximal tubular epithelial cells also

expresses further specific receptors, including megalin (*Lrp2*) and cubulin. The majority of filtered soluble proteins, including Lcn2, are reabsorbed in the kidney by the megalin-cubulin receptor complex [3,58-60]. Interaction with the megalin-cubulin complex facilitates the uptake, internalization, and transport of Lcn2 and rLcn2 to the sites of inflammation, including the proximal tubular interstitium, where it may exert protective effects [61,62] (**Figure 2**). However, another specific receptor known as the organic cation transporter *24p3R* facilitating the transport of Lcn2 along with several low and high molecular weight proteins, is predominantly expressed in distal tubules and collecting ducts [30,63,64].

Besides playing a crucial role in renal function by reabsorbing essential nutrients, maintaining electrolyte and acid-base balance, regulating water reabsorption, and participating in various metabolic processes, proximal tubules in kidney transplantation additionally contribute to the immune response through antigen presentation, chemokine/cytokine production, and modulation of immune cell activation [65-68]. In response to stimuli such as IRI and inflammatory mediators, proximal tubular cells can express Lcn2; however, the precise source and the route of endogenously produced Lcn2 has not yet

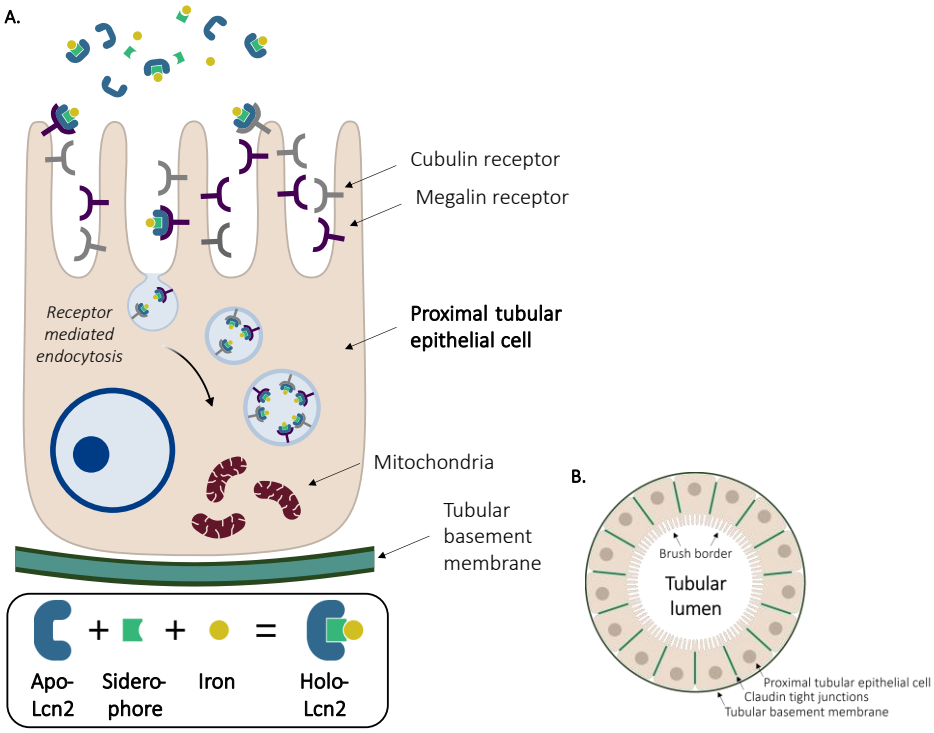

Figure 2: Schematic overview of the megalin-cubulin complex-mediated uptake of Lcn2/rLcn2 in a proximal tubular epithelial cell.

(A) Sagittal and **(B)** cross section of a proximal tubule:

(A) PTEC are lined along the luminal surface of the proximal tubules. They possess a characteristic brush border of microvilli on the apical surface expressing various receptors for solute uptake. PTEC are separated by tight junctions comprised of claudins. Characteristically, high numbers of mitochondria are located at the basal site of the cells responding to the high demand of energy for transport processes. The tubular basement membrane protects the cells from mechanical stress and separates them from adjacent tissues.

(B) Iron-free apo-Lcn2 or bacterial siderophore-iron loaded holo-Lcn2 (rLcn2) are taken up by receptor mediated endocytosis through binding to the megalin (*Lrp2*)-cubulin complex located on the apical surface of the PTEC. Own illustration based on [2,3].

been fully investigated. Understanding the intricate interactions between proximal tubules and the immune system is essential for comprehending the complex dynamics of kidney transplantation and developing strategies to improve transplant outcomes.

1.4 AIM OF THE STUDY

Based on the findings that perioperative treatment with rLcn2 significantly reduces histological lesions and infiltration of immune cells into the inflamed tissue, as well as significantly improves renal function [16-18], we hypothesize that rLcn2 provides renoprotection by modulating recipient alloimmunity and regulating inflammatory responses mediated by proximal tubular epithelial cells (PTEC). Consequently, the primary objective of this study is to gain a comprehensive understanding of the immunoregulatory and cytoprotective effects mediated by exogenously administered recombinant Lipocalin-2 (rLcn2) during allograft injury in kidney transplantation. Elucidating the underlying molecular and cellular mechanisms is crucial for the successful translation of the rLcn2-therapy into clinical practice.

The presented research encompasses the influence of rLcn2 on immune cell activation, differentiation, and function to elucidate its role in modulating the immune response against the transplanted kidney. To address the mechanisms by which rLcn2 mitigates tissue damage and promotes survival signalling, one objective is to examine the effects of rLcn2 on oxidative stress, inflammatory responses, and cell survival pathways in primary PTEC –the structural units of the nephron– to understand how rLcn2 contributes to the protection of the transplanted kidney. Considering that endogenously expressed Lcn2 does not appear to confer protection against AKI and AR [17], another objective was to investigate the cellular sources of endogenous Lcn2 during these conditions. This approach aimed at a comprehensive understanding of its limitations in preventing damage and its transition into a protective role.

By addressing these research questions, the overall aim is to contribute to the development of targeted therapies and enhance our understanding of the potential limitations and opportunities associated with Lcn2 as a therapeutic agent in clinical practice.

2 MATERIALS AND METHODS

2.1 EQUIPMENT

Table 1: List of equipment/laboratory materials used in this study.

Name	Supplier	Cat. No.
10x Magnetic Separator	10x Genomics, Pleasanton, California, USA	120250
µMACS™ Separator	BD Biosciences, San Jose, California, USA	130-042-602
10x Vortex Adapter	10x Genomics, Pleasanton, California, USA	120251
70 mL, Polycarbonate Bottle Assembly, 38 x 102 mm	Beckman Coulter Diagnostics, Brea, California, USA	355622
Applied Biosystems™ MicroAmp™ Fast Optical 96-Well Reaction Plate, 0.1 mL	Applied Biosystems™| Thermo Fisher Scientific Inc., Waltham, Massachusetts, USA	4346907
BD Discardit™ II Syringe, 2 mL	BD Biosciences, San Jose, California, USA	300928
BD Discardit™ II Syringe, 5 mL	BD Biosciences, San Jose, California, USA	309050
BD Discardit™ II Syringe, 10 mL	BD Biosciences, San Jose, California, USA	309110
BD Discardit™ II Syringe, 20 mL	BD Biosciences, San Jose, California, USA	300296
BZO Seal Film Adhesive Optical Film	Biozym Scientific GmbH, Hessisch Oldendorf, Germany	712350
CASY-Cups	OMNI Life Science GmbH & Co KG, Bremen, Germany	5651794
Cell culture plate, 6 well, surface: Standard, flat base	Sarstedt AG & Co.KG, Nümbrecht, Germany	833.920
Cell culture plate, 12 well, surface: Standard, flat base	Sarstedt AG & Co.KG, Nümbrecht, Germany	833.921
Cell culture plate, 24 well, surface: Standard, flat base	Sarstedt AG & Co.KG, Nümbrecht, Germany	833.922
Cell scraper with 2-position blade, sterile	Sarstedt AG & Co.KG, Nümbrecht, Germany	83.1832
Cell Strainer, 40 µm	VWR International, Radnor, Pennsylvania, USA	732-2757
Corning® 96-well Clear Flat Bottom Polystyrene Not Treated Microplate, with Lid, Sterile	Corning, Glendale, Arizona, USA	1015536
Corning® 96-well Clear V-Bottom Polystyrene Not Treated Microplate, Sterile	Corning, Glendale, Arizona, USA	1017254
Corning® Primaria™ 60 mm x 15 mm Standard Cell Culture Dish	Corning, Glendale, Arizona, USA	353802
Corning® Primaria™ 100 mm x 20 mm Standard Cell Culture Dish	Corning, Glendale, Arizona, USA	353803
Corning® Primaria™ 75 cm² Rectangular Straight Neck Cell Culture Flask with Vented Cap	Corning, Glendale, Arizona, USA	353810
Countess Cell Counting Chamber Slides	Invitrogen, Carlsbad, California, USA	C10228
Counting chamber Neubauer improved Dark lines, 0.1 mm	Carl Roth, Karlsruhe, Germany	PC73.1
DNA LoBind Microcentrifuge Tubes	Eppendorf, Hamburg, Germany	22431021
Falcon® 40 µm Cell Strainer, Blue, Sterile	Corning, Glendale, Arizona, USA	352340
Falcon® 5 mL Round Bottom Polystyrene Test Tube, with Snap Cap, Sterile	Corning, Glendale, Arizona, USA	352054
Falcon® 5 mL Round Bottom Polystyrene Test Tube, without Cap	Corning, Glendale, Arizona, USA	352008
Falcon® 5 mL Round Bottom Polystyrene Test Tube, without Cap, Nonsterile	Corning, Glendale, Arizona, USA	352008
Falcon® 60 mm TC-treated Easy-Grip Style Cell Culture Dish, Sterile	Corning, Glendale, Arizona, USA	353004

Falcon™ 15 mL Conical Centrifuge Tubes	Fisher Scientific GmbH, Schwerte, Germany	10773501
Falcon™ 50 mL Conical Centrifuge Tubes	Fisher Scientific GmbH, Schwerte, Germany	10788561
gentleMACS™ C Tubes	Miltenyi Biotec B.V. & Co, Bergisch Gladbach, Germany	130-093-237
Invitrogen™ iBlot™ 2 Transfer Stacks, nitrocellulose, regular stacks	Invitrogen | Thermo Fisher Scientific Inc., Waltham, Massachusetts, USA	IB2300
LS Columns	Miltenyi Biotec B.V. & Co, Bergisch Gladbach, Germany	130-042-401
MACS® SmartStrainers (100 µm)	Miltenyi Biotec B.V. & Co, Bergisch Gladbach, Germany	130-098-463
MACS® SmartStrainers (30 µm)	Miltenyi Biotec B.V. & Co, Bergisch Gladbach, Germany	130-098-458
MicroAmp™ Fast Optical 96-Well Reaction Plate, 0.1 mL	Thermo Fisher Scientific Inc., Waltham, Massachusetts, USA	4346907
Microscope slides Corners grounded 90°, With frosted edge	Carl Roth, Karlsruhe, Germany	H870.1
Nunc™ Lab-Tek™ Chamber Slide, 4 well Permanox® slide	Thermo Fisher Scientific Inc., Waltham, Massachusetts, USA	177437
Nunc™ Lab-Tek™ II Chamber Slide System	Thermo Fisher Scientific Inc., Waltham, Massachusetts, USA	10098850
pluriStrainer® Mini 20 µm	pluriSelect, Leipzig, Germany	43-10020-40
pluriStrainer® Mini 40 µm	pluriSelect, Leipzig, Germany	43-10040-40
pluriStrainer® Mini 100 µm	pluriSelect, Leipzig, Germany	43-10100-46
pluriStrainer® 200 µm	pluriSelect, Leipzig, Germany	43-50200-03
RNase-free Microfuge Tubes	Thermo Fisher Scientific Inc., Waltham, Massachusetts, USA	AM12400
Safe-lock tubes 1.5 mL, colourless	Eppendorf, Hamburg, Germany	30120086
Safe-Lock Tubes, 0,5 mL, colourless	Eppendorf, Hamburg, Germany	0030121023
Tissue culture dish, (Ø x H): 60 x 15 mm, surface: Cell+	Sarstedt AG & Co.KG, Nümbrecht, Germany	833.901.300
Tissue-Tek® Cryo-Mold, Biopsy 10 x 10 x 5 mm	Electron Microscopy Sciences, Hatfield, Pennsylvania, USA	62534-10
Transferpipettes	Sarstedt AG & Co.KG, Nümbrecht, Germany	861.171
Whatman® Gel Blotting Papers 3MM, Thickness 0.34 mm	Carl Roth, Karlsruhe, Germany	0043.1

2.2 CHEMICALS AND REAGENTS

Table 2: List of chemicals and reagents used in this study.

Chemicals	Supplier	Cat. No.
0.05 % Trypsin in PBS with 0.02% EDTA, w/o Mg^{2+}, Ca^{2+}	Bio&SELL GmbH, Feucht, Germany	L 2143
1X Phosphate Buffered Saline (PBS)	Gibco™, Grand Island, New York, USA	14190-144
2-Propanol	Carl Roth, Karlsruhe, Germany	AE73.2
3,3',5-Triiodo-L-thyronine (sodium salt hydrate)	Cayman Chemical, Ellsworth, Ann Arbor, Michigan, USA	16028
alpha-Ketoglutaric acid,>=98.5 % (NaOH, titration) (K-1750)	Sigma-Aldrich, Saint Louis, Missouri, USA	K1750-100G
Ammonium chloride	Merck KGaA, Darmstadt, Germany	12125-02-9
Aqua-Poly/Mount	Polysciences Inc., Warrington, Pennsylvania, USA	18606-20
Aquatex®	Sigma-Aldrich, St. Louis, USA	108562
β-Glycerophosphate disodium salt pentahydrate, ≥97 %	Carl Roth, Karlsruhe, Germany	6847.1

Bovine Serum Albumin heat shock fraction, pH 7, ≥98 %	Sigma-Aldrich, Saint Louis, Missouri, USA	A7906
Bovine Serum Albumin, lyophilized powder, BioReagent, suitable for cell culture	Sigma-Aldrich, Saint Louis, Missouri, USA	A9418
Bovine Serum Albumin, fatty acid free, low endotoxin, lyophilized powder	Sigma-Aldrich, Saint Louis, Missouri, USA	A8806-1G
Brefeldin A	Cayman Chemical, Ann Arbor, Michigan, USA	CAY11861-25
BSA Fraktion V	Carl Roth, Karlsruhe, Germany	8076.4
Calcium D-gluconate monohydrate, >= 98 %	Sigma-Aldrich, Saint Louis, Missouri, USA	G4625-500G
Cell Stimulation Cocktail (500X)	eBioscience™ | Thermo Fisher Scientific Inc., Waltham, Massachusetts, USA	4970-93
Cell Stimulation Cocktail (with protein transport inhibitors) (500X)	eBioscience™ | Thermo Fisher Scientific Inc., Waltham, Massachusetts, USA	00-4975-03
Collagenase, Type IV, powder	Gibco™, Grand Island, New York, USA	17104019
Complete Epithelial Cell Medium /w Kit	Cell Biologics Inc, Chicago, Illinois, USA	M6621
cOmplete™ Tablets, Mini, EDTA-free Protease Cocktail	Roche Holding, Basel, Schweiz	11836170001
cOmplete™, Mini, EDTA-free Protease Inhibitor Cocktail	Merck KGaA, Darmstadt, Germany	11697498001
D(+)-Sucrose ≥ 99.9 %, ultrapure DNase-, RNase-free	VWR International, Radnor, PA, USA	0335-500G
DMEM, no glucose, no glutamine, no phenol red	Gibco™, Grand Island, New York, USA	A1443001
DNase I grade II	Roche Holding, Basel, Schweiz	10104159001
Ethanol ≥ 70 %, denatured	Carl Roth, Karlsruhe, Germany	T913.3
Ethanol ≥ 99.8 %, denatured	Carl Roth, Karlsruhe, Germany	K928.4
Ethylenediaminetetraacetic acid disodium salt dihydrate	Sigma-Aldrich, Saint Louis, Missouri, USA	6381-92-6
FcR Blocking Reagent, mouse	Miltenyi Biotec B.V. & Co, Bergisch Gladbach, Germany	130-092-575
Fetal Bovine Serum (FBS) Superior stabil®	Bio&SELL GmbH, Feucht, Germany	S 0615
Formaldehyde 4 %	VWR International, Radnor, PA, USA	9713.5000
Foxp3 / Transcription Factor Staining Buffer Set	eBioscience™ | Thermo Fisher Scientific Inc., Waltham, Massachusetts, USA	00-5523-00
Gelatin from porcine skin	Sigma-Aldrich, Saint Louis, Missouri, USA	G1890
Gibco™ Gentamicin Reagent (50 mg/ml)	Gibco™, Grand Island, New York, USA	15750-060
Gibco™ RPMI 1640 Medium, no glutamine	Thermo Fisher Scientific Inc., Waltham, Massachusetts, USA	31870074
Gibco™ RPMI 1640 Medium, with glutamine	Thermo Fisher Scientific Inc., Waltham, Massachusetts, USA	11879020
Gibco™ William's E Medium, no phenol red	Gibco™, Grand Island, NewYork, USA	A1217601
Glucose 5 % Braun Mini-Plasco connect	B. Braun SE, Melsungen, Germany	PZN-03159474
Glycerol, 1 L, ROTIPURAN® ≥ 99,5 %, p.a., anhydrous	Carl Roth, Karlsruhe, Germany	3783.1
Ham´s F12 Medium, w/o: L-Glutamine, w/o: Phenol red	PAN-Biotech GmbH, Aidenbach, Germany	P04-14559
Hematoxylin solution, Gill No.1	Sigma-Aldrich, St. Louis, USA	GHS132
Huminsulin® Normal (100 IE/ml)	LILLY Deutschland GmbH, Gießen, Germany	PZN-02526396
Hydrocortison BioReagent, suitable for cell culture	Sigma-Aldrich, Saint Louis, Missouri, USA	H0888
Ionomycin calcium salt	Sigma Aldrich, St. Louis, Missouri, USA	I0634-1MG
MACSQuant® Tyto® Running Buffer	BD Biosciences, San Jose, California, USA	130-107-207
Magnesium sulfate heptahydrate	Sigma-Aldrich, Saint Louis, Missouri, USA	10034-99-8
MILLIPLEX MAP Lysis buffer for Multiplexing	Merck KGaA, Darmstadt, Germany	43-040
Monensin Solution (1,000X)	BioLegend, San Diego, California, USA	420701

Mouse EGF	Miltenyi Biotec B.V. & Co, Bergisch Gladbach, Germany	130-094-036
Mouse IL-2	Miltenyi Biotec B.V. & Co, Bergisch Gladbach, Germany	130-094-055
Natriumacetate-Trihydrate	Merck KGaA, Darmstadt, Germany	6131-90-4
Natriumacid ≥98 %	Carl Roth, Karlsruhe, Germany	4221
Nuclease-free Water	Invitrogen, Carlsbad, California, USA	AM9937
Opal dyes	Akoya Biosciences, Marlborough, USA	FP1488001KT
PageRuler™ Prestained Protein Ladder, 10 to 180 kDa	Thermo Fisher Scientific Inc., Waltham, Massachusetts, USA	26616/26617
Paraformaldehyd powder, 95 %	Sigma-Aldrich, Saint Louis, Missouri, USA	158127
Paraformaldehyde	Carl Roth, Karlsruhe, Germany	0335.1
PBS, pH 7.4	Gibco™, Grand Island, New York, USA	10010015
PCR-grade Water; Nuclease-free Water	Jena Bioscience GmbH, Jena, Germany	PCR-258L
Phorbol-12-myristat-13-acetate ≥ 99 % (TLC)	Sigma-Aldrich, Saint Louis, Missouri, USA	P8139-1MG
Phosphatase Inhibitor Cocktail 3, DMSO solution	Sigma-Aldrich, Saint Louis, Missouri, USA	P0044
Pierce™ BCA Protein Assay Reagent A	Thermo Fisher Scientific Inc., Waltham, Massachusetts, USA	23223
Pierce™ BCA Protein Assay Reagent B	Thermo Fisher Scientific Inc., Waltham, Massachusetts, USA	23224
Potassium bicarbonate	Sigma-Aldrich, Saint Louis, Missouri, USA	298-14-6
Potassium phosphate dibasic trihydrate	Sigma-Aldrich, Saint Louis, Missouri, USA	16788-57-1
Potassium phosphate dibasic trihydrate,ReagentPlus(R), >= 99.0 %	Sigma-Aldrich, Saint Louis, Missouri, USA	P5504-100G
Potassium phosphate monobasic	Merck KGaA, Darmstadt, Germany	7778-77-0
Pre-Separation Filters (20 µm)	Miltenyi Biotec B.V. & Co, Bergisch Gladbach, Germany	130-101-812
Propidium iodide solution (1.0 mg/mL)	Sigma-Aldrich, Saint Louis, Missouri, USA	P4864
Protein Block Serum-Free	Dako, Carpinteria, USA	X0909
Protein Standard analytical standard, 200 mg/mL (BSA)	Sigma-Aldrich, Saint Louis, Missouri, USA	P5369
Proteinase K, 100 mg	Carl Roth, Karlsruhe, Germany	7528.1
QIAzol Lysis Reagent	Qiagen, Hilden, Germany	79306
RiboLock RNase Inhibitor (40 U/µl)	Thermo Fisher Scientific Inc., Waltham, Massachusetts, USA	EO0384
Ribonucleoside Vanadyl Complex	New England BioLabs (NEB), Ipswich, Massachusetts, USA	S1402S
rLcn2-Apo (rLcn2; iron-free) and rLcn2-Holo (rLcn2:Siderophore:Fe)	Ao.Univ.-Prof. Dr. Hubert G. Schwelberger, Medizinische Universität Innsbruck, MolekularBiologisches Labor, Innsbruck, Austria	N/A
RNAlater™ Stabilization Solution	Thermo Fisher Scientific Inc., Waltham, Massachusetts, USA	AM7020
RNase AWAY™ Surface Decontaminant	Thermo Fisher Scientific Inc., Waltham, Massachusetts, USA	11952385
RNase-Free DNase Set	Qiagen, Hilden, Germany	79254
RNaseZAP™ Cleaning agent for removing Rnase	Thermo Fisher Scientific Inc., Waltham, Massachusetts, USA	AM9780
Roti® - Histol	Carl Roth, Karlsruhe, Germany	6640.1
ROTI® Histofix	Carl Roth, Karlsruhe, Germany	5666.2
Roti®-Histokitt II	Carl Roth, Karlsruhe, Germany	T160.2
SDS pellets ≥ 99 %	Carl Roth, Karlsruhe, Germany	CN30.7
Sodium fluoride	Merck KGaA, Darmstadt, Germany	106441
Sodium orthovanadate	Sigma-Aldrich, Saint Louis, Missouri, USA	S6508
Sodium pyrophosphate tetrabasic	Merck KGaA, Darmstadt, Germany	P8010

Sodium pyruvate (100 mM)	Bio&SELL GmbH, Feucht, Germany	L 0473
Sodium selenite, BioReagent	Sigma-Aldrich, Saint Louis, Missouri, USA	S5261
Sucrose, ultrapure, ≥ 99 %	ICN Biomedicals Inc., Aurora, Ohio, USA	821713
TaqMan™ Fast Advanced Master Mix	Applied Biosystems™| Thermo Fisher Scientific Inc., Waltham, Massachusetts, USA	4444557
TaqMan™ Gene Expression Master Mix	Thermo Fisher Scientific Inc., Waltham, Massachusetts, USA	4371135
Toluol, EMSURE® ACS, ISO, Reag. Ph. Eur.	Merck KGaA, Darmstadt, Germany	MERC1.08325.1000_P
Transferrin, Apo-, Low Endotoxin Grade, Human Plasma	Merck KGaA, Darmstadt, Germany	178481
Triton® X 100	Carl Roth, Karlsruhe, Germany	3051.3
Trypsin/EDTA in PBS, 0.05%/0.02% - w/o Ca^{2+}, Mg^{2+}	Bio&SELL GmbH, Feucht, Germany	BS.L2143
Tween 20®	Sigma-Aldrich, Saint Louis, Missouri, USA	P1379-250ML
VECTASHIELD® Antifade Mounting Medium (H-1000-NB)	Vector Laboratories, Newark, NJ, USA	VEC-H-1000
Xylene, Baker analyzed	Avantor™, Radnor, PA, USA	8080.5000

Table 3: List of fluorescence antibodies for flow cytometrical analysis used in this study.

Antibody	Supplier	Cat. No.
7-AAD Viability	eBioscience™ | Thermo Fisher Scientific Inc., Waltham, Massachusetts, USA	00-6993-42
Alexa Fluor® 647 anti-mouse CD206 (MMR) Antibody, Clone C068C2	BioLegend, San Diego, California, USA	141711
APC anti-mouse CD159a ($NKG2A^{B6}$) Antibody, Clone 16A11	BioLegend, San Diego, California, USA	142808
APC Annexin V	BioLegend, San Diego, California, USA	640920
APC anti-mouse CD335 (NKp46) Antibody, Clone 29A1.4	BioLegend, San Diego, California, USA	137608
APC anti-mouse Perforin Antibody, Clone S16009B	BioLegend, San Diego, California, USA	154404
APC/Cyanine7 anti-mouse Ly-6C Antibody, Clone HK1.4	BioLegend, San Diego, California, USA	128025
APC-eFluor™ 780, CD44 Monoclonal Antibody, Clone IM7	eBioscience™ | Thermo Fisher Scientific Inc., Waltham, Massachusetts, USA	47-0441-82
BD Horizon™ BUV395 Rat Anti-Mouse CD45, Clone 30-F11	BD Biosciences, San Jose, California, USA	564279
BD Pharmingen™ Purified NA/LE Hamster Anti-Mouse CD3e, Clone 145-2C11	BD Biosciences, San Jose, California, USA	553057
BD Pharmingen™ Purified NA/LE Hamster Anti-Mouse CD28, Clone 37.51	BD Biosciences, San Jose, California, USA	553294
Brilliant Violet 421™ anti-mouse CD11c Antibody, Clone N418	BioLegend, San Diego, California, USA	117343
Brilliant Violet 421™ anti-mouse CD62L Antibody, Clone MEL-14	BioLegend, San Diego, California, USA	104436
Brilliant Violet 421™ anti-mouse IL-17A Antibody, Clone TC11-18H10.1	BioLegend, San Diego, California, USA	506926
Brilliant Violet 510™ anti-mouse/human CD45R/B220 Antibody, Clone RA3-6B2	BioLegend, San Diego, California, USA	103248
Brilliant Violet 605™ anti-mouse CD8a Antibody, Clone 53-6.7	BioLegend, San Diego, California, USA	100744
Brilliant Violet 650™ anti-mouse I-A/I-E Antibody (MHC-II), Clone M5/114.15.2	BioLegend, San Diego, California, USA	107641

Brilliant Violet 650™ anti-mouse IFNγ Antibody, Clone XMG1.2	BioLegend, San Diego, California, USA	505832
Brilliant Violet 711™ anti-mouse CD4 Antibody, Clone RM4-5	BioLegend, San Diego, California, USA	100550
Brilliant Violet 785™ anti-mouse/human CD11b Antibody, Clone M1/70	BioLegend, San Diego, California, USA	101243
DAPI (4',6-Diamidino-2-Phenylindole, Dihydrochloride)	Invitrogen, Carlsbad, California, USA	D1306
FITC anti-mouse CD335 (NKp46) Antibody, Clone 29A1.4	BioLegend, San Diego, California, USA	137606
PE anti-mouse CD103 Antibody, Clone 2E7	BioLegend, San Diego, California, USA	121406
PE anti-mouse CD314 (NKG2D) Antibody, Clone CX5	BioLegend, San Diego, California, USA	130208
PE/Cyanine7 anti-mouse CD69 Antibody, Clone H1.2F3	BioLegend, San Diego, California, USA	104512
PE/Cyanine7 anti-mouse Ly-6G Antibody, Clone 1A8	BioLegend, San Diego, California, USA	127617
PE/Cyanine7 anti-mouse/rat/human CD27 Antibody, Clone LG.3A10	BioLegend, San Diego, California, USA	124216
PE/Dazzle™ 594 anti-mouse CD107a (LAMP-1) Antibody, Clone 1D4B	BioLegend, San Diego, California, USA	121624
PerCP-Vio® 700 anti-mouse, CD3ε Antibody, Clone REA641	Miltenyi Biotec B.V. & Co, Bergisch Gladbach, Germany	130-109-841
RFP Antibody Pre-adsorbed, Rabbit Polyclonal	Rockland Immunochemicals, Inc., Pottstown, PA, USA	600-401-379
Zombie Aqua™ Fixable Viability Kit (Live/Death-L/D)	BioLegend, San Diego, California, USA	423101

Table 4: List of beads used in this study.

Beads	Supplier	Cat. No.
Anti-Prominin-1 MicroBeads, mouse	Miltenyi Biotec B.V. & Co, Bergisch Gladbach, Germany	130-092-333
Anti-Rabbit, IgG MicroBeads	Miltenyi Biotec B.V. & Co, Bergisch Gladbach, Germany	130-048-602
CD45 MicroBeads, mouse	Miltenyi Biotec B.V. & Co, Bergisch Gladbach, Germany	130-052-301
GFP MicroBeads (from µMACS™ GFP Isolation Kit)	Miltenyi Biotec B.V. & Co, Bergisch Gladbach, Germany	130-091-125
MILLIPLEX MAP ß-Tubulin Total Magnetic Bead MAPmate™ - Cell Signaling Single Plex or Multiplex Assay	Merck KGaA, Darmstadt, Germany	46-713MAG
Precision Count Beads™	BioLegend, San Diego, California, USA	424902
ProLine Universal Calibration Beads	Bio-Rad Laboratories, Inc., Hercules, California, USA	1451086

2.3 MEDIA, BUFFER, AND SOLUTIONS

Table 5: List of media, buffer, and solutions used in this study.

Chemical / Reagent	Volume / Weight	Final concentration
Digestion medium		
Mouse-medium	6.0 mL	
Collagenase IV	60.0 µL	
DNase (stock: 100 mg/mL)	48.0 µL	
Medium E		
DMEM (phenol free)	225.0 mL	1:1
Ham's F12	225.0 mL	1:1
L-Glutamine	5.0 mL	2.0 mM
Transferrin	250.0 µL	5.0 µg/mL
T3 (Triiodo-L-thyronine)	20.0 µL	4.0 pg/mL
Sodium Selenite	5.0 µL	5.0 ng/mL
filter through 0.22 µm		
Mouse-medium		
RPMI-1640 with L-Glutamine	500.0 mL	
FBS (heat-inactivated)	50.0 mL	10.0 %
Penicillin/Streptomycin (100µg/mL)	5.0 mL	1.0 %
98b Buffer (pH 7.4)		
NaCl	8,18 g	140,0 mmol/L
KH_2PO_4	0,05 g	0,4 mmol/L
K_2HPO_4 x 3 H_2O	0,37 g	1,6 mmol/L
$MgSO_4$ x 7 H_2O	0,25 g	1,0 mmol/L
Na-Acetat x 3 H_2O	1,36 g	10,0 mmol/L
α-Ketoglutarat (K-1750)	0,14 g	1,0 mmol/L
Ca-Gluconat x 1 H_2O	0,58 g	1,3 mmol/L
add up to 1 L with dH_2O, adjust pH and filter through 0. 22µm		
ACK-Lysis Buffer (pH 7.2-7.4)		
NH_4Cl	8.29 g	
$KHCO_3$	1.00 g	
Na_2EDTA	37.20 mg	
add up to 1 L with dH_2O and adjust pH		
HBSS buffer solution 1 (10X, pH 7.4)		
KCl	4.0 g	5.4 mM
Na_2HPO_4 x $7H_2O$	0.9 g	0.3 mM
KH_2PO_4	0.6 g	0.4 mM
$NaHCO_3$	3.5 g	4.2 mM
NaCl	80.0 g	137.0 mM
D-glucose	10.0 g	5.6 mM
add up to 1 L with dH_2O and adjust pH		

HBSS buffer solution2 (10X, pH 7.4)

$CaCl_2$ x $2H_2O$	1.91 g	1.3 mM
$MgCl_2$ x $6H_2O$	1.00 g	0.5 mM
$MgSO_4$ x $7H_2O$	1.00 g	0.6 mM

Add dH_2O to 1 L and adjust pH to 7.4

Lysis Buffer (1mL)

TST-Buffer	920 µL	1X
Complete	10 µL	1X
NaOrV	10 µL	1.0 mM
β-GP	10 µL	10.0 mM
NaF	10 µL	5.0 mM
$Na_4P_2O_2$	40 µL	1.0 mM

PEB Buffer

Phosphate-buffered saline (PBS) 1X	500 mL	
BSA	2.50 g	0.5 %
EDTA	0.37 g	2.0 mM

PBS/BSA (1%)

BSA	5.0 g
PBS	50.0 mL

filter through 0.22 µm

RIPA buffer (lysis buffer for tissues)

NP-40	10.00 mL	1.0 %
CHAPS	10.00 g	1.0 %
SDS	1.00 g	0.1 %
NaCl	8.77 g	0.15 M
Na-Phosphate	1.42 g	10.0 mM
EDTA	0.74 g	2.0 mM
NaF	2.10 g	50.0 mM

add up to 1 L with dH_2O

added shortly before use:

Na-Vanadate	0.2 µL/mL RIPA buffer	0.2 mM
Protease Inhibitors	10 µL/mL RIPA buffer	1.0 mM

TST Buffer (2X)

Tris (pH 8.0)	10.0 mL	100 mM
SDS	2.0 mL	0.2 %
Triton X 100	1.0 mL	1.0 %

add up to 100 mL with ddH_20

Sucrose (330 mosmol, pH 7.4)

dH_2O	800.0 mL
PBS (10X)	100.0 mL
Sucrose	23.94 g
NaN_3	0.20 g

add up to 1 L with dH_2O

FBS (heat-inactivated)
Incubation in a pre-heated water bath at 56 °C for 30 min (according to freely available culture protocols). Storage at -20 °C until further use.

2.4 READY-TO-USE KITS

Table 6: List of commercially available ready-to-use kits used in this study.

Kit	Supplier	Cat. No.
Multi Tissue Dissociation Kit 2	Miltenyi Biotec B.V. & Co, Bergisch Gladbach, Germany	130-110203
µMACS™ GFP Isolation Kit	Miltenyi Biotec B.V. & Co, Bergisch Gladbach, Germany	130-091-125
Chrom Next GEM Bead Kit v3.1, 4 rxns	10x Genomics, Pleasanton, California, USA	1000128
Chromium Next GEM Chip G Single Cell Kit	10x Genomics, Pleasanton, California, USA	1000120
Chromium Next GEM Single Cell 3′ GEM, Library & Gel Bead Kit v3.1	10x Genomics, Pleasanton, California, USA	1000121
Chromium Next GEM Single Cell 3' GEM, Library & Gel Bead Kit v3.1, 4 rxns	10x Genomics, Pleasanton, California, USA	1000128
Chromium Next GEM Single Cell Fixed RNA Sample Preparation Kit, 16 rxns	10x Genomics, Pleasanton, California, USA	PN-1000414
High-capacity cDNA Reverse Transcription Kit, 1000 reactions	Applied Biosystems | Thermo Fisher Scientific, Waltham, Massachusetts, USA	4368813
MILLIPLEX Akt/mTOR Phosphoprotein Magnetic Bead 11-Plex Kit - Cell Signalling Multiplex Assay	Merck KGaA, Darmstadt, Germany	48-611MAG
MILLIPLEX Multi-Pathway Magnetic Bead 9-Plex Kit - Cell Signalling Multiplex Assay	Merck KGaA, Darmstadt, Germany	48-680MAG
NK Cell Isolation Kit, mouse	Miltenyi Biotec B.V. & Co, Bergisch Gladbach, Germany	130-115-818
Nuclei EZ Prep Nuclei Isolation Kit	Sigma-Aldrich, Saint Louis, Missouri, USA	NUC-101
Pan T Cell Isolation Kit II, mouse	Miltenyi Biotec B.V. & Co, Bergisch Gladbach, Germany	130-095-130
RevertAid First Strand cDNA Synthesis Kit	Thermo Fisher Scientific Inc., Waltham, Massachusetts, USA	K1622
RNAscope® 2.5 HD Reagent Kit–BROWN	Advanced Cell Diagnostics, Hayward, USA	322300
RNAScope® Multiplex Fluorescent V2 Assay	Advanced Cell Diagnostics, Hayward, USA	323270
RNAscope® Probes	Advanced Cell Diagnostics, Hayward, USA	323100
RNeasy® Mini-Kit	Qiagen, Hilden, Germany	74104

2.5 LABORATORY DEVICES

Table 7: List of laboratory devices used in this study.

Instrument	Company
4200 TapeStation System	Agilent Technologies, Santa Clara, California, USA
BD LSR Fortessa Cell Analyzer	BD Biosciences, San Jose, California, USA
BMG FLUOstar® OPTIMA	BMG Labtech, Ortenberg, Germany
CASY Cell counter	OMNI Life Science GmbH & Co KG, Bremen, Germany
CO_2 incubator CB 160 with sterilizable sensor	BINDER GmbH, Tuttlingen, Germany
Countess II FL Automated Cell Counter	Thermo Scientific, Waltham, MA, USA
FACS AriaII SORP "Calliope"	BD Biosciences, San Jose, CA, USA

gentleMACS™ Octo Dissociator with Heaters	Miltenyi Biotec B.V. & Co, Bergisch Gladbach, Germany
Heraeus - Fresco 21 with 24 x 1.5/2.0mL Rotor with ClickSeal™ Biocontainment Lid	Thermo Fisher Scientific Inc., Waltham, Massachusetts, USA
Heraeus - MicroStrar 17R with 24 x 1.5/2.0mL Rotor with ClickSeal™ Biocontainment Lid	Thermo Fisher Scientific Inc., Waltham, Massachusetts, USA
Heraeus - Multifuge X1R with M-20 swing-out rotor	Thermo Fisher Scientific Inc., Waltham, Massachusetts, USA
Heraeus - Multifuge X3R	Thermo Fisher Scientific Inc., Waltham, Massachusetts, USA
Liquid suction system Vacusafe	INTEGRA Biosciences GmbH, Biebertal, Germany
MACSQuant® Tyto®	Miltenyi Biotec B.V. & Co, Bergisch Gladbach, Germany
Milli-Q® Direct Water Purification System	Merck KGaA, Darmstadt, Germany
Mixer Mill MM 400 Retsch	Retsch GmbH, Haan, Germany
Multiplex MAGPIX®	Luminex Corporation, Austin, Texas, USA
Multiskan Ascent 354 Microplate Reader	Thermo Scientific, Waltham, MA, USA
NanoDrop Spectrophotometer	Thermo Scientific, Waltham, MA, USA
S3e Cell sorter	Bio-Rad Laboratories, Inc., Hercules, California, USA
StepOnePlus Cycler	Applied Biosystems™| Thermo Fisher Scientific Inc., Waltham, Massachusetts, USA
Ultracentrifuge Optima-XPN-80, rotor: 45Ti	Beckman Coulter Diagnostics, Brea, California, USA
ZEISS Axio Observer Z1 (Microscope)	Zeiss, Oberkochen, Germany

2.6 SOFTWARE APPLICATIONS

Table 8: List of software applications used in this study.

Software product	Version	Company
BD FACSDiva™	8.0.2	BD Biosciences, San Jose, California, USA
Cell Ranger	3.0.2	10x Genomics, Pleasanton, California, USA
EndNote X9	X9.3.3	Clarivate Analytics, London, United Kingdom
FASTQC quality control tool	0.11.9	Babraham Institute Bioinformatics, Cambridge, United Kingdom
FlowJo™ Software	10.8.1	BD Biosciences, San Jose, California, USA
GraphPadPrism 9	9.5.0	GraphPad Software Inc., San Diego, California, USA
MACSQuantify™ Tyto Software	2.13.0	Miltenyi Biotec B.V. & Co, Bergisch Gladbach, Germany
Microsoft Office 365	18.2301.1131.0	Microsoft, Redmond, Washington, USA
OPTIMA - MARS Data analysis software	3.01 R2	BMG Labtech, Ortenberg, Germany
OPTIMA - Reader Control Software	2.20 R2	BMG Labtech, Ortenberg, Germany
ProSort™	1.5	Bio-Rad Laboratories, Inc., Hercules, California, USA
R	4.2.2	https://www.r-project.org/
RStudio	2022.12.0 (Build 353)	RStudio, Boston, Massachuetts, USA
StepOne-Software	v2.3	Thermo Fisher Scientific Inc., Waltham, Massachusetts, USA
xPONENT® Software for Luminex Instruments	3.1	Luminex Corporation, Austin, Texas, USA
ZenPro	2.3	Zeiss, Oberkochen, Germany

2.7 MURINE KIDNEY TRANSPLANTATIONS (mKTx)

All procedures and experiments conducted on animals followed the national and institutional guidelines as outlined in the German Animal Welfare Act (TierSchG) and the German Animal Welfare Experimental Animal Regulation (TierSchVersV). Approval for the animal experiments were given by the State Office for Health and Social Affairs (LaGeSo, Berlin, Germany; Licenses T 0200/16, T 0107/18, G 0236/18, and L 0217/15).

Kidney transplantations in mice were performed at the Research Institute for Experimental Medicine (FEM), Campus Virchow Klinik (CVK), Charité—Universitätsmedizin Berlin, by Dr. Muhammad Imtiaz Ashraf as previously described [17,69]. For functional analysis of the graft, the contralateral kidney was removed 24 hours before retrieving of the kidney graft. Prior to graft retrieval, blood samples were obtained from the inferior vena cava, followed by transcardial perfusion of the entire animal with ice-cold 1X PBS to thoroughly clear organs of any residual blood cells. Thereafter, kidney graft, spleen, and lymph nodes were harvested for subsequent analyses, including immunophenotyping, histology, gene expression, and biochemical analyses. During this study, only male mice, aged 12-16 weeks, were used. Sham operated mice underwent a surgical procedure resembling to the transplant recipient, excluding the actual transplantation. An overview of performed kidney transplantations is listed in Table 9.

Table 9: Overview of murine kidney transplantations (mKTx) performed in this study.

Group code	Type of mKTx	n	Cold-Ischemia Time [h]	Treatment, peri-operative	Donor	Recipient	Removal of CLK	Termination post Tx
Allo-4	allogeneic	6	4	Saline	BALB/c wt	C57BL/6 wt	N/A	Day 7
Allo-Lcn2	allogeneic	8	4	250 µg rLcn2	BALB/c wt	C57BL/6 wt	N/A	Day 7
B6-I	N/A	5	6	Saline	C57BL/6 wt	N/A	N/A	N/A
B6-I-LN	N/A	5	6	250 µg rLcn2	C57BL/6 wt	N/A	N/A	N/A
Lcn-G5.1	syngeneic	6	6	N/A	C57BL/6 wt	C57BL/6 wt	N/A	0.5 h
Lcn-G5.2	syngeneic	6	6	N/A	C57BL/6 wt	C57BL/6 wt	Day 0	24h
Lcn-G5.4	syngeneic	3	1.5	N/A	C57BL/6 wt	C57BL/6 wt	Day 6	Day 7
Lcn-G6.1	syngeneic	6	6	250 µg rLcn2	C57BL/6 wt	C57BL/6 wt	N/A	0.5h
Lcn-G6.2	syngeneic	6	6	250 µg rLcn2	C57BL/6 wt	C57BL/6 wt	Day 0	24 h
Lcn-G7.3	allogeneic	7	4	N/A	BALB/c wt	C57BL/6 wt	N/A	Day 3
Lcn-G7.4	allogeneic	4	1.5	N/A	BALB/c wt	C57BL/6 wt	Day 6	Day 7
Lcn-G8.3	allogeneic	8	4	250 µg rLcn2	BALB/c wt	C57BL/6 wt	N/A	Day 3
Lcn-G13.3	syngeneic	3	1.5	N/A	BALB/c wt	BALB/c wt	Day 6	Day 7
Lcn-G14.3	allogeneic	5	1.5	N/A	C57BL/6 wt	BALB/c wt	Day 6	Day 7
Lcn-G15.1	allogeneic	7	6	N/A	BALB/c wt	C57BL/6 wt	N/A	Day 28
Lcn-G24	allogeneic	5	1.5	N/A	C57BL/6 wt	BALB/c wt	Day 6	Day 28

2.7.1 RECOMBINANT LCN2

Recombinant Lcn2, both iron-bound holo-rLn2 (rLcn2:Siderophore:Fe) and iron-free apo-rLcn2 (rLcn2), was synthesized by Prof. Hubert Schwelberger, Medical University of Innsbruck, Austria as previously described [17] and provided for the entire study.

2.8 IMMUNOPHENOTYPING

Immune cells were isolated and characterized from kidney graft, spleen, lymph nodes, and blood of transplanted mice by application of standard procedures given below. The following groups were used: Allo-4, Allo-Lcn2, Lcn-G7.3 and Lcn-G8.3. Detailed information on the different transplant groups is provided in Table 9.

2.8.1 KIDNEY GRAFT

Mouse kidneys were harvested either at pod-3 or pod-7, dissected in 6 mL digestion medium and shaken in a water bath for 45 min at 37 °C at 130 rpm. After that the reaction was stopped with ice cold mouse medium. To break the tissue, the cell suspension was vigorously resuspended for 3 min with a 10 mL pipette until only small pieces of tissue were left. Subsequently, the kidney pulp was grinded through a 100 µm cell strainer while being washed with 25 mL ice cold mouse medium. The cell suspension was then centrifuged at 300 rpm for 8 min at 4 °C to remove debris. While the pelleted debris was discarded, the supernatant was again centrifuged at 1,200 rpm for 10 min at 4°C.

To specifically isolate leukocytes, the remaining cells in the pellet were suspended in 270 µL PBS/1 % BSA plus 30 µL CD45 microbeads incubated for 15 min at 4 °C. After the incubation, the cells were washed with 10 mL PBS/1 % BSA and centrifuged at 1,200 rpm for 10 min at 4 °C. The supernatant was discarded, and the cells were resuspended in 1 mL PBS/1 % BSA, which was applied on a prewashed LS columns topped with a 30 µm pre-separation filter on a MACS-Separator Multistand. The column was washed 3 times with 3 mL ice-cold PBS/1 % BSA. Finally, magnetic-labelled cells were flushed out into a 15 mL Falcon Tube with 3 mL of PBS/1 % BSA using the supplied plunger. Cell counts were determined using a CASY counter.

2.8.2 SPLEEN

After procurement, spleens were cut into smaller pieces and grinded through a 100 µm cell strainer placed on a 50 mL Falcon-Tube while being rinsed with approximately 25 mL mouse medium. Following centrifugation at 1,200 rpm for 10 min at 4 °C and discarding the supernatant, the cells were resuspended for 4 min in 5 mL ACK-Lysis Buffer. Afterwards, 10 mL PBS/1 % BSA was added, and the solution was filtered using 30 µm cell strainer and again centrifuged at 1,200 rpm for 10 min at 4 °C. As

a final step, the supernatant was discarded, the cells were resuspended in 6 mL PBS/1 % BSA, and cell counts were determined using a CASY counter.

2.8.3 LYMPH NODES

Mouse lymph nodes were grinded through a 100 µm cell strainer into a 50 mL Falcon tube while being rinsed with approximately 25 mL mouse medium and subsequently centrifuged at 1,200 rpm for 10 min at 4 °C. The supernatant was discarded and the cells were resuspended in 6 mL PBS/1 % BSA. Cell counts were determined using the CASY counter.

2.8.4 BLOOD

To isolate immune cells from blood, approximately 1 mL blood was collected from the inferior vena cava of the mouse and incubated at room temperature for 30 min. The blood was centrifuged at 8,000 x g for 10 min at 4 °C to isolate serum. Serum samples were sent to Labor Berlin for analysis of serum creatinine and urea levels. The remaining blood cells in the pellet were suspended in 1 mL of PBS including 1 % BSA. 700 µL of this suspension was added into 7 mL ACK-Lysis Buffer in a 50 mL Falcon tube which was then inverted 10 times and left for 2 min on a roll mixer. Afterwards, the suspension was centrifuged for 5 min at 400 x g, 4 °C and the supernatant was removed. Pelleted cells were resuspended in 10 mL ACK-Lysis Buffer and mixed by inverting the Falcon tube 5 times. After a 2-minute incubation at room temperature, 10 mL PBS/1 % BSA were added to the cell suspension to stop the lysis reaction. Finally, cells were centrifuged for 5 min at 400 x g, 4 °C. After the supernatant was removed, cells were resuspended in 3 mL PBS/BSA and counted using a CASY counter.

2.8.5 STAINING OF CELLS WITH ANTIBODIES AFTER ISOLATION FROM SPLEEN, LYMPH NODES, KIDNEY, AND BLOOD

From each sample, as many cells as possible, but not more than $10x10^6$ cells/mL were placed in each Falcon tube, respectively, and 2-3 mL 1X PBS were added. The tubes were centrifuged at 1,500 rpm, 7 min, 4 °C, and the supernatant was discarded. Next, samples were incubated for 10 min at 4 °C in 1X PBS containing 10 % FcR Blocking reagent. Subsequently, the cells were incubated for 20 min at room temperature with fluorescently labelled primary antibodies, following specifically designed and established flow cytometry panels (Table 10).

After antibody staining, cells were washed with 2-3 mL of PBS/1 % BSA and centrifuged at 1,500 rpm for 7 min at 4 °C. The supernatant was discarded, and cells were resuspended in 100 µL 1X PBS to record percentage of various immune cells with a BD LSR Fortessa Cell Analyzer. To record the total cell counts of immune cells, cells were resuspended in 50 µL Precision Count Beads™ and 50 µL PBS and subsequently recorded with a BD LSR Fortessa Cell Analyzer.

Table 10: Panels used for staining of isolated immune cells from spleen, lymph nodes, kidney, and blood.

Marker	Fluorochrome	Dilutions
NK-Panel		
NKp46	FITC	1: 100
CD27	PE-Cy7	1: 100
CD3	PerCP-Vio700	1: 400
CD45	UV395	1: 400
B220	BV510	1: 400
CD8a	BV605	1: 800
NKG2D	PE	1: 800
L/D	BV510	1: 1000
NKG2A	APC	1: 3200
CD11b	BV786	1: 3200
Innate-Panel		
NKp46	FITC	1: 100
CD11c	BV421	1: 200
CD103	PE	1: 200
CD3	PerCP-Cy5.5	1: 400
CD206	AlexaFluor647	1: 400
Ly6C	APC-Cy7	1: 400
Ly6G	PE-Cy7	1: 400
CD45	UV395	1: 400
B220	BV510	1: 400
CD8a	BV605	1: 800
L/D	BV510	1: 1000
CD11b	BV786	1: 3200
MHCII	BV650	1: 6400

Marker	Fluorochrome	Dilutions
T-Panel		
CD103	PE	1: 200
CD69	PE-Cy7	1: 200
CD3	PerCP-Cy5.5	1: 400
CD45	UV395	1: 400
B220	BV510	1: 400
CD8a	BV605	1: 800
CD44	APC-eFluor 780	1: 800
L/D	BV510	1: 1000
CD4	BV711	1: 1600
CD62L	BV421	1: 3200
Functional-Panel		
CD107a	PE-Texas-Red	1: 800
Surface Marker		
NKp46	FITC	1: 100
CD3	PerCP-Cy5.5	1: 400
CD45	UV395	1: 400
B220	BV510	1: 400
CD8a	BV605	1: 800
L/D	BV510	1: 1000
CD4	BV711	1: 1600
Intracellular Marker		
IL-17	BV421	1: 100
IFNγ	BV650	1: 200
Perforin	APC	1: 800

2.8.6 *EX VIVO* CELL STIMULATION

After isolation, the maximum possible quantity of cells was added into a 15 mL Falcon tube and mixed with 5 mL mouse medium. Following centrifugation at 1,500 rpm for 7 min at 4 °C, cells were resuspended in 1 mL mouse medium, supplemented with either only murine IL-2 (2 µL/mL) or additional addendum of 1 µg/mL apo-rLcn2 or 1 µg/mL holo-rLcn2. 10^7 cells/1 mL per well of a 12 well flat bottom plate were incubated overnight at 37 °C and 5 % CO_2.

The next day, cells were harvested by washing each well with 3 mL 37 °C-preheated mouse medium. Cells were transferred into a 15 mL Falcon tube and counted using a CASY counter. Cells were split according to the number of samples with a final number of 10^6 cells/400 µL in each FACS tube. To stimulate cells, 200 U/mL IL-2, 1 µL/mL Brefeldin A, 1 µL/mL Monensin, and 2 µL/mL cell stimulation cocktail were added to each sample and incubated for 4 hours at 37 °C and 5 % CO_2.

Following stimulation, cells were washed with 3 mL PBS, centrifuged at 1,500 rpm for 7 min at 4 °C, and the supernatant was discarded. After resuspending the pellet in 50 µL 1X PBS, samples were incubated for 10 min at 4 °C in 1X PBS containing 10% FcR Blocking reagent and stained with surface

markers for 30 min in the dark at room temperature. Then, cells were washed with 3 mL ice cold 1X PBS and centrifuged at 1,500 rpm for 7 min at 4 °C. The pellet was resuspended in 100 µL Fixation-Permeabilization Concentrate mixed with 300 µL Perm Diluent and incubated for 30 min at 4 °C. Subsequently, 800 µL 1X Permeabilization Buffer were added to each sample and samples were centrifuged at 1,500 rpm for 10 min at 4 °C. In the next step, cells were stained for 30 min in the dark at room temperature with intracellular antibodies (Table 10; *Functional Panel*) mixed in 100 µL 1X Permeabilization Buffer. Eventually, cells were resuspended in 100 µL 1X PBS after the final centrifugation at 1,500 rpm for 7 min at 4 °C and their relative frequencies were recorded with a BD LSR Fortessa Cell Analyzer.

2.8.7 PAN NK CELL ACTIVATION

After isolation of splenocytes (section 2.8.2) from C57Bl/6 wt mice, the cell suspension was centrifuged at 1,200 rpm for 10 min at 4 °C and the supernatant was discarded. The cell pellet was resuspended in 40 µL PBS/1 % BSA plus 10 µL of NK Cell Biotin-Antibody Cocktail per 10^7 total cells and incubated for 5 min at 4 °C. Afterwards, cells were washed with 2 mL PBS/1 % BSA per 10^7 cells and centrifuged at 1,200 rpm for 10 min at 4 °C. Next, 80 µL PBS/1 % BSA and 20 µL of Anti-Biotin microbeads were added per 10^7 cells, incubated for additional 10 min at 4 °C, subsequently centrifuged at 1,200 rpm for 10 min at 4 °C, and resuspended in 1 mL PBS/1 % BSA. To magnetically separate NK cells, cell suspension was loaded onto a prewashed LS-column on a MACS-Separator Multistand. The column was washed three times with 3 mL PBS/1 % BSA and the flowthrough containing the enriched NK cells was collected. Cell counts were determined using a CASY counter. Following the standard staining procedure as described in section 2.8.5, $1x10^6$ cells per sample were stained with the following antibodies: NKp46, CD45 and L/D.

Cells were resuspended in 1 mL mouse medium, supplemented with either only murine IL-2 (200 U/mL) or additional addendum of 1 µg/mL apo-rLcn2 or 1 µg/mL holo-rLcn2. 10^7 cells/1 mL per well of a 12 well flat bottom plate were incubated for 48 hours at 37 °C and 5 % CO_2. Both apo-rLcn2 and holo-rLcn2 were added immediately before incubation, and again after 24 hours. Subsequently, cells were harvested, and *ex vivo* stimulated as described in section 2.8.6.

2.8.8 INDUCTION OF NKG2D ON $CD8^+$ T CELLS (T CELL ACTIVATION)

To induce NKG2D on $CD8^+$ T cells, splenocytes were isolated from C57Bl/6 wt mice and treated as described in section 2.8.2. with the only differences being the addition of 10 µL Biotin-Antibody from the Pan T cell isolation kit II per 10^7 cells/mL in the first incubation step and the addition of 30 µL PBS/1 % BSA plus 20 µL Anti-Biotin microbeads per 10^7cells/mL in the last incubation step before the sorting process.

2.8.9 DATA ANALYSIS

Flow cytometric data was analysed using FlowJo™ and GraphPad Prism. The different panels were analysed in FlowJo™ by applying various gating strategies (Supplementary Figure S1 to Figure S4) to determine the amount of the stained and detected immune cell populations (in percent). Determination of total cell counts were calculated using the following formula:

$$Cells/\mu l\ per\ FACS\ tube = \frac{Cell\ count * Volume\ Beads\ [\mu l]}{Beads\ Count * Volume\ Cells\ in\ FACS\ tube[\mu l]} * Beadsconcentration\ [\frac{x}{\mu l}] * \frac{\frac{Volume\ cells}{tube}[\mu l]}{used\ volume\ cells\ [\mu l]}$$

$$Absolute\ Cell\ number = \frac{Cells}{mg}organ = \frac{\left(\frac{Cells}{\mu l}per\ FACS\ tube * Start\ volume\right)}{mg\ organ}$$

$$\frac{Total\ cell\ number}{mg\ organ} = \frac{Cells}{mg\ organ} * organ\ weight$$

Furthermore, t-Distributed Stochastic Neighbor Embedding (t-SNE) analysis was conducted through FlowJo™. From cell subsets of transplanted Balb/c to C57BL/6 kidneys and respective spleens without or with perioperative administration of rLcn2, t-SNE plots were generated on concatenated FCS files (n = 7-8) using an equal amount of 50,000 lymphocyte events per file and FlowJo™ default parameters (1000 iterations, perplexity of 30).

2.9 ISOLATION, CULTURING AND CHARACTERIZATION OF PRIMARY PROXIMAL TUBULAR EPITHELIAL CELLS (PTEC)

2.9.1 BREEDING OF mT/mG*PEPCK-Cre MOUSE LINE

At the FEM (Research Institute for Experimental Medicine within the Charité—Universitätsmedizin Berlin, Campus Buch), in-house available mT/mG*mice (Jackson Stock 007676: B6.129(Cg)-Gt(ROSA)26Sortm4(ACTB-tdTomato,-EGFP)Luo/J) were crossed with phosphoenolpyruvate carboxykinase (PEPCK)-Cre mice (provided by Prof. Dr. Duska Dragun Charité—Universitätsmedizin Berlin / Volker Haase, Vanderbilt University, Nashville, Tennessee, USA), leading to Cre recombinase mediated gene targeting in the proximal tubule epithelium. Upon Cre expression, PTEC were labelled with a membrane targeted GFP facilitating discrimination from other cell types within the kidney. The breeding program was supervised by PD Dr. med. Angelika Kusch and Dr. rer. nat. Rusan Catar, while the FEM staff, including animal well fair officers, veterinarians, and caretakers, was responsible for the practical implementation of the breeding and the legally enshrined animal welfare through specialist veterinary organisation, advice, and monitoring.

2.9.2 KIDNEY PREPARATION

Kidneys from either C57BL/6 wt or mT/mG*PEPCK-Cre mice were perfused with 1X HBSS Buffer, excised and transferred into ice-cold 1X HBSS Buffer. Subsequently, kidneys were decapsulated, split lengthwise in the sagittal plane, while the inner medullary portion and pelvis were removed. The remaining cortical and outer medullary regions were minced into small pieces (<1 mm^2) and transferred to a previously prepared ice-cold digestion solution, a mixture from 1X HBSS Buffer and enzymes from the Multi Dissociation kit 2. To obtain a single cell solution of proximal tubular epithelial cells, the gentleMACS™ dissociation protocol (Miltenyi Biotech), followed by fluorescence-activated cell sorting of viable PTEC, was applied with minor variations.

2.9.3 CELL ISOLATION PROCEDURE

Enzymes and buffers were mixed (4.8 mL 1x HBSS + 50 µL enzyme P + 100 µL enzyme D + 20 µL enzyme A+ 50 µL buffer Y) in gentleMACS™ C-tubes shortly before digestion and stored on ice. After addition of dissected kidney fragments, C-tubes were placed on the gentleMACS™ Octo Dissociator with Heaters and the program "37C_Multi_E" was run for predefined 31 min. Then, the cell suspension was filtered through a 100 µm filter into a 50 mL Falcon tube, and the tube was rinsed with 7.5 mL 1X HBSS buffer to collect the residues. Afterwards, the cell suspension was filtered through a 40 µm sieve into a new 50 mL Falcon, and the tube was again rinsed with 7.5 mL 1X HBSS buffer. 10 µL were taken for cell counting with a Neubauer improved counting chamber and the rest was centrifuged at 300 x g for 10 min at 4 °C. Cells were suspended in 20 mL Epithelial Cell Medium (ECM). 1 x 10^6 unsorted cells were seeded per 6 cm petri dish and topped with 3 mL ECM. The remaining cells were either sorted via magnetic labelling (using anti-prominin-1 microbeads, µMACS anti-GFP microbeads or anti-RFP and magnetic beads), via FACS-Sorting (FACS, MACSQuant®Tyto®) or via ultracentrifugation. Whenever cell counting was performed with the Neubauer improved counting chamber, the following formula was used to calculate the amount of cells/µL:

$$\frac{\text{Cells}}{1\mu\text{l}} = \frac{Total\ cell\ count}{counted\ area\ (mm^2) \times depth\ of\ chamber\ (mm) \times dilution}$$

5x10^5 unlabeled cells were used for verification of cell counts and to determine the ratio of GFP^+ cells to $tdTomato^+$ cells via flow cytometry.

2.9.4 FLUORESCENCE-ACTIVATED CELL SORTING (FACS)

BD FACS ARIA II / S3E™ CELL SORTER (DEPENDING ON AVAILABILITY)

Proximal tubular epithelial cells were isolated as described in sections 2.9.2 and 2.9.3 from mT/mG*PEPCK-Cre mice. With the BD FACS Aria II SORP “Calliope” (nozzle size 100 µm), GFP^+ proximal

tubule cells were separated from the GFP^- cells. $1x10^6$ cells from unsorted, sorted GFP^+ and sorted GFP^- samples were seeded into 6 cm petri dishes, respectively, and incubated at 37 °C at 5 % CO_2.

MACSQUANT®TYTO® CELL SORTER

In another approach to sort GFP^+ proximal tubule cells from GFP^- kidney cortex cells, freshly isolated cells were first filtered through 70 µm, then through 30 µm, resuspended in 10 mL MACSQuant® Tyto® Running Buffer and eventually sorted using a MACSQuant® Tyto® Cell Sorter according to the manufacturer's instructions (4 °C, approximately 150 min running time).

2.9.5 ULTRACENTRIFUGATION

To isolate proximal tubules, four kidneys from two mT/mG*PEPCK-Cre mice were excised, and the isolation protocol published by *Kamiyama et al.*, 2012, was followed with minor variations.

Kidneys were washed in sterile ice-cold 1X HBSS buffer (pH 7.4). Minced cortical and outer medullary regions were added to a solution of 4 mL 1X HBSS including 40 µL collagenase type IV and incubated for 30 min at 37 °C in a shaking water bath. Afterwards, the solution was filtered through a 250 µm mesh sieve and rinsed with 1 mL 1X HBSS. In a 70 mL polycarbonate bottle a Percoll gradient was created, consisting of 30 mL of 45 % Percoll and 5 mL of 90 % Percoll solution. The 5 mL of the kidney solution were added to the top of the tube. Ultracentrifugation of the samples was performed at 20,000 x g at 4 °C for 33 min in an Optima-XPN-80, rotor: 45Ti. The centrifugation resulted in the separation of four banded layers. Proximal tubules were accumulated in the third layer (from the top). This layer was aspirated and filtered through a 40 µm cell strainer. The proximal tubules accumulated on the grid of the sieve were collected by reverse-flushing the cell strainer with 10 mL cultivation medium (ECM). To remove the remaining Percoll solution, the tubule suspension was centrifuged at 1500 rpm at room temperature for 2 min. The pellet was resuspended in ECM, and the proximal tubules were seeded in a 6-well plate, with each well containing 1 mL proximal tubule solution plus 3 mL fresh ECM. The proximal tubules were incubated at 37 °C and 5 % CO_2, and medium change was performed every 48 hours.

2.9.6 CELL SORTING WITH MICROBEADS

ANTI-PROMININ-1 MICROBEADS

Proximal tubular epithelial cells (PTEC) were isolated as described in section 2.9.3 and centrifuged for 10 min with 300 x g at 4 °C, and the cell pellet was resuspended in 80 µL protein extraction buffer (PEB) including 20 µL anti-prominin-1 microbeads per $1x10^7$ cells. After incubation for 15 min at 4 °C, 10 mL PEB was added, and the cell suspension was centrifuged for 10 min with 300 x g at 4 °C. The cell pellet was resuspended in 1 mL PEB, loaded onto a prewashed LS column, and washed three times with 3 mL PEB. Prominin-1^+ cells were flushed out with 5 mL PEB into a 15 mL Falcon tube

and counted using a CASY counter. $5x10^5$ cells were used for flow cytometric analysis to verify the number of prominin-1^+ and prominin-1^- cells. After adding 10 mL PEB and another centrifugation step for 10 min with 300 x g at 4 °C, cells were resuspended in ECM. The amount of medium was determined according to the number of 6 cm petri dishes to be seeded with $1x10^6$ cells.

µMACS ANTI-GFP MICROBEADS

To sort cells using µMACS anti-GFP microbeads, samples were treated as described in the anti-prominin microbeads section (2.9.6), except that the cell pellet was incubated in 90 µL PEB including 10 µL anti-GFP microbeads per $1x10^7$ cells.

ANTI-RFP ANTIBODY AND MAGNETIC MICROBEADS

The anti-RFP antibody was diluted 1:50 in PEB. To sort cells using anti-RFP antibody and magnetic microbeads, the cell pellet was centrifuged for 10 min with 300 x g at 4 °C followed by incubating for 15 min at 4 °C in 90 µL PEB/10^7 cells including 10 µL anti-RFP antibody solution per $1x10^7$ cells. After washing with 10 mL PEB (10 min, 300 x g, 4 °C), the pelleted cells were resuspended in 80 µL PEB including 20 µL microbeads per $1x10^7$ cells and incubated at 4 °C for 15 min. Following another washing step with 10 mL PEB (10 min, 300 x g, 4 °C), the cells, resuspended in 1 mL PEB, were loaded onto a prewashed LS column, and processed as described in the anti-prominin-1 section 2.9.6.

2.9.7 CELL CULTURE

Cells were cultivated in Epithelial Cell Medium (ECM; Cell Biologics Inc, Chicago, Illinois, USA) at 37 °C and 5 % CO_2 for five to six days until growing to a confluent monolayer, unless described otherwise. The medium was changed for the first time after 24 hours, and again, if applicable, after 48 hours, depending on the cells' growth progression.

2.9.8 HYPOXIA / REOXYGENATION in PTEC

For *in vitro* analyses of intracellular signalling, oxidative stress, survival, and apoptosis signalling, murine primary PTEC were isolated, sorted with anti-prominin-1 microbeads, and cultured until grown to a confluent monolayer as described in sections 2.9.3, 2.9.6, and 2.9.7. Subsequently, cells were subjected to hypoxia (0.5% O_2) and nutrient deprivation (Medium E, w/o FCS) for 24 hours followed by reoxygenation in epithelial cell medium for 0.5 hours or 6 hours ± rLcn2 (1 µg/mL). Cell lysates were prepared as described in section 2.9.10 followed by multiplex analysis (described in section 2.9.12).

2.9.9 MICROSCOPIC PICTURES

For visualization, microscopic pictures of cell cultures were taken at each time point with a ZEISS Axio Observer Z1.

2.9.10 PROTEIN ISOLATION and PREPARATION OF LYSATES

ADHERENT CELLS

Petri dishes containing a confluent monolayer of cultured primary proximal tubular cells, isolated as described in section 2.9, were put on ice. Cell culture medium was quickly removed, and cells were washed twice with ice cold 1X PBS. 20 µL lysis buffer (section 2.3) were added to each sample/petri dish and incubated for 20 min on ice. Following, the adherent cells were scraped off with a cell scraper and transferred to respective 1.5 mL Eppendorf tubes. After 20-minute centrifugation at 14,000 rpm at 4 °C, the supernatant was transferred to a new 1.5 mL Eppendorf tube, respectively. Samples were either directly analysed or frozen at -80 °C for later determination of protein concentration.

TISSUE

Kidney tissue samples were harvested, shock-frozen in liquid nitrogen, and stored at -80 °C until further use.

Frozen kidney samples were placed into 1.5 mL Eppendorf safe-lock tubes containing 750 µL lysis buffer (RIPA buffer) and one magnetic bead. Following, the tubes were fixed in adapters on a vibration mill (Retsch MM400) and shaken for 2 min with a frequency of 30.0 [Hz] (1/s). Samples were stored on ice until the foam was reduced, and the cell suspension was transferred (without foam) to a new 1.5 mL Eppendorf tube to be centrifuged with maximum speed (14,000 x g) at 4 °C for 10 min. Finally, the supernatant was transferred to a new 1.5 mL Eppendorf tube and the samples' protein concentrations were either directly determined or after storage at -80 °C.

2.9.11 PROTEIN DETERMINATION (BCA ASSAY)

20 µL of each sample (pre-diluted 1:5 in dH_2O) were added to respective wells of a 96-well, flat-bottomed microtiter plate. dH_2O served as blank and samples were measured in duplicates. For protein quantification, a standard curve was prepared from a stock solution of 2000 µg/mL BSA in dH_2O. For the reagents-mix 80 µL copper(II) sulphate per row and 4 mL BCA Reagent A per row were mixed and 300 µL of it was added to each well. The plate was incubated for 30 min in an incubator at 37 °C. Absorption spectra were measured at 550 nm.

2.9.12 MULTIPLEX IMMUNOASSAY

Samples were collected from *in vivo* as well from *in vitro* settings (described in sections 2.7 and 2.9.6), containing either lysed cells from C57Bl/6 wt mouse primary proximal tubular cell culture (sorted with anti-prominin-1 microbeads) or from mouse renal transplants (groups: B6-I, B6-I-LN, Lcn-G5.1, Lcn-G5.2, Lcn-G6.1 and Lcn-G6.2; Table 9). For the multiplex immunoassays, the following expression kits were used: 1. MILLIPLEX® Multi-Pathway 9-Plex Magnetic Bead Kit and 2. MILLIPLEX Akt/mTOR Phosphoprotein Magnetic Bead 11-Plex Kit. 10 µg total protein of each sample was added to each well

of a V-shaped 96-well plate in a randomized manner, with β-actin as control. In total, five pooled samples per plate, including proteins from all measured samples, served as quality control. Preparation and performance of the two immunoassays were done according to the manufacturer's instructions by Dr. Raphaela Fritsche in the lab of Dr. Jennifer Kirwan at the Berlin Institute of Health (BIH) Metabolomics Platform, Käthe-Beutler-Haus Campus Buch, Charité—Universitätsmedizin Berlin.

2.9.13 RNA ISOLATION AND cDNA SYNTHESIS

RNeasy® MINI KIT

Total RNA was extracted either from C57Bl/6 wt mouse primary proximal tubular cell culture (2.9.6) or from mouse kidney tissues (groups: B6-I, B6-I-LN, Lcn-G5.1, Lcn-G5.2, Lcn-G6.1 and Lcn-G6.2; Table 9) using the RNeasy Mini Kit with RNase-free DNase treatment according to the manufacturer's instructions. For lysis of freshly isolated proximal tubular epithelial cells, the RLT buffer provided with the RNeasy mini kit was used. The amount of RLT buffer was calculated according to the manufacturer's instructions. The cultured proximal tubule cells were washed with 1X PBS before harvesting by direct lysis in the petri dishes with RLT buffer. To retrieve enough RNA, cells from five 6 cm petri dishes were pooled. For RNA isolation from tissue samples, samples were homogenized in RLT buffer as described in section 2.9.10. RNA concentration and quality were evaluated using a NanoDrop Spectrophotometer.

TRIzol™ REAGENT

Freshly isolated cells were centrifuged for 8,000 rpm at room temperature and resuspended in 500 µL TRIzol™. From cultured mouse primary proximal tubular cells, 100 µL TRIzol™ was added to each petri dish, incubated for 10 min at room temperature, and scraped off. To retrieve enough RNA, cells from five 6 cm petri dishes were pooled.

To procced for isolation of RNA, 200 µL chloroform was added to each sample, incubated at room temperature for 2 min and centrifuged for 15 min with 12,000 x g at 4 °C. From the resulting three layers, the upper watery phase containing RNA was carefully removed and transferred to a new 1.5 mL RNase free Eppendorf tube. 500 µL isopropanol was added to each sample, followed by incubation for at least one hour at 4 °C. Samples were then centrifuged for 10 min with 12,000 x g at 4 °C. Pellets were washed twice with 300 µL EtOH (75 %), resuspended in 300 µL EtOH (75 %) and centrifuged for 5 min with 7,500 x g at 4 °C. The supernatant was discarded, and the pellet was dried at 56 °C on a heating block until they were slightly wet. Finally, the pellets were resuspended in 20 µL DEPC water and RNA concentration and quality were evaluated using a NanoDrop Spectrophotometer.

cDNA SYNTHESIS

cDNA synthesis was done using the High-capacity cDNA Reverse Transcription Kit and 2 µg of total RNA according to the manufacturer's instructions. If necessary, synthesized cDNA was diluted with DEPC water, respectively.

MASTER MIX

25x dNTP mix (100 mM)	0.8 µL
Multiscribe reverse transcriptase	1.0 µL
10x RT Buffer	2.0 µL
RNase Inhibitor	1.0 µL
Nuclease-free water (DEPC)	3.2 µL
10x RT Random Primer	2.0 µL
RNA dilution	2.0 µg

CYCLING CONDITIONS

1. 25 °C 10 minutes
2. 37 °C 120 minutes
3. 85 °C 5 minutes
4. 4 °C ∞

2.9.14 REAL-TIME QUANTITATIVE PCR

The real-time quantitative PCR (RT-qPCR) analysis was carried out by utilizing 1 µL of synthesized cDNA and TaqMan™ Fast Advanced Master Mix, following the instructions provided by the manufacturer. The relative expression levels of the target mRNA were normalized to the expression of β-actin (Actb) mRNA, serving as the endogenous control. The calculations were performed using the $2^{-\Delta\Delta Ct}$ method [70]. The expression assays used for mRNA expression analysis are listed in Table 11.

Table 11: List of expression assays for RT-qPCR.

Expression Assay	Supplier	Cat. No.
Acta2 TaqMan gene, mouse, Mm00725412_s1	Thermo Fisher Scientific Inc., Waltham, Massachusetts, USA	4453320
Actb mouse expression assay, Mm02619580_g1	Thermo Fisher Scientific Inc., Waltham, Massachusetts, USA	4331182
Cdh1 mouse expression assay, Mm01247357_m1	Thermo Fisher Scientific Inc., Waltham, Massachusetts, USA	4453320
HAVcr1 mouse expression assay, Mm00506686_m1	Thermo Fisher Scientific Inc., Waltham, Massachusetts, USA	4331182
Lcn2 mouse expression assay, Mm01324470_m1	Thermo Fisher Scientific Inc., Waltham, Massachusetts, USA	4331182
Lrp-2 (megalin) mouse expression assay, Mm01328171_m1	Thermo Fisher Scientific Inc., Waltham, Massachusetts, USA	4331182
Ppia mouse expression assay, Mm02342429_g1	Thermo Fisher Scientific Inc., Waltham, Massachusetts, USA	4331182
Slc22a17 (24p3R) mouse expression assay, Mm00480680_m1	Thermo Fisher Scientific Inc., Waltham, Massachusetts, USA	4331182
Slc5a2 TaqMan gene, mouse, Mm00453831_m1	Thermo Fisher Scientific Inc., Waltham, Massachusetts, USA	4453320

2.9.15 IMMUNOHISTOCHEMISTRY OF PTEC

Four cover slips (Ø 15 mm) were placed in petri dishes (Ø 6 mm) and then coated with 2 % gelatin. PTEC were isolated, sorted with anti-prominin-1 microbeads, and cultured as described in section 2.9 until 70-80 % confluency.

Cultured cells were washed with PBS (1X), covered with 4 % paraformaldehyde (PFA), incubated for 15 min at room temperature, and subsequently washed with 1X PBS. Meanwhile, in a petri dish (Ø 12 mm) parafilm was placed on top of a piece of Whatman® paper (moistened with 1X PBS and marked according to the staining used).

Cells were either stained with α-Tubulin (dilution 1:1500 in 1 % BSA) as positive control or DAPI (dilution 1:1500 in 1X PBS) as counterstaining control. Additionally, the surface marker Megalin (dilution 1:1000 in 1 % BSA) and the intracellular marker Lcn2 (dilution 1:2000 in 1 % BSA) were used (listed in Table 12). Depending on the origin of the primary marker, either mouse or rabbit secondary antibodies (diluted 1:500 in 0.5 % BSA; Table 13) were applied.

Table 12: List of primary antibodies applied during immunohistochemical analyses.

Primary antibodies	Source	Dilution	Supplier	Cat. No.
α-Tubulin (DM1A) Mouse mAb #3873	Mouse	1:1500	Cell Signaling Technology, Danvers, Massachusetts, USA	3873S
Lcn2 (α-SIP24) with α-rabbit Ig-HRP (Sigma A-0545)	Rabbit	1:2000	Ao.Univ.-Prof. Dr. Hubert G. Schwelberger, Medizinische Universität Innsbruck, Molekularbiologisches Labor, Innsbruck, Austria	08Rb17 lot c
Megalin/LRP2 Antibody (H-10), mouse	Mouse	1:500	Santa Cruz Biotechnology, Inc, Dallas, Texas, USA	sc-515772

Either 100 µL 0.5 % Triton-X 100 (to samples with rabbit primary antibody) or 100 µL 1X PBS (to samples with mouse primary antibody) were poured onto the respective cover slip and incubated for 3 min at room temperature. Subsequently, the cover slips were washed with 1X PBS and 100 µL BSA (1 %) was added on top. Samples were incubated in the dark for one hour at room temperature.

Table 13: List of secondary antibodies applied during immunohistochemical analyses.

Secondary antibodies	Host	Dilution	Supplier	Cat. No.
Goat Anti-Mouse IgG H&L (Alexa Fluor® 568) preadsorbed	Goat	1:500	Abcam, Cambridge, United Kingdom	ab175701
Goat Anti-Rabbit IgG H&L (Alexa Fluor® 568) preadsorbed	Goat	1:500	Abcam, Cambridge, United Kingdom	ab175696
Other Antibodies				
DAPI, 25 mg, CAS No. 28718-90-3		1:1500	Carl Roth, Karlsruhe, Germany	6335.1

After removing BSA from cover slips, 100 µL of each antibody, or 100 µL BSA (1%) on the negative control, were added onto cover slips, respectively, and incubated in the dark for one hour at room temperature. Following washing with 1X PBS, 100 µL of the respective secondary antibody dilutions were added before incubation in the dark for one hour at room temperature. Cover slips were washed with 1X PBS, 100 µL DAPI was added per cover slip and incubated for 5 min at room temperature. After removing the DAPI solution, cover slips were inverted and placed onto microscopic glass slides, primed with a drop of Aqua-Poly/Mount, and dried overnight at room temperature. Finally,

microscopic pictures were taken with a ZEISS Axio Observer Z1, and the slides were stored at 4 °C for further use.

2.9.16 RNASCOPE *IN SITU* HYBRIDIZATION

PREPARATION OF PARAFFIN EMBEDDED KIDNEY SLICES FROM MURINE KIDNEY TRANSPLANTS

Histopathological analysis of transplanted kidneys (Groups: Lcn-G5.4, Lcn-G7.4, Lcn-G13.3, Lcn-G14.3; **Table 9**) was performed at the Institute of Translational Physiology, Charité - Universitätsmedizin Berlin, Germany by Vera Anna Kulow. In brief, organs were fixed over night at room temperature in paraformaldehyde (4 %), rinsed with 1X PBS and incubated for 2 hours in 330 mosmol sucrose solution including 0.02 % NaN_3 at 4 °C. Subsequently, organs were dehydrated using a tissue processor, embedded in paraffin, and cut into 1.5 µm slices using a microtome.

Renal sections were then stained using periodic acid Schiff reagent (PAS) staining. Histomorphological evaluation and imaging of renal sections was performed with an Eclipse Ti2-A Microscope, a DS-Ri2 Camera, and the Nikon NIS-Elements Software.

CRYO-PRESERVATION OF MT/MG*PEPCK-CRE KIDNEY SLICES

For embedding, tissues from mT/mG*PEPCK-Cre mice were preserved in Tissue-Tek® Cryomold® mounting dishes, completely immersed in tissue freezing medium (O.C.T.), and subsequently frozen in liquid nitrogen. Cryo-tissue sections of 4 µm were prepared using a microtome.

PREPARATION AND FIXATION OF ANTI-PROMININ-1 SORTED PTEC

Prominin-1 sorted PTEC were isolated as described in section **2.9**, and cultured for three days on Nunc™ Lab-Tek™ Chamber Slide™ (4 wells) until approximately 50 % confluency was reached. Afterwards, cells were fixed on the slides with 1 mL Histofix (10 %) per well for 10 min. For immunohistochemical analysis, slides were washed thrice with 1X PBS, chambers were detached, and the slides were stored in 1X PBS, while the slides for RNAscope *in situ* hybridisation were stored in Histofix until further analysis.

RNASCOPE *IN SITU* HYBRIDISATION PROCEDURE

Deparaffinized slices from microscope slides with PTEC grown to 50 % confluency were analysed by Tobias Sieckmann (Institute of Translational Physiology, Charité—Universitätsmedizin Berlin, Germany) using the RNAscope™ 2.5 HD Assay – BROWN Kit according to the manufacturer's instructions with minor changes [71]. In brief, target retrieval was carried out for 15 min with a food steamer (Braun, Kronberg im Taunus, Germany), and AMP5 hybridization was prolonged to one hour, while hematoxylin solution, Gill No.1 was used for counterstaining followed by washing steps in tap water. Mounting of slides was done with Aquatex. The RNAscope Multiplex Fluorescent V2 Assay was used according to the manufacturer's instructions for fluorescent staining, and Opal dyes at a dilution of 1:750 were used for

labelling. Lastly, kidney slices were mounted using Vectashield H1000 mounting medium for fluorescence [71]. The used probe is listed in Table 14.

Table 14: Probe for RNAScope Assays 2.5 HD Brown and Multiplex Fluorescent V2.

Target	Product number	Channel
Lrp2	425881-C3	C3

2.9.17 IMMUNOHISTOCHEMISTRY COMBINED WITH RNASCOPE *IN SITU* HYBRIDIZATION

RNAscope *in situ* hybridization was performed as described in section 2.9.16. After target retrieval, hybridization of probes, amplifiers and fluorophore, slices with PTEC (50 % confluency) were incubated for one hour at room temperature in serum-free protein blocking solution (Dako, Carpinteria, USA). For immunohistochemical analysis, PTEC cells were washed thrice in 1X PBS, incubated for 30 min in 0.5 % Triton X 100 at room temperature, and washed again as described before. Blocking was performed for one hour in 5 % milk buffer, after which the cells were incubated in primary antibody solution (Vimentin; final concentration 1 µg/µL) overnight at 4 °C. The next day, cells were washed with 1X PBS and incubated in secondary antibody solution (dilution 1:200) for one hour at room temperature. After washing with 1X PBS for 5 min, cells were stained for 10 min with DAPI (dilution 1:500), washed again twice, mounted with Roti®-Histokitt II, and analysed using a fluorescence microscope.

2.9.18 scRNAseq OF PRIMARY PROMXIMAL EPITHELIAL CELLS (PTEC)

Primary proximal tubular epithelial cells were isolated from C57Bl/6 wt mice and sorted using anti-prominin-1 microbeads as described in section 2.9. The whole procedure was carried out at room temperature, using 98b buffer instead of HBSS buffer for isolation process. Single cells from two animals were combined and resuspended in 10 mL PEB (1X PBS/2.5 % BSA/ 2 mM EDTA). To determine the number of cells, the Countess II FL Automated Cell Counter (based on PI staining for determination of dead cells), and for verification the Neubauer Improved Counting Chamber were used. Generated samples are listed in Table 15 and comprise of n = 2-3 unsorted and n=3 anti-prominin-1 sorted samples per isolation day. Samples were retrieved on isolation day (day 0) and after day 3 and 6 of cell culture.

Samples from day 0 were resuspended in chilled 1X PBS/0.04 % BSA and processed for fixation, while the day 3 and day 6 samples were trypsinized for 25 min to detach cells, which were then transferred to a new tube. Before fixation, cells cultured for 72 hours (day 3) from twelve cultured petri dishes (approx. 30000 cells/petri dish) and cells from four petri dishes (approx. 100,000 cells/petri dish) cultured for 144 hours (day 6) were combined and resuspended in chilled 1X PBS/0.04 % BSA.

Table 15: Overview of samples used for scRNAseq analysis. The "U" in the names stands for "unsorted".

No.	Sample ID	Day of cell culture	Specification	Total amount of cells in 1mL final sample [cells/mL]
1	RNASeq-1U-D0	0	Pooled from 2 C57Bl/6 wt mice	$2.00x10^6$
2	RNASeq-3U-D0	0	Pooled from 2 C57Bl/6 wt mice	$2.00x10^6$
3	RNASeq-6U-D0	0	from 1 C57Bl/6 wt mouse	$1.30x10^6$
4	RNASeq-1-D0	0	Pooled from 2 C57Bl/6 wt mice	$2.00x10^6$
5	RNASeq-3-D0	0	Pooled from 2 C57Bl/6 wt mice	$2.00x10^6$
6	RNASeq-5-D0	0	Pooled from 2 C57Bl/6 wt mice	$1.85x10^6$
7	RNASeq-1-D3	3	pooled from 16 petri dishes	$1.94x10^5$
8	RNASeq-3-D3	3	pooled from 9 petri dishes	$3.25x10^5$
9	RNASeq-5-D3	3	pooled from 20 petri dishes	$9.27x10^5$
10	RNASeq-6U-D3	3	pooled from 8 petri dishes	$5.20x10^5$
11	RNASeq-7U-D3	3	pooled from 8 petri dishes	$2.02x10^5$
12	RNASeq-1-D6	6	pooled from 4 petri dishes	$2.25x10^5$
13	RNASeq-3-D6	6	pooled from 4 petri dishes	$7.74x10^5$
14	RNASeq-5-D6	6	pooled from 5 petri dishes	$1.10x10^6$
15	RNASeq-6U-D6	6	pooled from 4 petri dishes	$1.53x10^6$
16	RNASeq-7U-D6	6	pooled from 4 petri dishes	$1.42x10^6$

Cells for single cell RNA sequencing were fixed using the Chromium Next GEM Single Cell Fixed RNA Sample Preparation Kit (10x Genomics) according to the manufacturer's instructions and stored at -80 °C until further use.

Probe Hybridization and Multiplexing, GEM Generation and Barcoding, GEM Recovery and Pre-Amplification, Library Construction as well as sequencing were carried out using the Chromium Fixed RNA Mouse Transcriptome Kit according to the Chromium Fixed RNA Profiling Reagent Kits User Guide for multiplexed samples (#CG000527, Rev C) in collaboration with Francesca Solinas from the Genomics Core Facility at the Max Delbrück Centre—Berlin Institute for Medical Systems Biology (MDC-BIMSB) in Berlin, Germany under the supervision of Dr. Thomas Conrad. In short, the 16 above-mentioned samples (Table 15) were incubated with a transcriptome-wide panel of gene specific hybridization probes carrying a specific barcode for each sample. Following a comprehensive washing step, samples were pooled and encapsulated in a droplet emulsion using a Chromium iX instrument. Bound hybridization probes were extended by barcoded primers within the droplets and amplified by PCR after breaking of the droplet emulsion. Subsequently, sequencing of the pooled samples was performed on an Illumina NovaSeq 6000 instrument.

DATA ANALYSIS AND VISUALIZATION

Deplexing, alignment and quantification of the sequencing data against the mm10 mouse genome reference (ref-data-gex-mm10-2020-A) together with the corresponding probe set (Chromium_Mouse_Transcriptome_Probe_Set_v1.0.1_mm10-2020-A.csv) was performed by Benedikt Obermayer-Wasserscheid, PhD, from the Core Unit Bioinformatics (CUBI) at the Berlin Institute of

Health (BIH), Charité—Universitätsmedizin, Berlin, Germany, using Cell Ranger v7.1.0 Gene Expression Software from 10x Genomics (Pleasanton, CA, USA).

Processed data were further analysed with Seurat [72], using all cells with at least 500 sequenced genes and at most 15 % mitochondrial RNA content. From the Seurat package, the *IntegrateData* function was used to remove batch effects and the *DoubletFinder* function to identify doublets [73]. Azimuth (v0.4.6) served to assign initial cell type labels using the kidney reference from the Human Cell Atlas [74]. Next, doublets and 6 clusters dominated by non-epithelial predicted cell types or mitochondrial genes were excluded, and batch integration, dimensionality reduction and clustering were repeated. From this cleaned dataset, day 0 samples were isolated, stressed cells or cells with more than 5% mitochondrial RNA removed, and UMAPs (Uniform Manifold Approximation and Projection for Dimension Reduction) and clustering after batch integration were computed, followed by annotating the resulting clusters using predicted labels as well as marker genes from the literature. The combined day 3 and day 6 samples were separately batch-integrated, re-clustered and annotated. After removing another two clusters with diffuse localization in the UMAP from that dataset, we used scanpy (v1.9.3) [75] to compute a diffusion map and diffusion pseudotime, together with a Leiden clustering in diffusion map space that was then used to assign different epithelial, mesenchymal, or PTEC-like fates.

Differential gene expression was visualized using either RStudio or CZ CELLxGENE Discover software.

2.10 GENE EXPRESSION UNDER VARIOUS KIDNEY TRANSPLANTATION CONDITIONS

2.10.1 HISTOPATHOLOGY

Histopathological analysis of transplanted kidneys (Groups: Lcn-G5.4, Lcn-G7.4, Lcn-G13.3, Lcn-G14.3; Table 9) was performed as described in section 2.9.16.

2.10.2 GRAFT SURVIVAL

Kidneys were transplanted from Balb/c to C57Bl/6 mice and vice versa as described in section 2.7. On pod-7, the contralateral kidney was surgically removed. Until pod-28, continuous medical surveillance was conducted to monitor and ensure animal well-being as well as survival of the graft. This was assessed by weekly functional analysis of the graft (determination of serum creatinine levels), combined with monitoring several clinical indicators, including for instance body weight, pain symptoms, respiratory/breathing abnormalities, and behavioural indications. For mice showing serum creatinine levels higher than 2 mg/dL and/or serious health indications euthanasia was prematurely administered, and the time point was noted down for generation of a Kaplan-Meier survival graph.

2.10.3 SINGLE-NUCLEUS-RNA-SEQUENCING

NUCLEI EXTRACTION

Syngeneic and allogeneic transplantations were carried out by Dr. phil. M. Imtiaz Ashraf. Transplanted kidneys were used from the following groups: Lcn-G5.4, Lcn-G13.3 (both syngeneic) and Lcn-G7.4, Lcn-G14.3 (both allogeneic); n = 2 or n = 3 (**Table 9**). After harvest, the middle part of each kidney was dissected into smaller pieces, incubated for 24 hours at 4 °C in RNA*later*™ stabilization solution, and stored at -80 °C until further use [76].

Isolation of nuclei was performed as described by *Leiz et al*., 2021 and 2023 [76,77]. In brief, frozen kidney pieces were transferred into a petri dish containing 1 mL Nuclear EZ Lysis Buffer, along with 1 U/µL RiboLock RNase Inhibitor and Ribonucleoside-vanadyl complex at a final concentration of 10 mM, and thoroughly minced using a razor blade. In Dounce tissue grinder tubes, the kidney tissues were further homogenized through 25 strokes with a pestle A and filtered through a 100 µm strainer. The filter was washed with an additional 1 mL of lysis buffer. After washing the tissue grinder tubes, the homogenate was returned to the Dounce tissue grinder tubes, respectively, and homogenized with 15 strokes using a pestle B. The homogenate was transferred to a pre-cooled 15 mL falcon tube. To this, 2 mL of nuclear lysis buffer were added, followed by incubation on ice for 5 min. The homogenate was then filtered through a 40 µm strainer and centrifuged at 500 x g and 4 °C for 5 min. The resulting pellet was reconstituted in nuclear lysis buffer containing 1 U/µL RiboLock and corroborated with a sucrose cushion (10 %). After centrifuging for 5 min with 500 x g at 4 °C, supernatants and cell debris were removed, and the pellets resuspended in 0.04 % BSA supplemented with 1 U/µL RiboLock. Subsequently, the cell suspensions were filtered through a 20 µm strainer, and nuclei were sorted with a BD FACS Aria II SORP “Calliope” into a 1X PBS/ 4 % BSA/ RiboLock solution based on DAPI staining. Final concentration of nuclei per sample were determined with a Countess II FL Automated cell counter. [76,77]

GEM GENERATION, LIBRARY PREPARATION AND SEQUENCING

Gel Bead-in Emulsion (GEM) generation, cDNA synthesis andlibrary preparation were conducted by Dr. Janna Leiz at the Genomics Core Facility, Max Delbrück Centre - Berlin Institute for Medical Systems Biology (MDC-BIMSB) in Berlin, Germany, following the User Guide from the Chromium Next GEM Single Cell 3′ GEM, Library & Gel Bead Kit v3.1 (Document #CG000204, Revision D) [76,77]. Around 5,000 – 10,000 nuclei per sample were targeted depending on the final suspension concentration. Quality assessment of cDNAs and libraries was carried out with the Agilent 4200 TapeStation system. Using the Illumina Nova Seq 6000, approximately 20,000 reads per nucleus (paired end) were sequenced by the Genomics Core Facility. Cell Ranger 3.0.2 Gene Expression Software from 10x Genomics (Pleasanton, CA, USA) was used by Dr. med. Christian Hinze to align the sequencing data and the mouse mm10 genome.

QUALITY CONTROL AND CLUSTERING

Datasets were imported into R using Seurat version 3.2.1 and Seurat objects were generated [78]. Solely nuclei meeting specific criteria were included in the analysis: those with a gene numbers (nGene) between 1,500 and 7,500, less than 20,000 unique molecular identifier (nUMI), and less than 4 % mitochondrial RNA content. Genes expressed in less than three nuclei were excluded from further analysis. Individual datasets were merged into a single object, log normalized using scale.factor = 10000, and variable features were identified (selection.method = "vst", nfeatures = 2000). To perform the integrated analysis, a group of anchors linking the datasets was determined by taking into account dimensions 1 to 30 and utilizing 5 anchor points (k.anchor). Subsequently, nuclei were clustered based on highly variable genes, and UMAPs were created by employing 30 principal components from principal component analysis with a resolution of 0.5. The default parameters were utilized for all other settings.

To determine cell types, the Seurat package's *FindMarkers* function was applied, considering marker genes expressed in at least 25 % of nuclei and with a minimum log-fold-change of 0.25. Known marker genes were used for annotation. [79-81]. Clusters representing the same cell type were consolidated into one cluster, and cluster colours were assigned using RColorBrewer v1.1-2 [82]. For sub clustering of proximal tubular cells and immune cells, nuclei with respective identities were used as subsets. Neighbouring nuclei were clustered based on 30 dimensions, using a resolution of 0.5. Subcluster were identified according to known marker genes [83-85] in case of proximal tubular cells and by application of the *FindMarkers* function and using online databases for reference [86-88] with respect to the immune cells. Within each subset, clusters representing the same cell type were summarized into one cluster, and further analysis focused on the expression of specific injury marker genes such as "Lcn2", "Havcr1" and the receptors "*Lrp2*" and "*Slc22a17*".

2.11 STATISTICS

Groups sizes in all experiments were $n \geq 3$, as specified in the respective results sections. GraphPad Prism 9 was used for statistical analyses. For comparison of two groups, Mann-Whitney-U Test was used. For multiple comparisons of normally distributed data ordinary one-way ANOVA was performed, compared to Kruskal-Wallis test with Dunn's post-hoc test for non-equally distributed data. Moreover, two-way ANOVA was applied to analyse variations between groups to the variation within groups. Data are presented as mean values ± standard deviation (SD) unless stated otherwise. Calculations resulting in a p-value ≤ 0.05 were considered as statistically significant.

3 RESULTS

3.1 COMPREHENSIVE IMMUNOPHENOTYPING

Following kidney transplantation, the adaptive immune response undergoes dynamic changes. Alterations in the balance between effector and regulatory T-cell subsets, B-cell activation and antibody production, antigen-presenting cell maturation and antigen presentation can influence the immune response against the transplanted kidney [89,90]. Furthermore, the innate immune system as the initial defence against pathogens can impact the recognition of danger signals, initiation of inflammatory responses, and modulation of adaptive immune cell activation [90]. Hence, to gain a deeper understanding of the role of rLcn2 in allogeneic immune responses during renal allograft rejection, we conducted phenotypic and functional analyses of both innate and adaptive immune cells, isolated from kidney grafts as well as secondary lymphoid tissues of rLcn2-treated recipient mice.

3.1.1 TREATMENT WITH rLCN2 SPECIFICALLY ALTERS ADAPTIVE IMMUNE CELL POPULATIONS

rLcn2 has been shown to ameliorate kidney function after kidney transplantation by mitigating cellular infiltration and histological lesions [17]. To elucidate whether rLcn2 influences abundance and functionality of adaptive immune cells, an extensive immunophenotyping was performed after allogeneic kidney transplantations from Balb/c to C57Bl/6 mice either with or without perioperative admission of rLcn2. To investigate early immune events, such as interstitial infiltration of lymphocytes, immune cells were phenotyped at post-operative day 3 (pod-3). On post-operative day 7 (pod-7), the analysis focused on immune cells present during the critical phase of acute cellular rejection, evident by the occurrence of for instance glomerulitis, tubulitis, PALA (periarterial lymphocytic aggregation), and interstitial infiltration [17]. Applied gating strategies are depicted for each panel in **Supplementary Figure S1 to Figure S4**.

Across adaptive immune cell populations, flow cytometrical analysis of isolated cells from spleen, lymph nodes, kidney graft and blood, revealed significant alterations on relative frequencies from pod-3 to pod-7. In spleen samples for instance, T-cell-frequencies, including their memory subsets, were predominantly increased at pod-7 compared to pod-3, while the frequencies of tissue resident T-cells and naïve memory T-cells were lowered in spleen as well as in kidney graft samples. Similarly, in kidney graft and blood samples, relative frequencies of T-cell- and effector memory T-cell-populations were significantly increased, while central memory and naïve memory T-cells significantly decreased from pod-3 to pod-7. Besides, relative frequencies of central memory and effector memory T-cells isolated from lymph nodes significantly increased on pod-7 compared to pod-3 (**Figure 3**).

In response to perioperative treatment with rLcn2, we observed a significant decrease in the relative frequencies of effector memory and naïve memory T-cells in spleen on pod-7. Moreover, the relative abundance of effector memory T-cells was also significantly lowered by afore mentioned treatment in kidney graft and blood samples (**Figure 3**).

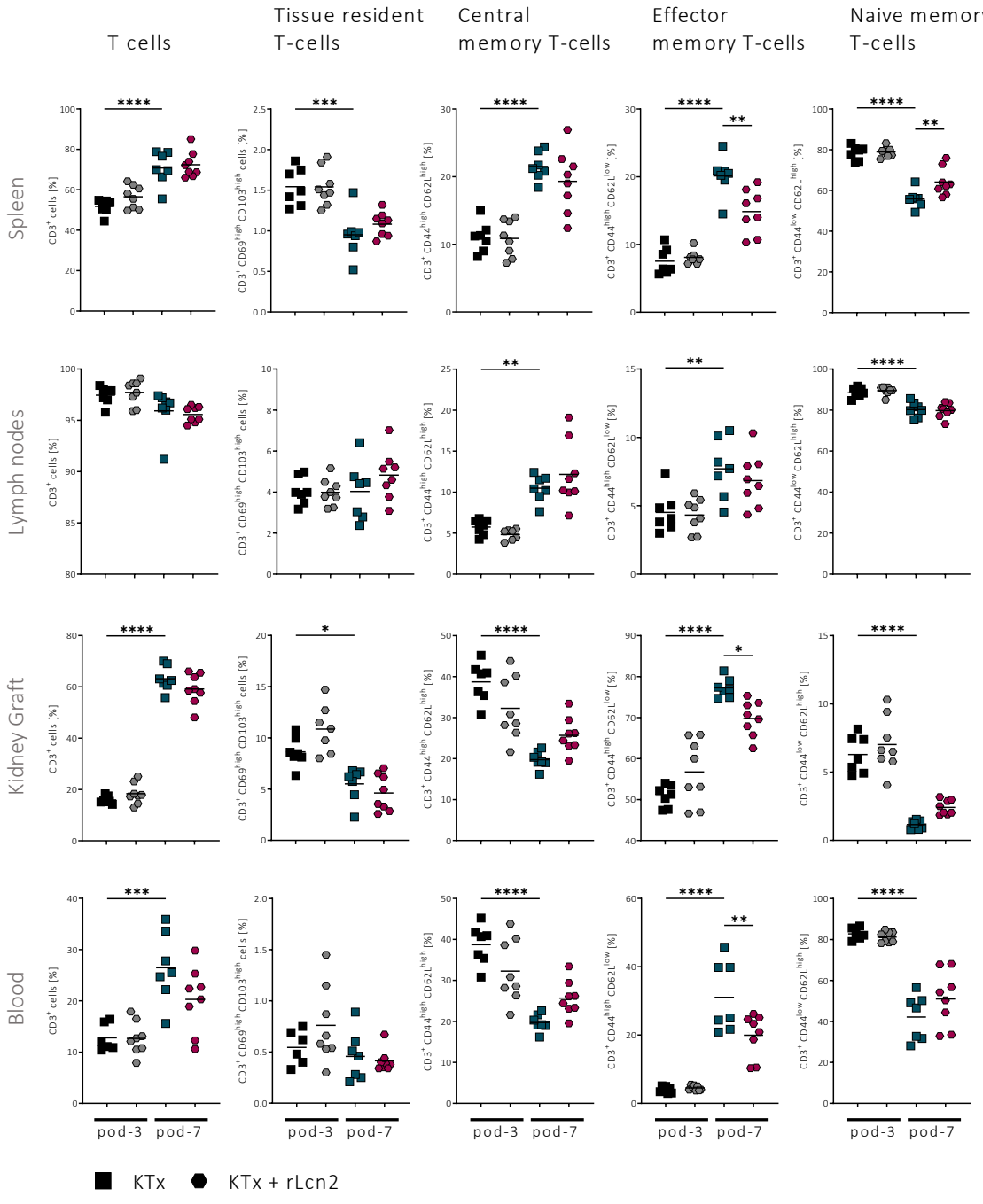

Figure 3: Relative frequencies of distinctive pan T-cell and T-cell subsets change substantially due to treatment with rLcn2.

Immune cells were isolated from spleens, lymph nodes, kidney grafts, and blood after allogenic murine kidney transplantations from Balb/c to C57Bl/6 mice (n=7-8) on pod-3 and pod-7. Immune cells were stained with a cocktail of monoclonal antibodies (*T-Panel*, **Table 10**). Relative frequencies of T-cell and T-cell subpopulations were acquired on a BD LSRFortessa™ Cell Analyzer and analysed using FlowJo™ and GraphPad Prism software. Horizontal lines represent the respective mean. Statistical analysis: Ordinary one-way ANOVA; * $p < 0.05$, ** $p \leq 0.01$, *** $p \leq 0.001$, **** $p \leq 0.0001$.

Upon closer inspection, relative helper T (T_h)-cell- and T_h subset-frequencies between pod-3 and pod-7 encompassed a significant increase of overall T_h-cell- as well as central memory and effector memory T_h-cell-populations in spleen samples. In lymph nodes, relative frequencies of central memory T_h-cells significantly increased, while relative frequencies of naïve memory T_h-cells significantly decreased. Within kidney graft samples, we detected a significant increase of relative T_h-cell-frequencies, compared to significantly decreased effector memory and naïve memory T_h-cell relative frequencies. Moreover, central memory and effector memory T_h-cell relative frequencies were significantly increased, while the relative frequencies of naïve memory T_h-cells significantly decreased from pod-3 to pod-7 in blood samples (**Figure 4**).

Significant effects due to perioperative treatment with rLcn2 were detected on the relative frequencies of overall T_h-cell, central memory, and effector memory T_h-cells. In spleen samples, the relative abundance of central memory T_h-cells decreased, while significantly increasing in naïve memory T_h-cells at pod-7. The relative frequencies of T_h-cells in lymph nodes and kidney graft were significantly lower at pod-7. Naïve memory T_h-cells relative frequencies were significantly lower in blood samples (**Figure 4**).

Comparing the relative abundance of cytotoxic T (T_c)-cells and T_c-cells subsets on pod-3 and pod-7, the overall relative frequencies of T_c-cells significantly increased at pod-7 in samples from spleen, kidney graft, and blood. Contrarily, the relative frequencies of tissue resident T_c-cells significantly decreased on pod-7 in samples from spleen and blood. On the one hand, central memory T_c-cells' relative frequencies increased in spleen and lymph node samples, and significantly decreased in kidney graft and blood samples at pod-7. On the other hand, effector memory T_c-cells' relative frequencies significantly increased in all settings at pod-7. Naïve memory T_c-cells were significantly decreased in all settings (**Figure 5**).

Due to perioperative treatment with rLcn2, the relative frequencies of T_c-cells in blood and effector memory T_c-cells in spleen, lymph nodes, and blood were significantly lower. Besides, the relative abundances of T_c-cells in lymph nodes and naïve memory T_c-cells in spleen were significantly increased at pod-7 (**Figure 5**).

In summary, the perioperative treatment with rLcn2 exhibits distinct effects on T-cells and T-cell subpopulations derived from spleen, lymph nodes, kidney graft, and blood at pod-7. Notably, memory T-cell populations were primarily impacted at pod-7, while no detectable effects of the treatment were observed at pod-3.

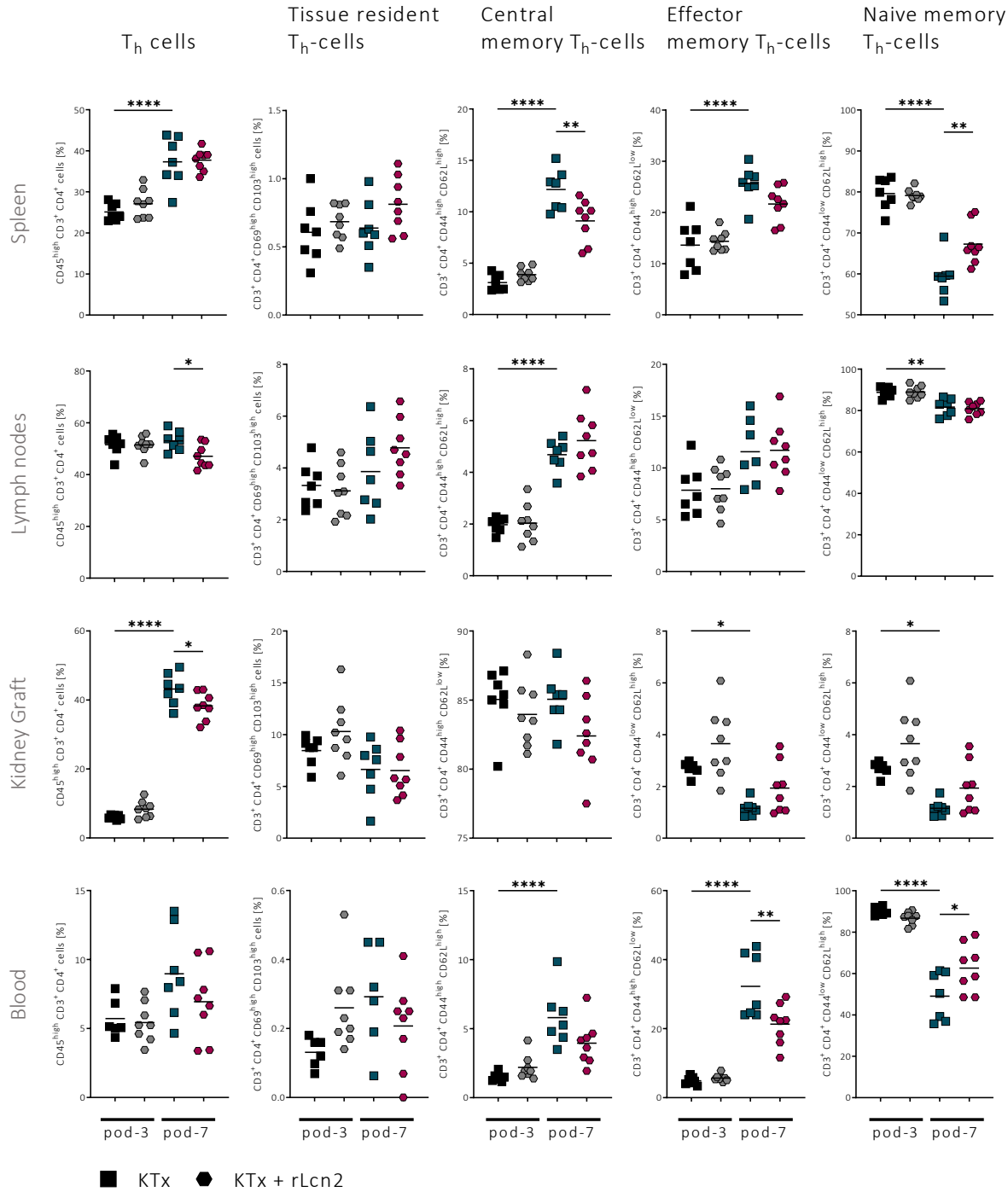

Figure 4: Relative frequencies of distinctive helper T (T_h)-cells and subgroups are significantly affected due to treatment with rLcn2.

Immune cells were isolated from spleens, lymph nodes, kidney grafts, and blood after allogenic murine kidney transplantations from Balb/c to C57Bl/6 mice (n=7-8) on pod-3 and pod-7. The same staining protocol and analysis methods as described in **Figure 3** were used to acquire the relative frequencies of T_h-cells and subgroups (*T-Panel*, **Table 10**). Horizontal lines represent the respective mean. Statistical analysis: Ordinary one-way ANOVA; * $p < 0.05$, ** $p \leq 0.01$, *** $p \leq 0.001$, **** $p \leq 0.0001$.

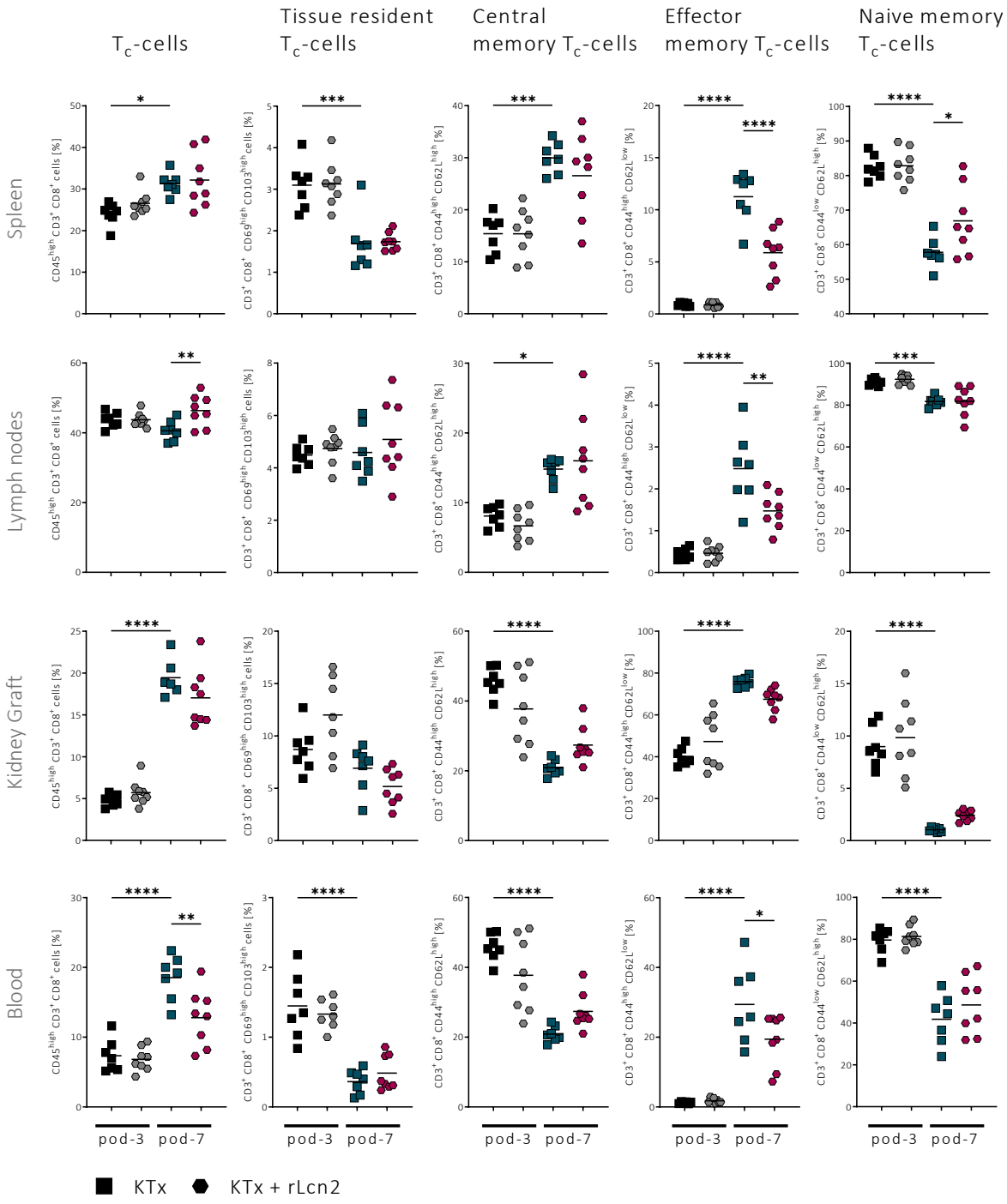

Figure 5: Altered relative abundances of distinctive T$_c$-cells and subgroups due to rLcn2-treatment.
Immune cells were isolated from spleens, lymph nodes, kidney grafts, and blood after allogenic murine kidney transplantations from Balb/c to C57Bl/6 mice (n=7-8) on pod-3 and pod-7. The same staining protocol and analysis methods as described in **Figure 3** were used to assess the composition of T$_c$-cells and subgroups (*T-Panel*, **Table 10**). Horizontal lines represent the respective mean. Statistical analysis: Ordinary one-way ANOVA; * $p < 0.05$, ** $p \leq 0.01$, *** $p \leq 0.001$, **** $p \leq 0.0001$.

3.1.2 TREATMENT WITH rLCN2 ALTERS RELATIVE INNATE IMMUNE CELL FREQUENCIES

Focusing on innate immune cells, we noted a significant increase in the relative abundance of mature and lymphoid dendritic cell-populations in spleen samples at pod-7 compared to pod-3. In lymph nodes, the relative abundance of eosinophils, neutrophils, as well as mature and tissue resident dendritic cells increased significantly at pod-7 (**Figure 6**), while macrophages and Ly6C^{low} macrophages significantly decreased (**Figure 7**). Examining innate immune cells isolated from the kidney graft revealed significantly lower relative frequencies of neutrophils, mature dendritic cells, and Ly6C$^{intermediate-high}$ macrophages at pod-7 in comparison to pod-3. On the contrary, relative abundances of lymphoid dendritic cells and Ly6C^{low} macrophages were significantly increased at pod-7. Mature dendritic cells

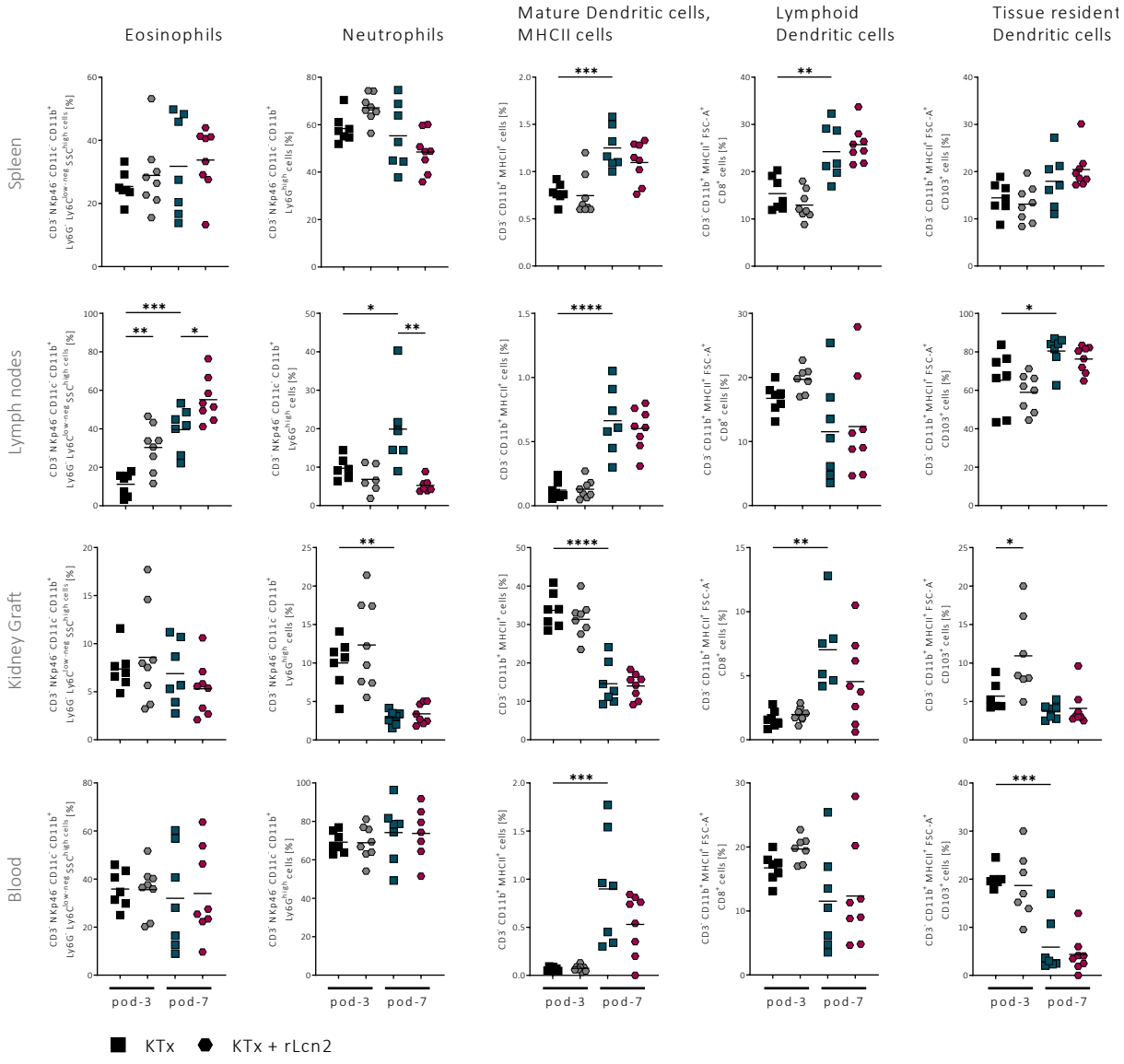

Figure 6: Perioperative treatment with rLcn2 significantly affects certain innate immune cell populations. Immune cells were isolated from spleens, lymph nodes, kidney grafts, and blood after allogenic murine kidney transplantations from Balb/c to C57Bl/6 mice (n=7-8) on pod-3 and pod-7. The same staining protocol and analysis methods as described in **Figure 3** were employed to evaluate the impact of rLcn2-treatment on specific innate immune cell populations (*Innate Panel*, **Table 10**). Horizontal lines represent the respective mean. Statistical analysis: Ordinary one-way ANOVA; * $p < 0.05$, ** $p \leq 0.01$, *** $p \leq 0.001$, **** $p \leq 0.0001$.

were present in significantly higher relative frequencies in blood samples at pod-7, while tissue resident dendritic cells were significantly lower at the same time point (**Figure 6** and **Figure 7**).

Perioperative administration of rLcn2 led to a significant lowering of the relative frequencies of neutrophils in lymph nodes at pod-7 and to an increase of eosinophils at pod-3 and pod-7 (**Figure 6**).

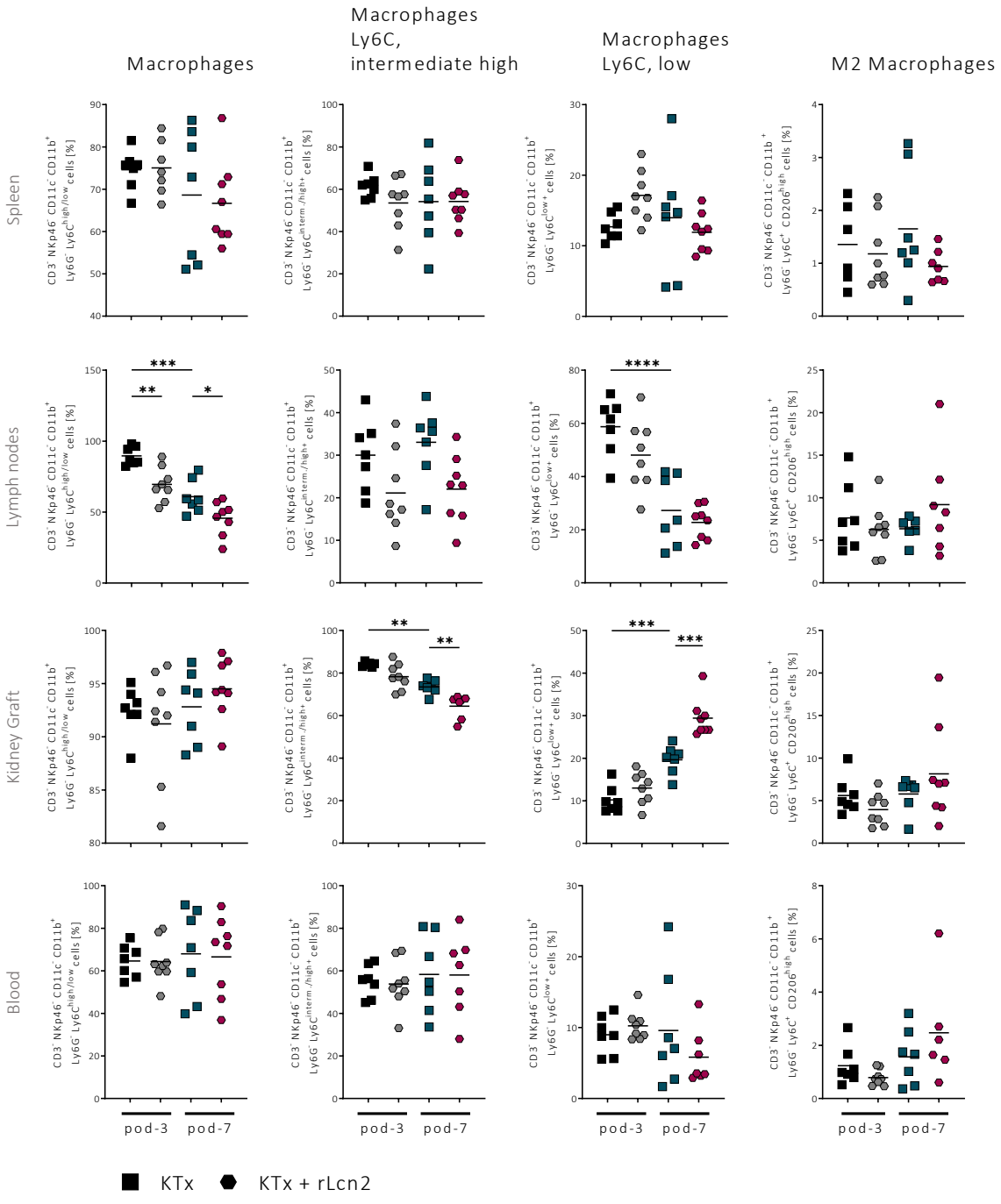

Figure 7: Intermediate mature macrophages were significantly reduced in kidney grafts due to treatment with rLcn2 on pod-7.

Immune cells were isolated from spleens, lymph nodes, kidney grafts, and blood after allogenic murine kidney transplantations from Balb/c to C57Bl/6 mice (n=7-8) on pod-3 and pod-7. The same staining protocol and analysis methods as described in **Figure 3** were used to quantify the frequencies of distinct macrophage populations (*Innate Panel*, **Table 10**). Horizontal lines represent the respective mean. Statistical analysis: Ordinary one-way ANOVA; * $p < 0.05$, ** $p \leq 0.01$, *** $p \leq 0.001$, **** $p \leq 0.0001$.

The relative abundance of macrophages in lymph nodes was significantly lower following rLcn2-treatment at pod-3 and pod-7 (**Figure 7**). Relative frequencies of tissue resident dendritic cells isolated from kidney grafts were significantly increased at pod-3 (**Figure 6**). At pod-7, Ly6C$^{intermediate-high}$ macrophages were significantly decreased, while Ly6C^{low} macrophages were significantly higher in abundance than at pod-3 in samples treated with rLcn2 from kidney grafts (**Figure 7**).

To summarize, the administration of rLcn2 resulted in significant decreases of specific innate immune cell populations at pod-7, such as neutrophils and macrophages from lymph nodes, as well as Ly6C$^{intermediate-high}$ macrophages from kidney grafts. Consequently, Ly6C^{low} macrophages in kidney grafts were significantly reduced. However, eosinophils isolated from lymph nodes exhibited a significant increase both at pod-3 and pod-7 following rLcn2-treatment.

3.1.3 PAN NK CELL POULATIONS ARE NOT ALTERED UPON TREATMENT WITH rLCN2

Natural killer (NK) cells are a critical component in the innate immune system, involved in identifying and eliminating compromised cells, and they also contribute to immune regulation through the secretion of cytokines, such as IFNγ [91]. The exact role of NK cells in allograft rejection can be influenced by multiple factors, including the type of transplantation, the immunosuppressive regimen, the presence of donor-specific antibodies, and the balance between activating and inhibitory signals received by NK cells [92-94]. Exploring the impact of rLcn2-treatment on relative NK cell frequencies can provide valuable insights into the potential effects on renal allografts, shedding light on its functional consequences.

Comparing the relative abundances at pod-3 and pod-7, we detected a significant increase of NK cells in spleens, lymph nodes, and blood, and a significant decrease in kidney grafts at pod-7 (**Figure 8**). Significantly higher relative frequencies of naïve NK cells (in lymph nodes), intermediate mature NK cells (in spleen and blood), NKp46^{+}NKG2D^{+} cells (in spleen, kidney graft and blood), NKp46^{+}NKG2A^{+} and CD8^{+}NKG2D^{+} cells (in spleen, lymph nodes, kidney graft, and blood) were furthermore detected at pod-7 compared to pod-3 (**Figure 8** and **Figure 9**). Contrarily, significantly lower relative frequencies of intermediate mature NK cells from lymph nodes were detected at pod-7 compared to pod-3 (**Figure 8**).

Although perioperative treatment with rLcn2 did not alter pan, naïve or mature NK cell populations, it significantly affected intermediate mature NK cells in spleen and blood, by increasing their relative frequencies at pod-3 and lowering it at pod-7.

To explore the cytotoxic function of NK cells, it is essential to assess the relative abundances of activating (e.g. NKG2D) and inhibitory (e.g. NKG2A) surface receptors, as they play a crucial role in determining the functionality of NK cells. Consequently, the impact of perioperative rLcn2-treatment on the relative abundance of these receptors on NK cells was evaluated. Intriguingly, administering

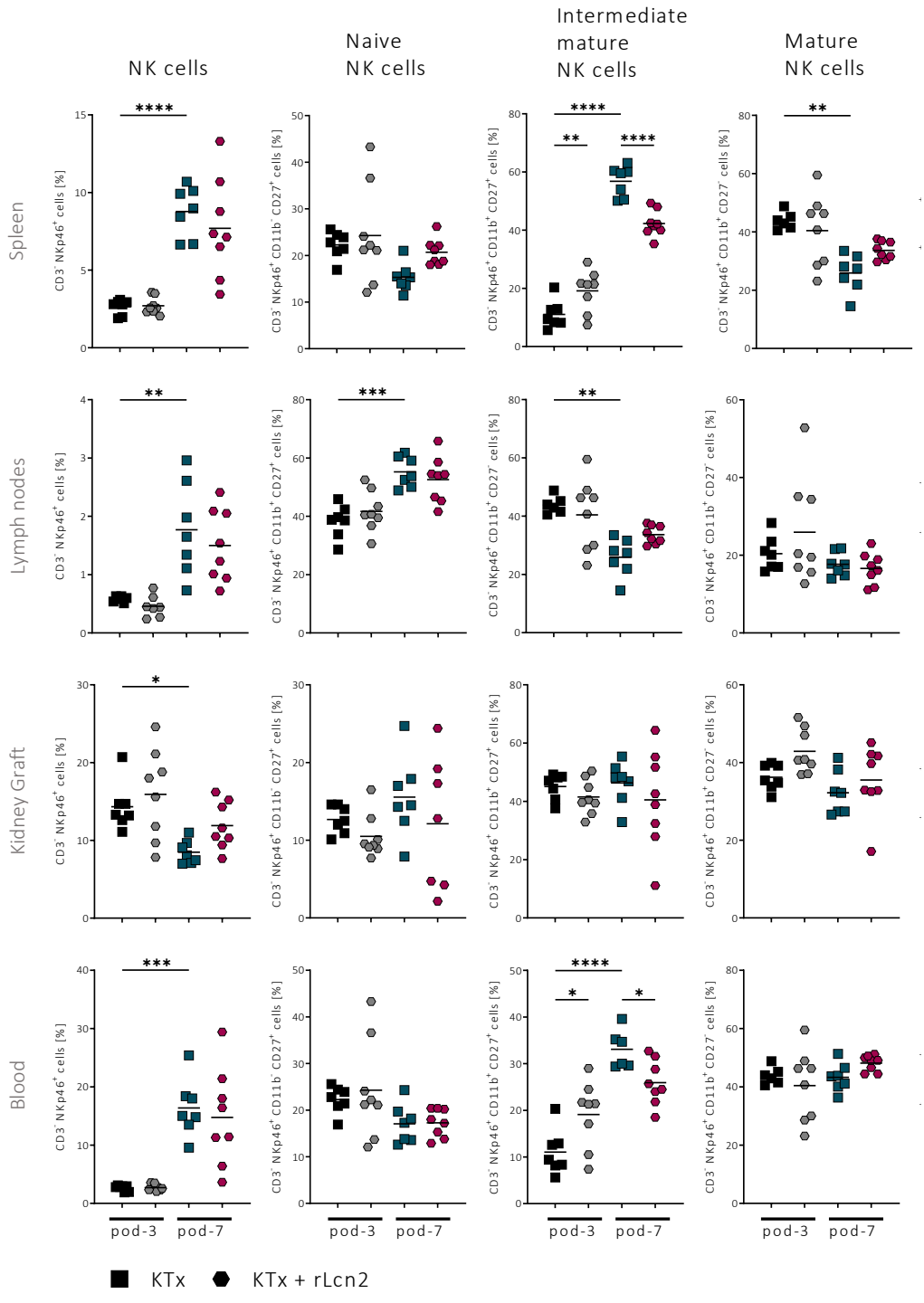

Figure 8: Treatment with rLcn2 significantly alters intermediate mature NK cells from spleen and blood.
Immune cells were isolated from spleens, lymph nodes, kidney grafts, and blood after allogenic murine kidney transplantations from Balb/c to C57Bl/6 mice (n=7-8) on pod-3 and pod-7. The same staining protocol and analysis methods as described in **Figure 3** were employed to assess the impact of rLcn2-treatment on NK cells (*NK-Panel*, **Table 10**). Horizontal lines represent the respective mean. Statistical analysis: Ordinary one-way ANOVA; * $p < 0.05$, ** $p \leq 0.01$, *** $p \leq 0.001$, **** $p \leq 0.0001$.

rLcn2 perioperatively resulted in a notable reduction in the relative frequency of $CD8^+NKG2D^+$ cells obtained from both spleen and blood samples at pod-7, as well as a significant decrease of $NKp46^+NKG2A^+$ cells isolated from blood samples at pod-7 (**Figure 9**).

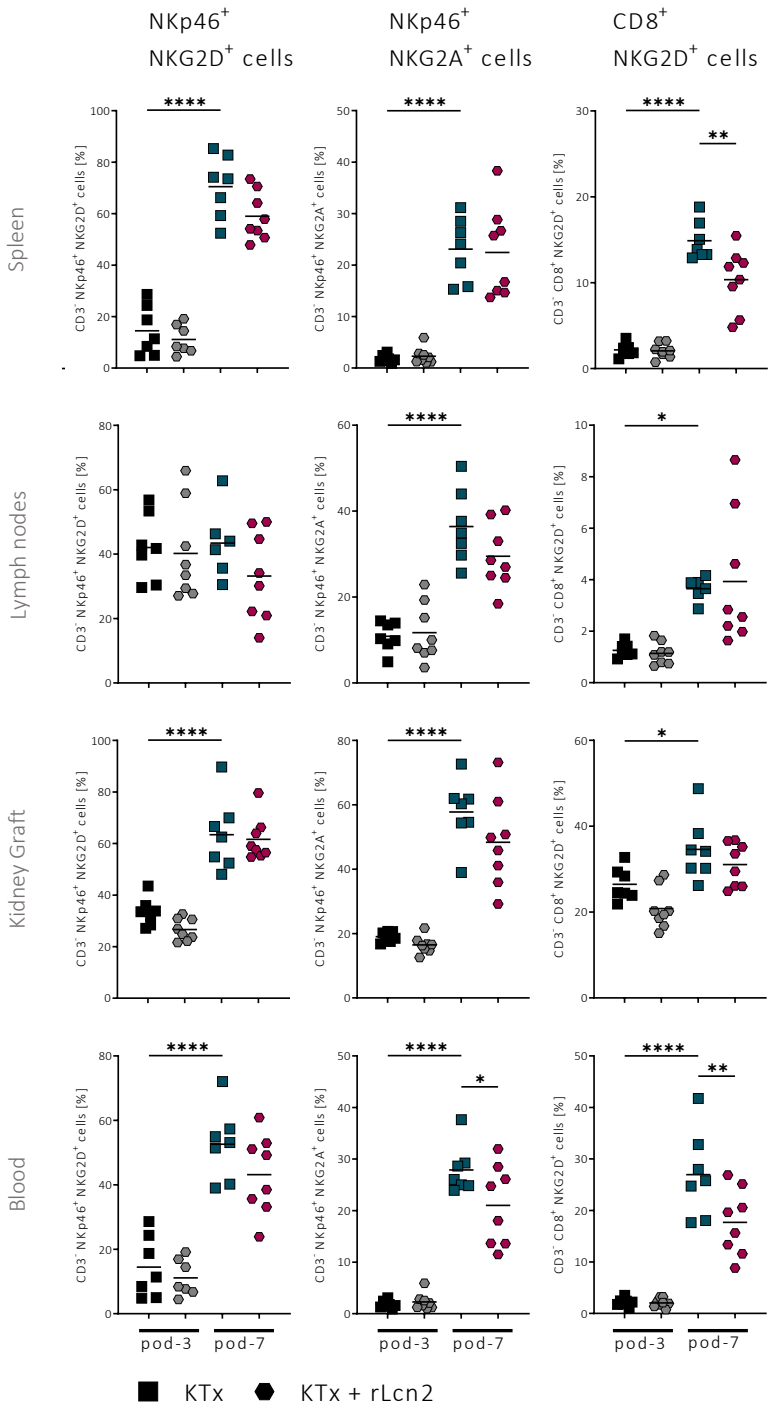

Figure 9: $CD8^+NKG2D^+$ cells are significantly reduced at pod-7 by rLcn2-treatment in both spleen and blood. Immune cells were isolated from spleens, lymph nodes, kidney grafts, and blood after allogenic murine kidney transplantations from Balb/c to C57Bl/6 mice (n=7-8) on pod-3 and pod-7. The same staining protocol and analysis methods as described in **Figure 3** were employed to assess the impact of rLcn2-treatment on subsets of NK cells (*NK-Panel*, **Table 10**). Horizontal lines represent the respective mean. Statistical analysis: Ordinary one-way ANOVA; * $p < 0.05$, ** $p \leq 0.01$, *** $p \leq 0.001$, **** $p \leq 0.0001$.

3.1.4 rLCN2-TREATMENT MIGHT HAVE AN INDIRECT EFFECT ON NKG2D$^+$ CELLS

NKG2D is characterized as the major recognition receptor for detection and elimination of transformed and infected cells and is mainly expressed on NK cells and CD8$^+$T-cells [95-97]. Upregulation of this receptor is only facilitated under stress conditions, such as infections or IRI. In mice, NKG2D expression on CD8$^+$ T-cells occurs after activation. However, even if the *in vivo* data suggest an effect of rLcn2-treatment, it remains unclear, whether the NKG2D expression on CD8$^+$T-cells are directly or indirectly affected by it.

To delineate the possible effect of rLcn2-treatment on the expression of NKG2D on CD8$^+$T-cells, isolated pan T cells were stimulated with anti-CD3 and anti-CD28 antibodies. Through the engagement of the T-cell receptor (TCR) complex (CD3) and the co-receptor (CD28) the activation and expansion of CD8$^+$ T-cells is enhanced, resulting in increased NKG2D expression[95]. Additionally, either apo-rLcn2 or holo-rLcn2 was applied to the cell culture to validate effects of the respective treatments.

Flow cytometric analysis of cells isolated after 48 hours of cell culture, verified significant expression of NKG2D on T_c-cells. However, neither the treatment with apo-rLcn2 nor with holo-rLcn2 affected the relative frequencies of CD8$^+$NKG2D$^+$ cells, suggesting that those cells are not directly affected by the treatment with rLcn2.

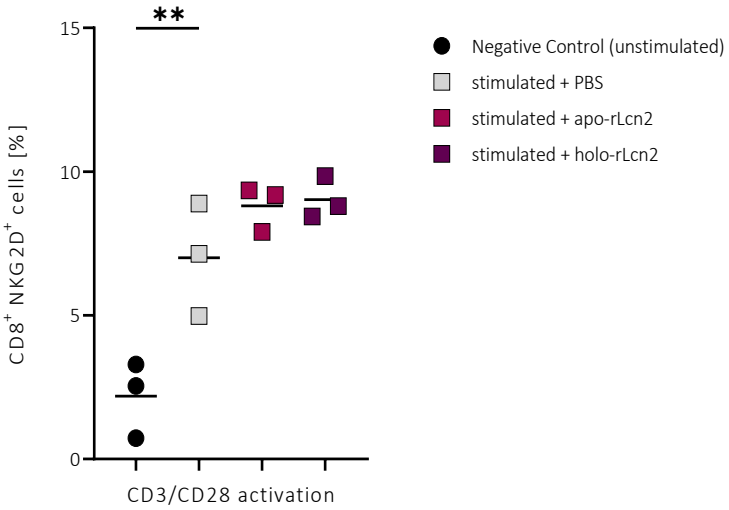

Figure 10: NKG2D expression on T_h-cells was significantly induced *in vitro* with CD3/CD28 antibody combination.

Ex vivo activated T-cells isolated from spleens of C57Bl/6 mice were either treated with apo-rLcn2 or holo-rLcn2 and harvested after 48 hours of culture. T-cells were stained with a cocktail of monoclonal antibodies (*Functional-Panel*, Table 10). Relative frequencies and MFI of immune cells were acquired on a BD LSRFortessa™ Cell Analyzer and analysed using FlowJo™ and GraphPad Prism software. Horizontal lines represent the respective mean. n = 3. Statistical analysis: Ordinary one-way ANOVA; * $p < 0.05$, ** $p \leq 0.01$, *** $p \leq 0.001$, **** $p \leq 0.0001$.

Since the NKG2D receptor is primarily expressed on activated NK cells, we proceeded with the *ex vivo* stimulation of leukocytes isolated from spleens from C57Bl/6 mice along with the specific induction of NK cell activation. T- and NK cells were stimulated with a combination of phorbol 12-

myristate 13-acetate (PMA) and ionomycin; a combination that provides strong and non-specific stimulation, bypassing the need for specific receptor engagement [98,99]. Treatment with PMA/Ionomycin led to rapid NK cell activation, characterized by increased expression of activation markers such as CD107a as well as enhanced production of pro-inflammatory cytokines including interferon-gamma (IFNγ) and IL-17 (**Figure 11**).

Intriguingly, pre-treatment of gentleMACS™ sorted NK cells with rLcn2 (apo-rLcn2 or holo-Lcn2) for 48 hours, led to a significant decrease in the relative abundance of CD107a$^+$ cells and IFNγ$^+$ NK cells (**Figure 11**). In correlation, the mean fluorescence intensities (MFI) of NKp46$^+$CD107a$^+$ cells were likely affected by said treatment, suggesting an effect of rLcn2-treatment with on the degranulation process of NK cells (**Figure 11B**).

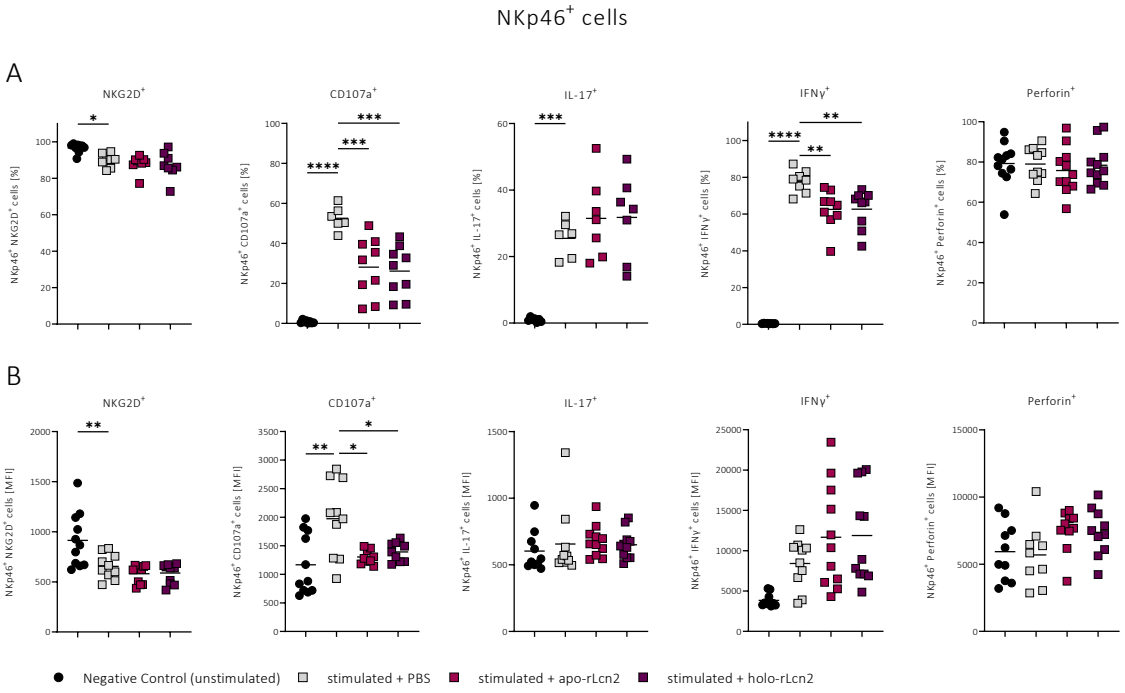

Figure 11: *Ex vivo* stimulation of NK cells suggests indirect effect of treatment with rLcn2.
Ex vivo activated NK cells isolated from spleens of C57Bl/6 mice were either treated with apo-rLcn2 or holo-rLcn2 and harvested after 48 hours of culture. NK cells were stained with a cocktail of monoclonal antibodies (*Functional-Panel*, **Table 10**). Relative frequencies and MFI of immune cells were acquired on a BD LSRFortessa™ Cell Analyzer and analysed using FlowJo™ and GraphPad Prism software. Horizontal lines represent the respective mean. Statistical analysis: Ordinary one-way ANOVA; * $p < 0.05$, ** $p \leq 0.01$, *** $p \leq 0.001$, **** $p \leq 0.0001$.

Despite successful activation, the treatment with rLcn2 did not alter the relative frequencies of CD4$^+$ and CD8$^+$T-cells and their subsets (**Supplementary Figure S11-Figure S13**). This aligns with the results obtained from the activated T-cell culture experiments (**Figure 10**), where treatment with either of the two rLcn2 variants had no effects either. However, it is noteworthy that the MFIs of CD4$^+$INFγ$^+$ (**Supplementary Figure S11**) and CD8$^+$IFNγ$^+$ cells (**Supplementary Figure S13**) were significantly elevated after treatment with apo-rLcn2 compared to the untreated control, adding another potential factor to its previously described proapoptotic role due to iron depletion [30].

All in all, we observed significant effects of the treatment with rLcn2 on the relative frequencies of intermediate mature NK cells and $CD8^+NKG2D^+$ cells from spleen and blood samples at pod-7. Intriguingly, *in vitro* experiments indicated that the observed effects on $CD8^+NKG2D^+$ cells might be mediated indirectly rather than through direct interactions with rLcn2. Moreover, pre-treatment of NK cells with rLcn2 led to a significant decrease in $CD107a^+$ and $IFN\gamma^+$ NK cells *in vitro*, indicating an effect on NK cell degranulation. However, the treatment did not result in any notable changes in the relative frequencies of $CD4^+$ and $CD8^+$ T-cells and their subsets.

3.1.5 THE FUNCTIONALITY OF IMMUNE CELLS SIGNIFICANTLY IMPROVES UPON TREATMENT WITH rLCN2

Not only were relative frequencies of adaptive and innate immune cells determined, but also their functionality was addressed by evaluation of the immune cells' activation profiles. This is particularly relevant to gain a more comprehensive understanding of the specific immune response under the treatment of rLcn2 and to assess their potential functional relevance.

Therefore, immune cells were isolated from the spleens and kidney grafts of Balb/c to C57Bl/6 transplanted mice that had been perioperatively treated with either rLcn2 or saline (control) at pod-3 and pod-7. The isolated cells were then cultured in RPMI medium for 24 hours, supplemented with IL-2 to facilitate T cell proliferation and activation. IL-2 was included as it is additionally recognized to support NK cell activity and helps create an environment conducive to robust immune cell responses [100,101]. Subsequently, the immune cells were *ex vivo* activated with a combination of PMA and ionomycin, and their degranulation capacity and cytokine expression patterns were analysed.

Comparing the activation and degranulation statuses between pod-3 and pod-7, we observed a significant increase of $CD4^+IL17^+$-cells in spleen samples and in $CD4^+CD107a^+$- and $CD4^+Perforin^+$-cells in kidney graft samples (**Figure 12**). Besides, the MFI was significantly higher in $CD4^+IFN\gamma^+$-cells in spleen samples and significantly lower in $CD4^+CD107a^+$ cells on pod-7 compared to pod-3. The MFI of kidney graft samples did not significantly change between the time points (**Figure 12**). Considering the functionality of certain immune cell populations, the perioperative treatment with rLcn2 resulted in a significant impact on the cells' degranulation capacities. Not only led the perioperative treatment with rLcn2 to a significant decrease in the relative abundance of $CD4^+CD107a^+$ and $CD4^+IFN\gamma^+$-cells in spleens at pod-7, but also to a significant reduction in the relative abundance of $CD4^+IFN\gamma^+$ cells in kidney grafts at pod-7 (**Figure 12**). Furthermore, the relative frequency of T_h17-cells was significantly lower in kidney grafts at pod-7 compared to pod-3, while the MFI did not change. However, in spleens, the MFI of T_h17 cells was significantly lower at pod-7 than at pod-3 (**Figure 13**).

The treatment with rLcn2 significantly reduced the relative frequencies of T_h1-cells in spleen and kidney graft samples at pod-7, as well as the MFI of T_h17-cells at pod-3. Contrarily, the MFI of T_h1-cells was significantly higher in spleens after treatment with rLcn2 at pod-7 (**Figure 13**).

At pod-7, the relative abundances of $CD8^+IFN\gamma^+$- and $CD8^+Perforin^+$-cells from spleen samples was significantly higher than at pod-3. In kidney graft samples, however, $CD8^+IL17^+$- and $CD8^+Perforin^+$-cells were significantly higher than at pod-3 (**Figure 14**). The MFI of $CD8^+CD107a^+$ cells was significantly lower, compared to an increased MFI of $CD8^+IL\text{-}17^+$- and $CD8^+Perforin^+$cells from spleens at pod-7 compared to pod-3 (**Figure 14**). Due to treatment with rLcn2, the relative abundances of $CD8^+CD107a^+$-cells in spleen and kidney graft samples, as well as of $CD8^+IFN\gamma^+$ cells from kidney grafts were significantly lowered by the treatment at pod-7. In addition, the treatment also significantly reduced the relative frequencies of $CD8^+Perforin^+$ cells from kidney grafts at pod-7 and the MFI of $CD8^+CD107a^+$-cells from spleens at pod-7 (**Figure 14**).

In comparison to pod-3, the relative frequencies of $NKp46^+Perforin^+$-cells was significantly higher in spleen samples, but also significantly lower in $NKp46^+CD107a^+$-cells from kidney grafts at pod-7 (**Figure 15**). In spleen samples, the MFI of $NKp46^+CD107a^+$-cells was significantly lower at pod-7 compared to pod-3, while it was significantly higher in $NKp46^+Perforin^+$ cells. The MFI in kidney graft samples was again not notably changed (**Figure 15**). Treatment with rLcn2 significantly reduced the relative abundance of $NKp46^+CD107a^+$ in spleen samples on pod-7 and concurrently let to a significant increase in the MFI of $NKp46^+Perforin^+$ cells in spleen samples. However, the relative abundances of $NKp46^+$ immune cells were not affected by the treatment with rLcn2 (**Figure 15**).

Altogether, in the context of rLcn2-treatment, the evaluation of immune cell functionality and degranulation capacity has indicated significant decreases in specific immune cell subsets. Notable reductions particularly occurred for T_h1 cells, as well as $CD107a^+$ and $IFN\gamma^+$ cells on both $CD4^+$ and $CD8^+$ cell populations in spleen and/or kidney graft samples. This suggests that rLcn2-treatment has a suppressive effect on the functionality and degranulation capacity of immune cells associated with T_h1 responses and cytotoxic activity.

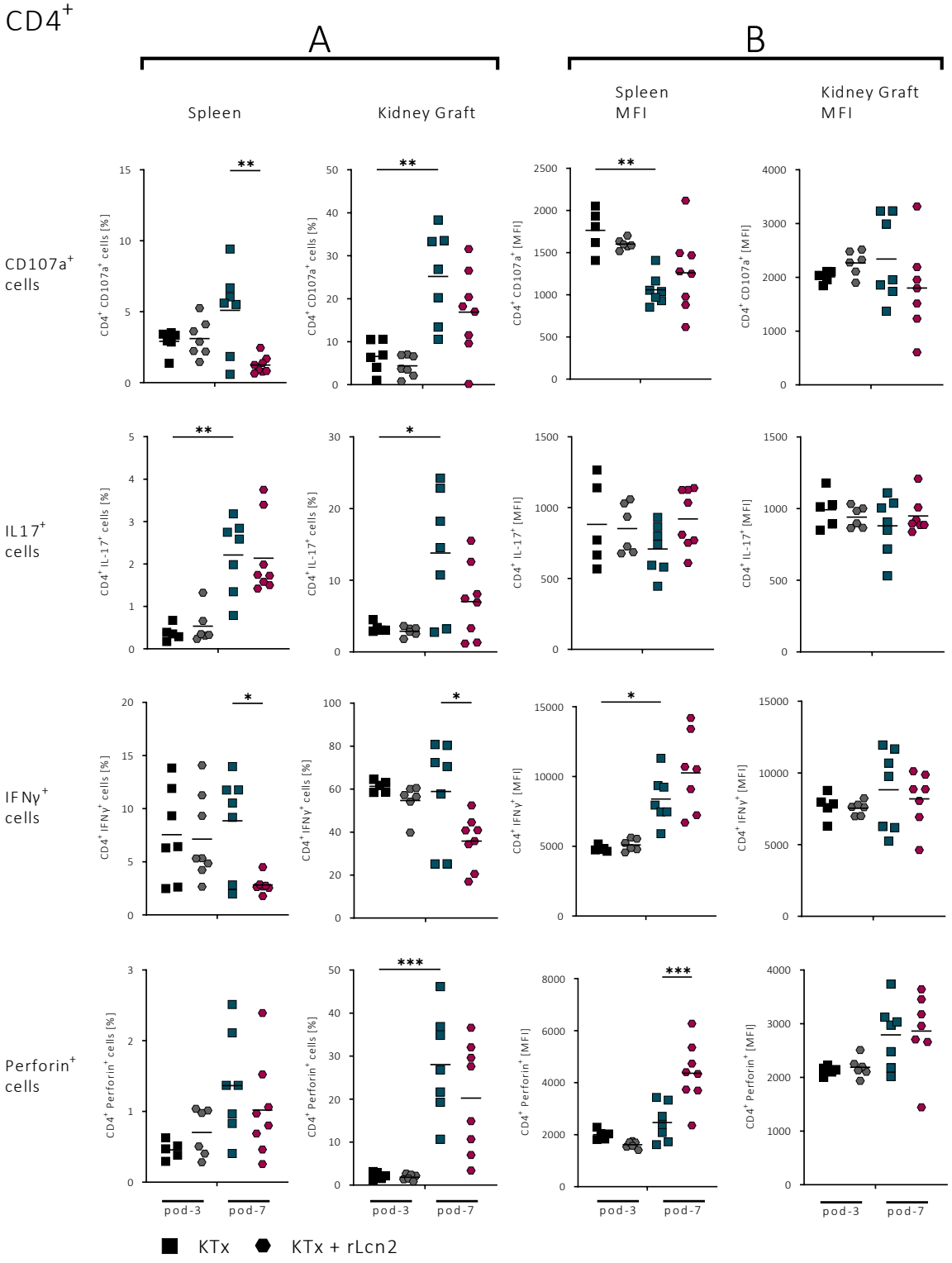

Figure 12: Treatment with rLcn2 significantly lowers distinctive CD4⁺ subsets after *ex vivo* activation.
Immune cells were isolated from spleens, and kidney grafts after allogenic murine kidney transplantations from Balb/c to C57Bl/6 mice (n=7-8) on pod-3 and pod-7. Extra- and intracellular staining of CD4⁺ immune cells was performed using a cocktail of monoclonal antibodies (*Functional Panel*, **Table 10**). Relative frequencies and MFI of CD107a⁺, IL-17⁺, IFNγ⁺, and Perforin⁺ cells were acquired on a BD LSRFortessa™ Cell Analyzer and analysed using FlowJo™ and GraphPad Prism software. Horizontal lines represent the respective mean. Statistical analysis: Ordinary one-way ANOVA; * $p < 0.05$, ** $p \leq 0.01$, *** $p \leq 0.001$, **** $p \leq 0.0001$.

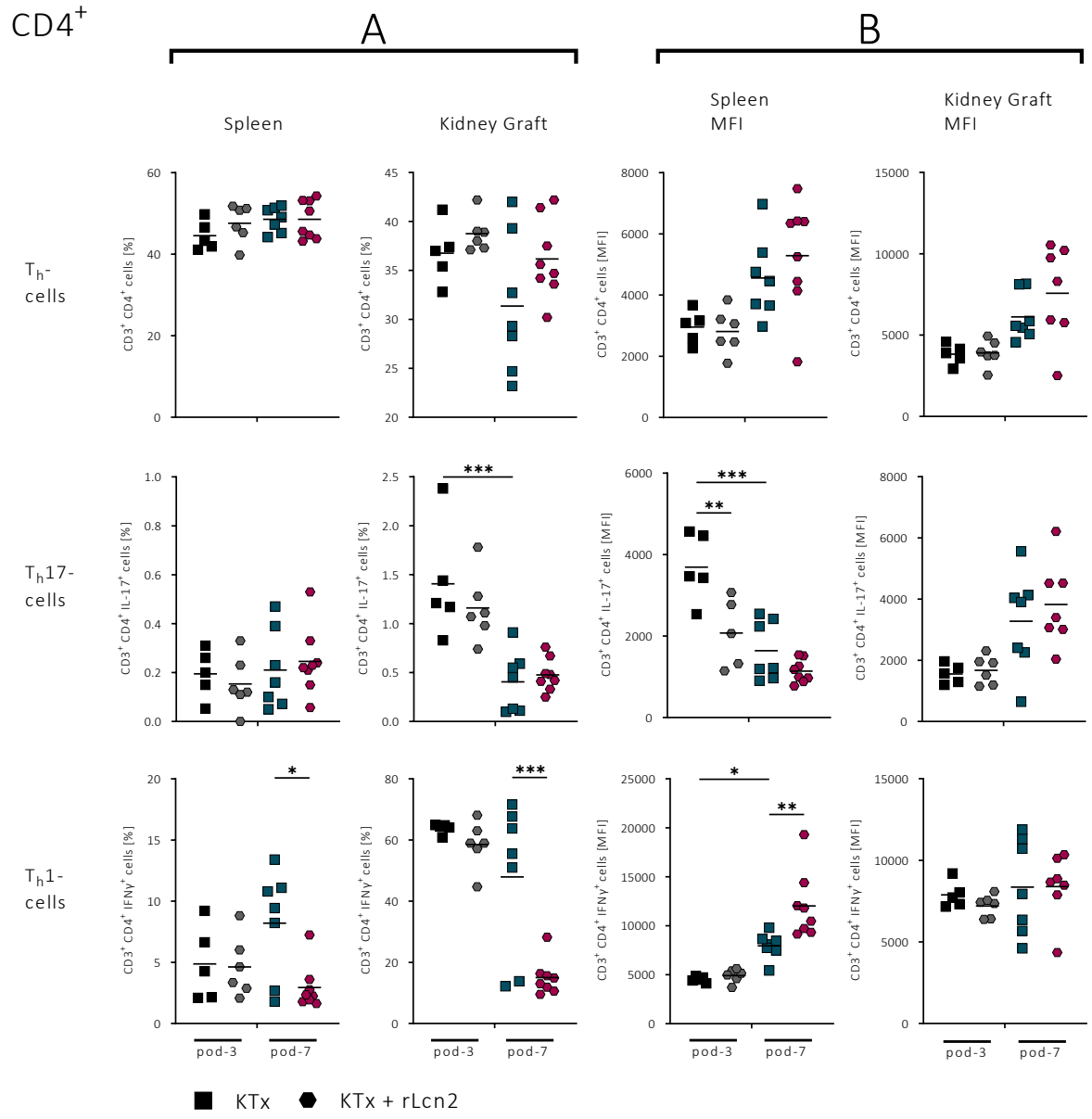

Figure 13: ***Ex vivo*** **activated T_h1 cells from kidney grafts are significantly reduced due to treatment with rLcn2.**

Immune cells were isolated from spleens, and kidney grafts after allogenic murine kidney transplantations from Balb/c to C57Bl/6 mice (n=7-8) on pod-3 and pod-7. The same staining protocol and analysis methods as described in **Figure 12** were used to quantify the relative frequencies of $CD4^+$ activated immune cells and subsets (*Functional Panel*, **Table 10**). Horizontal lines represent the respective mean. Statistical analysis: Ordinary one-way ANOVA; * $p < 0.05$, ** $p \leq 0.01$, *** $p \leq 0.001$, **** $p \leq 0.0001$.

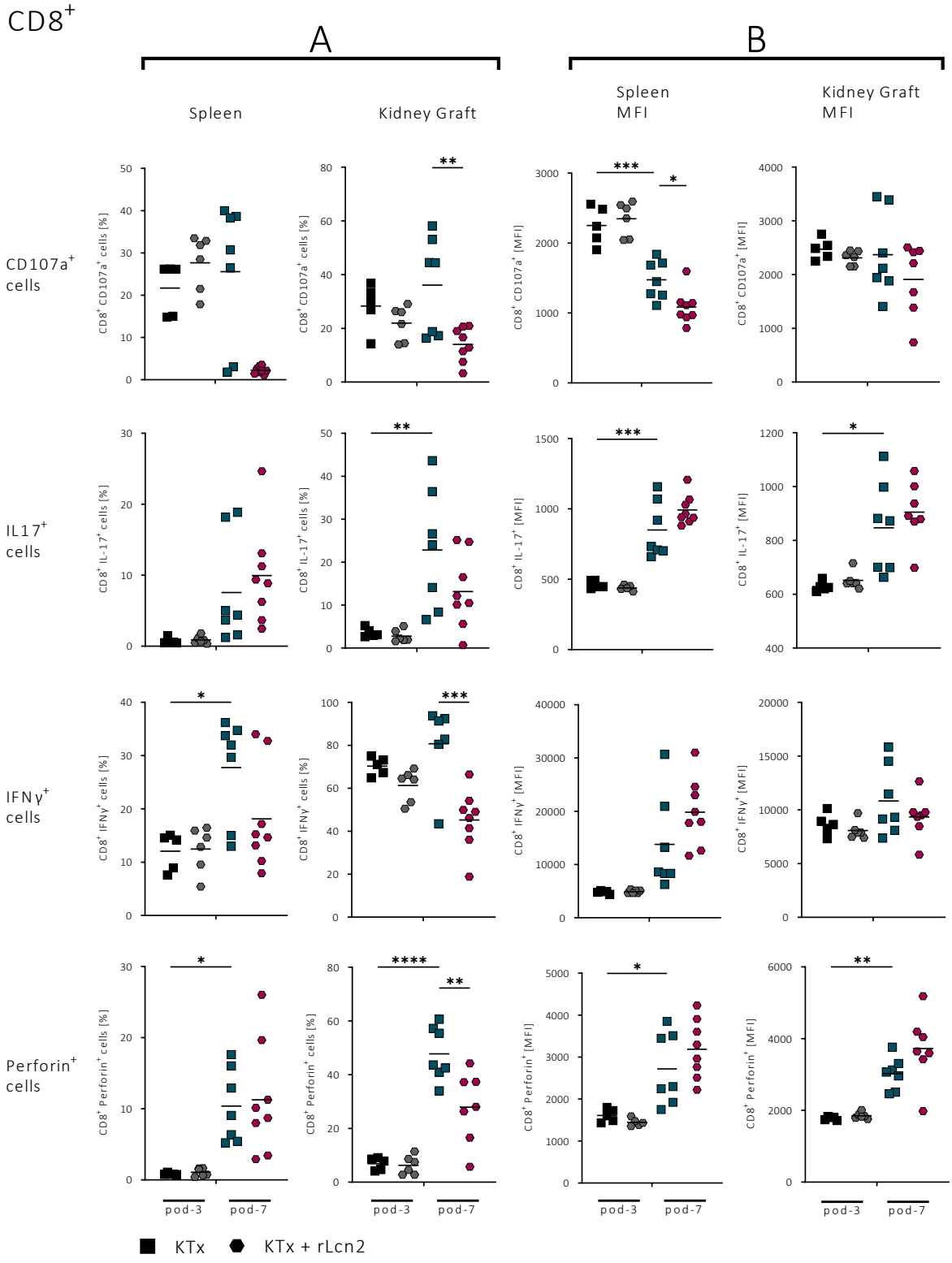

Figure 14: Distinctive subsets of *ex vivo* activated CD8⁺ cells are significantly reduced after rLcn2-treatment. Immune cells were isolated from spleens, and kidney grafts after allogenic murine kidney transplantations from Balb/c to C57Bl/6 mice (n=7-8) on pod-3 and pod-7. The same staining protocol and analysis methods as described in **Figure 12** were used to assess the relative frequencies of CD8⁺ activated immune cells and subsets (*Functional Panel*, **Table 10**). Horizontal lines represent the respective mean. Statistical analysis: Ordinary one-way ANOVA; * $p < 0.05$, ** $p \leq 0.01$, *** $p \leq 0.001$, **** $p \leq 0.0001$.

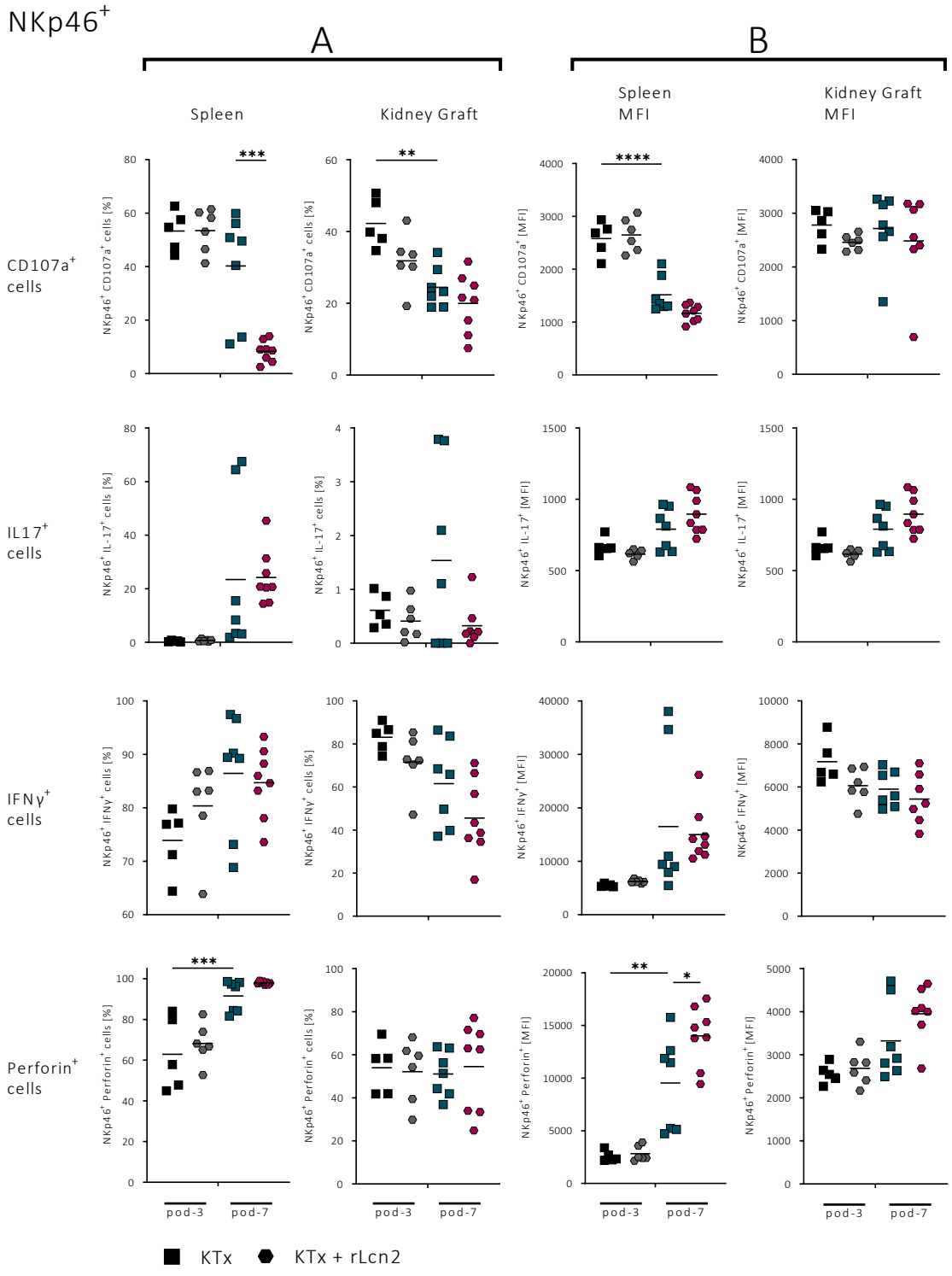

Figure 15: From *ex vivo* activated subsets of NKp46⁺ cells, only CD107a⁺ cells are significantly reduced after treatment with rLcn2.

Immune cells were isolated from spleens, and kidney grafts after allogenic murine kidney transplantations from Balb/c to C57Bl/6 mice (n=7-8) on pod-3 and pod-7. The same staining protocol and analysis methods as described in **Figure 12** were used to determine the relative frequencies of NKp46⁺ activated immune cells and subsets (*Functional Panel*, **Table 10**). Horizontal lines represent the respective mean. Statistical analysis: Ordinary one-way ANOVA; * $p < 0.05$, ** $p \leq 0.01$, *** $p \leq 0.001$, **** $p \leq 0.0001$.

3.1.6 IFNγ$^+$ CELLS ARE REDUCED IN KIDNEY GRAFTS DUE TO TREATMENT WITH rLCN2

The analysis of *ex vivo* activated immune cells allowed to facilitate a deeper understanding of the intricate immunological processes involved in graft-host interactions, identify key cellular players, and potentially discover novel therapeutic targets. For a more comprehensive characterization of the phenotypic and functional diversity of *ex vivo* activated immune cells derived from spleens and kidney grafts at pod-3 and pod-7 after allogeneic kidney transplantation (Balb/c to C57Bl/6) in mice, t-distributed stochastic neighbour embedding (t-SNE) analysis was employed. Incorporating t-SNE analysis enabled to overcome the limitations of traditional gating strategies, which often oversimplify the complexity of immune cell populations, instead providing an unbiased visualization of the heterogeneity within *ex vivo* activated immune cells.

The analysis incorporated markers for NK$^+$, CD4$^+$, and CD8$^+$ cells, as well as their subsets expressing CD107a, IFNγ, IL-17, or Perforin. To analyse clustering patterns and potential impacts of rLcn2-treatment on the immune response within kidney grafts at pod-3 and pod-7, a comparison was made between two groups: perioperatively treated with rLcn2 versus perioperatively treated with saline (untreated control group). Additionally, spleen samples were subjected to t-SNE analysis on pod-3 and pod-7, providing insights into the immune response within secondary lymphoid organs (**Figure 16-Figure 19**). Total counts from t-SNE analysis of spleens and kidney grafts are listed in **Supplementary Table S1**.

Overall, on both pod-3 and pod-7, t-SNE revealed distinct cell clusters of NK$^+$, CD4$^+$, and CD8$^+$ cells. These clusters were uniformly distributed and further categorized into subsets expressing CD107a, IFNγ, IL-17, or Perforin, originating from both rLcn2-treated and untreated samples (**Figure 16A-Figure 19A**). Cells from the respective subsets, probably having similar gene expression profiles, grouped together on the t-SNE plot, suggesting spatial organization based on functional or molecular similarities.

At pod-3, spleens exhibited a higher expression of NK cells and NK subsets; however, rLcn2-treated samples showed lower expression levels of CD4$^+$, CD8$^+$, and CD8$^+$CD107a$^+$ cells (**Figure 16A**, **Supplementary Table S1**). Surprisingly, the t-SNE plots of immune cells isolated from spleens at pod-3 displayed no significant differences between rLcn2-treated and untreated samples (**Figure 16B**). In contrast, kidney grafts from rLcn2-treated samples revealed a significant reduction in the number of NK$^+$, CD4$^+$, and CD8$^+$ cell subsets (**Figure 17A**, **Supplementary Table S1**). Notably, the overall numbers of NK$^+$ cells, CD4$^+$ cells, and CD8$^+$ cells remained relatively similar. Additionally, the t-SNE plots exhibited a decreased expression of IFNγ in rLcn2-treated kidney grafts compared to untreated kidney grafts (**Figure 17B**).

At pod-7, rLcn2-treated samples from spleens exhibited reductions in subsets, particularly NK$^+$CD107a$^+$ cells, CD4$^+$ IFNγ$^+$, CD4$^+$CD107a$^+$, and CD8$^+$ CD107a$^+$cells. This was further supported by relative abundance analysis (**Figure 12**-**Figure 15**). However, the overall populations of NK cells, CD4$^+$ cells, and CD8$^+$ cells remained relatively similar in number (**Figure 18A**, **Supplementary Table S1**). The t-

SNE plots of immune cells isolated from spleens at pod-7 did not reveal significant differences between rLcn2-treated and untreated samples (**Figure 18B**).

In kidney grafts at pod-7, subsets such as $CD4^+IFN\gamma^+$, $CD8^+CD107a^+$, $CD8^+IFN\gamma^+$, and $CD8^+Perforin^+$ cells were reduced in rLcn2-treated samples (**Figure 19A**, **Supplementary Table S1**). This was confirmed by the relative abundance analysis (**Figure 12**-**Figure 15**). The overall numbers of NK cells, $CD4^+$ cells, and $CD8^+$ cells exhibited no significant change, comparable to the immune cells derived from spleens on pod-7. The t-SNE plots of immune cells isolated from rLcn2-treated kidney grafts at pod-7 indicated a decreased expression of IFNγ compared to untreated kidney grafts (**Figure 19B**).

All in all, the t-SNE analysis of *ex vivo* activated immune cells during allogeneic kidney transplantation revealed distinct clusters of NK^+, $CD4^+$, and $CD8^+$ cells, categorized into subsets expressing CD107a, IFNγ, IL-17, or Perforin. Interestingly, rLcn2-treatment resulted in reductions of specific subsets, particularly of IFNγ, within the spleens and kidney grafts. However, overall populations of NK cells, $CD4^+$ cells, and $CD8^+$ cells remained similar.

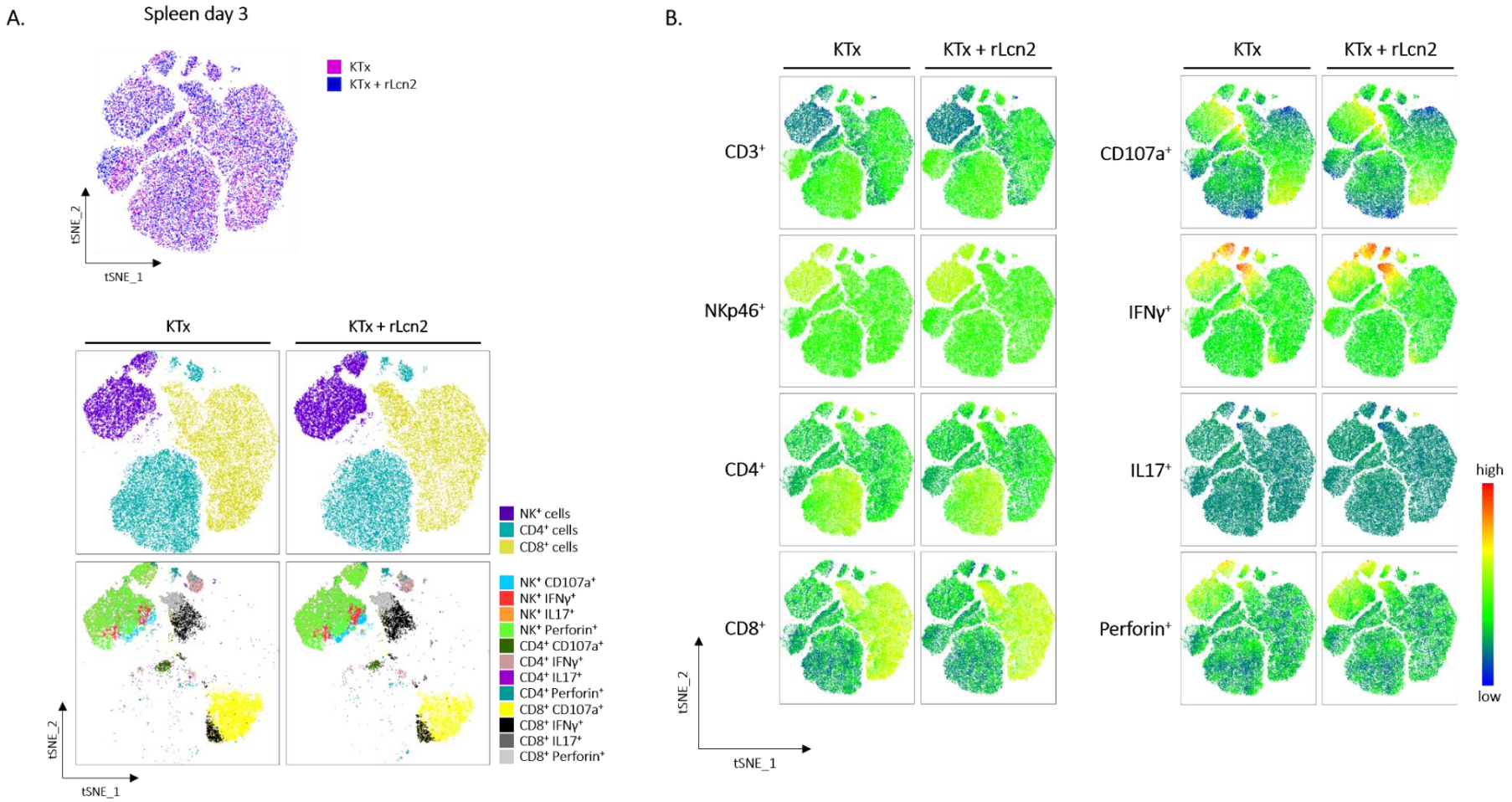

Figure 16: t-SNE analysis reveals enhanced NK cell expression in spleens on pod-3 of rLcn2 treated samples after allogenic mKTx.

(A) Visualization of t-SNE analysis generated using FlowJo™ software, depicting immune cells isolated from spleens at pod-3 after allogenic murine kidney transplantations (Balb/c to C57Bl/6). The analysis included samples with or without perioperative administration of rLcn2. The t-SNE plots were generated by concatenating FCS files (n = 7-8) and utilizing 50,000 lymphocyte events per file. FlowJo™ default parameters were applied (1000 iterations, perplexity of 30). Each data point represents an individual cell, and color-coding indicates distinct cell clusters. The analysis focused on evaluating the expression of NK+, CD4+, CD8+ cells, as well as subsets expressing CD107a, IFNγ, IL-17, or Perforin, comparing perioperatively treated samples with rLcn2 to untreated samples. Total cell counts of each cell cluster are provided in **Table S1**. **(B)** t-SNE plots illustrating the relative expression patterns of isolated immune cells from spleens at pod-3, comparing between rLcn2-treated and untreated samples. Expression levels are represented by color-coding in relative intensity.

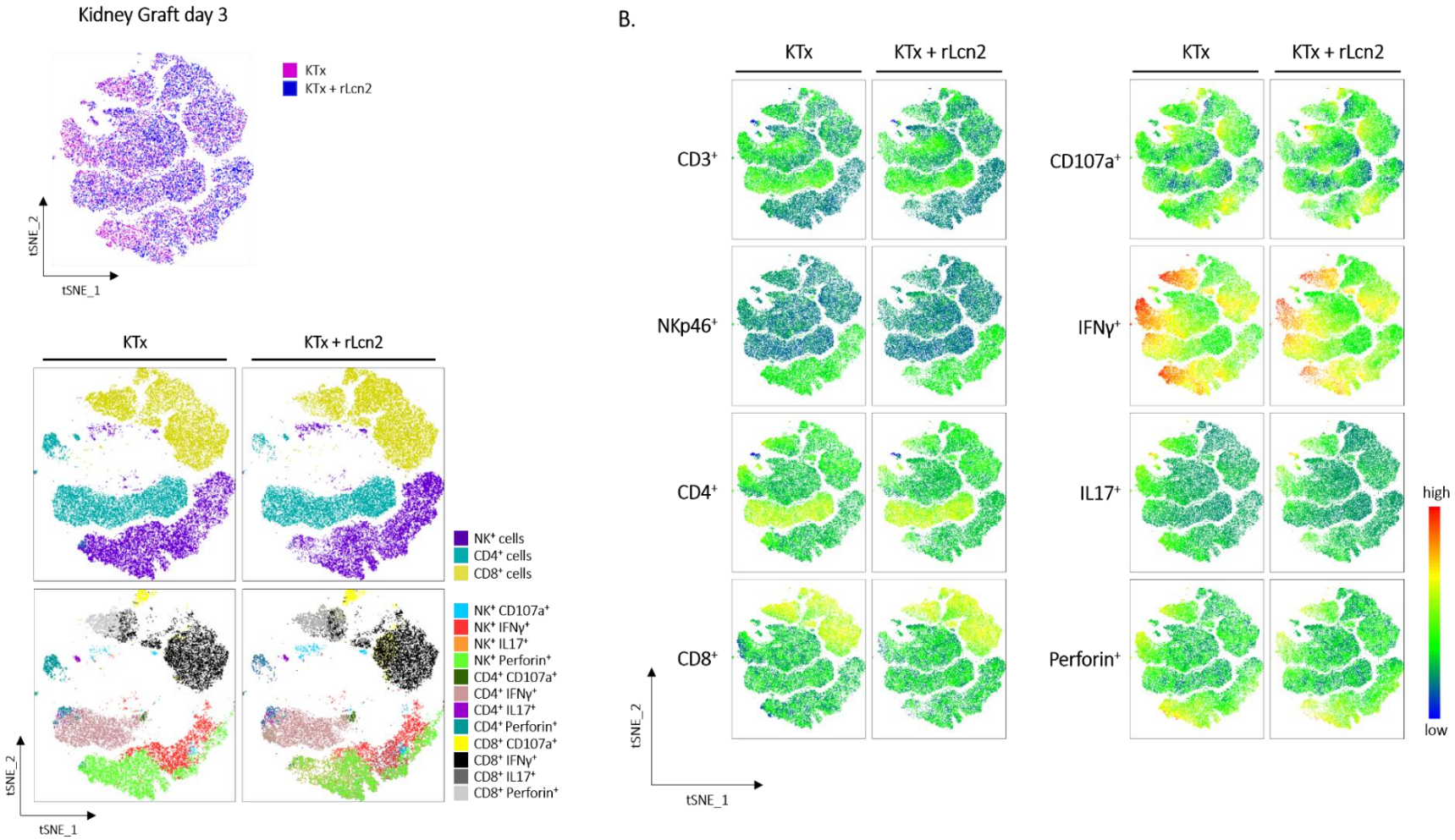

Figure 17: t-SNE analysis shows significantly reduced expression of subsets from NK⁺, CD4⁺, CD8⁺ cells at pod-3 in rLcn2-treated kidney grafts after allogenic mKTx.
(A) t-SNE analysis visualization of immune cells isolated from kidney grafts on pod-3 after allogenic transplantations. The same t-SNE analysis methods as described in **Figure 16** were utilized. Individual cells are represented by data points, color-coded to indicate distinct cell clusters. Evaluation of NK⁺, CD4⁺, CD8⁺ cells, and their subsets expressing CD107a, IFNγ, IL-17, or Perforin was conducted, comparing perioperatively treated samples with rLcn2 to untreated samples. Total cell counts of each cluster are provided in **Table S1**. **(B)** t-SNE plots depicting the relative expression patterns of isolated immune cells from kidney grafts at pod-3, comparing between rLcn2-treated and untreated samples, revealing decreased expression of IFNγ in rLcn2- treated kidney grafts compared to untreated kidney grafts. Expression is shown by colour coding in relative intensity.

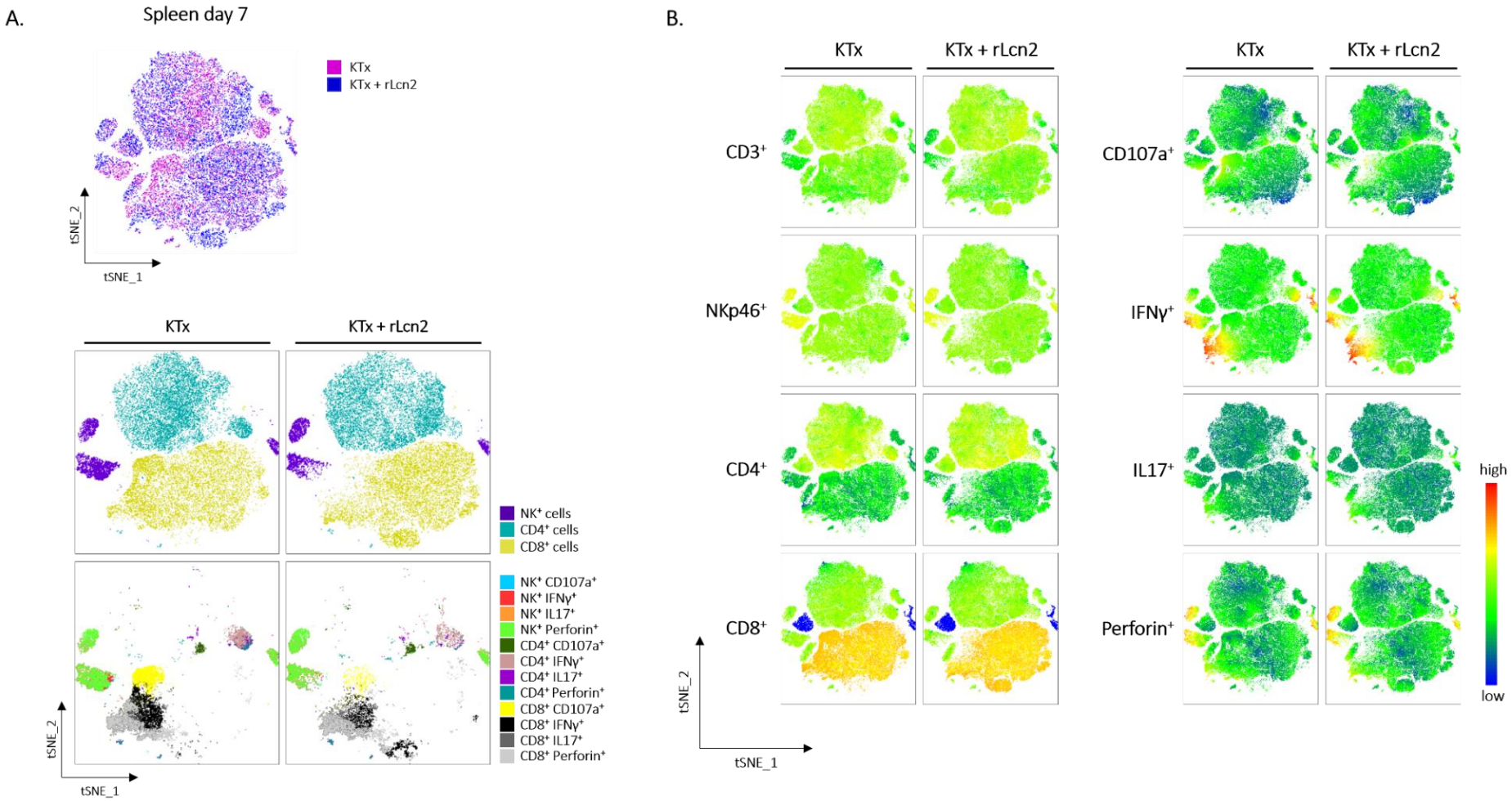

Figure 18: t-SNE analysis reveals distinct profiles of immune cell subsets in post-transplant spleens on pod-7 after mKTx.
(A) t-SNE analysis visualization of immune cells isolated from spleens on pod-7 after allogenic transplantations. The analysis employed the same methods as described in **Figure**. Data points represent individual cells, with color-coding indicating distinct cell clusters. Evaluation of NK^+, $CD4^+$, $CD8^+$ cells, and their subsets expressing CD107a, IFNγ, IL-17, or Perforin was performed, comparing perioperatively treated samples with rLcn2 to untreated samples. Total cell counts of each cluster are provided in **Table S1**. **(B)** t-SNE plots visualizing the relative expression patterns of isolated immune cells from spleens at pod-7, comparing between rLcn2-treated and untreated samples, showing no substantial differences between two conditions. Expression is shown by colour coding in relative intensity.

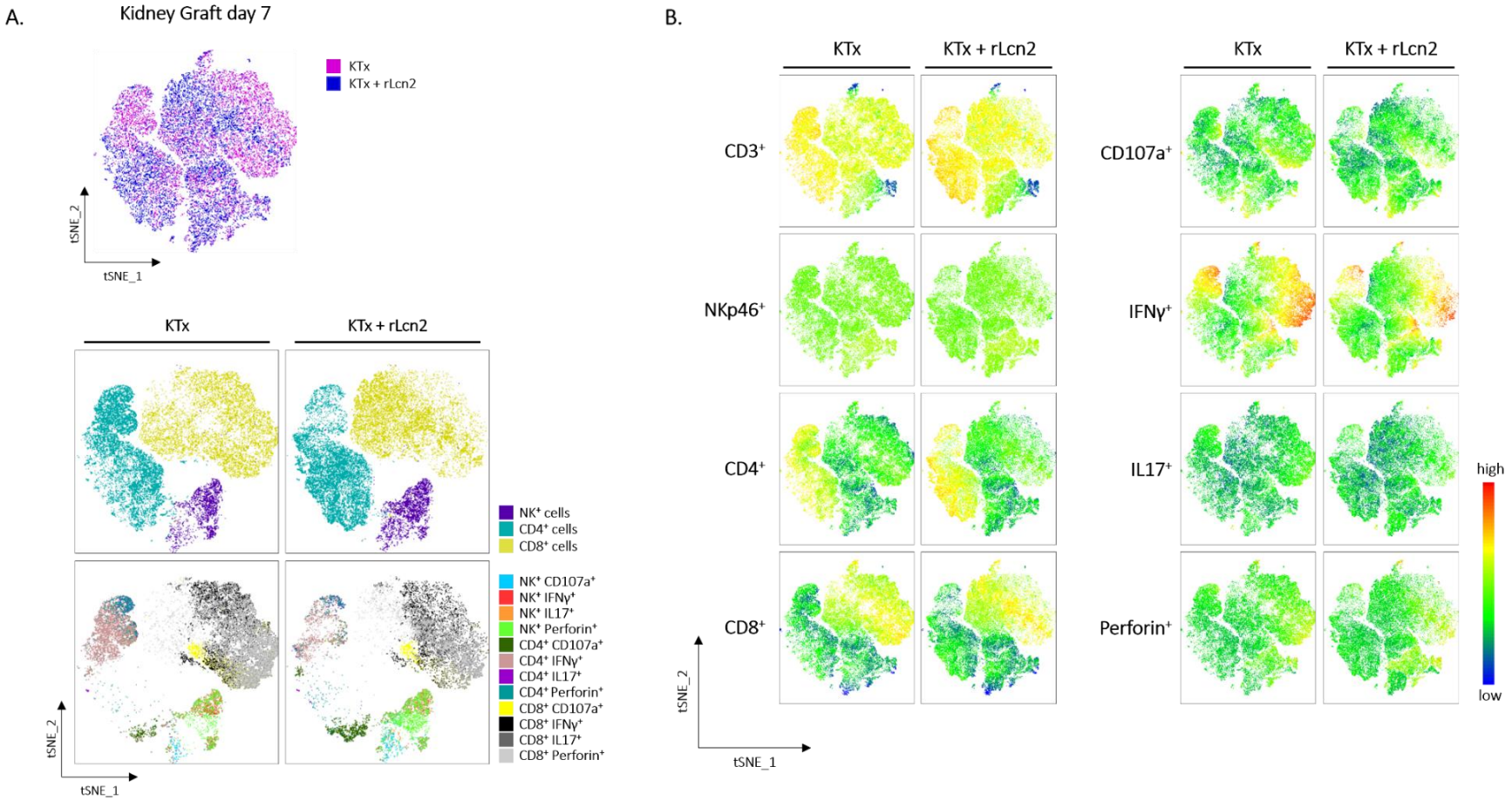

Figure 19: t-SNE analysis reveals significantly reduced immune cell expression, especially IFNγ⁺ subsets at pod-7 in rLcn2-treated kidney grafts after allogenic mKTx. **(A)** t-SNE analysis visualization of immune cells isolated from kidney grafts on pod-7 after allogenic transplantations. The same t-SNE analysis methods as described in Figure 1 were applied. Individual cells are displayed as data points, with color-coding representing distinct cell clusters. Evaluation of NK+, CD4+, CD8+ cells, and their subsets expressing CD107a, IFNγ, IL-17, or Perforin was performed, comparing perioperatively treated samples with rLcn2 to untreated samples. Total cell counts of each cluster are provided in **Table S1**. **(B)** t-SNE plots showing the relative expression patterns of isolated immune cells from spleens at pod-7, comparing between rLcn2-treated and untreated samples from kidney grafts at pod-7. Expression is shown by colour coding in relative intensity.

3.1.7 TOTAL IMMUNE CELL COUNTS ON POD-3 ARE DISTINCTIVLY AFFECTED BY rLCN2-TREATMENT

Interestingly, we observed a limited effect of the treatment with rLcn2 on targeted immune-cell populations at pod-3, while t-SNE analysis revealed clear effects on rLcn2-treated kidney grafts at that time point. This time point allows for the evaluation of early changes in immune cell responses, highlighting the importance to clearly elucidate possible treatment-mediated effects at this stage. Consequently, total cell counts (i.e. for absolute quantification) from spleen, lymph nodes, and kidney graft were obtained to validate the correlation between relative frequencies and the actual abundance of immune cells, as well as if there is an effect due to treatment with rLcn2 or not. This analysis helps to ensure the accuracy and reliability of the described findings (sections 3.1.1 to 3.1.6), contributing to a more comprehensive view of immune cell dynamics at pod-3 following treatment with rLcn2.

Significant lower counts of central memory T-cells (Supplementary Figure S5). and central memory T_c-cells were detected in lymph nodes (Supplementary Figure S7). Counts of T_h-cells and subsets remained unaffected at pod-3 after treatment with rLcn2 (Supplementary Figure S6). Furthermore, the treatment with rLcn2 significantly reduced the total cell counts of mature dendritic cells in kidney graft samples (Supplementary Figure S8), as well as the total cell counts of ofLy6C$^{intermediate-high}$ macrophages from spleens and M2 macrophages from kidney grafts (Supplementary Figure S9). In addition, significant lower numbers of NK-cells, naïve NK-cells, NKp46$^+$NKG2A$^+$-cells, and CD8$^+$NKG2D$^+$-cells isolated from lymph nodes and lower numbers of CD8$^+$NKG2D$^+$-cells isolated from kidney grafts were recorded (Supplementary Figure S10). On the contrary, total cell counts at pod-3 of the *ex vivo* activated immune cells showed significantly lower amounts of CD4$^+$CD107a$^+$, CD4$^+$IL-17$^+$, CD4$^+$IFNγ$^+$, CD4$^+$Perforin$^+$, NKp46$^+$CD107a$^+$, NKp46$^+$IL-17$^+$, NKp46$^+$IFNγ$^+$, and NKp46$^+$Perforin$^+$ cells in kidney graft samples, corroborating the findings from the t-SNE analysis described in section 3.1.6 and depicted in Figure 17A. Additionally, significantly lower total cell numbers of T_h1, CD8$^+$ IFNγ$^+$, CD8$^+$Perforin$^+$-cells of kidney graft samples were observed (Supplementary Figure S14 and Figure S15).

In summary, further analysis of total cell counts on pod-3 in allogenic murine kidney transplantation has demonstrated significant reductions in multiple immune cell populations, especially within the kidney graft, following perioperative treatment with rLcn2. Particularly, the functionality and degranulation capacity of CD4$^+$, CD8$^+$, and NKp46$^+$ immune cells were significantly affected in terms of total cell counts. On the contrary, the relative frequencies of these cell populations remained unaffected, suggesting that effects primarily relate to total cell numbers rather than alterations in relative proportions.

3.2 TARGETING STRUCTURAL CELLS OF THE KIDNEY: CULTURING OF PRIMARY PROXIMAL TUBULAR EPITHELIAL CELLS (PTEC)

One key objective of this study was to gain a deeper understanding of the intricate mechanisms through which rLcn2 confers cytoprotection to renal grafts and influences alloimmunity. To explore these mechanisms, particular attention was given to analysing various signalling pathways related to cell survival, apoptosis, and inflammation, with emphasis on isolated, cultured primary proximal tubular epithelial cells (PTEC). PTEC are of particular interest, as they are recognized as the primary functional component of the kidney nephron, responsible for reabsorbing essential substances from the filtrate and maintaining fluid and electrolyte balance [5,6]. They also actively participate in the regulation of immune responses within the kidney microenvironment [65-68]. PTEC exhibit higher expression levels of the receptor *Lrp2* compared to other compartments in the nephron, specifically recognizing and facilitating the uptake of Lcn2 [102]. By virtue of their elevated *Lrp2* expression, PTEC likely play an important role in the cellular response to rLcn2, suggesting their significance in the mechanism of action of this protein. Focusing on PTEC allowed to investigate the specific interactions and signalling pathways through which rLcn2 influences these renal cells, shedding light on the underlying molecular processes associated with its cytoprotective effects. Understanding the functions and responses of PTEC to rLcn2 can provide valuable insights into how this protein contributes to the preservation of renal grafts and the modulation of alloimmune responses.

To isolate primary PTEC, we utilized a genetically engineered mouse model called mT/mG*PEPCK-Cre, designed to express Cre-recombinase under the control of the PEPCK promoter, which is specific to PTEC. As a result, under the expression of Cre, the PTEC were labelled with green fluorescent protein (GFP) targeted to the cell membrane, enabling the distinction of PTEC from other adherent cell types within the kidney that continued to express tdTomato, resulting in red fluorescence. Thus, the presence of green fluorescence in PTEC enables the discrimination of PTEC from other cells within the kidney using fluorescence microscopy.

PTEC are primarily located in the kidney cortex [103,104] and were consistently found in close proximity to the surrounding red-fluorescent cells (**Figure 20A**, green box). Cells were isolated from kidney cortexes using a well-established gentleMACS™ dissociation protocol described in section **2.9.3** and subsequently cultured (**2.9.7**). After reaching a sub-confluent monolayer, cells were subjected to the established hypoxia/reoxygenation protocols outlined in section **2.9.8** to investigate oxidative stress, survival, and proinflammatory signalling.

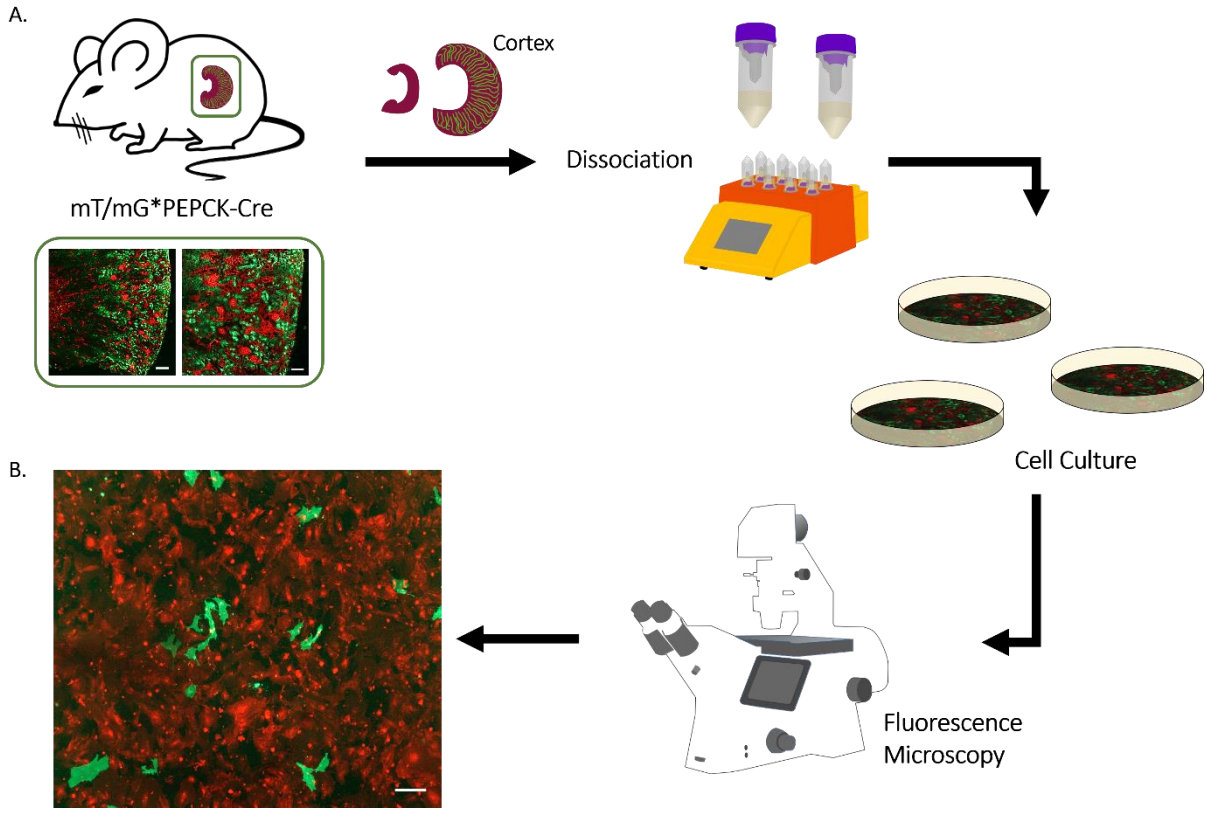

Figure 20: Cell culture of murine primary proximal tubular epithelial cells.
(A) Schematic overview of the isolation procedure of PTEC from cultured mT/mG*PEPCK-Cre mice. Green box: Images of a cryo-preserved kidney cortex section from a mT/mG*PEPCK-Cre mouse. Left image: Scale bar =200 µm, right image: scale bar = 100 µm. Own illustration. **(B)** Representative fluorescence microscopy image of a confluent PTEC culture grown for six days, displaying a ratio in favour of tdTomato$^+$ cells, rather than GFP$^+$ cells. Scale bar = 200 µm.

3.2.1 STANDARD ISOLATION PROCEDURE ONLY RETIREVES A LIMITED AMOUNT OF PTEC

Although applying the standard isolation procedure, challenges were encountered during the culturing of PTEC. The culture experiments revealed a limited number of cells expressing GFP fluorescence, as shown in **Figure 20B** and confirmed by flow cytometry measurements (**Figure 22**). Despite multiple culturing attempts, the green-fluorescent cells were consistently outgrown by the red-fluorescent cells.

Performing additional fluorescence-activated cell sorting (FACS) on cells isolated from the renal cortex, notably enriched the GFP$^+$ population to a maximum of 80 % (**Supplementary Figure S16**). However, most of the cells did not survive the initial 24 hours of culturing, likely due to shear stress and prolonged exposure to the sorting buffer. The growth rate of the surviving cells was notably slow, and they failed to reach confluency even after 13 days of culturing (**Figure 21**). Once again, red-fluorescent cells outpaced green-fluorescent cells in terms of growth. Additionally, obtaining sufficient protein for subsequent molecular biological analyses proved to be unattainable, rendering this approach unsuitable for the planned investigations.

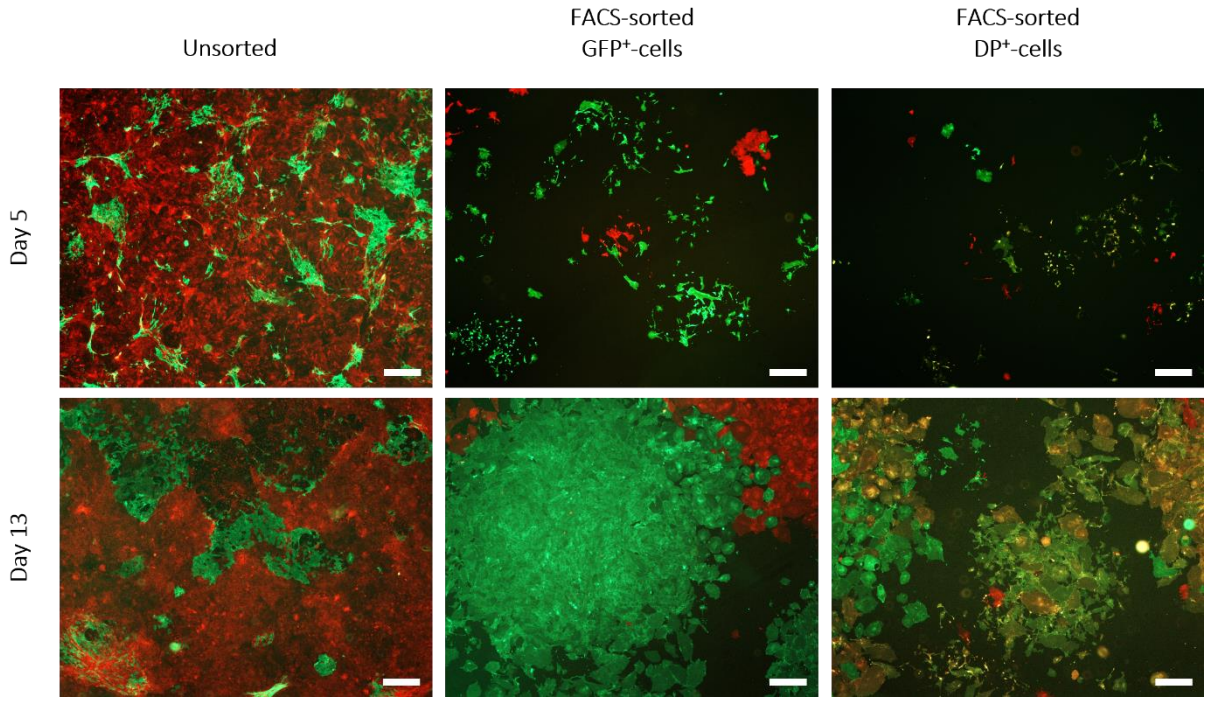

Figure 21: Cell culture of PTEC isolated from mT/mG*PEPCK-Cre mice sorted by Fluorescence-activated-cell-sorting (FACS) compared to unsorted.
Representative fluorescence microscopy images are shown. FACS substantially purifies GFP$^+$ cells from tdTomato$^+$ and double positive cells (for a representative sorting procedure see **Supplementary Figure S16**). Compared to unsorted PTEC that reach confluency after five days of cell culture, FACS-sorted GFP$^+$ cells formed larger clusters of GFP$^+$ cells. They, however, grew slower and did not reach confluency until day 13. Double positive (DP$^+$) cells showed similar growth patterns.

Subsequently, we attempted to enrich GFP$^+$ PTEC in culture using a MACSQuant® Tyto® cell sorter, which employs mild air pressure to drive cells through a microchip-based system. This softer approach, with reduced pressure and shear stress on the cells, sorted isolated primary PTEC from the mT/mG*PEPCK-Cre mouse model into GFP$^+$, tdTomato$^+$, and double positive cells with a satisfactory yield. Representative fluorescence microscopy images were captured to depict the results (**Supplementary Figure S17**).

However, in comparison to unsorted cells, MACSQuant® Tyto® sorted cells exhibited lower viability during the initial 24 hours after the sorting process. The surviving cells formed small colonies characterized by a notably sluggish growth rate. After seven days of culture, sorted cells achieved approximately 20 % confluency, in contrast to more than 90 % confluency in unsorted cells after only five days of culture. Moreover, sorted cells exhibited an unhealthy phenotype, displaying a flattened, elongated, and irregular morphology. These sorted cells did not reach confluency even after 15 days of culture, supporting the presence of delayed and compromised growth (**Supplementary Figure S17**).

As a next step, we isolated primary PTEC from mT/mG*PEPCK-Cre mice using a sorting method based on ultracentrifugation as described by *Kamiyama et al.*, 2012 [105]. After ultracentrifugation, proximal tubules exhibiting GFP fluorescence remained attached to glomeruli displaying tdTomato red

fluorescence. However, after 24 hours of culturing, most of the proximal tubules were washed out during the medium change, resulting in only a few remaining tubules being attached to the culture surface. Notably, these remaining PTEC tended to accumulate in the central region of the culture well. Over the course of seven days of cell culture, we observed the gradual formation of small and morphologically irregular colonies of PTEC. These colonies exhibited a distinct composition, comprising both green (GFP^+) and red ($tdTomato^+$) fluorescent cells. Most notably, these cells grew either close to one another or intricately interwoven within the colonies (Supplementary Figure S18). Nonetheless, the cells never grew to a confluent monolayer over the course of several days.

3.2.2 SORTING-BASED ENRICHMENT WITH ANTI-PROMININ-1 LEADS TO THE BEST OUTCOME

Ultimately, we conducted a series of magnetic-activated cell sorting (MACS) procedures, involving the labelling of cells with magnetic microbeads and subsequent sorting over a column to isolate and purify PTEC for subsequent cell culture. Three different types of microbeads were employed: µMACS-anti-GFP microbeads (binding to cell membrane-localized GFP), anti-RFP antibody (binding to cell membrane-localized tdTomato) combined with magnetic microbeads, and anti-prominin-1 microbeads (binding to the extracellular region of prominin-1, a surface glycoprotein expressed in the brush border of PTEC [106,107]). Fluorescence microscopic images were captured to document cells at various stages of culture. Representative images from day 4 and the final day of culture, corresponding to the specific sorting procedures, are shown in Figure 22. For a more comprehensive understanding, all stages and growth patterns of cells resulting from the three different MACS sorting procedures are depicted in Supplementary Figure S20.

After four days of culturing, unsorted PTEC displayed rapid growth and were more than 70 % confluent (Figure 22A). They reached confluency after six days of culture with a positive ratio for $tdTomato^+$ cells and exhibited the characteristic PTEC phenotype (Figure 22B, C). Despite yielding the purest GFP^+ PTEC population, µMACS-anti-GFP sorted cells, exhibited sluggish growth, irregular morphology, and were only approximately 10 – 15 % confluent after four days of culturing (Figure 22A). Although those cells only achieved sub-confluency after 19 days of culture, the amount of GFP^+-cells remained the same over the course of the culture (Figure 22B, C). PTEC sorted with anti-RFP antibody and magnetic microbeads required an average of eleven days to form a confluent monolayer while maintaining stable GFP expression (Figure 22B, C). However, these cells had already morphologically deviated from the typical PTEC phenotype after four days of cell culture (Figure 22A). Conversely, PTEC sorted with anti-prominin-1 demonstrated a growth pattern similar to that of unsorted PTEC at day four of the culture (Figure 22A). Like the unsorted PTEC, anti-prominin-1 sorted PTEC reached confluency within six days of culture and the characteristic PTEC phenotype was preserved (Figure 22B). The sorting

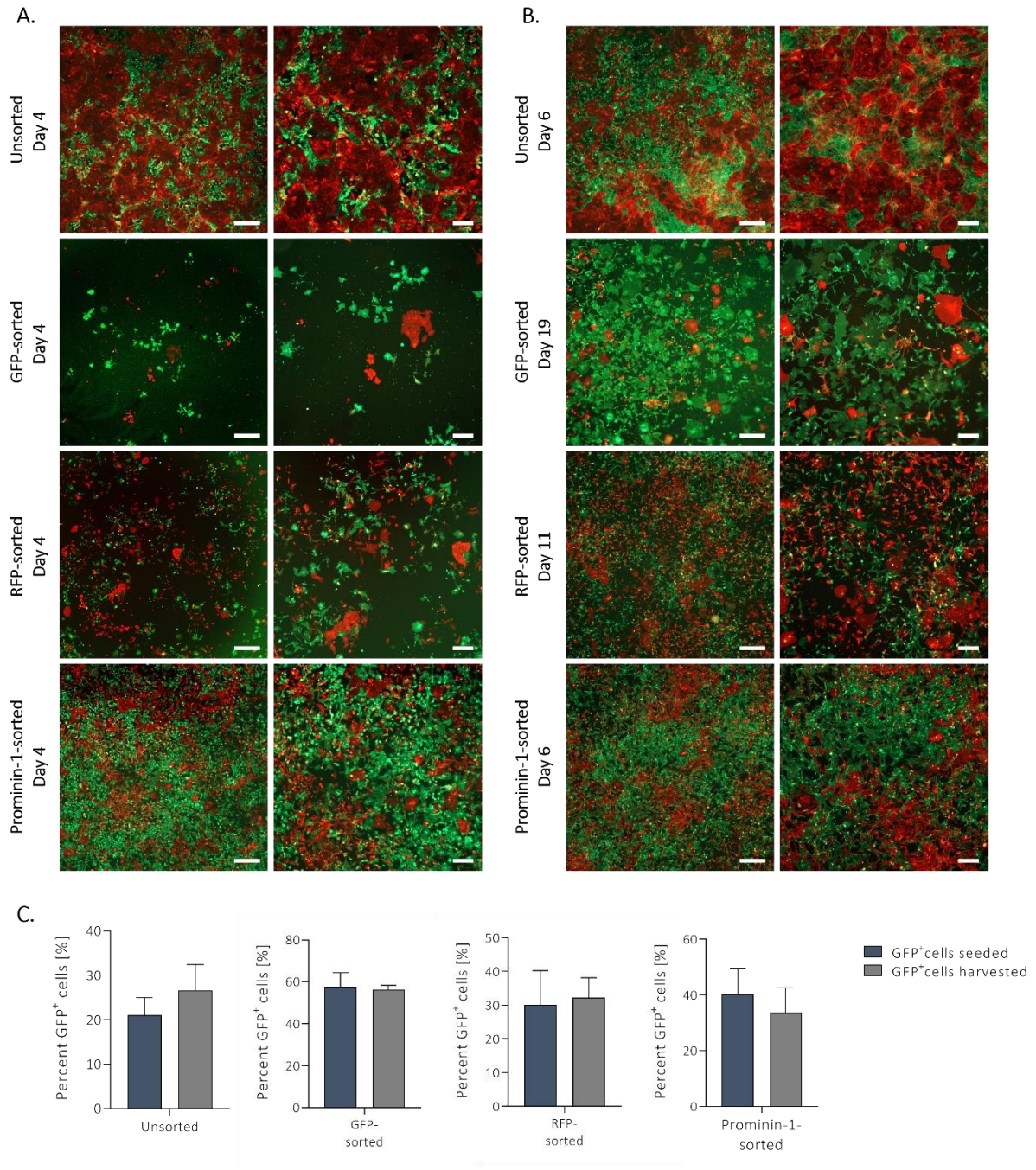

Figure 22: Anti-prominin-1 sorted PTEC have a higher percentage of GFP+ cells and do not express phenotypic changes compared to unsorted PTEC.

Three different MACS sorting procedures were performed to purify the PTEC population for further cell culture and compared to unsorted PTEC. Representative fluorescence microscopic images are shown. Images were taken after **(A)** four and **(B)** on the last day of cell culture (varying between 6 to 19 days), when cells were sub-confluent or 100 % confluent, and **(C)** the percentage of GFP^+ cells were measured via flow cytometry at the various timepoints, respectively. Scale bar left column = 200 µm, scale bar right column = 100 µm.

process resulted in an average of 40 % GFP^+ PTEC. However, their abundance slightly decreased to an average of 36 % after six days of culture (**Figure 22C**).

To verify the epithelial origin of the isolated primary PTEC after the respective MACS-sorting procedure and to assess whether cells maintained their PTEC identity or underwent dedifferentiation during the course of cell culture, we performed RT-qPCR analysis of candidate PTEC markers (Lrp2, Slc22a17, Slc5a2) [108], the epithelial cell marker Cdh1 [109], and the α-smooth muscle cell marker Acta2 [110].

For PTEC sorted with µMACS-anti-GFP microbeads, samples were collected immediately after sorting, as well as after eight days of cell culture, representing the earliest time point at which the minimum required amount of RNA could be isolated for subsequent analysis. Notably, the cell culture of GFP-sorted PTEC led to a loss of epithelial and specific PTEC markers. The expression of Lrp2 remained relatively stable over time, while Slc22a17 and Cdh1 expressions were nearly abolished. Slc5a2 expression approximately increased 12-fold, while Acta2 expression decreased approximately 6-fold on day 8 compared to day 0 (**Figure 23**). However, none of the observed changes were proven to be significant.

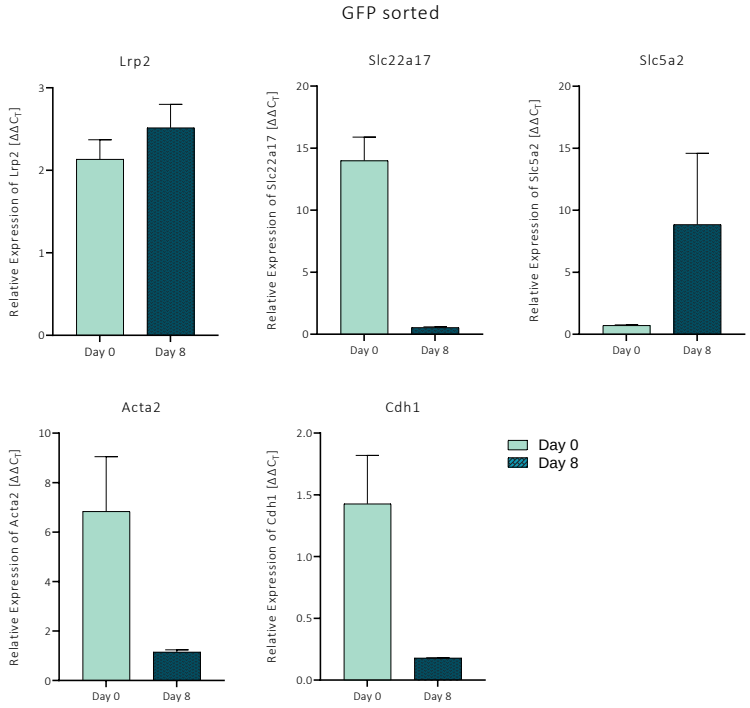

Figure 23: Cell culture of GFP-sorted PTEC leads to loss of epithelial cell and certain PTEC markers.
RT-qPCR analysis of candidate PTEC (**Lrp2, Slc22a17, Slc5a2**), epithelial (**Cdh1**), and α-smooth-muscle cells (**Acta2**) expression marker was performed on isolated primary PTEC after sorting with µMACS-anti-GFP microbeads (n = 3; **2.9.6**). Samples for RNA extraction were taken directly after sorting and after eight days of cell culture. Bar graphs represent mean values and error bars represent standard error of mean (SEM). Statistical analysis: Kruskal-Wallis-Test with Dunn's post-hoc test; * $p < 0.05$. Due to high variance of samples, no significance between the timepoints was detected.

RT-qPCR analysis of the same candidate markers was also performed on primary PTEC sorted with anti-RFP antibody and magnetic microbeads. Samples were collected immediately after sorting, after three, and after six days of cell culture. The expressions of Lrp2 and Acta2 remained relatively

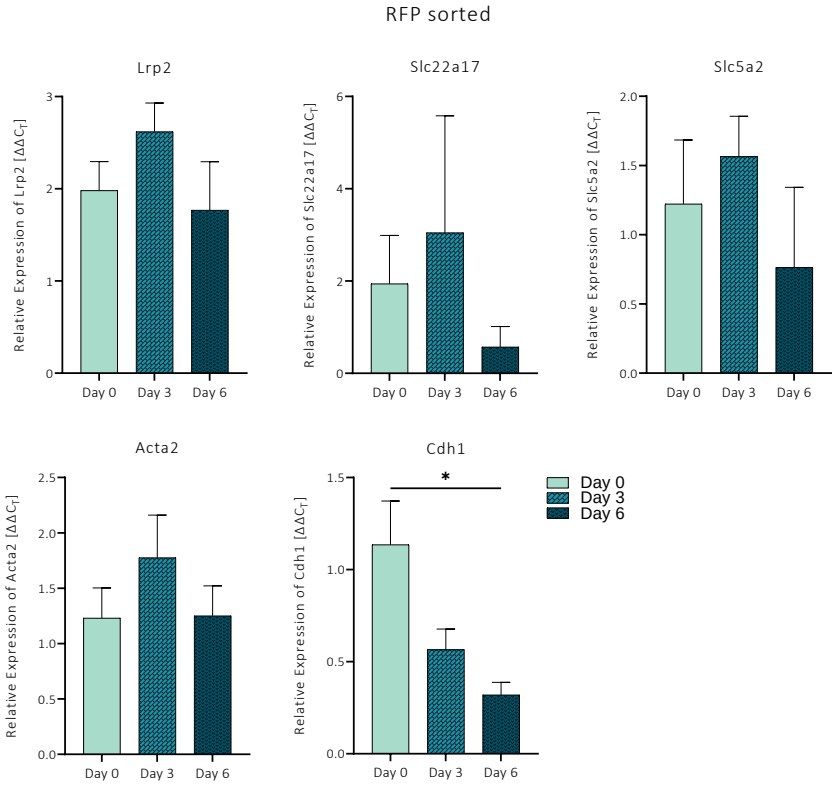

Figure 24: Cell culture of RFP-sorted PTEC leads to a significant loss of Cdh1 expression over time.
RT-qPCR analysis of candidate PTEC (**Lrp2, Slc22a17, Slc5a2**), epithelial (**Cdh1**), and α-smooth-muscle cells (**Acta2**) expression marker was performed on isolated primary PTEC after sorting with anti-RFP antibodies and magnetic microbeads (n = 4; **2.9.6**). Samples for RNA extraction were taken directly after sorting, after three, and six days of cell culture. Bar graphs represent mean values and error bars represent standard error of mean (SEM). Statistical analysis: Kruskal-Wallis-Test with Dunn's post-hoc test; * $p < 0.05$.

unchanged, while Slc22a17 expression was reduced approximately 3.4-fold over time, however, not significantly. Slc5a2 expression decreased (not significantly) approximately 1.5-fold until day six of culture, while Cdh1 expression significantly decreased from the isolation day to the last day of cell culture approximately 3.5-fold (**Figure 24**).

Lastly, we conducted RT-qPCR analysis on the expression of the above-mentioned candidate markers on cultured PTEC sorted using anti-prominin-1 microbeads. Samples were again obtained immediately after sorting, after three, and after six days of cell culture. Here, the cell culture of prominin-1 sorted PTEC exhibited a significant increase in Acta2 expression between day three and day six, however, displaying an almost three-fold lower expression than on the day of isolation. The expressions of Lrp2 and Cdh1 decreased over time 4.2- and 2.2-fold, respectively, while Slc5a17 and Slc5a2 initially increased on day three but decreased on day six back to the initial levels observed on day 0 (**Figure 25**).

In summary, sorting with GFP microbeads yielded the most favourable outcome, achieving a purity of approximately 60 %. However, these cells required approximately 20 days to reach a confluent monolayer, which is a critical requirement for subsequent analyses, indicating the necessity of co-

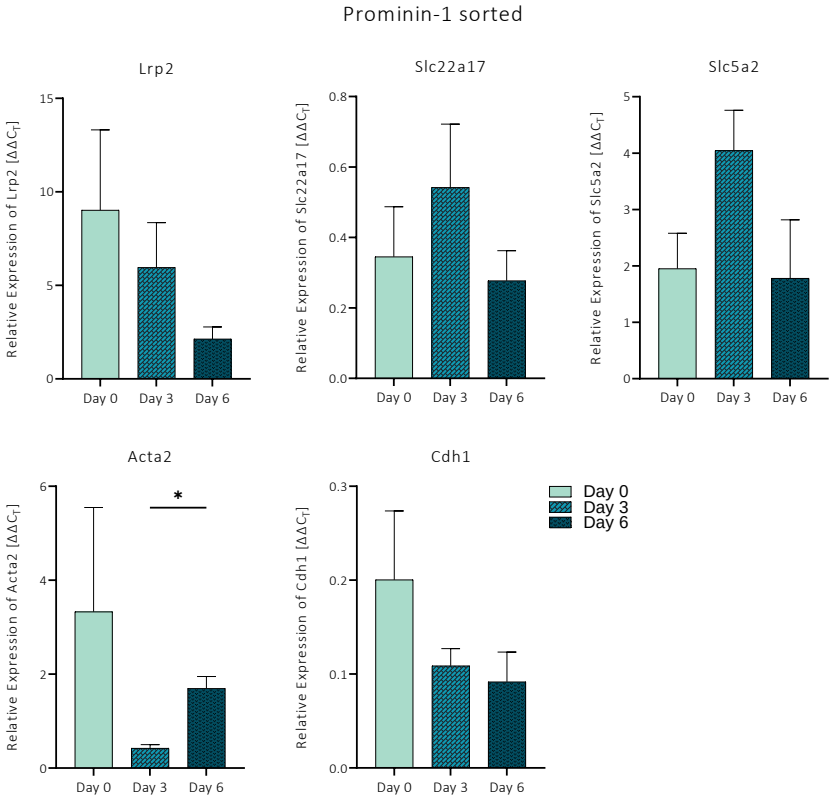

Figure 25: Cell culture of prominin-1 sorted PTEC leads to a significant increase of Acta2 expression.
RT-qPCR analysis of candidate PTEC (**Lrp2, Slc22a17, Slc5a2**), epithelial (**Cdh1**), and α-smooth-muscle cells (**Acta2**) expression marker was performed on isolated primary PTEC after sorting with anti-prominin-1 microbeads (n = 4; **2.9.6**). Samples for RNA extraction were taken directly after sorting, after three and six days of cell culture. Bar graphs represent mean values and error bars represent standard error of mean (SEM). Statistical analysis: Kruskal-Wallis-Test with Dunn's post-hoc test; * $p < 0.05$.

culturing with red-fluorescent cells for optimal growth. On the other hand, despite lower purity, prominin-1 sorted cells achieved confluency within five days of culture, making them more suitable for further analyses. Consequently, follow-up analyses were performed using anti-prominin-1 sorted cells. **Supplementary Figure S19** provides representative scatter plots from flow cytometric analysis of isolated and MACS sorted primary proximal tubular epithelial cells. An overview of growing patterns over time comparing the three MACS procedures is presented in **Supplementary Figure S20**.

3.2.3 rLCN2 SIGNIFICANTLY LOWERS THE PHOSPHORYLATION OF THE ERK1/2 PATHWAY

The expression of Lcn2-receptors *Lrp2* and *24p3R* is evident in various cell types within the kidney, particularly in epithelial cells of the renal tubules and the collecting duct [111-114]. In the context of renal transplantation, the administration of exogenous rLcn2 may be internalized by these cells through receptor-mediated endocytosis, facilitating the delivery of iron and offering renoprotective effects by attenuating tissue damage and inflammation, or by promoting cellular survival and regeneration [18].

To investigate the direct effects of rLcn2 on the most relevant structural cells of the kidney nephron and capture key molecular signatures, we isolated, enriched (using anti-prominin-1

microbeads), and cultured primary PTEC derived from the kidney cortexes of C57Bl/6 mice (2.9, 2.9.6 and 2.9.7). This enrichment method, enabled to obtain a more homogeneous population of PTEC for subsequent analysis (as described in section 3.2.2). Thus, to gain a deeper understanding of the molecular responses triggered by rLcn2-treatment at the cellular level, we conducted multiplex signalling analyses *in vitro*, simultaneously examining selected growth, survival, and apoptotic signalling pathways. By subjecting untreated or rLcn2-treated PTEC to hypoxia/reoxygenation protocols (described in section 2.9.8), we aimed to recapitulate an *in vitro* stress model that mimics IRI, a common occurrence in various kidney diseases. Within this controlled culture environment, it was possible to assess the specific signalling pathways and molecular responses triggered by rLcn2-treatment without the confounding factors present in the complex tissue environment of the whole kidney.

Heatmap visualization of the results revealed differential activation profiles for specific proteins. For a more comprehensive view of the data, the activation statuses of the analysed proteins are presented as bar graphs depicting scaled mean fluorescent intensity MFI in Supplementary Figure S22.

Overall, enhanced phosphorylation over time in both control and rLcn2-treated cells under hypoxic and reoxygenation conditions was only detected for CREB, GSK3β, mTOR, PTEN, and TSC2, however in different intensities. Phosphorylation of IR was consistently downregulated under both hypoxia and reoxygenation conditions, independent of the treatment, however not significantly (Figure 26).

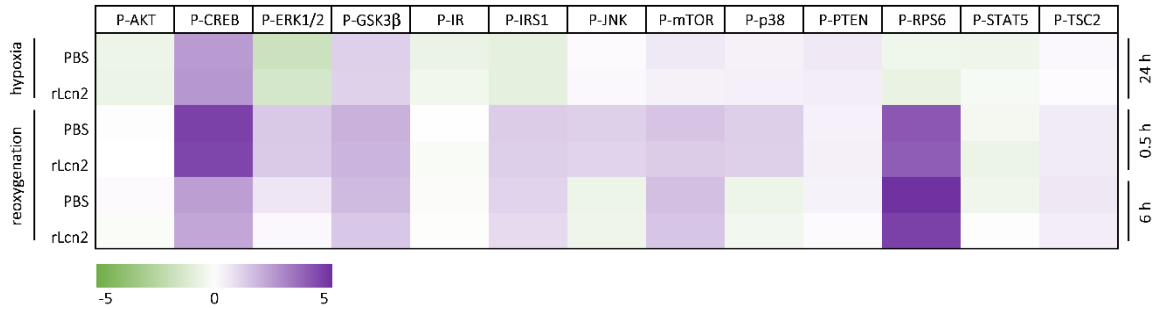

Figure 26: Intracellular signalling pathway analysis *in vitro* after isolation of primary PTEC from C57Bl/6 kidney cortexes followed by anti-prominin-1 microbeads-based MACS sorting.
Heat map of the log2 ratio to normoxia in control (PBS) and rLcn2-treated samples showing the mean fluorescent intensity (MFI) of measured phosphorylated analytes. Intracellular signalling analysis (multiplex assays, see 2.9.12) was performed on lysed anti-prominin-1 microbeads-sorted primary PTEC isolated from C57Bl/6 kidneys (n = 6-8). Sub-confluent primary PTEC were either pretreated with rLcn2 or vehicle and subjected to 24 h of hypoxia (0.5 % O_2, 0.5 % FCS), followed by either 0.5 h or 6 h of reoxygenation. Supplementary Figure S22 depicts a more comprehensive view on the analysed growth, survival, and apoptotic pathways shown in (A). Statistical analysis: Student's t-test; * $p < 0.05$.

Hypoxia alone resulted in upregulation of P-CREB, but a downregulation of ERK1/2, AKT, IR, IRS1, as well as RPS6 phosphorylation. Irrespective of the treatment, STAT5 displayed a consistent downregulation during both hypoxia and reoxygenation. Notably, after 0.5 hours of reoxygenation, a substantial increase in the phosphorylation of CREB, ERK1/2, GSK3β, IRS1, JNK, mTOR, p38, and RPS6

was evident, both in the control and Lcn2-treated cells (**Figure 26**). Compared to the 0.5-hour time point, phosphorylation levels of CREB, ERK1/2, JNK, and p38 decreased after 6 hours of reoxygenation, in both the untreated and treated samples, while increasing for RPS6. Apart from ERK1/2 after 6 hours (**Figure 26B**, **Supplementary Figure S22**), the differences between the control and Lcn2-treatments over time were not significant, indicating that the oxygen status carries greater importance compared to Lcn2-treatment.

All in all, the multiplex analysis of the activation status of various proteins involved in stress, inflammatory, and signalling pathways indicated that rLcn2-treatment did not significantly alter these pathways under any of the tested conditions (*in vitro*), except for the ERK1/2 pathway at 6 hours of reoxygenation following hypoxia.

3.2.4 rLCN2 DOES NOT AFFECT THE EXPRESSION OF CANDIDATE SIGNALLING MARKER *IN VIVO*

To comprehensively investigate the impact of rLcn2 and target alloimmune independent effects, we additionally conducted an extensive analysis of stress, inflammation, and survival signalling in mouse kidneys following syngeneic transplantations (C57Bl/6 to C57Bl/6; n = 5) at three different time points: after 6 hours of ischemia, after 6 hours of ischemia followed by 0.5 hours of reperfusion, and after 6 hours of ischemia followed by 24 hours of reperfusion. Either samples were treated with rLcn2 perioperatively or remained untreated as controls. Multiplex signalling assays encompassing 19 signalling molecules associated with Akt/mTOR, MAPK, JAK/STAT, and NFκB signalling pathways were employed, to gain insight into the signalling landscape (**Figure 27A, Supplementary Figure S21**). Background subtraction was performed, followed by scaling to the internal standard β-tubulin for all samples. However, due to signalling levels falling below the background threshold, analysis of expression profiles of CREB, NFκB, p70S6K, STAT3, STAT5, IGF1R, IRS1, and GSK3β was not feasible (**Supplementary Table S2**). The biological replicates (n = 5) were collectively analysed.

First, we generated a heatmap, which provided a broad overview of the activation status of numerous proteins, exposing distinctive patterns of protein activation across the examined samples (**Figure 27A**). Notably, differential activation profiles were observed for specific proteins, characterized by heightened phosphorylation levels in the absence of rLcn2-treatment, while lower levels were evident upon rLcn2 administration. This was particularly noticeable for JNK (following 24 hours I/R) and RSP6 (following both 0.5 hours and 24 hours I/R), indicating their dephosphorylation in response to treatment with rLcn2. Additionally, reduced phosphorylation levels were observed in the presence of rLcn2-treatment for ERK1/2, GSK3β, IR, and mTOR following 24 hours of ischemia/reperfusion, albeit to a low extent and not significant. Nonetheless, these observations provide evidence of their downregulation in the context of rLcn2-treatment.

Additionally, we evaluated kidney graft function by comparing serum creatinine and urea levels between rLcn2-treated and untreated groups after a prolonged cold ischemia period of 6 hours, followed by 24 hours of reperfusion. Notably, no discernible distinctions between the groups were detected in terms of serum creatinine and urea levels (**Figure 27B**).

Furthermore, to provide a more comprehensive view of the data, the activation statuses of the analysed proteins are also presented as bar graphs depicting scaled mean fluorescent intensity MFI in **Supplementary Figure S21**, showing individual values and comparisons.

As a result, a general decrease in phosphorylation was evident in samples subjected to 6 hours of ischemia, including perioperative treatment, when compared to the Sham operated control group. Remarkably, after 6 hours of ischemia, a pronounced activation of JNK and RPS6 phosphorylation (approximately 2- to 9-fold higher) was observed across rLcn2-treated and control samples reperfused for 0.5 hours. Moderate activation was observed for ERK and AKT. In samples subjected to 0.5 hours of I/R, treatment with rLcn2 resulted in decreased activities within the GSK3β, mTOR, PTEN, TSC-2, and RSP6 pathways, while the JNK, ERK1/2, and AKT pathways exhibited increased activities. However, no

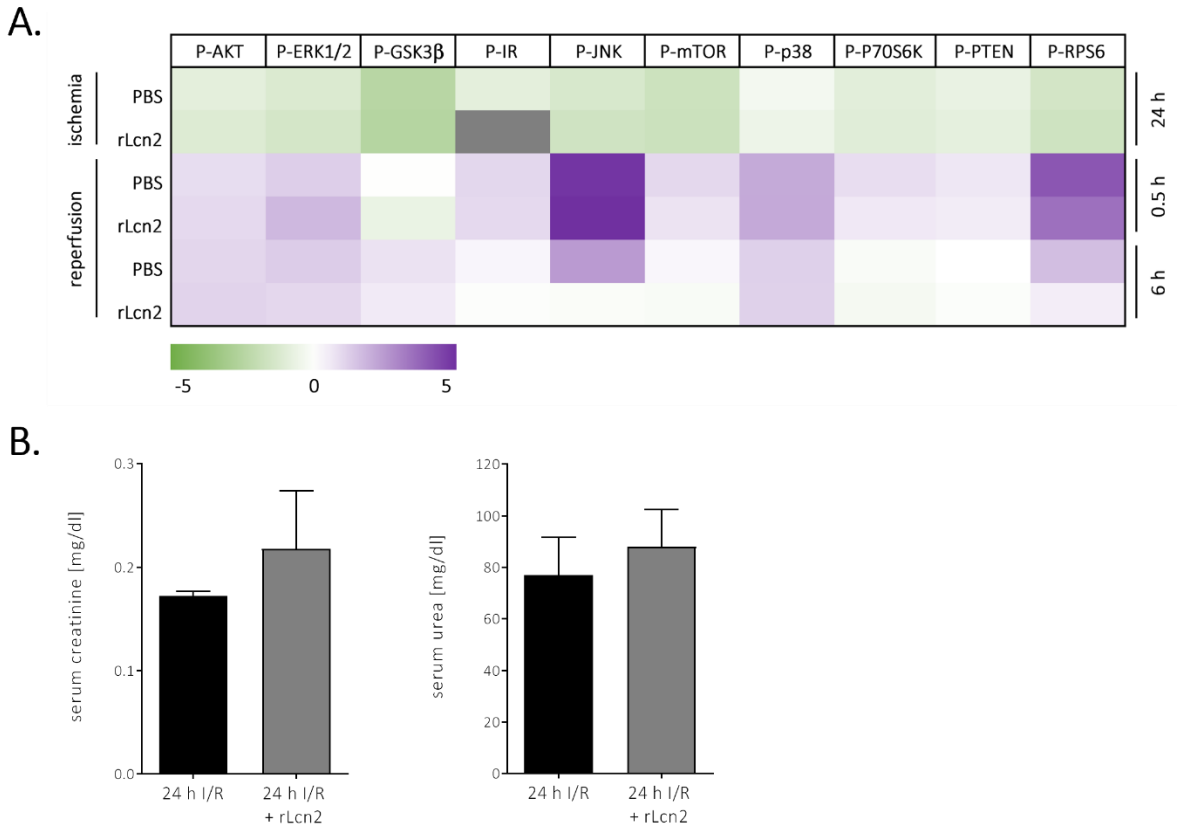

Figure 27: Effect of rLcn2 on stress, inflammation and survival signalling pathways and graft function.
(**A**) Heat map of the log2 ratio to normoxia in control (PBS) and rLcn2-treated samples showing the mean fluorescent intensity (MFI) of measured phosphorylated analytes. Intracellular signalling analysis (multiplex assays, see **2.9.12**) was performed on tissue lysates from syngenically transplanted kidneys (C57Bl/6 to C57Bl/6; n = 5). Transplantations were performed following 6 h of prolonged cold ischemia and kidneys were perioperatively treated either with rLcn2 or vehicle (as control). For preparation of tissue lysates, kidney grafts were retrieved either directly after 6 h of ischemia, or 6 h of ischemia + 0.5 h reperfusion or 24 h of reperfusion. **(B)** Serum creatinine and serum urea analysis after 6 h ischemia 24 h reperfusion comparing untreated and rLcn2-treated conditions.

statistically significant differences were detected in either scenario. For samples subjected to 24 hours of ischemia/reperfusion, treatment with rLcn2 led to decreased activities in the JNK, ERK1/2, GSK3b, IR, PTEN, TSC2, and RSP6 pathways, with only AKT showing increased activity (Supplementary Figure S21). All in all, the administration of rLcn2 did not yield discernible effects within these pathways during I/R or prolonged cold ischemia-reperfusion conditions.

3.2.5 ENHANCED LCN2 AND VIMENTIN EXPRESSION AFTER 3 DAYS OF CELL CULTURE

For rLcn2 to exert its proposed cytoprotective effect, it needs to be taken up by specific target cells, such as proximal tubular epithelial cells. This uptake process relies on the expression of *Lrp2*, also called megalin. This receptor has been implicated in immune response and renal function, and plays a crucial role in the reabsorption of proteins, vitamins, and other essential molecules such as Lcn2 from the filtrate back into the bloodstream [115]. Neither *in vivo* nor *in vitro* multiplex signalling pathway analyses were able to fully elucidate the dynamics of rLcn2 uptake in PTEC under specific hypoxia/reoxygenation or ischemia/reperfusion conditions.

Therefore, we utilized immunohistochemistry and RNAscope *in situ* hybridisation to gain additional insights into the expression status of receptors and specific markers in cultured primary PTEC. These techniques allowed for a more detailed assessment of protein and receptor expression patterns within the cells, providing a comprehensive understanding of cellular dynamics and potential cellular transitions or differentiations occurring during the culture period.

To assess the receptor and specific marker expression statuses, we conducted immunofluorescent staining of anti-prominin-1 sorted PTEC after three days of culture. This involved utilizing Lcn2 (Figure 28A, top left) and *Lrp2* (megalin; Figure 28A, bottom right) antibodies. As a staining control, α-tubulin was used, while DAPI was employed to stain cell nuclei. The results revealed that the majority of stained cells expressed Lcn2, indicating the activity of possible injury-related mechanisms. Megalin expression was detected in all stained cells. Furthermore, to gain a comprehensive understanding, we carried out combined immunofluorescence using a Vimentin antibody (Figure 28B, left and middle image) alongside fluorescent RNAscope *in situ* hybridization, utilizing a probe targeting *Lrp2* mRNA (Figure 28B, right image). DAPI staining was again used for cell nuclei (blue). After three days of cell culture, the expression of Vimentin was observed in numerous cells, suggesting the initiation of cellular transition or differentiation. In contrast, *Lrp2* expression was limited and generally exhibited weak signals as already seen during the RT-qPCR analysis (Figure 25).

In a nutshell, these findings revealed widespread expression of Lcn2 in the cultured PTEC, indicating the presence of potential injury. The observed Vimentin expression suggested the initiation of cellular transition or dedifferentiation. However, the expression of *Lrp2* was limited and weak after three days of cell culture, aligning with the previously conducted molecular analyses.

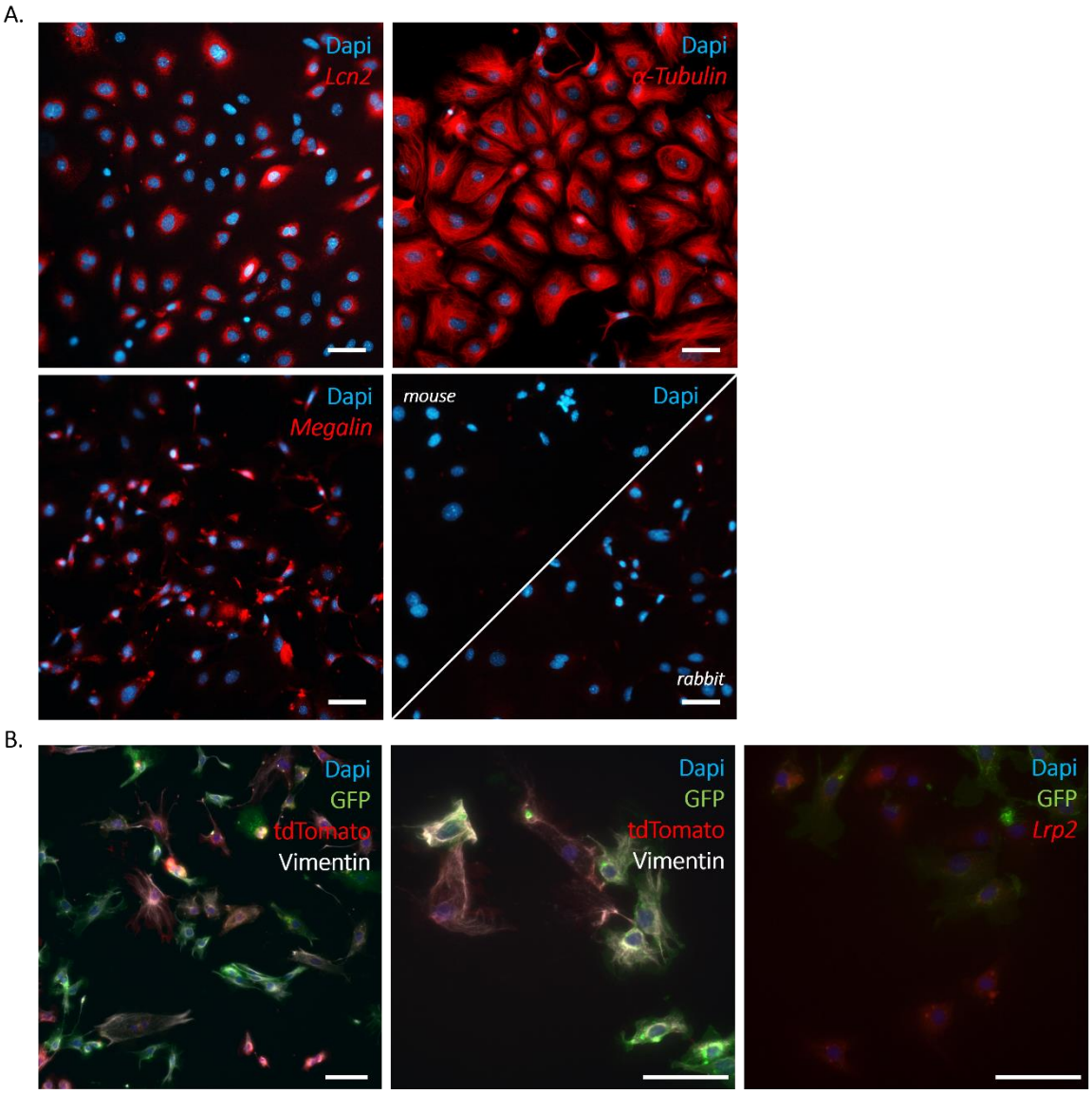

Figure 28: Proximal tubular cells express Lcn2 and Megalin in cell culture.
(A) Immunofluorescent staining of anti-prominin-1 sorted PTEC after three days of cell culture using Lcn2 (red, top left) and megalin (red, bottom right) antibodies. α-tubulin served as staining control (upper right), and cell nuclei were stained with DAPI (blue, negative controls, bottom right). Scale bars = 50 µm. **(B)** Combined immunofluorescence using a Vimentin antibody (white, left, and middle image) and fluorescent RNAScope *in situ* hybridization using a probe directed against *Lrp2* mRNA (red, right image) on anti-prominin-1 sorted PTEC after three days of cell culture. Cell nuclei were stained with DAPI (blue). Scale bars = 50 µm.

3.3 OPTIMIZATION OF CELL ISOLATION PROCEDURE PRIOR TO scRNAseq ANALYSIS

The results so far have provided valuable insights into the behaviour of primary PTEC in cell culture. Interestingly, we observed reduced expression of several PTEC markers (Lrp2, Slc22a17, Slc5a2), coinciding with the upregulation of the α-smooth muscle cell marker Acta2, and the downregulation of the epithelial cell marker Cdh1 as described in section **3.2.2**. Moreover, due to the upregulation of epithelial-mesenchymal transition (EMT) markers, such as Vimentin, and the reduced *Lrp2* expression after three days of cell culture (**3.2.5**), we anticipate that primary PTECs change their phenotype in

culture over time, which requires further analysis, such as single cell RNA sequencing (scRNAseq), to fully elucidate and characterize the fate of these cells in culture.

However, considering the potentially harsh dissociation protocol used for cell isolation, we aimed to minimize stress on the cells during the process, as dissociation stress could potentially affect the outcome of scRNAseq analysis. Considering this, one important aspect is that PTEC primarily rely on oxidative mitochondrial metabolism for their energy needs and have limited capacity for glycolysis, making them vulnerable to damage during AKI, particularly after ischemia [116]. Interestingly, despite significant amounts of glucose entering the proximal tubules, PTEC have a reduced ability to use glucose as an energy substrate. Instead, the glucose that enters the cells via SGLT2 is mainly passively transported out of the cells, re-entering the peritubular capillaries [117,118].

So, to reduce potential stress on the cells and to ensure the preservation of the cells' transcriptional profiles, we modified the isolation procedure, enabling a more reliable scRNAseq analysis. Instead of using cold temperatures and a glucose-containing buffer (HBSS), we conducted the isolation at room temperature using the glucose-free 98b buffer.

Modified isolation conditions resulted in large clusters of tdTomato$^+$ cells intersected with small colonies of GFP$^+$ cells in the unsorted PTEC culture, eventually forming a confluent monolayer by day five, without substantial phenotypical alterations. In contrast, anti-prominin-1 sorted PTEC cultures displayed healthy phenotypes and more numerous but smaller clusters of both GFP$^+$ and tdTomato$^+$

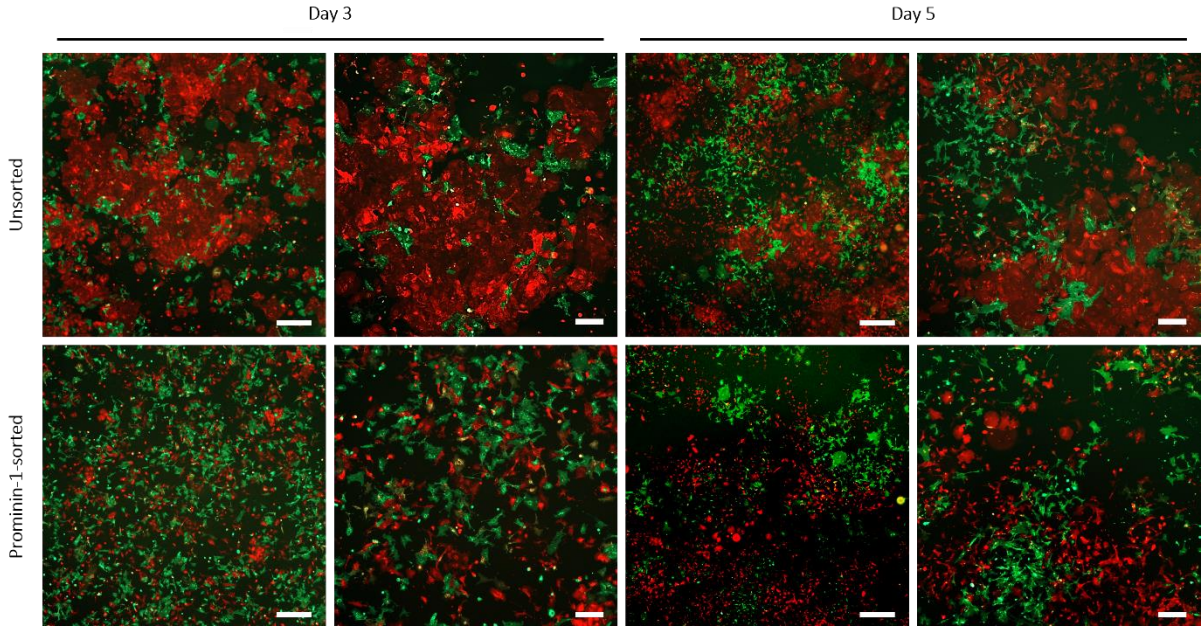

Figure 29: Isolation at room temperature using 98b buffer improves cell culture.
Prior to scRNAseq analysis, we modified the cell isolation procedure to reduce potential stress on the cells, induced e.g. by cold temperatures and the presence of glucose. Cells were isolated and sorted as described before (**sections 2.9.3** and **2.9.6**) with minor changes: all procedures were carried out at room temperature and the HBSS isolation buffer was replaced by the glucose-free 98b buffer. Cells were cultured in ECM medium for a total of six days. Representative fluorescence microscopy images are shown. Scale bars (left columns) = 200 µm, scale bars (right columns) = 100 µm.

cells, reaching a sub-confluent monolayer by day five (Figure 29). Overall, anti-prominin-1 sorted PTEC comprised more GFP^+ cells than unsorted PTEC, supporting the results described in section 3.2.2., and suggesting potential differences in cellular interactions depending on the isolation procedure.

In brief, these findings highlight the impact of the isolation and cell sorting procedures on cell distribution, allowing the PTEC to maintain their physiological state and to avoid cell collapse, as their primary role is focused on glucose transport rather than glucose utilization [116-119].

3.3.1 scRNAseq ANALYSIS OF CULTURED PRIMARY PTEC DENOTES TRANSDIFFERENTIATION

To gain a comprehensive understanding of developmental changes occurring in primary PTEC during the cultivation, we aimed at extensively characterizing these cells over the course of cell culture. A total of 16 samples from unsorted and anti-prominin-1 sorted and cultured PTEC were retrieved on the day of isolation (day 0), as well as on day 3, and day 6. For subsequent scRNAseq analysis, gene-specific hybridization probes with unique barcodes were utilized, with each barcode assigned to an individual sample, allowing for sample differentiation and identification during gene expression analysis. The 16 samples were pooled, encapsulated in droplets, and the bound probes were amplified prior to sequencing to assess gene expression profiles (2.9.18). A list of analysed samples can be found in Table 15. Given our particular interest in the dynamic changes and potential fate of both the unsorted and anti-prominin-1 sorted PTEC, our aim was to unravel whether these cells undergo dedifferentiation and/or transdifferentiation, and if so, to elucidate the specific cell types they differentiate into.

During initial analysis of the generated scRNAseq data, we assessed the quality of the pooled samples (Supplementary Figure S23A). We evaluated the total number of transcripts, the number of unique transcripts, and the percentage of mitochondrial RNA per single cell. Cells with more than 15% mitochondrial RNA were excluded from the analysis. To identify cells that exhibited a high level of stress during dissociation, a dissociation score was generated. Cells with a score higher than 0.25 were assumed to have undergone significant alterations in their gene expression profiles and deemed less reliable, hence excluded from further analysis (Supplementary Figure S23B). The Supplementary Figure S23C displays the initial UMAP (Uniform Manifold Approximation and Projection) plot, highlighting cell groups that were excluded before conducting further analysis. These included doublets, non-epithelial cells, and cells with a high mitochondrial RNA content.

Subsequently, after the effective removal of batch effects, the analysis was rerun on the processed dataset. The resultant UMAP visualization is presented in Supplementary Figure S24. Here, panel A illustrates the cellular distribution of anti-prominin-1 sorted and unsorted populations, while panel B showcases the distribution of cells categorized by the timepoints of their isolation. An encompassing overview of the cell distribution across various samples is provided in panel C, where the UMAP plot is color-coded by samples. Ultimately, panel D shows a UMAP plot with 29 distinct clusters,

obtained through clustering analysis based on highly variable genes. Notably, from this comprehensive dataset, it had become evident that a substantial disparity between cells obtained on day 0 in comparison to those derived from day 3 and day 6 was existent. Consequently, we performed separate analyses on cells per sampling day, recognizing the necessity to treat them as distinct entities. To identify cells that exhibited a high level of stress during dissociation, a dissociation score was generated. These cells, which may have undergone significant alterations in their gene expression profiles, were deemed less reliable for downstream analysis. Therefore, cells above the threshold of dissociation stress score were excluded from further analysis, ensuring that the remaining cells for downstream analysis were more accurately represented the transcriptional profiles of the PTEC in their native state (Supplementary Figure S23B).

Following an extensive survey of the existing literature, we meticulously selected a set of promising marker genes (Table 16) to discern the diverse cell types present within the day 0 dataset, as well as the day 3 and day 6 datasets.

Table 16: Overview of validated marker genes for cell type identification during scRNAseq analysis.

Marker Genes	Cell type	References
Lrp2, Acsm2, Slc34a1	Pan-proximal tubule (PT)	*Balzer et al.*, 2022 [108,120,121]
Slc5a12, Slc5a2, Slc6a19	Proximal convoluted tubule (PCT)	*Balzer et al.*, 2022 [108,120,121]
Slc13a3, Cyp4b1, Kap	Proximal straight tubule (PST)	*Balzer et al.*, 2022 [108,120-123]
Lcn2, Havcr1, Prom1	Injured PT	*Lake et al.*, 2023 [74,124,125]
Hnf1b	PT differentiation	*Dhillon et. al.*, 2021 [126]
Slc12a3	Distal convoluted tubule (DCT)	*Balzer et al.*, 2022 [108,120,121]
Cldn4	Collecting duct (CD)	*Gong et al.*, 2017 [127]
Hsd11b2	CD-transitional cells	*Novella-Rausell et al.*, 2023 [128]
Slc12a1	Thick ascending limb (TAL) / Loop of Henle	*Balzer et al.*, 2022 [108]
Sparc	Mesangium / smooth muscle cells	*Brekken et al.*, 2000 [129,130]
Ctnnb1, Epcam, Krt8	Epithelial cell marker	*Mihevc et al.*, 2020 [131,132]
Cdh1, Vim, S100a4	EMT (Epithelial-mesenchymal transition)	*Zeisberg et al.*, 2009 [133,134]
Krt7, Krt18	Cell differentiation / Renal epithelial cell injury	*Djudjaj et al.*, 2016 [135,136]
Top2a, Mki67	Proliferation	*Scholzen et al.*, 2000 [120,137,138]
Jun, Fosb, Cdkn1a	Cellular stress	*Ascension et al.*, 2021 [139-142]

Figure 30 presents a comprehensive UMAP visualization of merged unsorted and sorted day 0 samples depicting the summarized and identified clusters based on the expression of these marker genes. Analysis of the merged day 0 samples allowed identification of 19 distinct clusters (Figure 30B), of which clusters 0, 4, 5, 7, 8, 16, 17 were classified as cells originating from proximal straight tubules (PST). Clusters 1, 2, 3, 6, 9, 10 were classified as cells from proximal convoluted tubules (PCT). Notably, cluster 18 exclusively comprised cells from the proliferating proximal tubule (PT), whereas cluster 14 comprised of immunoactive proximal tubule cells (act. PT). Furthermore, we identified cluster 11 as cells originating from the distal convoluted tubules (DCT), clusters 12 and 15 as transitional collecting duct (CD) cells, and cluster 13 as cells from the thick ascending limb. The annotation of the 19 distinct clusters

from anti-prominin-1 microbeads-sorted and unsorted primary PTEC on day 0 is listed in **Supplementary Table S3**. The final annotation is shown in **Figure 32.**

The collation of various feature plots allows for the visualization of gene expression patterns of representative marker genes. These patterns include signature PTEC genes, genes associated with other cell types, injury, EMT, cell differentiation, proliferation, and cellular stress (**Figure 31**). The markers Ctnnb1 and Krt8, which are indicative of epithelial cells, showed ubiquitous expression across the

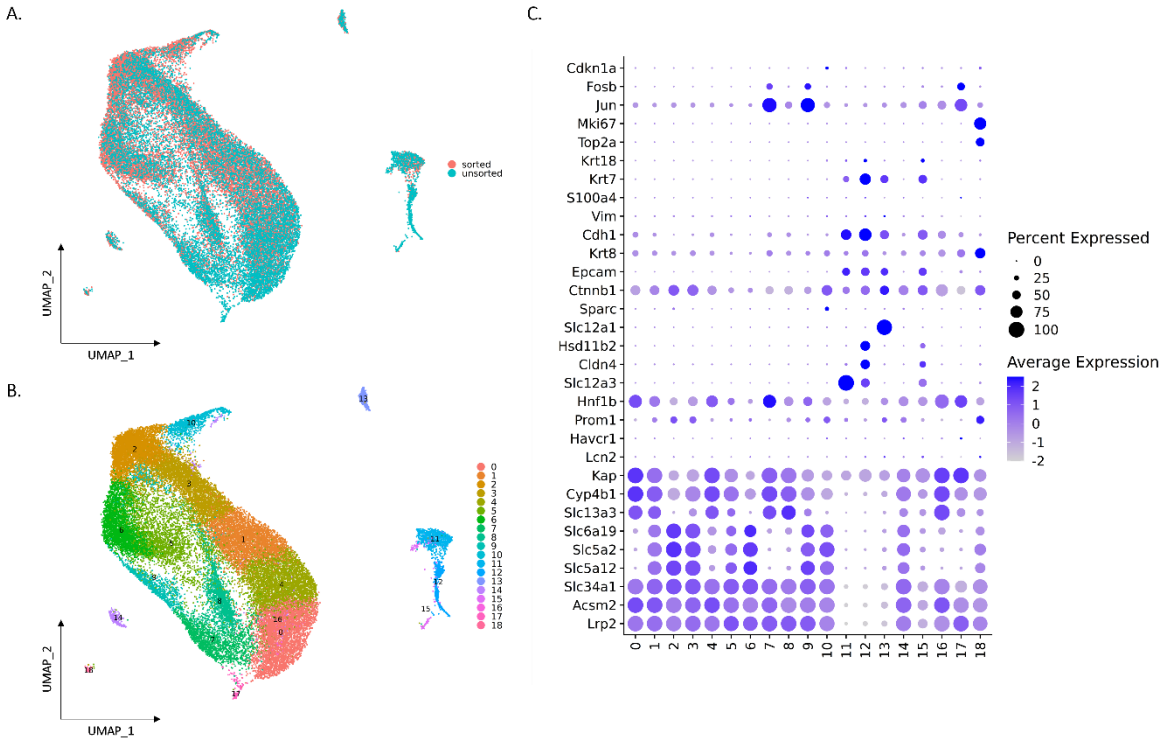

Figure 30: scRNAseq of anti-prominin-1 sorted and unsorted PTEC on isolation day (day 0).
(A) UMAP of sorted and unsorted PTEC on day 0. **(B)** UMAP showing 19 distinct clusters. **(C)** UMAP of summarized cluster (34133 cells, n = 3 each). **(C)** Dot plot displaying cell type-specific marker genes, with dot colour indicating average expression (scaled values) across the cells within each cell type, and dot size representing the percentage of cells expressing the respective gene within each cell type (n = 3 sorted + 3 unsorted).

clusters, while Cdh1, another marker for epithelial cells but also for EMT, was not expressed in any of the clusters. Moreover, Epcam was not expressed in any of the identified proximal tubule clusters. This was expected, as it is well-established that Epcam, a frequently employed marker for identifying epithelial cells, is not expressed in proximal tubular epithelial cells [143].

The overall expression pattern PT markers was noteworthy. Lrp2, Acsm2, and Slc34a1, which are considered PT markers, were expressed in all clusters designated as proximal tubular epithelial cells, except for clusters 11, 12, 13, and 15 (**Figure 30** and **Figure 31**). Distinct expression patterns were observed for markers associated with PCT and PST. PCT markers were mostly expressed in the upper half of the UMAP, specifically in clusters 1, 2, 3, 6, 9, and 10. On the contrary, PST markers showed

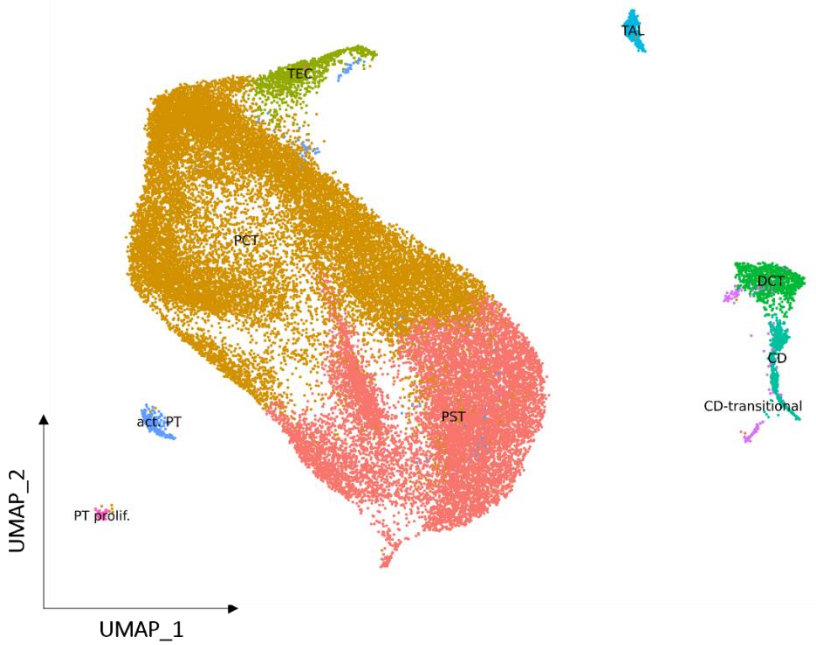

Figure 31: Annotated and summarized cluster of both sorted and unsorted PTEC from isolation day (day 0).
UMAP of summarized cluster (34133 cells, n = 3 sorted and unsorted each). The previously detected 19 distinct clusters were summarized and annotated according to their marker gene expression, respectively. PCT – proximal connecting tubule, PST – proximal straight tubule, PT prolif. – proliferating proximal tubule, act. PT – immunoactive proximal tubule, TAL – thick ascending limb, DCT – distal convoluted tubule, CNT – connecting tubule, CD-transitional – transitional collecting duct.

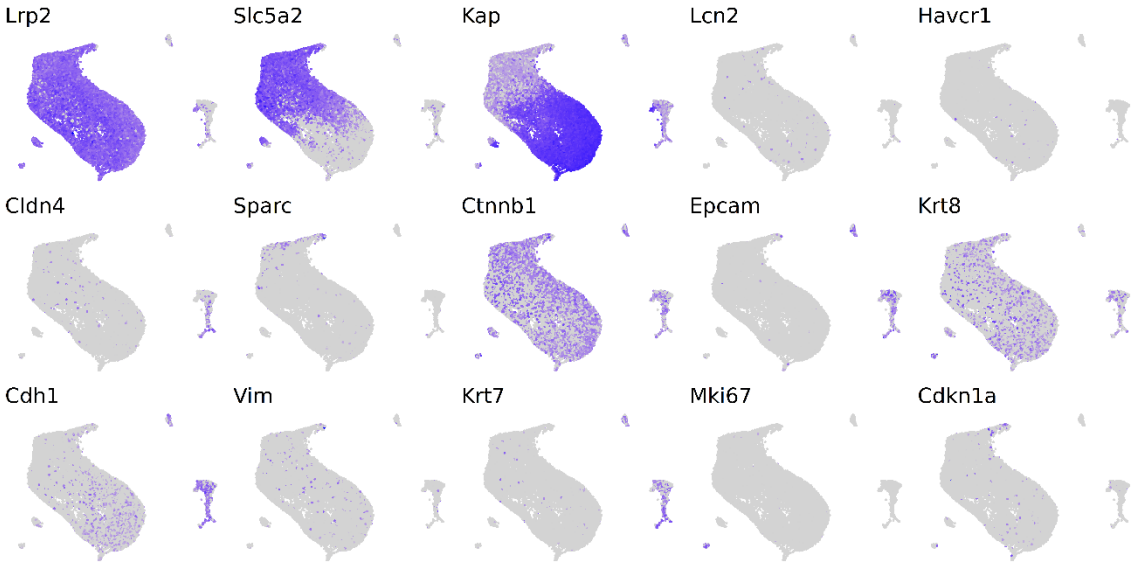

Figure 32: Gene expression patterns of representative marker genes on the isolation day of primary proximal tubular epithelial cells.
Feature plots showing gene expression patterns of signature PTEC genes and genes associated with other cell types, injury, epithelial-mesenchymal transition (EMT), cell differentiation, proliferation, and cellular stress (**Table 16**) Grey – low expression, dark purple – high expression. n = 3 sorted and 3 unsorted.

expression in the lower half of the UMAP, specifically in clusters 0, 4, 5, 7, 8, 16, and 17. Markers related to injury (Havcr1 and Lcn2), or cellular stress (Cdkn1a) were hardly expressed in any of the clusters, suggesting a lack of stress- or injury-related gene expression in the analysed samples. Cluster 18 was characterized by the expression of proliferation markers, indicating active cell proliferation. Additionally, through differential gene expression analysis, cluster 14 was identified as immunoactive proximal tubule (act. PT), highlighting its distinct gene expression profile. Hnf1b, a marker associated with proximal tubule differentiation, showed low levels of expression across all clusters, suggesting involvement in cell differentiation. Clusters 7, 9, and 17 exhibited low expression of Jun, which is a marker associated with cellular stress. However, the expression of Jun in these clusters was below the dissociation stress-score threshold and therefore limited.

Additionally, we analysed pathway activities within each cluster (**Figure 33**). Among the clusters, cluster 18 (PT prolif.) exhibited the highest pathway activity, particularly in relation to cell proliferation-related hallmarks such as DNA Repair, G2M checkpoint, E2F targets, MYC targets V1, and PI3K-AKT-mTOR. Clusters 11, 12, 13, and 15 (either DCT or CD) showed upregulation of TGF beta signalling, apical junction, KRAS signalling down, Hedgehog signalling, notch signalling, epithelial mesenchymal transition, angiogenesis, PI3K-AKT-mTOR, and oxidative phosphorylation hallmarks. On the other hand, clusters 10, 2, 3, 14, 17, 16, 8, 0, 1, and 4 (either PCT or PST) displayed upregulation of xenobiotic metabolism, glycolysis, fatty acid metabolism, and MTORC1 signalling. In clusters 5, 7, and 9 (either PCT or PST) TNF-alpha signalling via NFκB, hypoxia, and apoptosis pathways were notably upregulated. Slight upregulation of epithelial mesenchymal transition was furthermore detected in clusters 2, 5, 6, 7, 9, 10 (either PCT or PST).

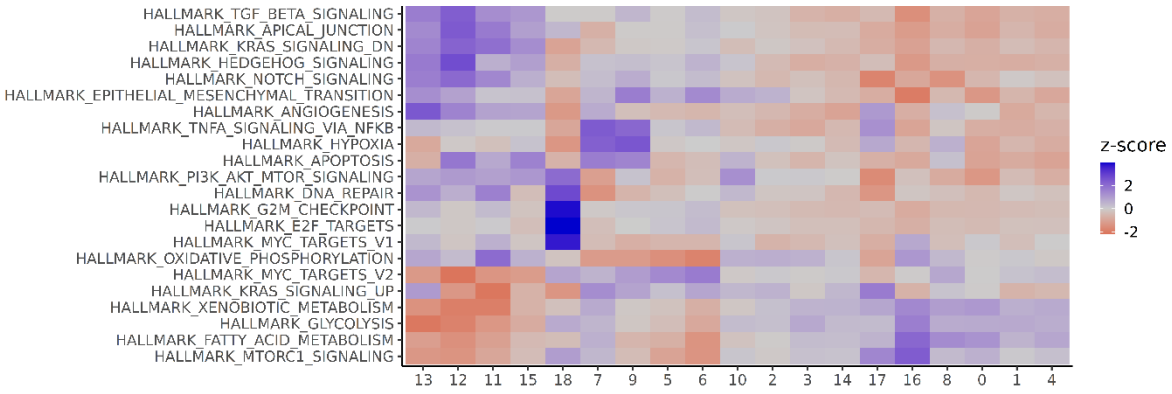

Figure 33: Pathway activities across the day 0 clusters.
Heatmap depicting the pathway activity across multiple scRNAseq clusters from merged unsorted and anti-prominin-1 sorted PTEC on the day of isolation (day 0). Z-Scores are calculated from log2-fold change in comparison to their respective control. Upregulation is displayed in blue; downregulation is displayed in red colour.

3.3.2 CELLS ON DAY 3 AND DAY 6 OF CULTURE DIFFER EXTENSIVELY COMPARED TO DAY 0

The evidence from merged unsorted and sorted day 3 and day 6 samples are depicted in **Figure 34A, B.** The figure presents a comprehensive UMAP visualization, showcasing the summarized and identified clusters based on the expression of specific marker genes. In total, we identified 27 distinct clusters after analysing day 3 and day 6 samples, as shown in **Figure 34C**. For identification purposes, we utilized selected markers listed in **Table 16**, which were visualized in a marker gene dot plot (**Figure 34D**). However, due to the mixed expression of several markers belonging to different cell types, it was challenging to pinpoint specific cell types accurately.

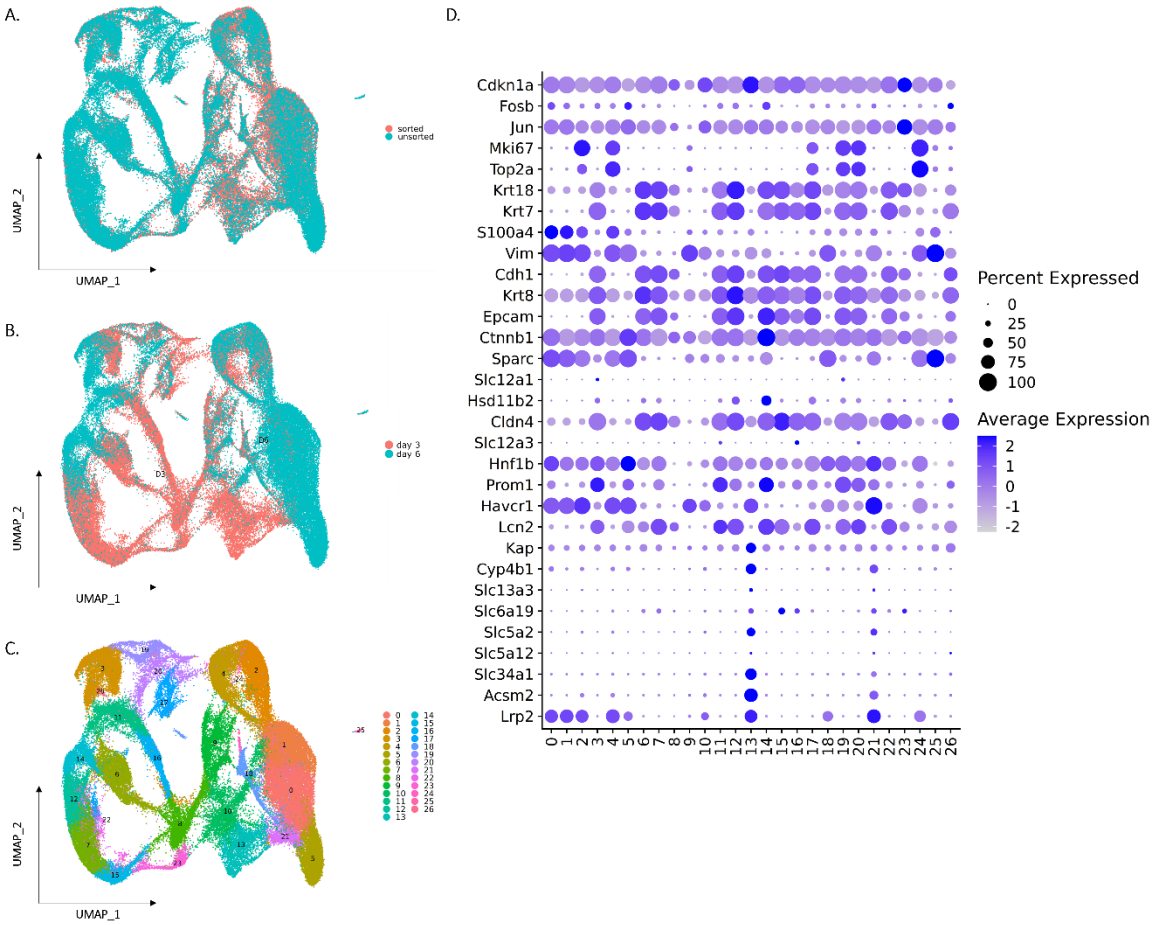

Figure 34: scRNAseq of anti-prominin-1 sorted and unsorted PTEC on day 3 and 6 of cell culture.
(A) UMAP of sorted and unsorted PTEC on day 3 and 6 of cell culture. **(B)** UMAP displaying the distribution of cells from day 3 (orange) and day 6 (green). **(C)** UMAP showing 27 distinct cluster (92,296 cells, n = 3 each). **(D)** Dot plot displaying cell type-specific marker genes, with dot colour indicating average expression (scaled values) across the cells within each cell type, and dot size representing the percentage of cells expressing the respective gene within each cell type (n = 3 sorted + 3 unsorted).

To provide further insights, we included feature plots expressing these selected markers (**Figure 35**). In all clusters ubiquitous expression of Cdkn1a, a marker showing that cells go into cell cycle arrest, and of Ctnnb1, a specific marker for epithelial cells, was observed. Proliferation markers Top2a and Mki67 were expressed in clusters 2, 4, 17, 19, 20, and 24. Hnf1b expression was detected in most of the

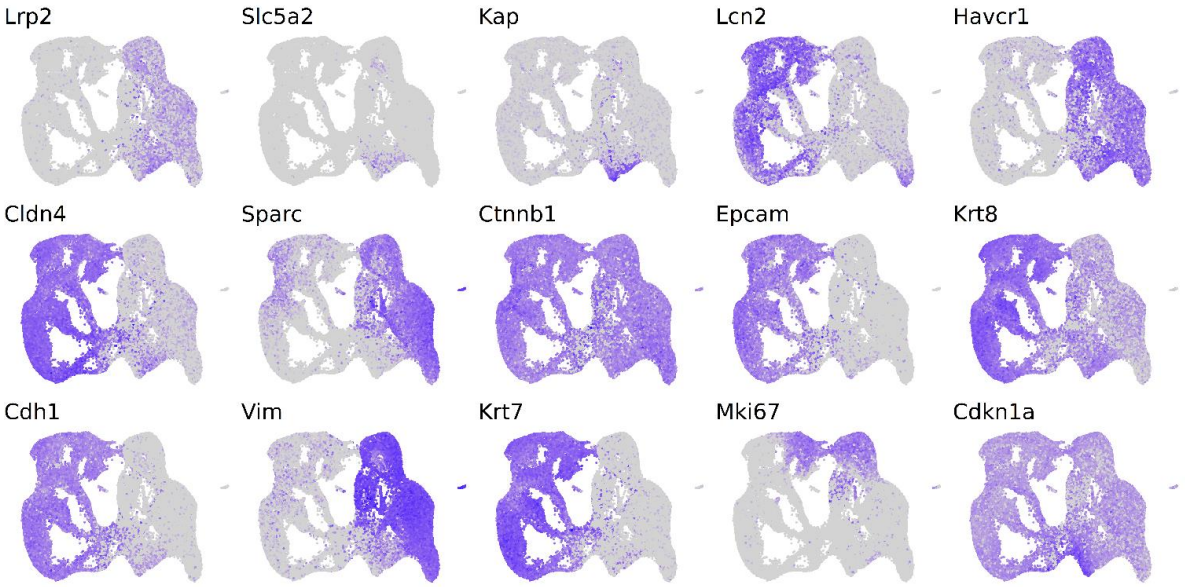

Figure 35: Gene expression patterns of representative marker genes on day 3 and day 6 of cultured primary proximal tubular epithelial cells.
Feature plots showing gene expression patterns of signature PTEC genes and genes associated with other cell types, injury, epithelial-mesenchymal transition (EMT), cell differentiation, proliferation, and cellular stress (**Table 16**). Grey – low expression, dark purple – high expression. n = 3 sorted and 3 unsorted.

clusters, with the highest expression in cluster 5, indicating that the cells have initiated differentiation processes. Interestingly, most clusters experienced a gradual loss of several PTEC-specific markers over time. Additionally, we noticed a distinct division of cells within the UMAP plot, with cells exhibiting differential expressions primarily segregated on either the left or right side. In detail, clusters 13 and 21 still exhibited some degree of expression of PTEC-specific markers such as Acsm2, Slc34a1, Slc5a2, and Cyp4b1. Notably, Lrp2 expression was observed primarily in clusters located on the right side of the UMAP (clusters 0, 1, 2, 4, 5, 9, 10, 13, 18, 21, 24, and 25). Except for cluster 25, these clusters also showed expression of injury-related marker Havcr1 and Vimentin, a marker associated with EMT. Moreover, Sparc, a marker for mesenchymal cells and fibrosis, was predominantly expressed in clusters on the right side on the UMAP. Cluster 25 showed the highest expression of Sparc and Vimentin The epithelial cell marker Cdh1 was not expressed in clusters segregated to the right side of the UMAP. Thus, the expression of Sparc, Vimentin, Havcr1 and Cdkn1a, as well as the lack of Cdh1 expression, indicate that these cells tend to transdifferentiate into a “mesenchymal-like” state.

Conversely, clusters on the left side of the UMAP (clusters 3, 6, 7, 8, 11, 12, 14, 15, 16, 17, 19, 20, 22, and 23) demonstrated expression of Lcn2 (induced upon injury in renal tubular epithelial cells), Cldn4 (specific to cells from the collecting duct), and Cdh1 (a marker for epithelial cells and EMT). Besides, the expression of Epcam, a marker for epithelial cells except for proximal tubules, was predominantly detected in clusters on the left side of the UMAP. In line with Epcam, Krt8, another marker for epithelial cells and cell differentiation, was widely expressed, however, also being higher in cells clustered on the left side of the UMAP. Higher Epcam, Krt8, Cdh1, Cldn4, and Lcn2 expressions

indicates that these cells have retained certain aspects of their “epithelial-like” phenotype. However, the absence of PTEC markers suggests that these cells have also initiated a process of transdifferentiation. This dual observation suggests phenotypic alterations in these cells, where they maintain some characteristics of epithelial cells while undergoing changes toward a different cellular identity.

Subsequent pathway activity analysis on the 27 distinct clusters revealed the strongest pathway activity in cluster26 (Hedgehog signalling, KRAS signalling down), cluster 23 (TNFα signalling via NFκB), cluster 5 (KRAS signalling up), cluster 25 (epithelial-mesenchymal transition), clusters 4, 24, 19, and 20 (G2M checkpoints and E2F targets), clusters 13 and 21 (xenobiotic metabolism and fatty acid metabolism), and cluster 16 (oxidative phosphorylation). Cluster 26 showed upregulation of the hedgehog signalling pathway, while oxidative phosphorylation and mTOR signalling pathway were strongly downregulated (**Figure 36**). In clusters 2,4, and 24 from the “mesenchymal-like” site of the UMAP and clusters 17, 19, and from the “epithelial-like” site proliferation-associated pathways, such as E2F targets, G2M checkpoint, MYC targets V1 and V2, DNA repair, and PI3-Akt-mTOR signalling were upregulated. Under healthy conditions proximal tubules rely on fatty acid oxidation (FAO) for energy production rather than on glycolysis. As soon as conditions change towards an unhealthy state, proximal tubules reduce FAO and start using glucose as substrate [117,144]. Upregulation of glycolysis and proliferation hallmarks as well as downregulation of fatty acid metabolism in these clusters is a strong indicator that they are comprised of diseased cells. Notably, clusters 13 and 21 exhibited a combination of retained PTEC-specific hallmarks, including fatty acid metabolism, along with the upregulation of the xenobiotic metabolism hallmark indicating that the cells are under stress or subjected to injurious stimuli, and they are responding by intensifying their metabolic processes to detoxify and eliminate xenobiotics. Together with the upregulation of oxidative phosphorylation indicative of a higher energy demand or an adaptation to cellular stress, this evidence suggests that the cells are actively responding

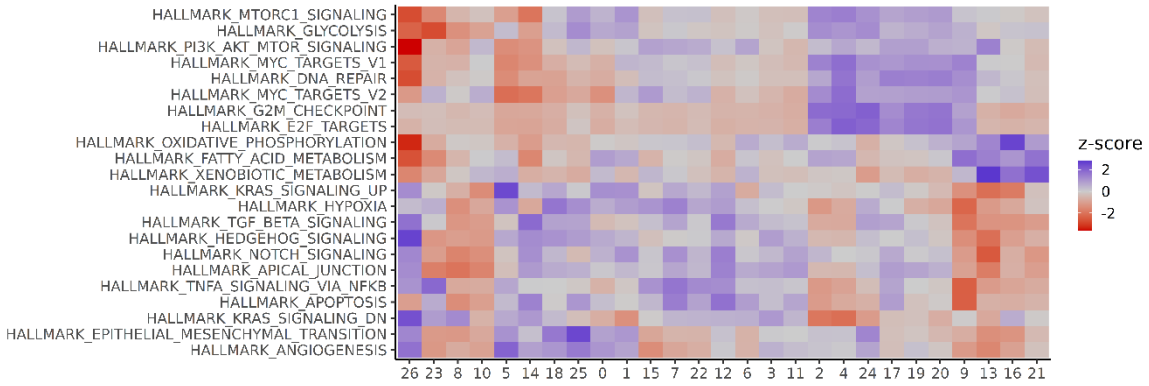

Figure 36: Pathway activities across day 3 and 6 of cell culture.
Heatmap depicting the pathway activity across multiple scRNAseq clusters from day 3 and day 6 of cultured primary PTEC. Z-Scores were calculated from log2-fold change in comparison to their respective control. Upregulation is displayed in blue, downregulation is displayed in red colour.

to physiological or environmental changes that require increased energy production. The presence of these features suggests a potential transition towards a dedifferentiated state in these specific clusters, making them intriguing candidates to represent the initial stages of dedifferentiation. To unravel the underlying mechanisms and implications of this dedifferentiation process, further in-depth investigation is required.

3.3.3 TRAJECTORY ANALYSIS REVEALS POSSIBLE FATES OF CULTURED PTEC

To infer the developmental trajectories of cells over time and to ascertain if the cells undergo dedifferentiation or if they transdifferentiate into other specific cell lineages, a comprehensive trajectory analysis was conducted using the merged unsorted and sorted samples from day 3 and day 6 (**Figure 37**). This resulted in a diffusion map embedding 13 distinct clusters, as well as a diffusion

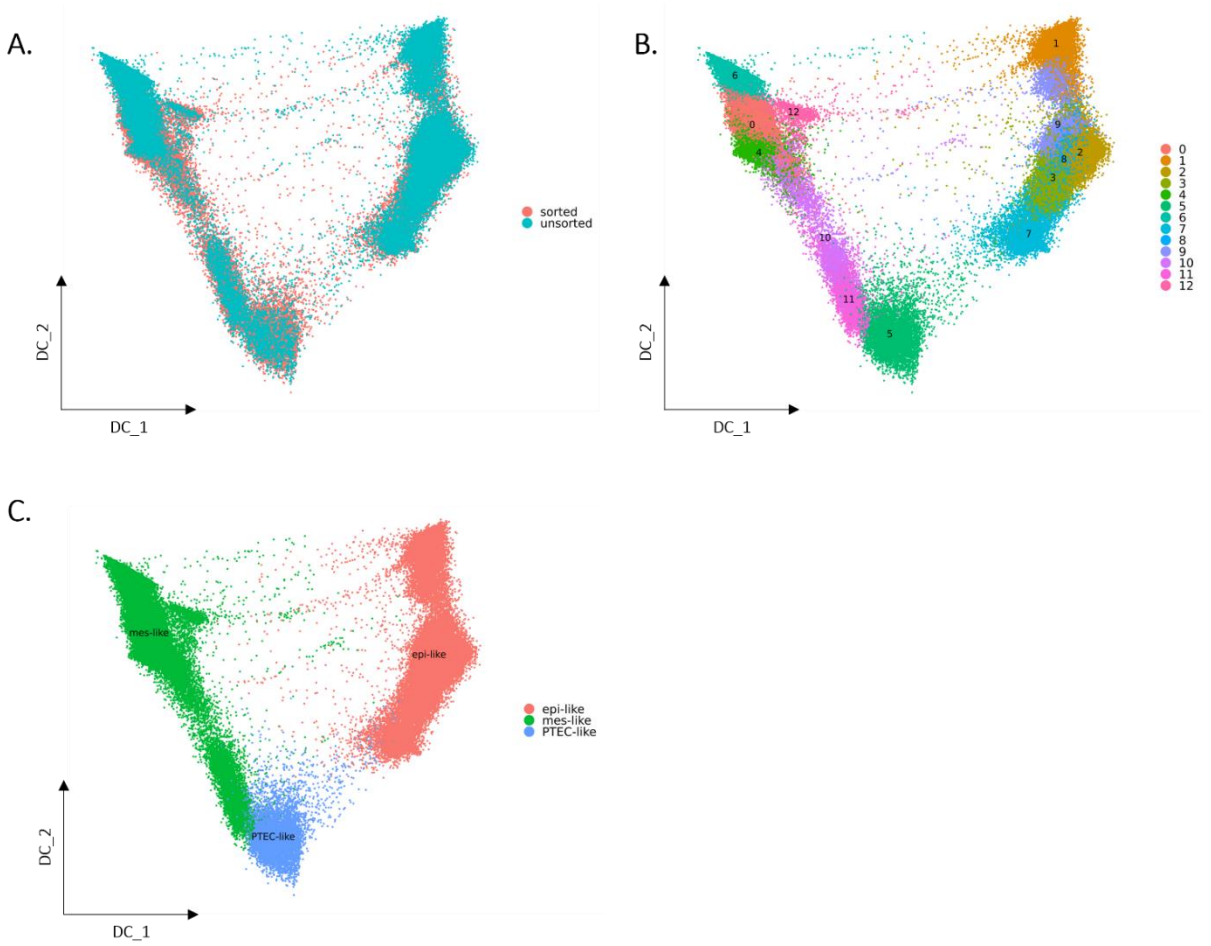

Figure 37: Trajectory analysis of day 3 and day 6 cultured primary PTEC.
(A) Diffusion map displaying the distribution of sorted and unsorted samples (n = 3 each). **(B)** Diffusion map showing 13 distinct clusters after trajectory analysis from day 3 and day 6 cultured PTEC. **(C)** The trajectory analysis suggest that cells that are in a PTEC-like state on day 3 of culture, might have two fates: either cells differenciate into mesenchymal-like (mes-like) cells or into epithelial-like (epi-like) cells over the course of culture. DC—diffusion component.

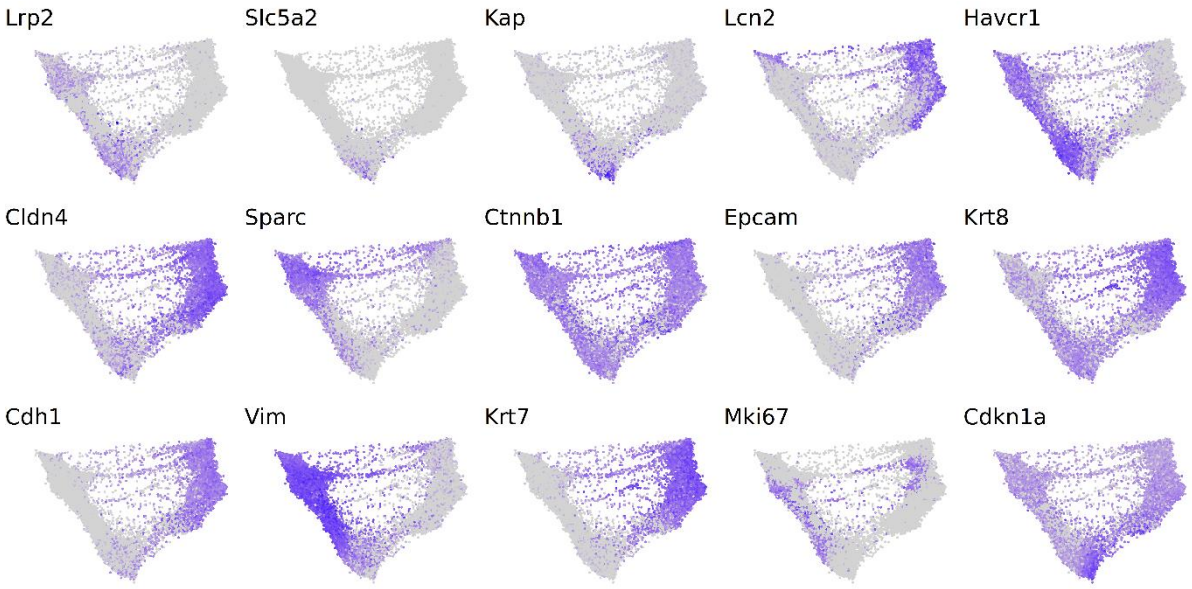

Figure 38: Gene expression patterns of representative marker genes on day 3 and day 6 of cultured primary PTEC after trajectory analysis.
Feature plots showing gene expression patterns of signature PTEC genes and genes associated with other cell types, injury, EMT, cell differentiation, proliferation, and cellular stress. (**Table 16**). Grey – low expression, dark purple – high expression. n = 3 sorted and 3 unsorted.

pseudotime ordering (**Figure 37B**). Through meticulous analysis of these clusters, considering differential gene expression and selected marker gene expression, the trajectory analysis suggests that cells in a PTEC-like state on day 3 of cell culture may follow one of two potential paths: differentiation into mesenchymal-like cells or into epithelial-like cells during the course of cell culture (**Figure 37C**). To provide further insights, we included feature plots expressing these selected markers in **Figure 38**.

This analysis established that most of the PTEC-specific markers were expressed in cluster 5, similar to the clusters 10, 13, and 21 from the previous day 3/day 6 analysis (**Figure 34C**). Representing the two possible fates, clusters 0, 4, 6, 10, 11, and 12 were summarised as epithelial-like cells, while clusters 1, 2, 3, 7, 8, 9 were summarised as mesenchymal-like cells, based on the expression of the respective markers, as presented in **Figure 38**.

In detail, cluster 5 still exhibited a partial expression of PTEC-specific markers such as Acsm2, Slc34a1, Slc13a3, Slc5a2, and Cyp4b1. Notably, Lrp2 expression was primarily observed in clusters comprising the mesenchymal-like cells. These clusters also showed expression of injury-related marker Havcr1 and Vimentin, a marker associated with EMT. Additionally, cells destined for the mesenchymal-like fate were shown to express Sparc, a recognized marker indicative of mesenchymal cells and associated with fibrosis. On the contrary, clusters consisting of epithelial-like cells displayed the expression of Lcn2, an injury-related marker, alongside Cldn4, which is specific to cells from the collecting duct, and Cdh1, a marker associated with both epithelial cells and EMT. The marker specific to epithelial cells (Ctnnb1) remained highly expressed across almost all clusters. Krt8, another marker

linked to epithelial cells and cell differentiation, exhibited widespread expression, with a notable concentration in cells destined for an epithelial-like fate. Comparably, the epithelial cell marker Epcam was predominantly expressed in cell clusters poised to undergo an epithelial-like fate. On the other hand, clusters comprising mesenchymal-like cells demonstrated expression of injury-related marker Lcn2 along with Cldn4, specific to cells from the collecting duct. Those cells, however lacked the expression of Cdh1, a marker for epithelial cells and EMT. Clusters 5 and 7 exhibited the most

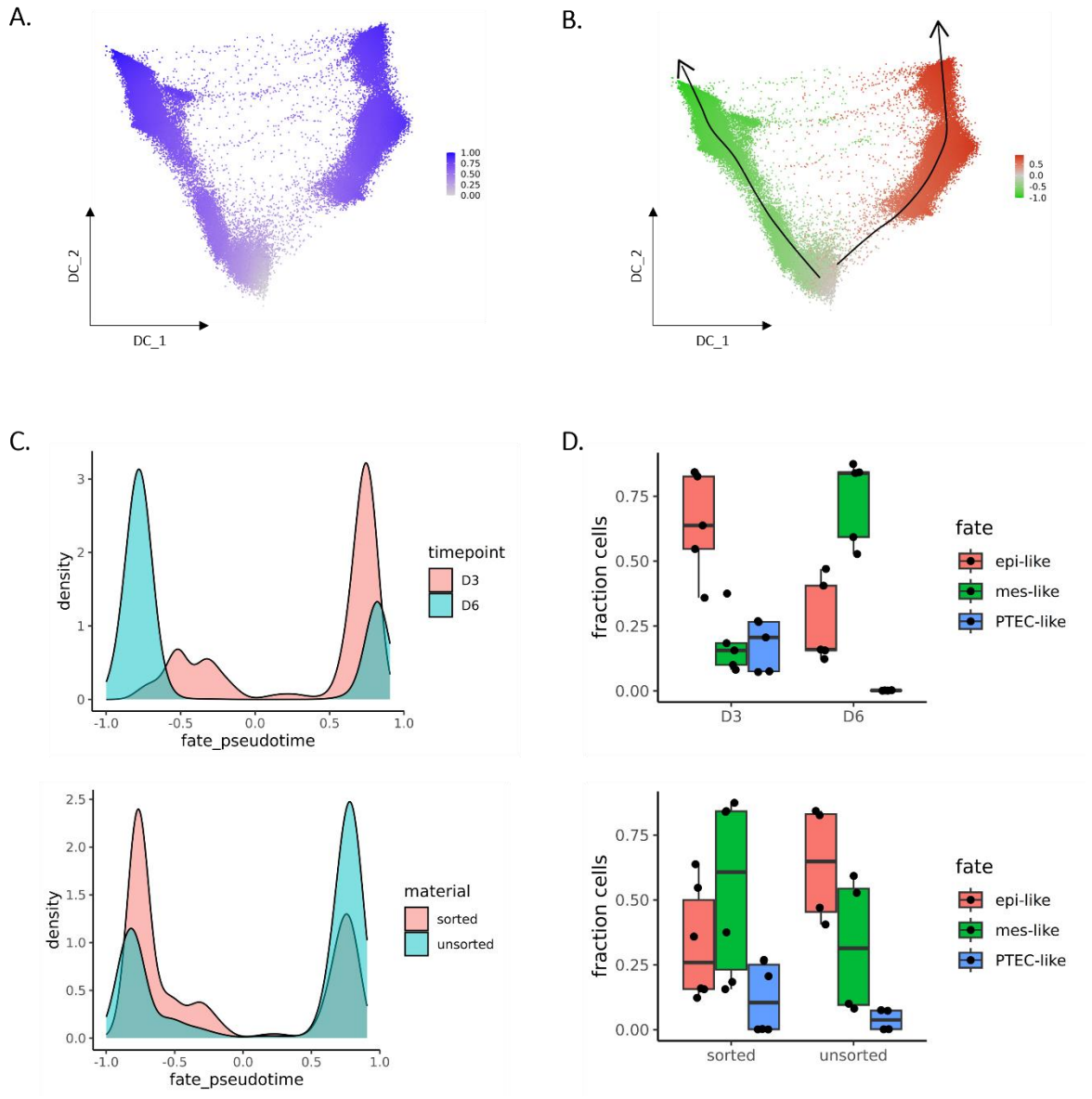

Figure 39: Branching pattern of cells along pseudotime axis indicates two dedifferentiation paths.
(A) The UMAP projection displays a clear separation of cells along the pseudotime axis, indicating two different stages of cellular transition. **(B)** UMAP of trajectory analysis introducing a pseudotime which is negative for mesenchymal-like cells and positive for epithelial-like cells. PTEC-like cells were assigned to either fate by comparing expression of epithelial- and mesenchymal-like genes. **(C, D)** Histograms and bar plots displaying the distribution of fate pseudotime depending on the timepoint of cell culture (day 3 or day 6) and origin (sorted or unsorted). Cells from day 3 of cell culture were at an early stage, while day 6 cells were at later stage. Sorted cells preferentially followed the mesenchymal-like fate compared to the epithelial like fate in unsorted cells. PTEC-like cells were detected on day 3 but were almost gone after 6 days of culture. A lager fraction of PTEC-like cells was observed in sorted cells compared to unsorted cells.

pronounced expression of the cellular stress marker Cdkn1a, despite its presence being observed across all clusters. Hnf1b, a marker for proximal tubule differentiation, displayed low expression levels across most clusters, while proliferation markers Top2a and Mki67 were only expressed in clusters 4 and 11 of the epithelial-like cells, as well as cluster 9 of the mesenchymal-like cells (**Figure 38)**.

Following that, we proceeded to separate the cells along the pseudotime progression, aiming to achieve a separation of the two distinct fates. Assuming the presence of two differentiation paths, we set pseudotime values as negative for mesenchymal-like cells and positive for epithelial-like cells (**Figure 39A, B**). To assign PTEC-like cells to either fate, the expression of epithelial- and mesenchymal-like genes was compared. Further examination of the distribution of fate pseudotime depending on the timepoint of cell culture (day 3 or day 6) and cell origin (sorted or unsorted) was conducted using density and box plots (**Figure 39C, D**). Cells from day 3 of cell culture were found to be at an early stage, while cells from day 6 were at a more advanced stage of dedifferentiation. Sorted cells rather followed the mesenchymal-like fate, compared to the epithelial-like fate in unsorted cells. Additionally, PTEC-like cells were detected on day 3, but were nearly absent after 6 days of culture. Moreover, a higher fraction of PTEC-like cells was observed in sorted cells compared to unsorted cells.

To gain a more comprehensive understanding of gene expression dynamics and functional changes during cellular differentiation and developmental, we analysed smooth gene expression patterns along the fate trajectory in a more refined manner. Using hierarchical clustering, this analysis identified distinct sets of genes with similar expression patterns, allowing for a detailed characterization of gene expression changes throughout the developmental trajectory. The results of the clustering analysis are presented in **Figure 40.**

The heatmap (**Figure 40A**) illustrates the gene expression patterns along pseudotime for significant genes, which cluster into nine distinct groups. Notably, Cluster 9 exhibits high expression at both ends of the trajectory and primarily consists of genes associated with DNA replication (e.g. Mcm3 [145]) and cell proliferation (e.g. Iqgap3 [146]). Cluster 6, also active on both sides of the trajectory, exhibits genes playing roles in certain physiological processes of the kidney, such as Klf4 and Mmp9. Klf4 is involved in the regulation of numerous cellular processes, including proliferation, differentiation, cell growth and inflammation, to maintain renal function [147-149]. Mmp9, however, is involved in proteolysis of components from the extracellular matrix and is upregulated in renal pathological conditions [150,151]. In addition, cluster 6 expressed Plod2, a gene that is primarily induced under hypoxic conditions and has been described to interact with EGFR, ultimately regulating the Akt pathway involved in cell proliferation and survival [152]. Clusters 1 and 8 displayed high expression in the epithelial-like state, with

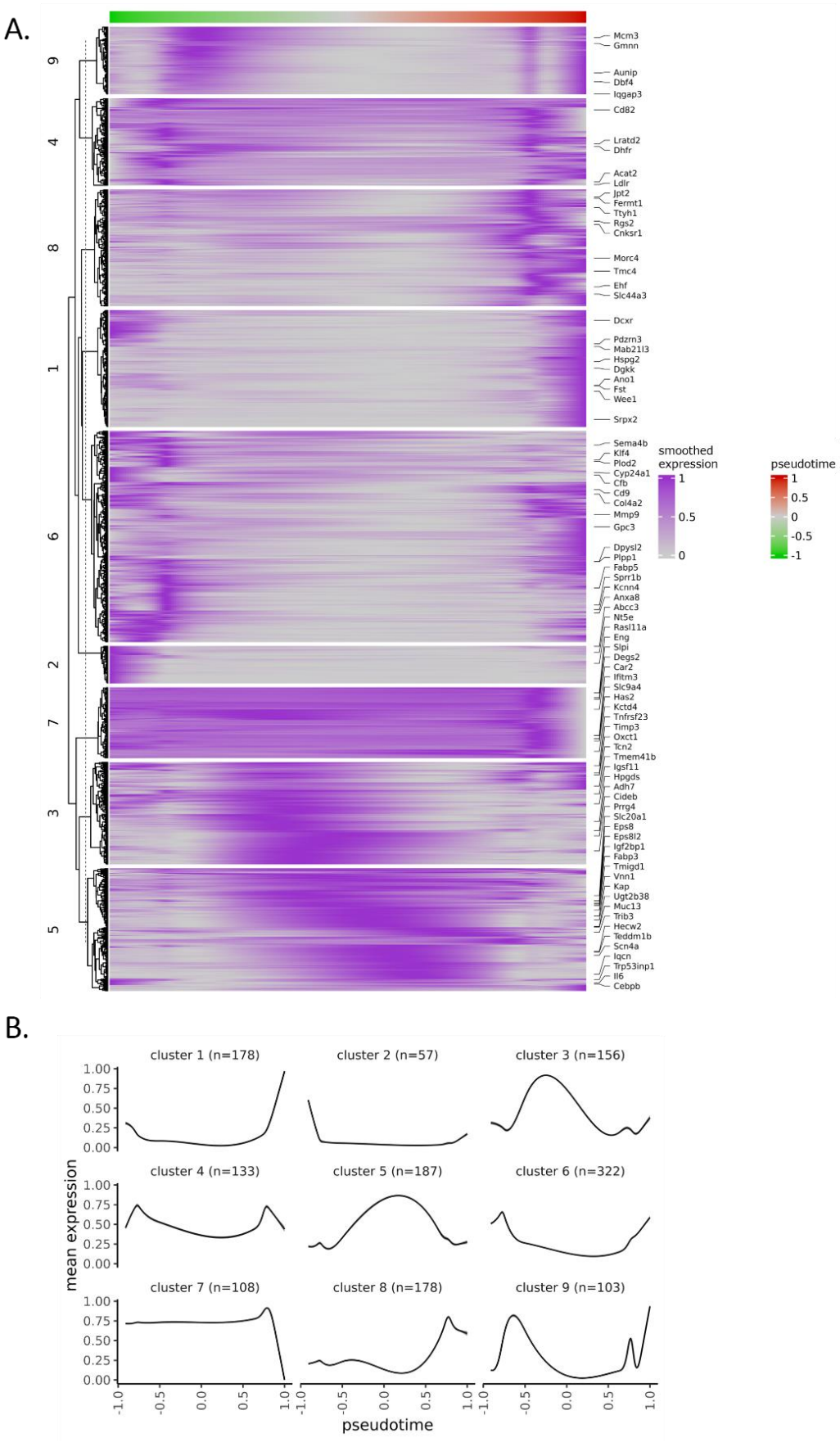

Figure 40: Smooth trajectory of gene expression changes over pseudotime.
(A) Heatmap representing gene expression patterns along pseudotime for significant genes, each with a different region of activity, that cluster into 9 distinct groups. **(B)** Average behaviour of genes [mean expression] per cluster along pseudotime. n refers to the number of genes per cluster.

genes involved in the regulation of proton secretion and protein reabsorption, e.g. Ano1 [153], or protection against oxidative stress and apoptosis, e.g. Fst [154]. Cluster 2 showed high expression in the mesenchymal-like state, with upregulated genes involved in inflammation and cell differentiation of mesenchymal cells (e.g. Nt5e [155-157]) or genes whose expression is linked to various types of cancer (e.g. Abcc3 [158]). Both clusters 4 and 7 exhibited gene expression along the whole trajectory. While cluster 4 exhibited genes related to fatty acid metabolism such as Acat2 and Ldlr [159-161], cluster 7 involves the expression of Eng, a marker for angiogenesis [162], or Has2, a gene expressed around PTEC after incidents such as AKI or CKD [163,164]. Moreover, cluster 7 included expression of Car2, highly expressed in renal intercalated cells known to activate systemic inflammatory responses [165]. Cluster 3 and 5 showed the highest activity in the middle of the trajectory. In cluster 3, for instance Timp3 was upregulated. Timp3 is described as endogenous inhibitor of matrix metalloproteinases (Mmp) that are key enzymes that regulate the integrity of the extra cellular matrix [166,167]. Cluster 5 represents the PTEC-like state and expresses genes and cytokines, such as IL-6, that are produced in response to proinflammatory signals including TNF-α and hypoxia [168-170]. Moreover, the expression of the PTEC-specific marker Kap [171] was detected, supporting the hypothesis that cells within this cluster still possessed PTEC-like features. Figure 40B provides the average dynamics per cluster along pseudotime.

Furthermore, to investigate the functional implications of the identified gene clusters, we conducted gene set enrichment analysis (GSEA) on the clusters derived from the smooth gene expression analysis along pseudotime (Figure 40). this analysis systematically assessed the enrichment of predefined gene sets or pathways within the gene clusters, enabling to uncover biological mechanisms underlying gene expression changes.

The dot plot representation of the GSEA results highlights overrepresented gene sets per cluster, offering a comprehensive view of functional changes across the nine clusters (Figure 41). Cluster 9 shows enrichment of pathways involved in DNA replication, cell cycle and G2M checkpoint, indicating that genes within this cluster contribute to the regulation of cell cycle stages. Genes within cluster 7 are involved in oxidative phosphorylation, various electron transport and IFNα/β signalling pathways. Genes of cluster 4 showed pathway activities in cholesterol homeostasis and biosynthesis, while cluster 2 exhibited enrichment of genes involved in interleukin and IL6-JAK-Stat3 signalling. Cluster 3 incorporated genes, among others, involved in the ROS pathway and glutathione metabolism, whereas genes within cluster 8 are involved in cell-to-cell communication and apical junction pathways. Cluster 5 demonstrated enrichment of genes related to apoptosis and th p53 pathway. Genes involved in extra cellular matrix receptor interaction and fibre formation pathways were predominantly expressed in cluster 1, while cluster 6 showed upregulated genes involved in extracellular matrix degradation, coagulation, and angiogenesis pathways (Figure 41).

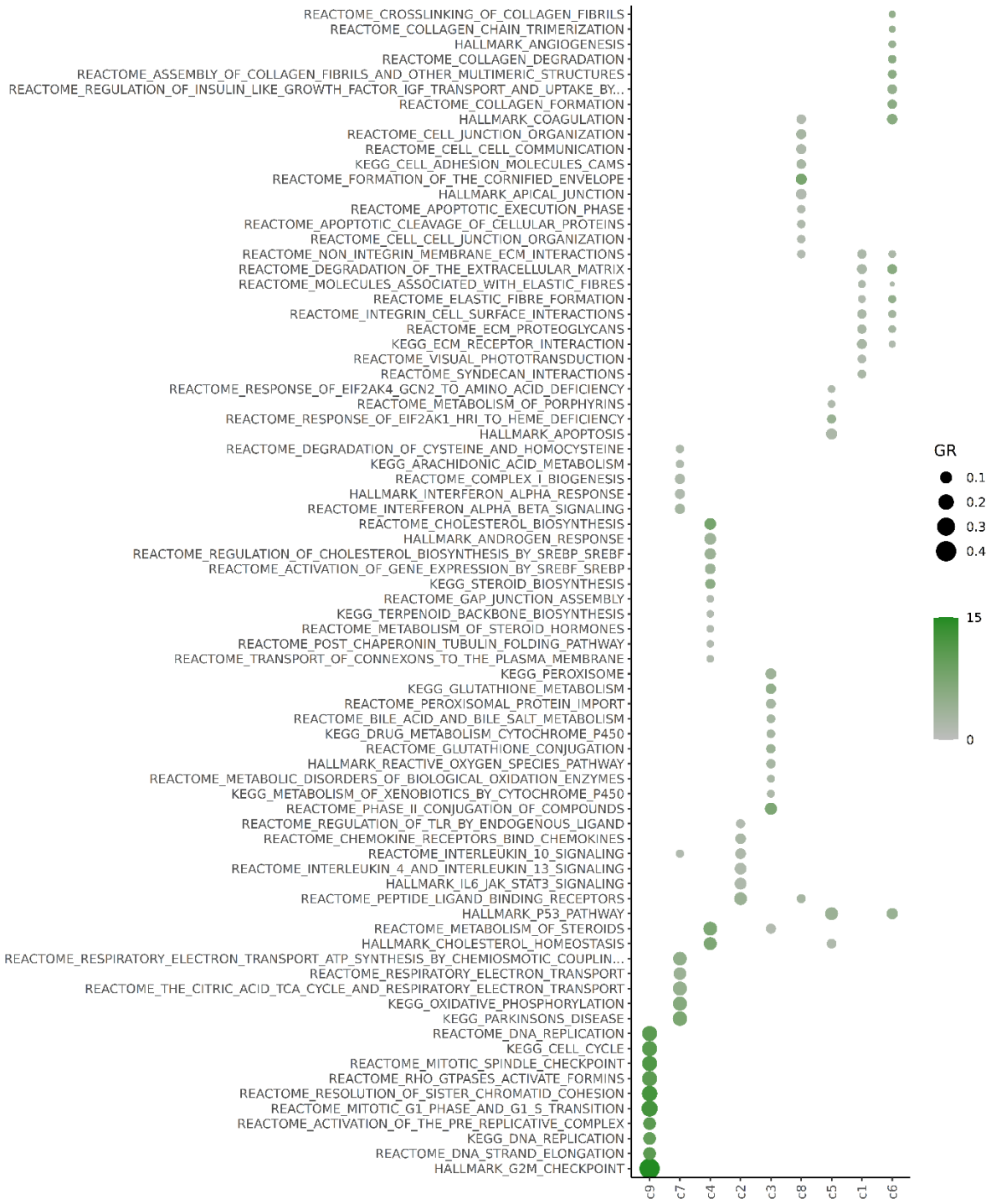

Figure 41: Gene set enrichment analysis (GSEA) on clusters from of smooth gene expression along pseudotime (Figure 40).

Dot plot representation of GSEA results showcasing the differential enrichment of gene sets, providing a comprehensive view of functional changes across the 9 clusters obtained from the smooth trajectory analysis along pseudotime. GR—Gene ratio.

To sum up, scRNAseq analysis on unsorted and prominin-1 sorted PTEC cultured over six days revealed significant differences in gene expression patterns between the day of isolation (day 0) and days 3 and 6 of cell culture, indicating the initiation of dedifferentiation or transdifferentiation processes.

Various cell clusters were identified and annotated based on gene expression patterns. Injury-associated markers were not expressed, suggesting a healthy cell population. Over time, PTEC-specific markers were lost, but some clusters still exhibited partial expression. Pathway analysis revealed dynamic changes in pathway activities, with inflammation-related signalling and cell cycle regulation becoming more prominent. Two clusters on day 3/day 6 still displayed PTEC-specific gene expression but also characteristics of early dedifferentiation. Trajectory analysis suggested two potential paths for cell development: a mesenchymal-like or an epithelial-like fate. Gene expression patterns along the trajectory provided insights into functional implications during cellular differentiation, enrichment of DNA replication and repair, interleukin signalling, apoptosis, and metabolic pathways.

3.4 EXPRESSION OF ENDOGENOUS LCN2 AND ITS RECEPTORS IN VARIOUS mKTx SETTINGS

Investigating the endogenous source of Lcn2 is a crucial aspect in understanding its role in kidney transplantation. Lcn2 expression is highly induced in damaged nephrons, immune cells, and rejecting kidney allografts, indicating its involvement in various pathological conditions [35-37]. However, the specific cellular source of endogenous Lcn2 during kidney rejection, whether it originates from kidney epithelia or graft-infiltrating and circulating polymorphonuclear cells, remains uncertain. Determining the primary source of Lcn2 is essential for unraveling the underlying biological processes and potential pathological implications. Moreover, this knowledge can facilitate the development of targeted interventions to selectively modulate Lcn2 production or activity, leading to improved therapeutic strategies for kidney rejection and related disorders. In addition to investigating the endogenous source of Lcn2 during kidney transplantation, it is crucial to examine the expression of specific receptors such as *Lrp2* and *Slc22a17* [30,62,63,172], as well as the expression of genes related to injury, such as Havcr1 [173,174]. Assessing Lrp2 expression helps understand the uptake capacity of Lcn2 by PTEC, while studying *Slc22a17* expression provides insights into the transport mechanisms of Lcn2 in the kidney. Havcr1 expression serves as a biomarker for kidney injury and offers information about the severity and location of damage [173,174]. Analyzing these receptor expressions alongside Lcn2 enhances the understanding of Lcn2 uptake, transport, and kidney injury mechanisms during transplantation, contributing to developing therapeutic strategies.

To elucidate these inquiries, a series of murine kidney transplantations were performed involving different donor-recipient combinations: allogeneic (Balb/c to C57Bl/6, C57Bl/6 to Balb/c) and syngeneic (Balb/c to Balb/c, and C57Bl/6 to C57Bl/6). By comparing the expression patterns of Lcn2 in the different transplantation settings, we aimed to decipher the relative contributions of immune cells and injured PTEC as the potential sources of endogenous Lcn2 during kidney rejection. Assessing these potential variations in Lcn2 expression and its effects, provides insights into the relationship between the severity of acute cellular rejection, the immune response, and Lcn2-production. We hypothesized

that more severe rejection episodes, characterized by extensive immune cell infiltration and tissue damage, may lead to higher Lcn2 expression levels. On the other hand, milder or tolerating rejection scenarios, where the immune response is less intense, may result in comparatively lower levels of Lcn2.

Following transplantation, histopathological examination and evaluation of graft function were conducted in the context of syngeneic and allogeneic kidney transplantations. Representative images captured from cross sections of the allogeneically transplanted kidneys at pod-7 demonstrated typical lesions of acute kidney rejection, i.e. tubulitis and interstitial inflammation (**Figure 42A**). Additionally, the analysis of serum creatinine and urea levels allowed for the assessment of graft function (**Figure 42B**). Prominent increase in serum creatinine and urea levels were discerned in Balb/c recipients of C57Bl/6 kidneys compared to the other groups. Correspondingly graft survival rates at the culmination of 28 days post-surgery served to illuminate the gravity of rejection responses encountered by the C57Bl/6 to Balb/c transplantation group in comparison to their counterparts in the Balb/c to C57Bl/6 transplantation group (**Figure 42C**).

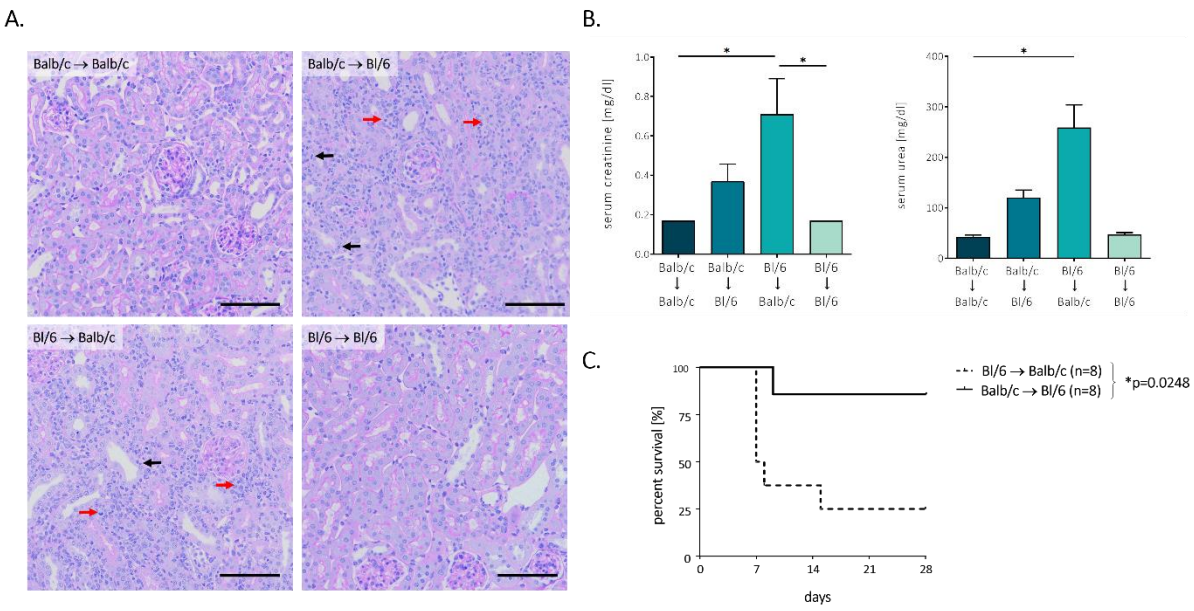

Figure 42: Histopathological observations and graft function analysis after various syngeneic and allogenic mKTx over time.
(A) Representative images from cross sections through syngenically (Balb/c to Balb/c and C57Bl/6 to C57Bl/6) and allogenically (Balb/c to C57Bl/6 and C57Bl/6 to Balb/c) transplanted kidney grafts 7 days after surgery. Black arrows indicate the presence of tubulitis, and red arrows indicate the presence of interstitial inflammation. Scale bar = 100 µm. **(B)** Serum creatinine and serum urea levels 7 days after allogenic and syngeneic transplantation. **(C)** Graft survival 28 days post transplantation surgery in allogenic transplantation settings (Balb/c to C57Bl/6 and vice versa). C57Bl/6 = Bl/6.

3.4.1 STRONGEST LCN2 EXPRESSION IN COLLECTING DUCT-PRINCIPAL CELLS

To unravel the cellular identities responsible for the source of Lcn2 within the intricate milieu of the kidney graft and infiltrating immune cells, as well as to discern the extent of Lcn2 receptor

expression, including *Lrp2* or *24p3R* (*Slc22a17*), of these implicated cell types, single-nucleus RNA-sequencing (snRNAseq) analysis was executed as described in section 2.10.3. This cutting-edge technique enabled a comprehensive assessments of Lcn2 expression patterns, with a particular focus on proximal tubules and immune cells. The analysis focused on the potential dynamic alterations in Lcn2 and its receptors' expression patterns amid diverse kidney transplantation (mKTx) conditions, (syngeneic and allogeneic; n = 1-3 per group, 10 transplantations in total; Supplementary Table S4), especially considering renal tubular segments. Yet, the samples Balb/c to C57Bl/6 (sample 2) and C57Bl/6 to C57Bl/6 (sample 2) exhibiting a nucleus count below 1000 and a significant proportion of ambient RNA had to be excluded from the analysis, as detailed in Supplementary Table S4.

A comprehensive assessment of 41,667 nuclei across all eight samples unveiled 25,719 distinct genes. Subsequent clustering, predicated on the top 2,000 highly variable genes, yielded a discernible partition of 26 clusters (depicted in Supplementary Figure S25), wherein cell type annotation was accomplished through reference to well-established marker genes [79-81,83] (Supplementary Table S5). Percent expressions of marker genes per cluster and syngeneic and allogeneic murine kidney transplantation groups are listed in Supplementary Table S6. Notably, expression of *Slc22a17*, one of the two receptors of Lcn2, was undetectable (Supplementary Figure S26A) and was therefore excluded from subsequent analyses. Given the widespread distribution of cluster 11 (Supplementary Figure S25), coupled with its pronounced prevalence of ambient RNA that made its assignment to a specific cell type difficult (data not shown), its exclusion from further examination was necessary.

Median genes and transcripts (designated by unique molecular identifiers (UMI) per nucleus exhibited similar characteristics within the syngeneic and allogeneic transplantation cohorts, as represented in Figure 43A-C. Following the excision of cluster 11, subclusters corresponding to distinct cell types were combined, ultimately defining 16 discrete cell types, encompassing proximal tubule (PT), thick ascending limb (TAL), immune cells, distal convoluted tubule (DCT), connecting tubule (CNT), endothelial cells (EC), collecting duct principal cells (CD-PC), thin limb (tL), collecting duct intercalated cells A and B (CD-IC-A/CD-IC-B), proliferating cells, podocytes, parietal epithelial cells (PEC), deep medullary epithelium of pelvis (DMEP), and macula densa. A comprehensive visualization of summarized cell type clusters was achieved through UMAP plotting (Figure 43D), complemented by dot plots illustrating the gene expression patterns of cluster-enriched markers (Figure 43E). Percent marker gene expressions per summarized cluster and syngeneic and allogeneic murine kidney transplantation groups are listed in Supplementary Table S7.

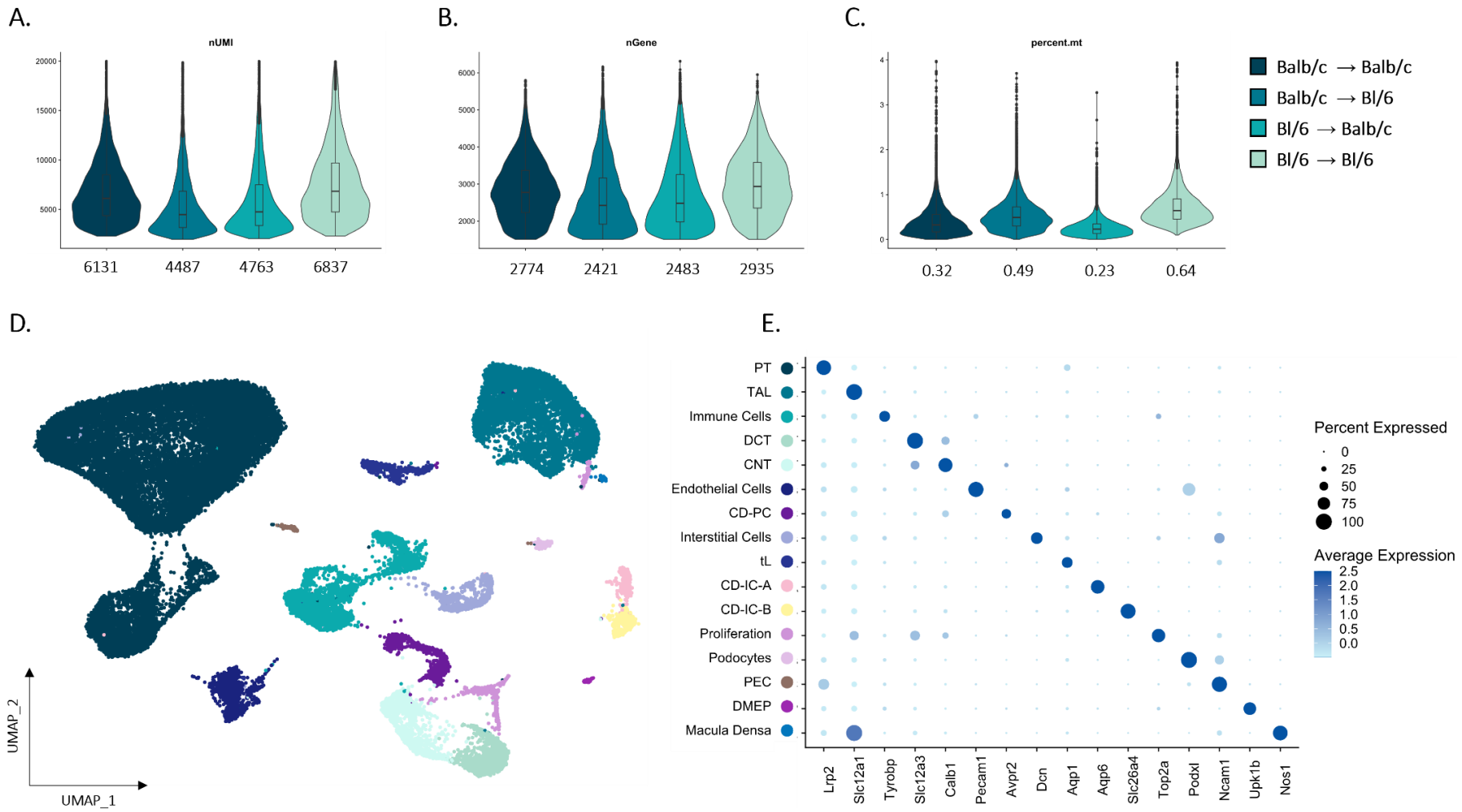

Figure 43: Single-nucleus RNA-sequencing.

(A, B, C) Distribution and median of the number of transcripts (measured by unique molecular identifiers (nUMI)) and genes (nGene), as well as percentage of mitochondrial RNA detected per nucleus in pooled samples of syngeneic and allogenic transplanted mice (n = 1-3 each). The numbers below plots correspond to the median. Nuclei with more than 5 % of mitochondrial RNA were excluded prior to analysis. **(D)** UMAP of summarized clusters (40,299 nuclei, n = 8). **(E)** Expression of cell type-specific marker genes. The dot colour indicates the average expression (scaled values) across the cells within each cell type, and the dot size represents the percentage of cells expressing the respective gene within each cell type (n = 8). PT – proximal tubule, TAL – thick ascending limb, DCT – distal convoluted tubule, CNT – connecting tubule, CD-PC – collecting duct principal cells, tL – thin limb, CD-IC – collecting duct intercalated cells, PEC – parietal epithelial cells, DMEP – deep medullary epithelium of pelvis. C57Bl/6 = Bl/6.

Analysis of the distribution of detected cell types in all four different kidney transplantation groups, revealed proximal tubules as the most abundant cell type (**Figure 44**), followed by TAL as second most abundant and macula densa as least frequent cell type. Immune cells constituted the third most predominant cell type, albeit, as anticipated, exclusively in the allogeneic transplantation groups.

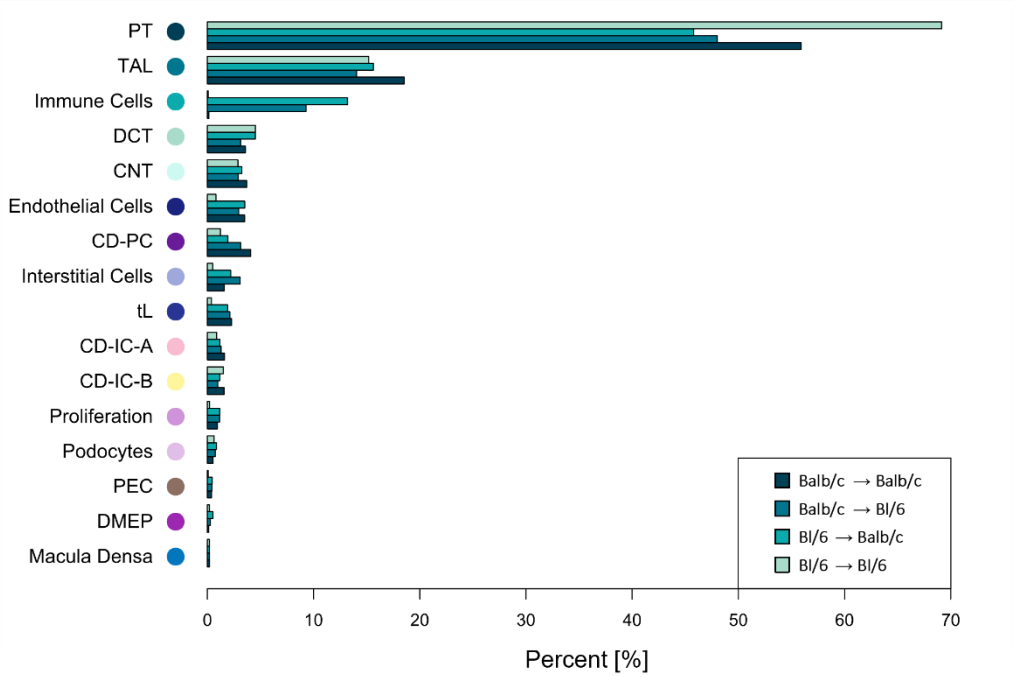

Figure 44: Frequencies of summarized cell types after murine kidney transplantation.
Bar plot representing the freqencies of various identified kidney cell types in the four different kidney transplantation settings, with proximal tubules being the most abundant cells. PT – proximal tubule, TAL – thick ascending limb, DCT – distal convoluted tubule, CNT – connecting tubule, CD-PC – collecting duct principal cells, tL – thin limb, CD-IC – collecting duct intercalated cells, PEC – parietal epithelial cells, DMEP – deep medullary epithelium of pelvis. C57Bl/6 = Bl/6.

Subsequent expression profiling of Lcn2 and its receptor *Lrp2*, as well as the injury-related marker gene Havcr1 (**Figure 45A**), revealed an ubiquitous expression of Lcn2 across various cell types, apart from proximal tubules, collecting duct intercalated cells (CD-IC), and podocytes, where its expression was notably absent. The strongest expression of Lcn2 was observed in collecting duct-principal cells (CD-PC). *Lrp2* was highest expressed in proximal tubules, followed by parietal epithelial cells, and macula densa. Other cell types moderately expressed *Lrp2*, while other cell types such as TAL, immune cells, DCT, tL, and CD-IC did not show *Lrp2* expression. Conversely, expression of Havcr1 was restricted to proximal tubules (**Figure 45A**). Upon examining the expression of those three crucial markers across the four distinct transplantation groups, higher expression of Lcn2 was generally observed in the allogeneic transplantation groups, especially in CD-PC. Within the allogeneic groups, C57Bl/6 to Balb/c group demonstrated higher Lcn2 expression compared to the Balb/c to C57Bl/6 group in all the cell types, except PEC. In contrast, *Lrp2* exhibited its highest expression in PTs from syngeneic transplantation groups, albeit with a lower intensity in PTs from allogeneic transplantation groups.

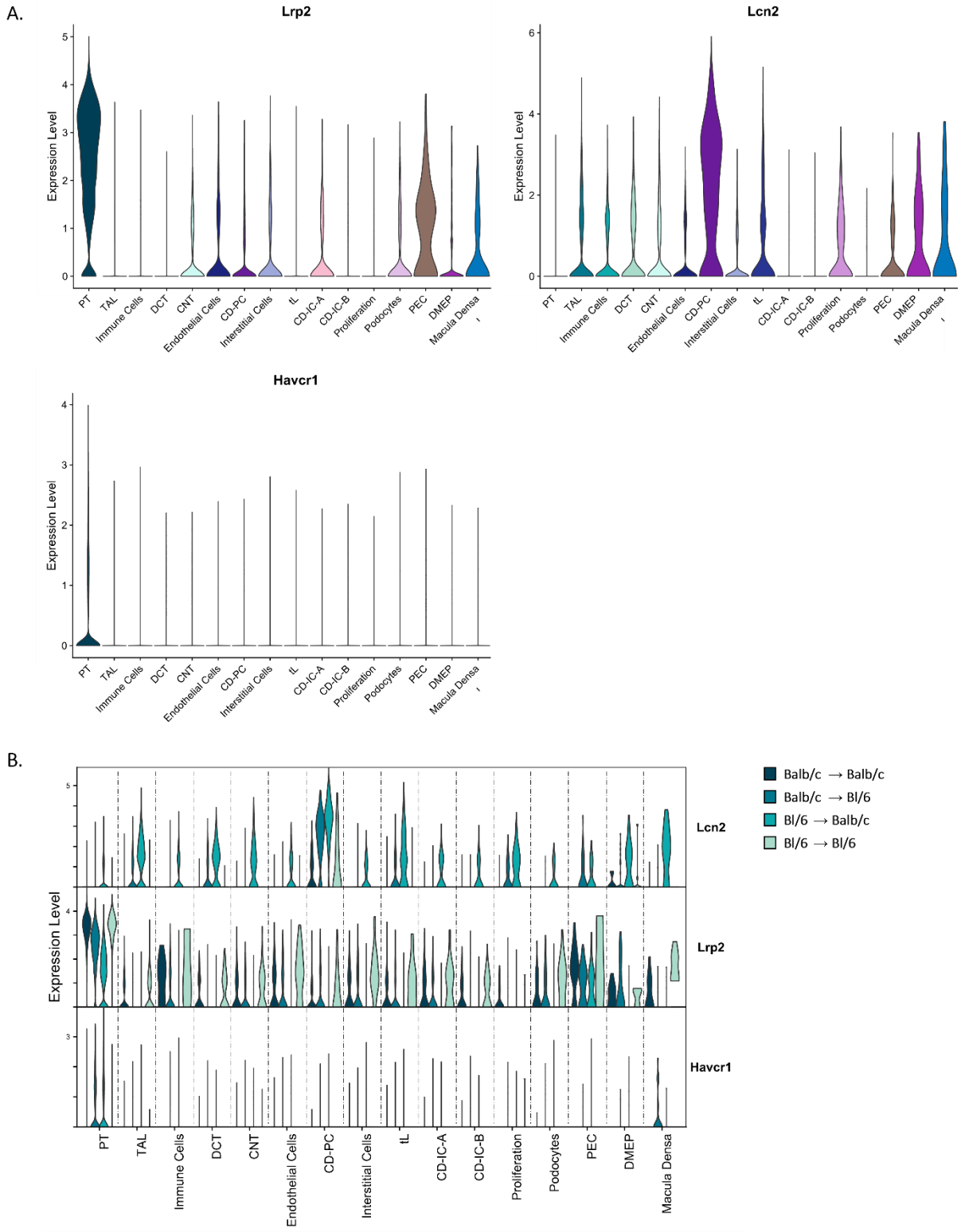

Figure 45: Violin plots of summarized cell types and injured cell markers.

(A) Expression of the receptor *Lrp2*, as well as the injury markers Lcn2 and Havcr1 across summarized cell types. *Lrp2* was highly expressed in proximal tubules, while Lcn2 was not expressed. Havcr1 was not expressed in any of the cell types, except in PTs. **(B)** Expression of *Lrp2*, Lcn2, and Havcr1 across summarized kidney cell types in different transplantation settings. PT – proximal tubule, TAL – thick ascending limb, DCT – distal convoluted tubule, CNT – connecting tubule, CD-PC – collecting duct principal cells, tL – thin limb, CD-IC – collecting duct intercalated cells, PEC – parietal epithelial cells, DMEP – deep medullary epithelium of pelvis. C57Bl/6 = Bl/6.

Notably, *Lrp2* expression was predominantly observed in cell types from syngeneic transplantation groups, with lower levels detected in the Balb/c to C57Bl/6 group. Additionally, Havcr1 displayed exclusive expression in PTs from allogeneic transplantation groups (**Figure 45B**). Overall percent expression of those selected genes in syngeneic and allogeneic murine kidney transplantation groups are listed in **Table S8**.

3.4.2 WITHIN THE PROXIMAL TUBULE ONLY INJURED PROXIMAL STRAIGHT TUBULES EXPRESS LCN2

Building upon the initial analysis of summarized cell types, we conducted an in-depth analysis of proximal tubule and immune cell subclusters, particularly focused on deciphering the expression patterns of *Lrp2*, Lcn2, and Havcr1. The obtained detailed insights into the expression profiles of these molecules, shed light on their roles within proximal tubule and immune cell subclusters.

Detailed analysis of the proximal tubule (PT) cluster revealed 10 distinct subclusters (**Figure 46A**). Notably, the frequencies of the subclusters vary between allogeneic and syngeneic transplantation groups. For instance, cluster 0 and cluster 3 were more abundant in allogeneic transplantation groups, and cluster 7 and 9 were not detectable in syngeneic transplantation groups.

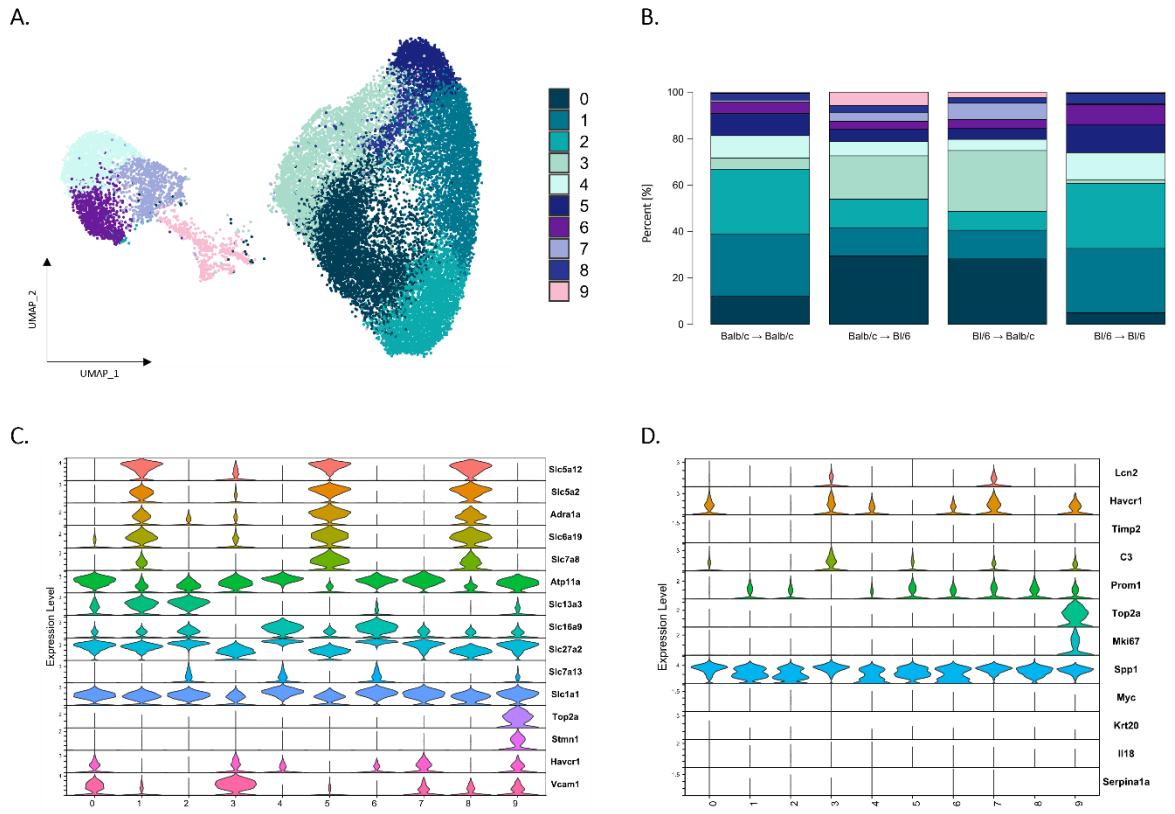

Figure 46: Detailed analysis of the proximal tubule cluster.
(A) UMAP of the re-analysed proximal tubule cluster showing 10 different subcluster. **(B)** Bar plot depicting the frequencies of the subclusters in the four performed transplantation settings. **(C)** Violin plot illustrating the expression of candidate proximal tubule markers and proliferation markers, while **(D)** shows the expression of various injury-related markers across the subclusters. Marker expression tested for: proximal convoluted tubule (PCT): Slc5a2, Slc5a12, Adra1a, Slc6a19, Slc7a8; proximal straight tubule (PST): Atp11a, Slc13a3, Slc16a9, Slc27a2, Slc7a13, Slc1a1; proliferation: Top2a, Stmn1; failed repair: Vcam1. C57Bl/6 = Bl/6.

On the other hand, clusters 1, 2, 4, 5, 6 and 8 were higher in abundance in syngeneic transplantation groups. Within the allogeneic transplantation groups, cluster 2, 4, and 9 were more frequent in Balb/c to C57Bl/6, and clusters 3 and 7 were more frequent in C57Bl/6 to Balb/c transplantation groups. Comparing the two syngeneic groups, clusters 0 and 3 were more abundant in Balb/c to Balb/c transplantation groups, while clusters 1, 4, 5, 6 and 8 were more abundant in C57Bl/6 to C57Bl/6 transplantation groups (Figure 46B). Percent expression of PT subclusters from syngeneic and allogeneic transplantation groups are listed in (Supplementary Table S9).

For cell type identification represented by those 10 distinct subclusters, validated marker gene expressions were measured, including markers related to injury (Figure 46C, D). Clusters 1, 5 and 8 were identified as healthy proximal convoluted tubules (PCT), based on their expression of markers such as Slc5a2, Slc5a12, Adra1a, Slc6a19, and Slc7a8. Clusters 2, 4, and 6 expressing Atp11a, Slc13a3, Slc16a9, Slc27a2, Slc7a13, and Slc1a1 were identified as proximal straight tubules (PST). High expression of proliferation markers Top2a, MKi67, and Stmn1, along with the expression of markers for PST, cluster 9 was identified as PST-Proliferation. Apart from the expression of PST markers, cluster 0, 3 and 7 additionally expressed injury-related markers Lcn2, Havcr1, C3, and Vcam1 (linked to failed repair), and were thus identified as PST-Injury.

Subsequent expression profiling of Lcn2 and its receptor *Lrp2*, as well as the injury-related marker gene Havcr1 on the PT subclusters (Figure 47A), revealed a ubiquitous expression of *Lrp2* across all PT subclusters, while Lcn2 was only moderately expressed in clusters 3 and 7. Havcr1 expression was hardly detectable in clusters 1, 2, 5, and 8. Splitting the expression of those markers according to transplantation groups demonstrated that Lcn2 expression was only detectable in C57Bl/6 to Balb/c transplantation groups in every subcluster (Figure 47B). Other transplantation groups did not express Lcn2. *Lrp2* expression was measured in each of the four transplantation groups and in all subclusters. The level of expression reached its peak in the syngeneic transplantation groups, while it was at its nadir in the C57Bl/6 to Balb/c transplantation groups. The predominant detection of Havcr1 expression was observed within the allogeneic transplant groups and among the previously delineated subclusters. Notably, Havcr1 expressions originating from Balb/c to Balb/c transplantation groups were solely detected in clusters 3, 4, 6, and 9. Cluster 7 stands as the exclusive entity encompassing Havcr1 expression originating from all four transplantation groups (Figure 47B).

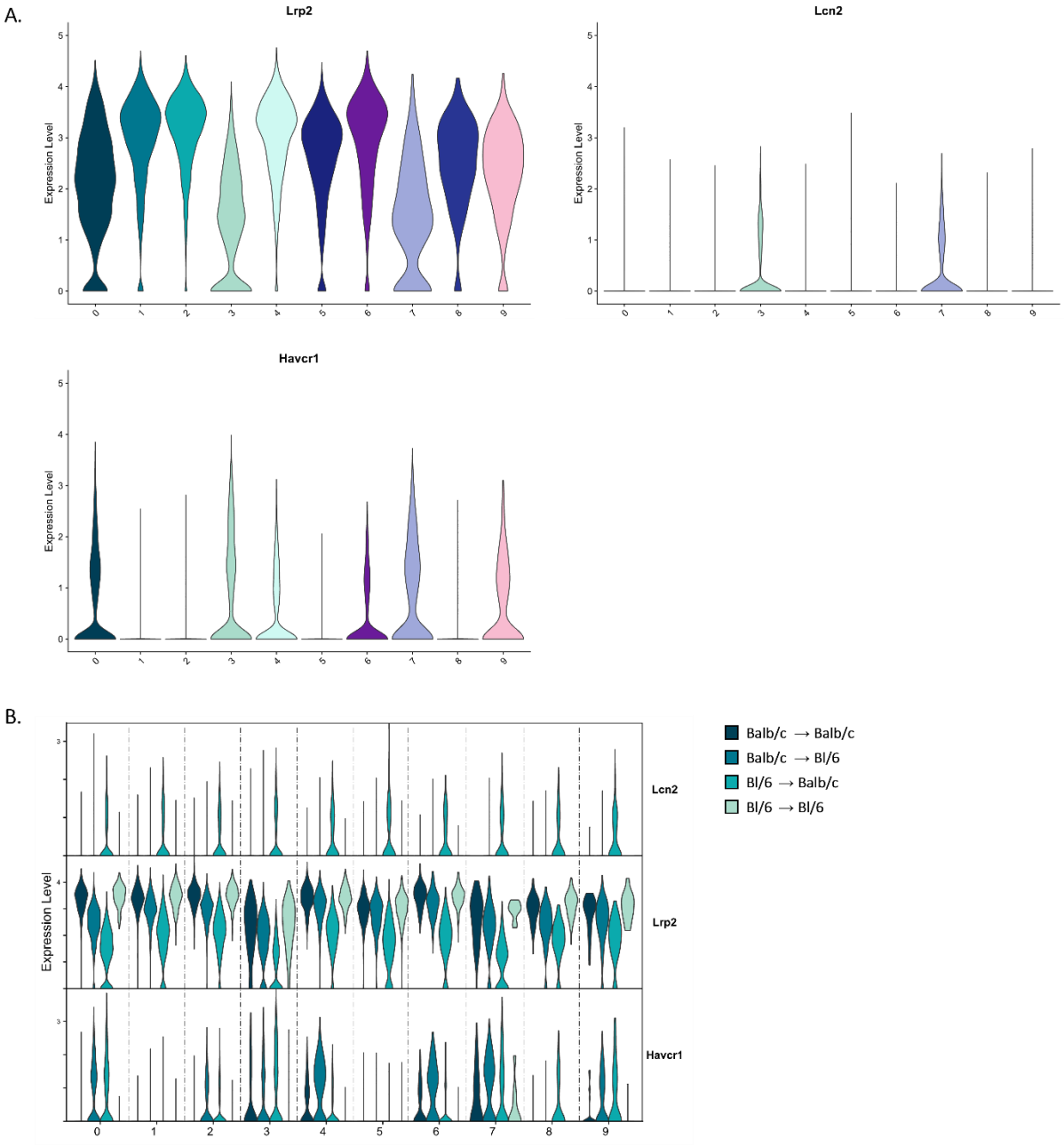

Figure 47: Proximal tubules (PT) subcluster gene expression.
(A) Violin plots depicting the expression of the receptor *Lrp2*, as well as the injury marker Lcn2 and Havcr1 across PT subcluster. **(B)** Stacked violin plot showing the expression of *Lrp2*, Lcn2, and Havcr1 across PT subcluster in different transplantation settings. C57Bl/6 = Bl/6.

Next, we proceeded to succinctly summarize the respective subclusters of the proximal tubules, culminating in the identification of four distinct subgroups: proximal convoluted tubules (PCT; clusters 1, 5, 8), proximal straight tubules (PST; clusters 2,4,6), PST-Injury (clusters 0, 3, 7), and PST-Proliferation (cluster 9), as depicted in **Figure 48A**. Segregated based on transplantation groups, the occurrence of injured PST was most prevalent in the allogeneic transplantation groups, with the highest abundance observed in the C57Bl/6 to Balb/c group, as delineated in **Supplementary Table S10**. These observations are in line with the finding from the graft function, graft survival, and histological analyses (as described in the beginning of section **3.4**). In contrast, both PCT and PST displayed a higher frequency in the

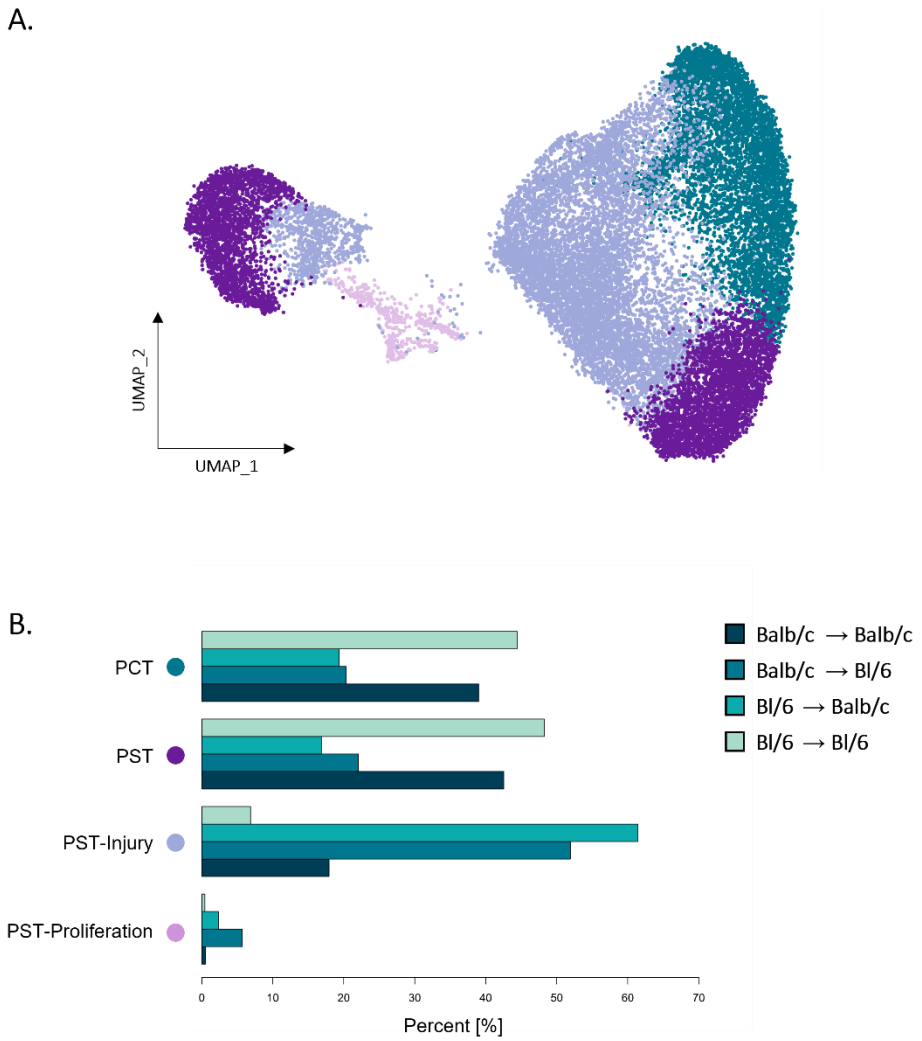

Figure 48: Summarized proximal tubule subclusters.
(A) UMAP illustration of the summarized proximal tubule clusters. Colours of the different cell types correspond to the ones used for the respective cell types depicted in B. **(B)** Bar plot showing the celltype frequencies of summarized cell types within the proximal tubule cluster seperated by the four different transplantation settings. The highest amount pf injured PST cells was found in C57Bl/6 to Balb/c transplanted mice. PCT –proximal convoluted tubule, PST –proximal straight tubule. C57Bl/6 = Bl/6.

syngeneic transplantation groups when compared to the allogeneic transplantation groups. Proliferating PST were generally low-frequent, although their highest frequency was observed within the allogeneic transplantation groups.

As a next step, gene expression profiling was performed to investigate the activity of Lcn2, *Lrp2*, and Havcr1 in summarized PT subclusters (**Figure 49A**). *Lrp2* exhibited widespread expression, while Havcr1 was found in the PST-Injury and PST-Proliferation subclusters. In contrast, Lcn2 expression was only observed in the PST-Injury subcluster. Additionally, Lcn2 expression was ubiquitously present in all subclusters, but restricted to the C57Bl/6 to Balb/c transplantation group (**Figure 49B, C; Supplementary Table S11**), suggesting that injured PST cells derived from this specific transplantation group may serve as a source for endogenous Lcn2 production following injury. *Lrp2* expression was detected in all transplantation groups and subclusters, with the highest levels observed in the syngeneic

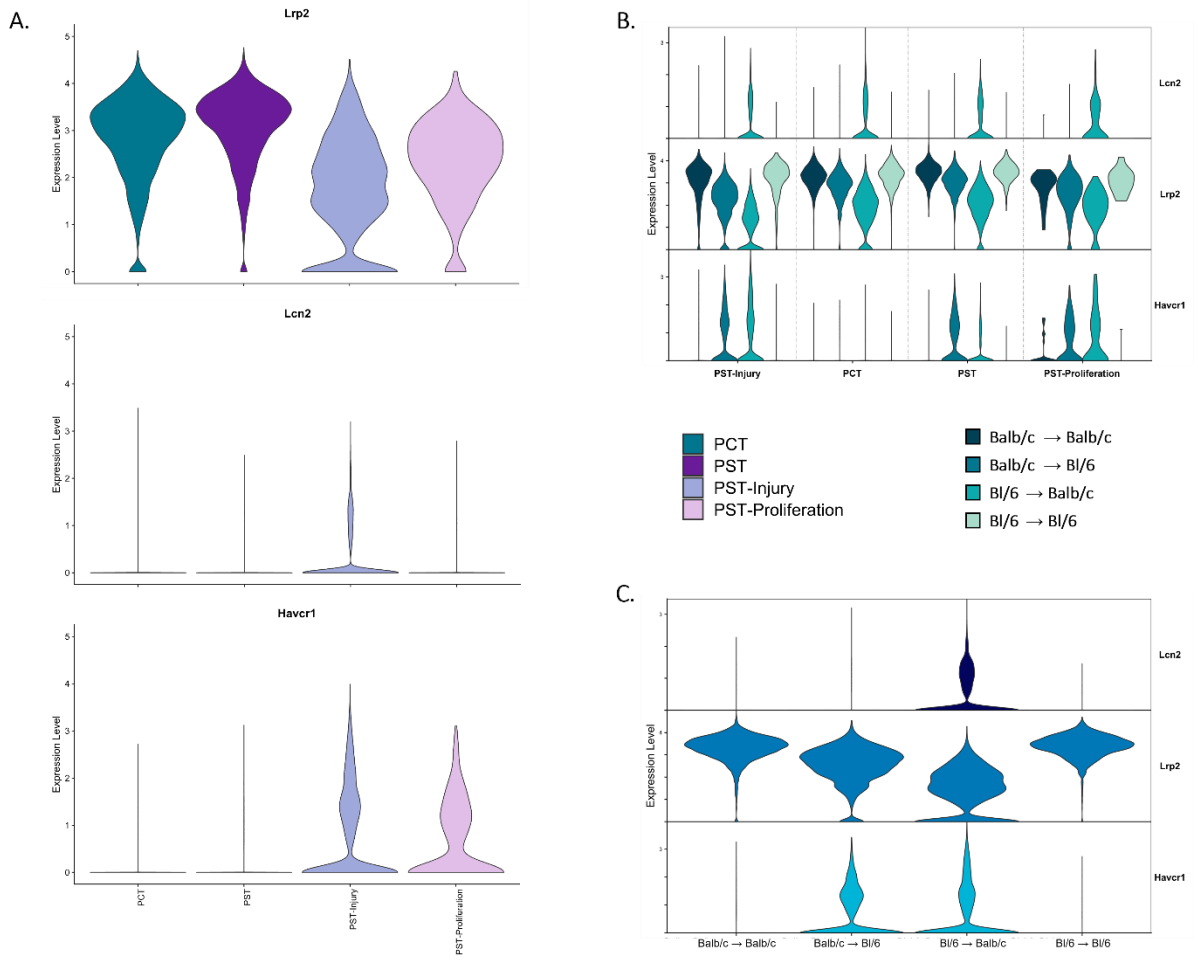

Figure 49: Gene expression in summarized proximal tubules (PT) subclusters.
(A) Violin plots depicting the expression of thr receptor *Lrp2*, as well as the injury marker Lcn2 and Havcr1 across summarized PT subclusters. **(B)** Stacked violin plot depicting the expression of *Lrp2*, Lcn2, and Havcr1 across the summarized PT subclusters separated by transplantion settings. **(C)** Stacked violin plot showing the expression of *Lrp2*, Lcn2, and Havcr1 across different transplantation settings. PCT –proximal convoluted tubule, PST –proximal straight tubule. C57Bl/6 = Bl/6.

transplantation groups. Conversely, Havcr1 expression was predominantly observed in the allogeneic transplantation groups, with only minimal expression detected in cells from the PST-Proliferation cluster of the Balb/c to Balb/c transplantation group.

3.4.3 MOST OF THE ANALYSED IMMUNE CELL TYPES EXPRESS LCN2

Meticulous examination of the immune cell cluster revealed the presence of 12 distinct subclusters, characterized by notable variations between the allogeneic and syngeneic transplantation groups (**Figure 50A, B**). While the syngeneic transplantation groups exhibited two to four frequently occurring subclusters, the allogeneic transplantation groups displayed a more diverse composition of immune cell subclusters. The two syngeneic transplantation groups also exhibited some differences in composition, with cluster 0 being the most abundant in both groups, albeit slightly more prevalent in the Balb/c to Balb/c transplantation group. The C57Bl/6 to C57Bl/6 group consisted solely of clusters 0 and 9, whereas the Balb/c to Balb/c transplantation group additionally exhibited clusters 8 and 10.

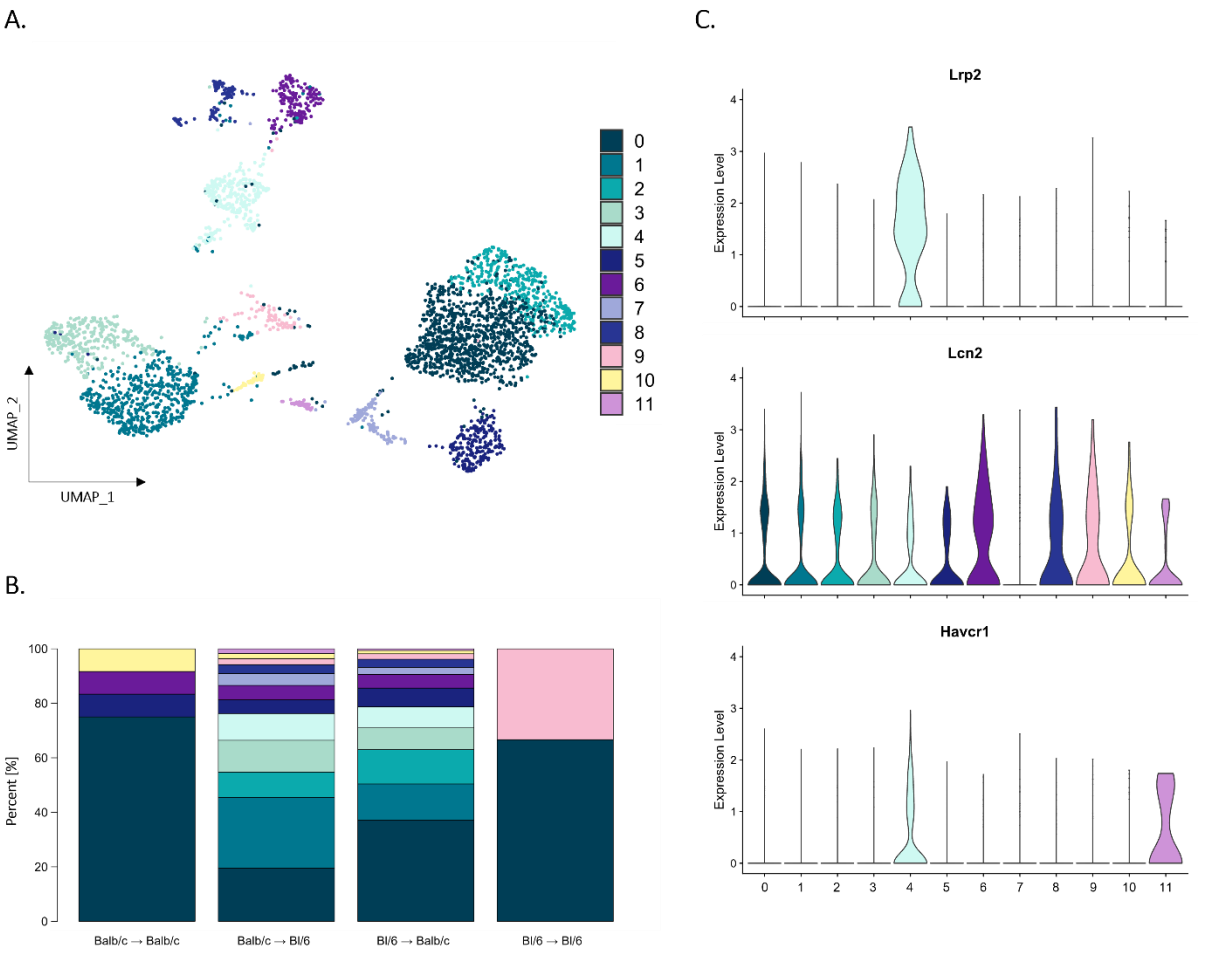

Figure 50: Detailed analysis of the immune cell cluster.
(A) UMAP plot after detailed analysis of the immune cell cluster showing 12 different subclusters. **(B)** Bar plot showing the immune cell subcluster frequencies separated according to the respective transplantation settings. Allogenic transplantation groups revealed a more distinct immune cell composition, whereas syngeneic transplantation groups comprised of only two or four immune cell subcluster. **(C)** Violin plots depicting the expression patterns of *Lrp2*, Lcn2 and Havcr1 across the 12 subclusters. C57Bl/6 = Bl/6.

Despite having a similar immune cell subcluster composition, the allogeneic transplantation group C57Bl/6 to Balb/c displayed a higher abundance of cluster 0 and a lower abundance of cluster 1 compared to the Balb/c to C57Bl/6 transplantation group (**Figure 50B**). Percent expression of immune cell-subclusters from syngeneic and allogeneic transplantation groups are listed in **Supplementary Table S12**. Further analysis of the expression profiles of the key marker genes in this study, namely *Lrp2*, Lcn2, and Havcr1, within the immune cell subclusters revealed that *Lrp2* expression was restricted to a specific subcluster (subcluster 4), while Lcn2 was expressed in nearly all immune cell subclusters, except subcluster 7. The highest expression of Lcn2 was detected in clusters 6, 8, and 9, followed by a moderate expression in clusters 0, 1, 2, and 3. Clusters 4, 5, and 11 had the lowest Lcn2 expression, while in cluster 7 Lcn2 was not detectable. Havcr1, on the other hand, was only expressed in subclusters 4 and 11 (**Figure 50C**).

To identify the specific immune cell types represented by these subclusters, the *FindMarkers* function of the Seurat package in R was utilized to identify marker genes alongside validated marker genes from online databases [86-88]. In addition to proliferation markers, such as Top2a, Mki67, and Stmn1, the expression profiles of immune cell-specific markers and markers associated with injury were explored (**Figure 51**).

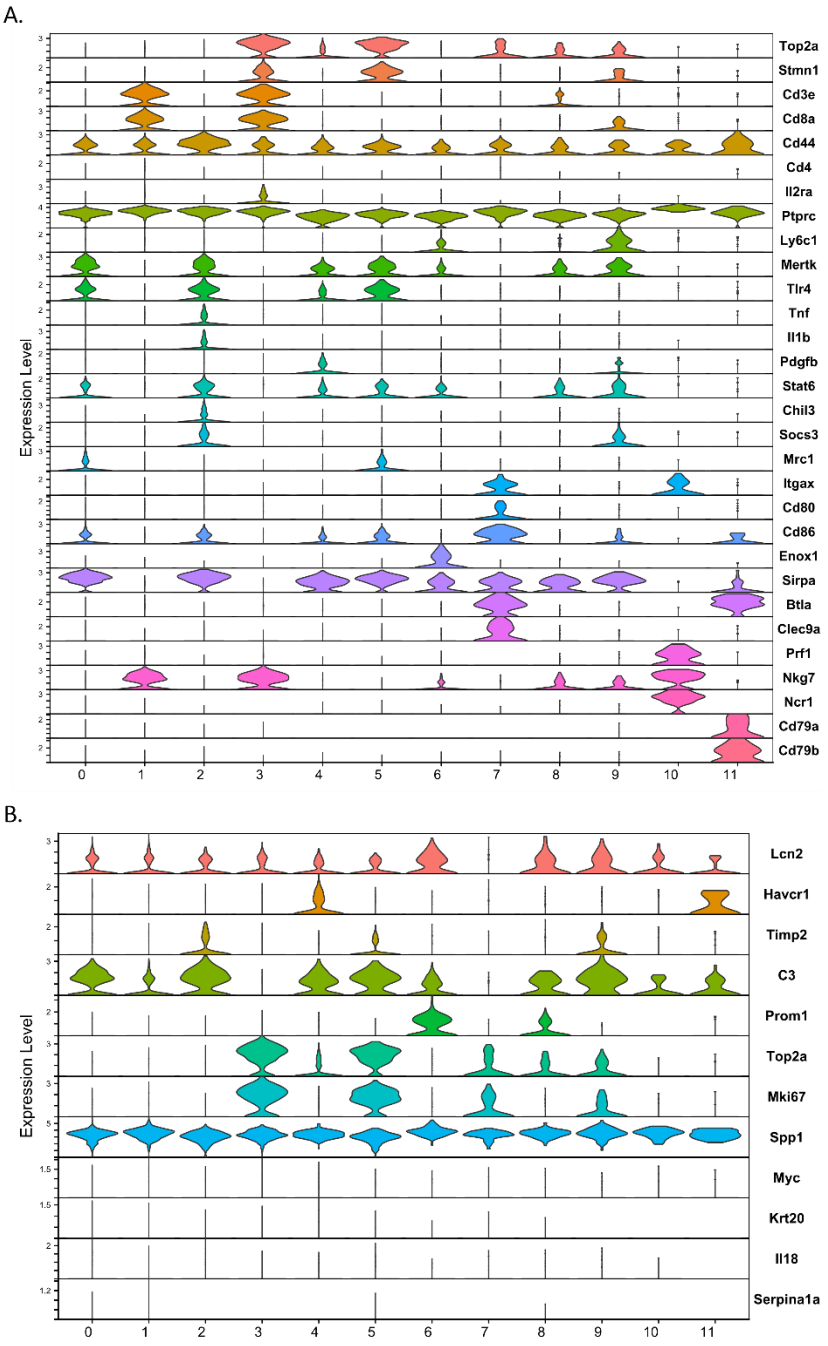

Figure 51: Candidate immune cell marker gene expression in immune cell subclusters.
(A) Violin plot illustrating the expression of candidate immune cell markers and proliferation markers, while **(B)** shows the expression of various injury-related markers across the subclusters. The following markers were tested: Proliferation –Top2a, Stmn1; T cells – CD3e; cytotoxic T cells – CD8a; helper T cells – CD4; active T cells – Il2ra; memory T cells – CD44; Macrophages – Ptprc, Ly6c1, Mertk; M1 Macrophages – Tlr4, Tnf, Il1b; M2 Macrophages – Pdgfb, Stat6, Chil3, Socs3; Macrophage/Dendritic cells – Mrc1, Itgax; Dendritic cells – CD80, CD86, Enox1, Sirpa, Btla, Clec9a; NK cells – Prf1, Nkg7, Ncr1; B cells – CD79a, CD79b.

Clusters 0 and 2 were identified as macrophages, exhibiting overall markers for macrophages, including those associated with M1 and M2 polarization, making it challenging to differentiate between M1 and M2 states. Therefore, those clusters were identified as Polarizing M1/M2 macrophages. Expressing markers such as Stat6 for instance, clusters 2, 4, and 8 were designated as M2 macrophages. Subcluster 5, which also expressed the proliferation markers Top2a and Stmn1, was designated as Macrophages—Proliferation. Clusters 1 and 3 were designated as T-cells based on the expression of markers such as CD3e, CD8a, and CD44. Cluster 3 additionally expressed the T-cell marker Il2ra and proliferation markers, earning it the designation of T-cells—Proliferation. Cluster 6, which expressed markers associated with macrophages, dendritic cells, and cellular stress (such as C3 and Prom1), was identified as a stressed intermediate state of DC/macrophages. Cluster 7 was identified as active, mature dendritic cells based on representative cell type markers, cluster 10 as NK cells, and cluster 11 as B cells.

Next, we summarized the respective subclusters of the immune cell cluster, which resulted in the identification of nine distinct subgroups: Polarizing M1/M2 macrophages (clusters 0, 2), macrophages—proliferation (cluster 5), M2 macrophages (clusters 2, 4, 8), stressed intermediate state dendritic cells/macrophages (cluster 6), T-cells (cluster 1), T-cells—proliferation (cluster 3), dendritic cells (cluster 7), NK cells (cluster 10), and B cells (cluster 11; Figure 52A).

Among the various transplantation groups, polarized M1/M2 macrophages emerged as the most prevalent immune cell types, irrespective of syngeneic or allogeneic transplantation (Figure 52B). However, the C57Bl/6 to Balb/c transplantation group displayed a comparatively lower abundance of these macrophages. Notably, the C57Bl/6 to C57Bl/6 group exhibited an absence of proliferating macrophages and stressed intermediate stage DC/macrophages, consequently resulting in the highest frequency of M2 macrophages within this group. As expected, T-cells, proliferating T-cells, dendritic cells, and B cells were exclusively detected in the allogeneic transplantation groups, whereas NK cells were found in minimal quantities in both allogeneic transplantation groups and the Balb/c to Balb/c transplantation group. Generally, immune cells from the C57Bl/6 to Balb/c transplantation group exhibited greater abundance compared to the Balb/c to C57Bl/6 transplantation group. Furthermore, the frequencies of proliferating macrophages, stressed intermediate stage DC/macrophages, dendritic cells, NK cells, and B cells remained below 10 % (Figure 52A; Supplementary Table S13).

Following, we additionally examined the gene expression of Lcn2, *Lrp2*, and Havcr1 in the summarized subclusters of immune cells (Figure 53A). *Lrp2* expression was exclusively detected in M2 macrophages, while Havcr1 expression was limited to M2 macrophages and B cells. Stressed intermediate state dendritic cells/macrophages showed the highest Lcn2 expression, followed by polarizing M1/M2 macrophages, M2 Macrophages, T-cells, and proliferating T-cells. Moderate Lcn2 expression was detected in proliferating macrophages, NK cells, and B cells. Dendritic cells did not

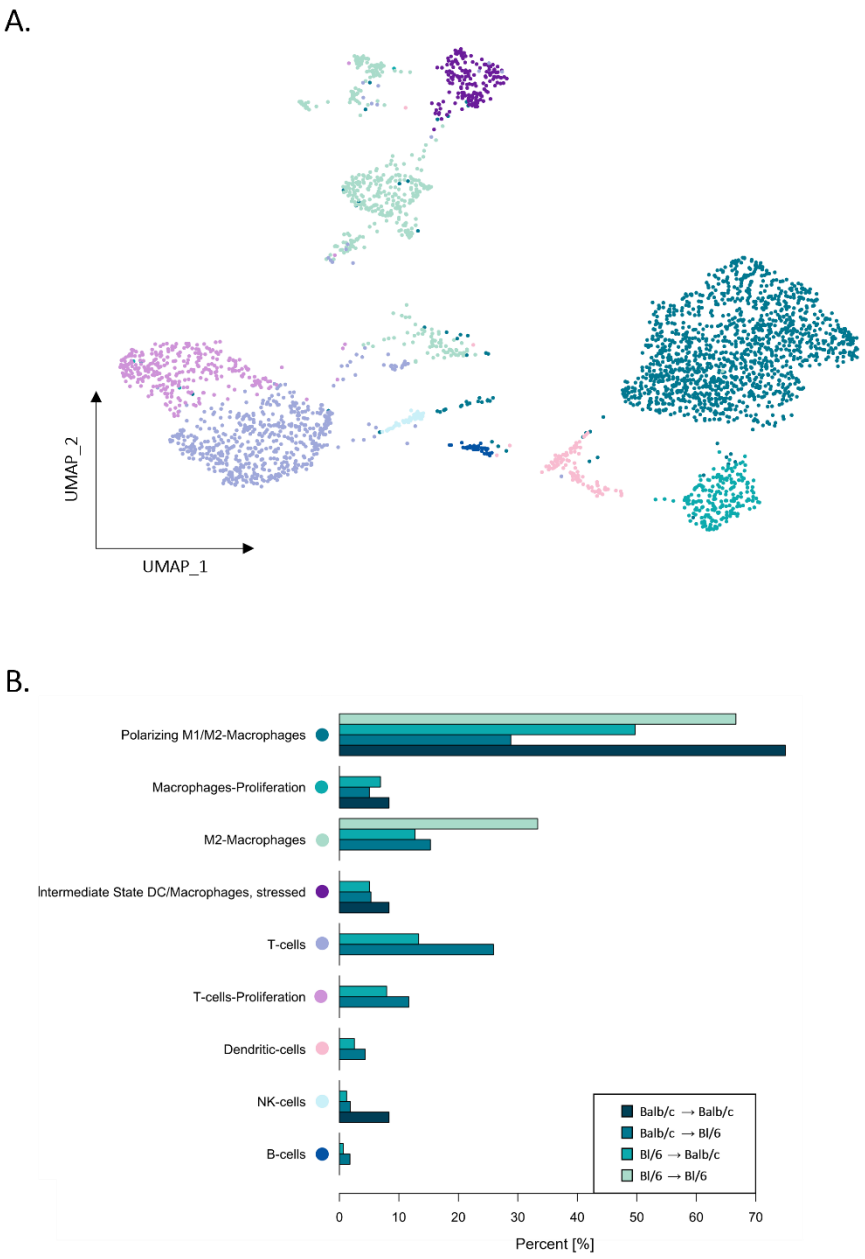

Figure 52: Summarized immune cell cluster.
(A) UMAP of summarized immune cell cluster. Colours of the different cell types correspond to the ones used for the respective cell types depicted in B. **(B)** Bar plot showing the celltype frequencies of summarized cell types within the immune cell cluster seperated by the four different transplantation settings. C57Bl/6 = Bl/6.

exhibit Lcn2 expression. The percentage expression of these marker genes can be found in **Supplementary Table S14**.

Consistent with the expression profile analysis of PT subclusters, Lcn2 expression predominantly originated from the C57Bl/6 to Balb/c transplantation group (**Figure 53A**). Solely proliferating T-cells expressing Lcn2 were additionally found to originate from the Balb/c to C57Bl/6 group. *Lrp2* expression was observed in polarizing M1/M2 macrophages, primarily from the syngeneic transplantation groups. Notably, the highest expression of *Lrp2* was identified in M2 macrophages from the allogeneic transplantation groups. Similarly, Havcr1 expression was exclusively detected in M2 macrophages and

B cells derived from the allogeneic transplantation groups (Figure 53B). Overall, the expression of Lcn2 was limited to the C57Bl/6 to Balb/c transplantation group, which interestingly did not exhibit *Lrp2* expression, except in M2 macrophages and B-cells. Conversely, *Lrp2* was expressed in the other three transplantation groups, with the highest expression observed in the C57Bl/6 to C57Bl/6 group and the lowest in the Balb/c to C57Bl/6 transplantation group. Havcr1 expression remained below the set threshold in all four transplantation groups (Figure 53C).

In summary, the analysis of cell type distribution in four kidney transplantation groups revealed proximal tubules as the most abundant cell type, while immune cells were the third most predominant cell type, mainly in allogeneic transplantation groups. Higher expression of Lcn2 was generally observed in allogeneic transplantation groups, particularly in the C57Bl/6 to Balb/c group. Lcn2 was predominantly expressed in injured PST and stressed intermediate state dendritic cells/macrophages, specifically in the C57Bl/6 to Balb/c group, suggesting that these cells may serve as a main source of endogenous Lcn2 following injury. *Lrp2* exhibited the highest expression in proximal tubules, followed by parietal epithelial cells and macula densa. Lrp2 expression in the proximal tubule cluster was predominant in cell types from syngeneic transplantation groups, but also in the allogeneic group (Balb/c to C57Bl/6), albeit to a lesser extent. Havcr1 expression was restricted to proximal tubules and was predominantly observed in allogeneic transplantation groups, particularly in injured proximal straight tubules (PST) and proliferating PST subclusters. This supports that Havcr1 is a marker for injury, specifically in proximal tubules, potentially associated with the transplantation process.

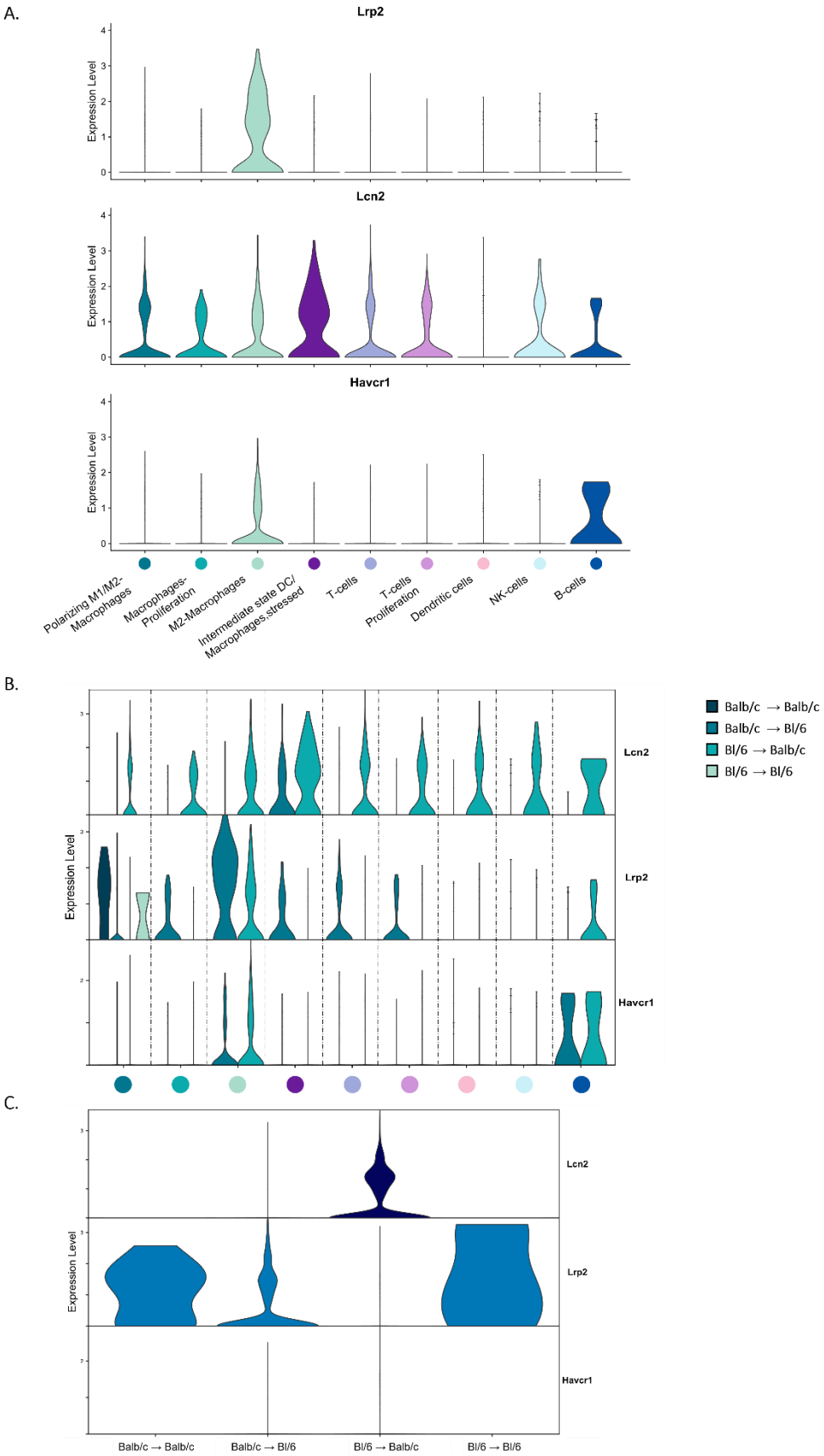

Figure 53: Detailed analysis of the immune cell subclusters.
(A) Violin plots depicting the expression of the receptor *Lrp2*, as well as the injury marker Lcn2 and Havcr1 across summarized immune cell subcluster. **(B)** Stacked violin plot showing the expression of *Lrp2*, Lcn2, and Havcr1 in immune cell subcluster across different transplantation settings. **(C)** Stacked violin plot showing the expression of *Lrp2*, Lcn2, and Havcr1 across different transplantation settings. C57Bl/6 = Bl/6.

4 DISCUSSION

In this study, we provide a detailed understanding of the immunomodulatory effects of rLcn2, highlighting its impact on immune cell populations. Using a murine kidney transplantation model, our findings demonstrate that perioperative administration of rLcn2 induces distinct alterations in both adaptive and innate immune cell populations. Moreover, we demonstrate that particularly the functionality and degranulation capacities of immune cells are significantly impacted by the rLcn2-treatment, especially in the kidney graft. Additionally, by utilizing a specific mT/mG*PEPCK-Cre mouse model, we present an effective method for isolating, enriching, and culturing primary proximal tubular epithelial cells (PTEC). Through scRNAseq analysis we identified two potential fates of cultured PTEC, characterized by differential gene expression patterns and variating regulation of signature signalling pathways. Furthermore, we have delineated the main cellular origins of Lcn2 expression, which include injured PST cells and stressed intermediate state dendritic cells/macrophages, specifically in the allogeneic C57Bl/6 to Balb/c transplantation setting.

4.1 rLCN2 MODULATES DISTINCT IMMUNE CELL POPULATIONS AND THEIR FUNCTIONALITY

Previous research has described that perioperative administration of rLcn2 to the recipient leads to notable functional and morphological improvements in allograft injury [17]. To investigate the molecular and cellular events underlying the renoprotective effects of rLcn2, we herein conducted comprehensive immunophenotypic analyses.

After allogeneic kidney transplantation at pod-3 and pod-7, our analysis has revealed that the effects of rLcn2-treatment on immune cell populations are tissue-specific and vary across different settings (spleen, lymph nodes, kidney graft, and blood). Moreover, we ascertained that rLcn2 does not exert a broad immunosuppressive effect, but rather elicits specific modulatory effects on selective immune cell populations.

Specifically, several types of adaptive and innate immune cell populations, including for instance effector memory T-and T_c-cells, neutrophils, and macrophages, significantly decreased in their abundance and activation following treatment with rLcn2.

Among adaptive immune cells, helper and cytotoxic T-cells are critical components in the host defence mechanisms. The regulation of immune responses, including the initiation of allograft rejection, is centrally orchestrated by T_h-cells, fostered through their ability to differentiate into various effector subsets, such as T_h1 and T_h17, that contribute to cytokine secretion, recruitment of other immune cells, and direct cytotoxic activities [175-177]. T_c-cells represent one of the most important populations when it comes to allograft rejection, as they induce programmed cell death in damaged or foreign cells, such as pathogens or graft cells [178]. Acute ischemic events lead to a dysfunctionality of the endothelium,

resulting in increased permeability and expression of several adhesion molecules responsible for the recruitment of effector cells into the tissue [179,180]. Effector memory T cells are memory cells that have encountered and responded to previous infections or antigens. However, in the context of organ transplantation, these memory T-cells can cause problems if they react against the donated organ's antigens, undermining the success of the transplantation process [181,182]. Thus, their decrease with rLcn2-treatment indicates a potential dampening of the memory immune response and that rLcn2 may play a role in modulating long-term immune memory, eventually leading to reduced tissue damage within the allograft.

In terms of innate immune cells, rLcn2-treatment led to significant reduction of neutrophils and certain macrophage populations in kidney grafts and lymph nodes, suggesting an influence on their recruitment or survival. Neutrophils, on the one hand, are the first line of defence in the immune system, eliminating pathogens through phagocytosis and releasing antimicrobial proteins. However, excessive neutrophil infiltration can lead to tissue damage and graft rejection [183,184]. The decrease in neutrophils suggests a reduction in their detrimental effects, possibly promoting graft survival. Macrophages, on the other hand, are versatile immune cells involved in both innate and adaptive immune responses, phagocytosing pathogens, presenting antigens to T-cells, and contributing to tissue repair [185-187]. The modulation of macrophage populations indicates a shift towards a more regulated immune response, promoting tissue healing and reducing the risk of graft rejection. Ly6C$^{intermediate\text{-}high}$ macrophages represent a specific subset of macrophages that are often associated with pro-inflammatory responses, as they produce inflammatory cytokines and contribute to the recruitment and activation of other immune cells [188,189]. The decrease in Ly6C$^{intermediate\text{-}high}$ macrophages indicates a potential shift towards a less pro-inflammatory macrophage phenotype. This modulation can help attenuate excessive inflammation, reduce tissue damage, and promote allograft survival.

Although the perioperative treatment with rLcn2 did not affect the pan NK cell populations, it did impact specific subsets, such as intermediate mature NK cells. NK cells provide rapid responses against infected or transformed cells and can directly kill target cells without prior sensitization [91]. Moreover, intermediate mature NK cells are known for a high cytokine release and killing capacity [190,191]. The decrease in intermediate mature NK cells suggests a potential modulation of NK cell activity, which can help maintain a balanced immune response and prevent excessive cytotoxicity that may lead to graft rejection. However, it should be noted that besides lowering above-mentioned innate immune cell populations, rLcn2-treatment concurrently stimulated other populations, such as eosinophils, indicating differential effects of the treatment on various immune cell populations.

Moreover, many of the immune cell populations whose dynamics varied with rLcn2-treatment, such as CD4$^+$, C8$^+$, and NKp46$^+$ cells, possess cytotoxic functions and the ability to recognize and

eliminate various types of target cells, including infected, injured, and even graft cells. These cells are characterized by their expression of molecules such as CD107a, IFNγ, Perforin, or NKG2D.

CD107a serves as a key indicator of NK cell degranulation and cytotoxic activity, while intracellular detection of IFNγ allows for assessment of their functional state [192-195]. Activated NK cells produce the cytokine IFNγ and release cytotoxic granules containing molecules like Perforin and granzymes to induce target cell death [196]. Perforin, stored within NK cell granules, is a cytotoxic molecule, and its intracellular expression can provide insight into the cytotoxic potential of NK cells [197,198]. NKG2D is an important receptor on NK cells and $CD8^+$ T cells, serving as an activating receptor that recognizes stress-induced ligands on target cells, triggers cytotoxicity and provides co-stimulatory signals for activation [199,200]. In NK cells, NKG2D signalling alone is sufficient to directly kill target cells. However, in $CD8^+$ T-cells, simultaneous activation of the T-cell receptor is required for NKG2D to be functional [97]. In conditions like IRI following kidney transplantation, NKG2D ligands are upregulated. Engagement of these ligands activates NK cells, provides T-cell co-stimulation, boosts T_c-cell mediated cytotoxicity, and serves as a link between innate and adaptive immunity during IRI [199-201]. Higher expression of NKG2D ligands is associated with rejection episodes and can contribute to graft loss [200]. Moreover, activated NK cells can trigger organ rejection through NKG2D, affecting the maturation of both donor and recipient antigen-presenting cells, ultimately impacting the alloreactive T-cell response [200]. Notably, activated T_h1 cells play a crucial role in coordinating immune responses and promoting inflammation [202,203].

Although the decrease of various immune cell populations may initially appear counterintuitive and suggest a reduction in cytotoxic capabilities, it points to a modulation of the immune response towards a more controlled and regulated state. Excessive cytotoxicity can lead to tissue damage and graft rejection, so a balanced immune response is crucial for allograft survival. Interestingly, *in vitro* experiments indicated that the effects on $CD8^+NKG2D^+$ cells were mediated indirectly rather than through direct interactions with rLcn2. Elucidating the underlying mechanisms would require identifying immune cell populations expressing receptors for Lcn2 and combining them with other cells like macrophages, dendritic cells, or neutrophils in cell culture experiments under Lcn2-treatment.

Despite the overall composition of immune cells did not substantially change on pod-3 compared to pod-7, the total cell counts of specific immune cell populations were significantly affected by the treatment with rLcn2 at this earlier time point. Total cell counts of immune cell populations from central memory T-cells, mature dendritic cells, macrophages, $Ly6C^{intermediate\text{-}high}$ macrophages, M2 macrophages, NK-cells, $CD8^+NKG2D^+$ cells, and most of the *ex vivo* activated immune cell subsets in kidney graft samples, were affected by the treatment at pod-3. Hence, processes leading to modifications in the immune cell composition by pod-7, were probably already initiated by pod-3.

However, it is important to note that total cell counts for pod-7 are not available, preventing a direct comparison of cell counts between time points.

Nevertheless, the decision to measure total cell counts at pod-3 contributed to assessing the immediate effects of the treatment on immune cell populations and their overall abundance. This early time point allowed for the detection of significant alterations or early changes in immune cell composition. In contrast, at pod-7, our focus shifted to analysing the relative frequencies of immune cells, rather than their total counts. This is because the later time point is more relevant for understanding the distribution and proportions of immune cell subsets, providing insights into changes over time. Moreover, measuring total cell counts at pod-3 serves as a baseline reference for identifying significant alterations observed at later time points. By establishing the initial cell counts, it becomes possible to evaluate the magnitude and direction of changes in immune cell populations following treatment with rLcn2, which is essential for assessing the impact of the treatment on the immune response. Thus, our findings convincingly show that the combination of both approaches promotes a more comprehensive, complementary understanding of immune cell dynamics enabling to assess disease progression, evaluate treatment efficacy, and examine cell-cell interactions and ratios within the immune system.

In summary, observed decreases in immune cell populations collectively contributes to improved allograft survival by attenuating detrimental effects to the graft such as inflammation and cytotoxicity. Their decrease indicates a potential modulation of the immune response towards a more regulated state, helping to maintain immune tolerance towards the allograft, attenuating inflammatory processes, and preventing an overactive immune response that might lead to graft rejection. Nonetheless, further studies are required to gain a comprehensive understanding of the specific mechanisms and functional implications of immune cell population changes in response to rLcn2-treatment over time. Exploring the functional consequences in more detail, such as the cells' ability to mount effective immune responses, can provide valuable insights into the implications of rLcn2-mediated immunomodulation. Additionally, conducting a thorough analysis of the temporal dynamics through a comprehensive time-course study can offer a more detailed understanding of immune cell alterations following rLcn2-treatment. Examining multiple time points, including earlier stages, may reveal additional insights into the kinetics of immune cell changes and help identify critical intervention windows.

4.2 CELL CULTURE OF PTEC REVEALS DECREASED *LRP2* EXPRESSION AND IMPAIRED rLCN2 UPTAKE IN SORTED PTEC

Proximal tubular epithelial cells (PTEC) have multiple functions and interactions in the kidney, including the production of chemokines and cytokines that contribute to the inflammatory response during allograft rejection and attracting immune cells, and can also interact with immune cells, influencing their activation and behaviour. Additionally, PTEC play a crucial role in reabsorbing essential nutrients, ions, and water from the glomerular filtrate, regulating electrolyte balance, maintaining acid-base balance, ensuring water retention, and participating in metabolic processes, making them particularly sensitive to ischemic injury [5,6,48-53,57].

To dissect the underlying molecular mechanisms and signalling pathways involved in the PTEC functionalities, we harnessed various methods to isolate primary PTEC from mice, including FACS, ultracentrifugation, and immunomagnetic separation, focusing on obtaining pure and viable cell populations. However, challenges were encountered in terms of cell viability, growth rate, and obtaining sufficient cell yield for subsequent molecular analyses. On the one hand, among the diverse isolation procedures, sorting with GFP microbeads achieved the highest purity of approximately 60 %, but these cells had slow growth rates and exhibited a flattened and elongated morphology. Over the course of cell culture, the cells displayed reduced cell densities, resulting in insufficient protein and RNA yields for further analyses. Similarly, RFP-antibody isolated PTEC displayed slow growth rates and drastic morphological changes, such as cellular shrinkage and the occurrence of cellular debris early on in culture. Deviations from their characteristic phenotypes and reduced growth rates represent first indicators of compromised cell viability, cellular stress, damage, or dedifferentiation [119]. On the other hand, prominin-1 sorting sufficiently enriched the PTEC population in culture, with cells reaching confluency within five days while maintaining the characteristic morphology, resembling the unsorted cell culture. Overall, this prominin-1 sorted cell culture had lower purity compared to GFP-sorted cell culture, highlighting the necessary trade-offs between purity, growth characteristics, and healthy culturing conditions for further analyses. Nonetheless, as described by *Van der Hauwaert et al.*, 2013 [204], the use of primary cultured cells to study renal epithelial functions is justified due to their ability to retain phenotypic characteristics and specific functions, such as hormonal responses and transport systems, which closely resemble the *in vivo* human nephron at the physiological level. Unlike immortalized cell lines that tend to dedifferentiate and lose tubule-specific characteristics, primary cultured cells provide a more accurate representation of renal epithelial behaviour, allowing for a better understanding of their functions and responses in a physiologically relevant context [204,205].

Over the past decades, several challenges in culturing human and murine PTEC have been described [204,206-211]. Not only have PTEC been described to gradually lose the differentiated functions in primary culture and early exhibit signs of apoptosis [209,212], but they have also been observed to lose their

phenotypic properties after passaging [207,213]. However, the purity of established primary proximal tubular epithelial cell cultures obtained through various applied isolation techniques was never doubted [105,106,131,204,207,210,211,214]. Our culturing strategies have shown that cell growth in pure cultures of PTEC is not supported, but rather that growth in mixed colonies of GFP^+ and $tdTomato^+$ cells is favoured, indicating potential interactions, and signalling crosstalk between PTEC and adherent other cell types. Only this environment led to distinct cellular arrangements and proper growth of cells. Furthermore, the limited proliferative capacity of isolated PTEC in our different cultivation approaches, especially in the unsorted culture of PTEC, added to the difficulty of successfully maintaining pure cultures. These observations underscore the importance of understanding the behaviour and dynamics of primary PTEC in culture, as it provides insights into the physiological and pathological processes within the renal proximal tubules. Additionally, 2D monolayer cultures of renal epithelial cells have been described to reduce lifespan and functional specialization, possibly due to the absence of fluidic mechanosensory stimuli in the *in vivo* proximal tubule environment [207,215].

Moreover, *Wagner et al.*, 2003 [208], expressed concerns about the suitability of proximal tubule PTEC for long-term *in vitro* studies. They found that microdissection of proximal tubule segments from mice kidneys resulted in higher susceptibility to membrane damage compared to other nephron segments, suggesting potential initiation of cellular trans- or dedifferentiation.

Cell dedifferentiation is characterized by the enhanced expression of Vimentin, which is a marker of mesenchymal cells [206,216]. Additionally, strongly upregulated Lcn2 in damaged nephron epithelia indicates cellular stress and injury [35-37]. In our study, we detected the expression of Lcn2 and Vimentin from as early as 3 days in cultured cells. Furthermore, we observed an increase in the expression of Acta2, a marker for α-smooth muscle cells [110], after 6 days of cell culture, along with a decrease in the epithelial cell marker Cdh1 [109]. These changes indicate the initiation of processes like epithelial-mesenchymal transition (EMT), where cells lose their epithelial characteristics and acquire mesenchymal properties, which is often linked to tissue remodelling or fibrosis [217].

The reduced expression of epithelial and specific PTEC markers suggests a potential alteration or impairment in the cellular phenotype and function of the sorted PTEC. This can significantly impact the reliability and validity of subsequent analyses and experiments conducted on these cells. Moreover, the significant increase in Acta2 expression in prominin-1 sorted PTEC suggests a phenotypic shift or activation towards a smooth muscle-like state, potentially indicating a fibrogenic response. Furthermore, both RT-qPCR and RNAscope *in situ* hybridization revealed a decrease in the expression of *Lrp2*, which is the receptor for Lcn2 [218]. This reduction in *Lrp2* expression leads to a diminished uptake of rLcn2, thereby impairing the protective effect of rLcn2 on PTEC. However, it is important to consider that differences in the sensitivity and detection limits of these techniques may contribute to variations in observed expression levels.

The loss of epithelial markers and receptors in sorted PTEC could be influenced by various factors, including the sorting procedure itself, prolonged cell culture duration, or the absence of crucial factors or signalling molecules present in the native microenvironment of PTEC. During the sorting process, exposure to sorting buffer may alter nutrient concentrations or the availability of growth factors. Disruption of cell-cell interactions during sorting can affect paracrine signalling and nutrient/growth factor exchange between neighbouring cells. Additionally, the sorting process may result in the loss of certain cell populations or alter the distribution of specific cell types, indirectly affecting nutrient availability or growth factor signalling within the sorted cell population.

For future studies, optimization of cell culture and sorting procedures is required. Fine-tuning the sorting conditions, such as buffer composition, temperature, and sorting speed, can help minimize the impact on cell viability and marker expression. It is important to find a balance between efficient sorting and minimizing cellular stress. Moreover, providing PTEC with a culture environment that closely resembles their native microenvironment can help maintaining their phenotype. This can include using specialized culture media, growth factors, and extracellular matrix components that mimic the conditions found in the kidney [65,219-222]. Other strategies could include an establishment of co-culture systems where sorted PTEC are cultured alongside supportive cell types, such as endothelial cells or fibroblasts, to provide a more physiologically relevant environment [223,224]. The presence of these cells can enhance paracrine signalling and provide important factors for maintaining PTEC phenotype. Additionally, culturing sorted PTEC in three-dimensional culture systems, such as hydrogels or organoid cultures [220,225], could better mimic *in vivo* conditions, by providing a more structurally and functionally relevant environment, which may help maintain marker expression.

All in all, further investigations are necessary to better understand the underlying mechanisms responsible for the observed marker loss and to identify strategies to mitigate or overcome challenges in culturing to obtain even more representative PTEC populations.

4.3 rLCN2 DOES NOT ALTER SIGNALLING PATHWAYS *IN VIVO* NOR *IN VITRO*.

Understanding the impact of rLcn2-treatment on signalling pathways is a crucial aspect, as it illuminates the molecular mechanisms through which rLcn2 influences cellular function and aids in the identification of key molecular players and signalling cascades that mediate the cellular response to Lcn2. This knowledge can contribute to a deeper understanding of the biological processes and cellular functions regulated by Lcn2, particularly in the context of tissue injury and inflammation after kidney transplantation. As the sorting of cells with anti-prominin-1 microbeads resulted in sufficiently enriched PTEC cell suspensions and the culturing of those cells did not alter their morphology over time, we analysed various stress, inflammatory, and survival signalling pathways on both cultured PTEC as well as on tissue samples from kidney grafts. However, in none of the *in vitro* and *in vivo* multiplex signalling

pathway analyses, we could fully elucidate the dynamics of rLcn2 uptake in PTEC under specific hypoxia/reoxygenation or ischemia/reperfusion conditions.

In brief, the analyses of multiple signalling pathways revealed distinct patterns with some proteins showing lower phosphorylation levels with rLcn2 administration. Importantly, the overall analysis did not find significant effects of rLcn2-treatment on the analysed pathways during hypoxia/reoxygenation or prolonged cold ischemia-reperfusion conditions, except for the ERK1/2 pathway *in vitro*. Moreover, no significant differences were observed in kidney graft function between the rLcn2-treated and untreated groups, as measured by serum creatinine and urea levels.

Missing effects following rLcn2-treatment on the investigated signalling pathways and mRNA expression suggests that the renoprotective effects of rLcn2 may operate through alternative mechanisms. These signalling pathways are part of a complex regulatory network involved in stress, inflammation, and survival responses. The lack of response to rLcn2 suggests that effects on renal protection may be mediated through intricate interactions within this network, bypassing the specific nodes targeted by the signalling assays. Moreover, the absence of treatment effects *in vitro* can likely be attributed to the observed loss of *Lrp2*, which is responsible for the uptake of rLcn2 into cells. This suggests that the protective effects of rLcn2 on PTEC via *Lrp2*-mediated intake could not occur. Additionally, the strong indication of ongoing trans- or dedifferentiation processes, accompanied by morphological and functional changes, supports the hypothesis that these cellular transformations contribute significantly to the absence of treatment effects. These processes may alter the responsiveness of cells to the treatment or interfere with the signalling pathways involved, making them less susceptible to the protective effects of rLcn2.

In this context, the significant reduction of phosphorylation on the ERK1/2 is noteworthy. ERK1/2 is a part of the mitogen-activated protein kinase (MAPK) signalling pathway, which plays a crucial role in transmitting signals from the cell surface to the nucleus, regulating various cellular processes such as cell growth, proliferation, differentiation, and survival. The phosphorylation of ERK1/2 typically leads to its activation and subsequent activation of downstream targets involved in cell proliferation and survival [226-230]. Subjecting cells to 24 hours of hypoxia followed by 6 hours of reoxygenation, significantly decreased phosphorylation of the ERK1/2 pathway when treated with rLcn2. This reduction in ERK phosphorylation has implications for the response of PTEC to ischemic injuries and may ultimately impact their survival. The observed effect of rLcn2-treatment on ERK1/2 phosphorylation suggests that this pathway plays a role in the response of PTEC to hypoxia and reoxygenation, and that rLcn2-treatment may modulate this response.

Initially, this finding may appear contradictory to our hypothesis that rLcn2 promotes cell survival and proliferation. However, several studies have reported pro-apoptotic functions of ERK1/2 pathway [231-235]. *Hui et al.*, 2020 [231], described that the ERK1/2 signalling pathway regulates the

expression of Lcn2. It is generally acknowledged that endogenous Lcn2 plays a vital role in inflammation and immune responses associated with kidney injury and is upregulated in various renal diseases, including those related to transplantation. Hence, the activity of the ERK1/2 pathway may contribute to the increased expression of Lcn2 during kidney injury or transplantation, ultimately influencing the extent of inflammation and tissue damage in the transplanted kidney. The finding that the ERK1/2 signalling pathway regulates the expression of endogenous Lcn2 together with our findings that rLcn2 reduces the phosphorylation of the ERK1/2 pathway in PTEC *in vitro*, highlights an important link between these two factors and opens avenues for further research and potential interventions in kidney transplantation.

Tao et al., 2019 [232], suggested that inhibiting the ERK1/2 pathway can provide renal protection by preventing epithelial-to-mesenchymal transition (EMT), thereby potentially reducing the development and progression of fibrosis and other adverse renal changes. Furthermore, the study suggests that ERK1/2 inhibition can attenuate renal tubule injury by enhancing cellular resistance to oxidative stress. Oxidative stress, which occurs during imbalances between the production of reactive oxygen species (ROS) and the body's ability to eliminate them, is a common feature of kidney injury [236,237]. By inhibiting the ERK1/2 pathway, cellular resistance to oxidative stress is increased, potentially reducing tubule injury, and promoting renal protection. The study also mentions the involvement of multiple signalling pathways and matrix metalloproteinases (MMPs) in ERK1/2 inhibition-mediated renal protection. MMPs are enzymes involved in tissue remodelling, and their dysregulation is associated with kidney injury and fibrosis [150]. Inhibiting the ERK1/2 pathway may lead to the inactivation of these signalling pathways and MMPs, thus contributing to renal protection.

Overall, the modulation of the ERK1/2 pathway by rLcn2-treatment provides a starting point for future research and sheds light on the molecular mechanisms underlying the effects of rLcn2 on cellular responses to hypoxia and reoxygenation. There is a possibility that rLcn2 primarily affects alternative pathways or molecular targets, such as EGFR (epidermal growth factor receptor), which has been previously reported to be responsible for the progression of CKD [238]. Moreover, previous studies have indicated that Lcn2 is involved in the regulation of EGFR trafficking [239] and there is also evidence suggesting the participation of EGFR in the dedifferentiation process of renal PTEC [240].

Also, our study might not have captured the optimal time point or dosage of rLcn2-treatment required to observe significant effects on stress response proteins. The timing and concentration of rLcn2 administration are critical factors that require optimization to elicit noticeable changes in stress response protein expression. Stress response pathways are complex, involving a network of interconnected molecules and signalling cascades. It is possible that rLcn2 might have subtle or indirect effects on stress response proteins that were not readily detectable in our experimental regimes. Further investigations using different time points, doses, or experimental models could provide specific

insights into the relationship between rLcn2 and stress response pathways. The lack of clear effects on stress response proteins could also be attributed to biological variations among individual samples or experimental limitations could also contribute to. It is possible that sample sizes or assay sensitivity used in the study might not have been sufficient to detect subtle changes in stress response protein expression induced by rLcn2-treatment.

Furthermore, it is worth noting that the effects observed by *Ashraf et al.*, 2016 [17], on kidney transplant injury primarily occurred in an allogeneic setting. In context of our findings, this suggests that the impact of rLcn2-treatment may be specific to the context of allograft transplantation. It is plausible that rLcn2 may have minimal or no effect on cold ischemia/reperfusion injury, which is a distinct form of kidney damage. Instead, the immunophenotyping results of our study imply that rLcn2-treatment may exert its influence by modulating the immune response rather than directly affecting regulatory pathways.

It is important to consider that molecular changes at the protein level, post-translational modifications, or alterations in signalling pathways not captured by the specific pathway analysis could still occur, suggesting the involvement of alternative mechanisms or pathways in mediating the renoprotective effects of rLcn2. More refined molecular analyses, such as protein quantification, immunohistochemistry, or pathway-specific assays, may help elucidate the underlying mechanisms of rLcn2-treatment and its effects on graft function. Integrating multiple experimental approaches can provide a more comprehensive understanding of the molecular changes associated with rLcn2-treatment and its impact on kidney graft recovery.

4.4 DUAL FATE OF PTEC IN CELL CULTURE

For a thorough understanding developmental changes in primary PTEC during culture and to extensively characterize their molecular and gene expression profiles, we conducted scRNAseq analysis at three different timepoints. We particularly aimed to capture the heterogeneity and transcriptional changes within the PTEC population, enabling to elucidate potential developmental changes and processes during the culturing period.

Comparing cell expression profiles between unsorted and anti-prominin-1 sorted (merged) PTEC on day 0 (direct after isolation) to cells from day 3 and day 6 revealed and profound differences, necessitating a thorough and separate analysis of these timepoints. On day 0, cells expressed distinct markers, allowing for cluster annotation, with hardly any expression of injury-related, stress, or dedifferentiation markers. Similar clustering and annotation of cells from the proximal tubules have been described by e.g. *Hinze et. al.*, 2021 [241]. However, on day 3 and day 6, cells showed diverse expression patterns. We observed upregulation of injury-related markers (Lcn2, Havcr1, Prominin-1), the epithelial cell marker (Epcam), EMT and dedifferentiation markers (Vimentin, Cdh1, Krt7, Krt18), the

stress-related markers (Fosb, Jun), the cell cycle arrest marker (Cdkn1a), proliferation markers (Top2a, Mki67), and the collecting duct (CD) marker (Cldn4). Most PTEC markers were downregulated in all clusters, except for cluster 13 and 21 (where cluster 21 additionally expressed Havcr1). *Lrp2* expression persisted in 10 of the 27 clusters, while markers Slc12a1 and Slc12a3 were nearly depleted. These findings indicate profound changes in cell profiles, suggesting potential injury, stress, dedifferentiation, and altered cellular functions during the progression from day 0 to day 6. Yet, these diverse expression patterns observed within the clusters presented a challenge in annotating them as specific cell types. This difficulty arose from the wide range of gene expression patterns, unaligned with the expression profiles typically associated with distinct cell types. The lack of clear and consistent marker expression hindered the ability to confidently assign specific cell identities to the clusters. Consequently, the complex and heterogeneous nature of the expression patterns made it impossible to accurately associate clusters with specific cell types.

The striking differences between day 0 and day 3/day 6 were also reflected in the up- or downregulation of signature signalling pathways, corroborating the observed changes in gene expression profiles. Day 0 featured a high level of cell proliferation-related pathway activity, such as G2M checkpoint, DNA repair, and E2F target, indicating active cellular division and growth [242,243]. Various signalling pathways associated with cell-cell communication, tissue development, and energy production were upregulated. Additionally, diverse metabolic activities, including xenobiotic metabolism, glycolysis, and fatty acid metabolism, as well as modest epithelial mesenchymal transition were observed in selected clusters, suggesting potential metabolic and phenotypic adaptations in response to the culture environment.

The upregulation of oxidative phosphorylation implies an increased energy demand or adaptation to cellular stress, which can support repair processes and maintain cellular homeostasis. The upregulation of xenobiotic metabolism indicates a protective mechanism against stress and injurious agents, as cells attempt to detoxify and eliminate xenobiotics. The slight upregulation of EMT markers suggests cellular plasticity and a potential transition towards a mesenchymal-like state. Furthermore, upregulation of glycolysis suggests a shift in energy production towards glucose utilization, which may provide a survival advantage under certain conditions. This metabolic alteration might coincide with the increased energy demands during cellular stress or the need for rapid proliferation.

By day 3/day 6, notable changes occurred in specific clusters. For instance, there was a shift towards upregulation of hedgehog, TNFα, and KRAS signalling pathways, which are involved in cellular signalling and proliferation [242,243]. Epithelial-mesenchymal transition, a process associated with tissue remodelling and cellular plasticity, was observed in several clusters. The activation of G2M checkpoints and E2F targets suggests cell cycle regulation and DNA replication [242,243], while the upregulation of xenobiotic metabolism, fatty acid metabolism, and oxidative phosphorylation, indicated potential

responses to cellular stress or injurious stimuli [242,243]. Under healthy conditions, proximal tubules primarily rely on fatty acid oxidation (FAO) for energy production rather than glycolysis [117,118,144]. However, diseased cells in several clusters showed upregulation of glycolysis and proliferation hallmarks, along with downregulation of fatty acid metabolism. This suggests a transition towards an unhealthy state and a necessity for repair mechanisms. Clusters 13 and 21 stood out by exhibiting a combination of retained PTEC-specific hallmarks, including fatty acid metabolism, along with upregulation of the xenobiotic metabolism hallmark. This indicates that these cells are under stress or subjected to injurious stimuli, and they are responding by intensifying their metabolic processes to detoxify and eliminate xenobiotics. Additional upregulation of oxidative phosphorylation in these clusters suggests higher energy demand and adaptation to cellular stress. Collectively, these features suggest a potential transition towards a dedifferentiated state, making them interesting candidates to represent the initial stages of dedifferentiation. Overall, these changes imply a dynamic cellular response during the progression of cell culture. The observed alterations in signalling pathways and metabolic processes may reflect adaptations to the *in vitro* environment, potential dedifferentiation processes, or cellular stress responses. Further investigation is necessary to elucidate the precise mechanisms and implications of these changes in cultured cells.

To model the relationships between individual cells on day3/day6 of cell culture based on their gene expression profiles, we performed gene trajectory analysis–illuminating gene expression dynamics and potential fates during PTEC culture. The findings indicate two potential paths that the cells may follow: (i) a mesenchymal-like fate or (ii) an epithelial-like fate. Notably, sorted cells exhibited a tendency towards the mesenchymal-like fate, while unsorted cells showed a propensity towards the epithelial-like fate. Furthermore, the presence of PTEC-like cells decreased from day 3 to day 6, with a higher proportion observed in the sorted cells compared to the unsorted cells. These observations suggest that the sorting process may have influenced the cellular composition, promoting the dedifferentiation to mesenchymal-like cells, which has not been previously reported under similar conditions.

Smooth gene trajectory analysis and GSEA facilitated the identification of key genes, pathways, and regulatory networks that drive cellular behaviour. By identifying differentially expressed genes along these trajectories, we gained insights into the underlying molecular processes and regulatory networks that govern cellular fates. This allowed us to link gene expression patterns to important biological processes, cellular states, and disease phenotypes.

The smooth gene trajectory analysis revealed distinct clusters representing different cellular states along the fate trajectory. Specifically, the identification of a mesenchymal-like state in Cluster 2 and epithelial-like states in Clusters 1 and 8 highlights the existence of distinct cellular phenotypes during the differentiation process. Besides, the identification of a PTEC-like state in Cluster 5 holds particular importance. This cluster exhibited the expression of genes and cytokines associated with

proinflammatory responses, including IL-6 [244]. Notably, the presence of the PTEC-specific marker Kap [123] within this cluster suggests the retention of PTEC-like features. The duality within this PTEC-like state implies its potential role as the initiation cluster or cells of differentiation.

GSEA offers functional insights into the identified gene clusters, uncovering the underlying biological mechanisms influencing gene expression dynamics. Each cluster displayed distinct pathway enrichments, suggesting their involvement in key cellular processes. For instance, the enrichment of pathways related to inflammation and cellular responses in Cluster 5 further supports its characterization as a PTEC-like state. Moreover, the enrichment of genes related to apoptosis and the p53 pathway in Cluster 5 suggests the potential involvement of these processes in the differentiation of PTEC-like cells. Cluster 9's enrichment in DNA replication, cell cycle, and G2M checkpoint pathways indicates a role in regulating cell cycle stages. This finding suggests that cell proliferation and division are important processes during dedifferentiation or repair.

The enrichment of pathways related to inflammation, cell differentiation, and extracellular matrix regulation in various clusters (such as Clusters 2, 3, 4, 6, and 8) suggests their potential roles in shaping the cellular phenotype and maintaining tissue homeostasis. These findings suggest an intricate interplay between cellular signalling, matrix remodelling, and functional specialization during cellular differentiation or developmental processes.

Taken together, the analysis revealed diverse cell clusters after three and six days of culture exhibiting altered gene expression dynamics and changed activities of signalling pathways, possibly due to de- or transdifferentiation processes. Future research could focus on functionally characterizing these clusters, helping to annotate the specific cell types and to understand their roles in kidney injury and repair processes. This could involve experimental validation of key genes or pathways associated with specific clusters by immunohistochemistry or RNAscope *in situ* hybridization, exploring their involvement in inflammation, tissue regeneration, and other relevant biological processes.

4.5 ENDOGENOUS LCN2 IS PRODUCED BY INJURED PROXIMAL STRAIGHT TUBULAR CELLS AND STRESSED INTERMEDIATE DENDRITIC CELLS/MACROPHAGES

Previous research has described the rLcn2-mediated renoprotection after mKTx, resulting in the reduction of histological lesions and improvement of graft function. Contrarily, *Ashraf et al*., 2016, additionally showed that endogenously produced Lcn2 exerted no renoprotective effects [17]. Investigating the endogenous source of Lcn2 is crucial for comprehending its role in kidney transplantation. Lcn2 expression is highly induced in damaged nephrons, immune cells, and rejecting kidney allografts, indicating an involvement in various pathological conditions [35-37]. However, the specific cellular source of endogenous Lcn2 during kidney rejection remains uncertain, whether it originates from kidney epithelia or graft-infiltrating and circulating polymorphonuclear cells. Determining the

primary source of Lcn2 is essential for unraveling the underlying biological processes and potential pathological implications. Additional analysis of the expression of specific Lcn2 receptors, like *Lrp2*, enhances the understanding of Lcn2 uptake and transport mechanisms during transplantation, contributing to the development of innovative therapeutic strategies.

Therefore, we investigated the sources of endogenous Lcn2 during kidney rejection and evaluated different syngeneic and allogeneic transplantation groups. As expected, proximal tubules were the most abundant cell type in all transplantation groups, with allogeneic transplantations leading to more severe rejection and alterations in kidney function compared to syngeneic groups [120,245]. Besides featuring more severe histological lesions (section **3.4**), reduced survival (section **3.4**), and reduced functionality (section **3.1.5**), the C57Bl/6 to Balb/c group expressed levels of Lcn2 compared to the Balb/c to C57Bl/6 group. Collectively, these findings highlight the contrasting inflammatory response, immune cell activation, and allograft outcomes observed between these two groups, aligning with previously published data [246]. These observations support the findings by *Haase-Fielitz et al*., 2009 [247], that Lcn2 expression corresponds with the degree of graft damage, emphasizing its value as a reliable biomarker of AKI/acute rejection and its potential role in modulating immune response and allograft outcomes.

The susceptibility of the proximal tubule's S3 segment (the proximal straight tubule) to injury and AKI is well-documented [119,248-251]. Consequently, we detected widespread Lcn2 expression across various cell types, particularly in injured proximal straight tubules and stressed intermediate state dendritic cells/macrophages, suggesting their role as a primary source of endogenous Lcn2 production following injury. Moreover, Havcr1 expression was limited to injured proximal straight tubules and proliferating PST subclusters in proximal tubules, primarily seen in allogeneic transplantation groups. In the immune cell cluster, Havcr1 expression was restricted to M2 macrophages and B-cells. These findings suggest the occurrence of renal injury, immune cell activation, and the potential involvement of Lcn2 and Havcr1 in the immune response and tissue remodelling processes associated with graft acceptance or rejection, highlighting the complex interplay between injured cells and immune cells in the context of kidney transplantation.

Lrp2, also known as megalin and being the receptor for Lcn2, showed pronounced expression in proximal tubules but notably reduced levels in the allogeneic transplantation groups. In the immune cell cluster, *Lrp2* expression primarily originated from the Balb/c to C57Bl/6 group, with M2 macrophages showing the highest expression, suggesting a role of *Lrp2* in cellular function and immune modulation within the kidney. In the context of allogenic transplantation, the lower expression of *Lrp2* might have several implications for graft outcomes and kidney health. *Lrp2* is a multifunctional endocytic receptor expressed in the kidney, playing a crucial role in the reabsorption of essential molecules, including proteins like rLcn2, and vitamins, from the filtrate back into the bloodstream [58-62]. Therefore,

the reduced expression of *Lrp2* in allogenic transplantation settings suggests a potential impairment in the renal reabsorption process, which could lead to altered renal function and compromised kidney health, ultimately contributing to graft dysfunction. In contrast, the widespread presence of *Lrp2* expression in syngeneic kidney transplantation settings suggests that the normal physiological function of *Lrp2* is preserved.

In conclusion, further research is required to elucidate the implications and underlying mechanisms of Lcn2 expression, particularly in injured PST cells and stressed intermediate state dendritic cells/macrophages. Additionally, understanding the role of *Lrp2* and Havcr1 in immune modulation, determining the subcellular localization of Lcn2 and *Lrp2* expression, and investigating the functional consequences of these molecules in kidney rejection holds promise to advance our understanding of rejection processes and identify therapeutic targets. Combining techniques such as immunohistochemistry, spatial transcriptomics, gene knockdown or overexpression, gene expression profiling, and proteomic analysis, has valuable potential to advance the development of targeted strategies, ultimately improving the outcomes of allogeneic transplantation and enhancing patient care.

4.6 CONCLUSIONS

In this study, we shed light on the multifaceted effects of rLcn2-treatment following kidney transplantation, highlighting its diverse immunomodulatory effects. These effects encompassed significant alterations in the relative frequencies of various innate and adaptive immune cell populations, along with changes in their functionality, which may contribute to the facilitation of renoprotection. Additionally, we established a reliable method for isolating and culturing murine primary proximal tubular epithelial cells and investigated their response to rLcn2-treatment. Notably, via single-cell RNA sequencing, our study is the first to elucidate two possible cellular fates of PTEC in cell culture —a mesenchymal-like and an epithelial-like state. This indicates a likelihood of dedifferentiation or transdifferentiation of PTEC during culture, potentially explaining the limited effects of rLcn2-treatment at the molecular level following ischemia reperfusion injury. Furthermore, we identified injured proximal straight tubule cells and stressed intermediate state dendritic cells/macrophages as the primary sources of endogenous Lcn2, shedding light on the cellular dynamics involved in Lcn2 production during allograft rejection. Collectively, these findings provide a foundation for a deeper understanding of the molecular aspects of rLcn2-treatment in the context of kidney transplantation.

5 REFERENCES

1 Stein, M. C., Braun, F., Krebs, C. F. & Bunders, M. J. Kidney organoid systems for studies of immune-mediated kidney diseases: challenges and opportunities. *Cell Tissue Res* **385**, 457-473, doi:10.1007/s00441-021-03499-4 (2021).

2 Carpenter, T. O. (ed Anawalt B In: Feingold KR, Blackman MR, et al.) (South Dartmouth (MA): MDText.com, Inc.; 2000-. https://www.ncbi.nlm.nih.gov/books/NBK279172/, 2000).

3 Bondue, T. *et al.* Urine-Derived Epithelial Cells as Models for Genetic Kidney Diseases. *Cells* **10**, doi:10.3390/cells10061413 (2021).

4 Tisher, C. C. Functional anatomy of the kidney. *Hosp Pract* **13**, doi:10.1080/21548331.1978.11707333 (1978).

5 Sands, J. M. & Verlander, J. W. in *Comprehensive Toxicology* Vol. 7 1-22 (2010).

6 Gallardo, P. A., Vio, C.P. *Functional Anatomy of the Kidney. In: Renal Physiology and Hydrosaline Metabolism.* . (Springer, Cham. , 2022).

7 Jager, K. J. *et al.* A single number for advocacy and communication-worldwide more than 850 million individuals have kidney diseases. *Kidney Int* **96**, 1048-1050, doi:10.1016/j.kint.2019.07.012 (2019).

8 Kovesdy, C. P. Epidemiology of chronic kidney disease: an update 2022. *Kidney Int Suppl (2011)* **12**, 7-11, doi:10.1016/j.kisu.2021.11.003 (2022).

9 Halloran, P. F. Immunosuppressive drugs for kidney transplantation. *N Engl J Med* **351**, 2715-2729, doi:10.1056/NEJMra033540 (2004).

10 Kosieradzki, M. & Rowinski, W. Ischemia/reperfusion injury in kidney transplantation: mechanisms and prevention. *Transplant Proc* **40**, 3279-3288, doi:10.1016/j.transproceed.2008.10.004 (2008).

11 Salvadori, M., Rosso, G. & Bertoni, E. Update on ischemia-reperfusion injury in kidney transplantation: Pathogenesis and treatment. *World J Transplant* **5**, 52-67, doi:10.5500/wjt.v5.i2.52 (2015).

12 Perico, N., Cattaneo, D., Sayegh, M. H. & Remuzzi, G. Delayed graft function in kidney transplantation. *Lancet* **364**, 1814-1827, doi:10.1016/S0140-6736(04)17406-0 (2004).

13 Siedlecki, A., Irish, W. & Brennan, D. C. Delayed graft function in the kidney transplant. *Am J Transplant* **11**, 2279-2296, doi:10.1111/j.1600-6143.2011.03754.x (2011).

14 Meier-Kriesche, H. U., Schold, J. D. & Kaplan, B. Long-term renal allograft survival: have we made significant progress or is it time to rethink our analytic and therapeutic strategies? *Am J Transplant* **4**, 1289-1295, doi:10.1111/j.1600-6143.2004.00515.x (2004).

15 Jardine, A. G., Hartmann, A. & Holdaas, H. Long-term renal allograft survival: a quiet revolution. *Kidney Int* **94**, 853-855, doi:10.1016/j.kint.2018.08.005 (2018).

16 Schmidt-Ott, K. M. *et al.* Neutrophil gelatinase-associated lipocalin-mediated iron traffic in kidney epithelia. *Curr Opin Nephrol Hypertens* **15**, 442-449, doi:10.1097/01.mnh.0000232886.81142.58 (2006).

17 Ashraf, M. I. *et al.* Exogenous Lipocalin 2 Ameliorates Acute Rejection in a Mouse Model of Renal Transplantation. *Am J Transplant* **16**, 808-820, doi:10.1111/ajt.13521 (2016).

18 Mori, K. *et al.* Endocytic delivery of lipocalin-siderophore-iron complex rescues the kidney from ischemia-reperfusion injury. *J Clin Invest* **115**, 610-621, doi:10.1172/JCI23056 (2005).

19 Kjeldsen, L., Johnsen, A. H., Sengeløv, H. & Borregaard, N. Isolation and primary structure of NGAL, a novel protein associated with human neutrophil gelatinase.

Journal of Biological Chemistry **268**, 10425-10432, doi:10.1016/s0021-9258(18)82217-7 (1993).

20 Aigner, F. *et al.* Lipocalin-2 regulates the inflammatory response during ischemia and reperfusion of the transplanted heart. *Am J Transplant* **7**, 779-788, doi:10.1111/j.1600-6143.2006.01723.x (2007).

21 Flower, D. R., North, A. C. & Sansom, C. E. The lipocalin protein family: structural and sequence overview. *Biochim Biophys Acta* **1482**, 9-24, doi:10.1016/s0167-4838(00)00148-5 (2000).

22 Cowland, J. B. & Borregaard, N. Molecular characterization and pattern of tissue expression of the gene for neutrophil gelatinase-associated lipocalin from humans. *Genomics* **45**, 17-23, doi:10.1006/geno.1997.4896 (1997).

23 Moschen, A. R., Adolph, T. E., Gerner, R. R., Wieser, V. & Tilg, H. Lipocalin-2: A Master Mediator of Intestinal and Metabolic Inflammation. *Trends Endocrinol Metab* **28**, 388-397, doi:10.1016/j.tem.2017.01.003 (2017).

24 Qiu, S., Chen, X., Pang, Y. & Zhang, Z. Lipocalin-2 protects against renal ischemia/reperfusion injury in mice through autophagy activation mediated by HIF1alpha and NF-kappab crosstalk. *Biomed Pharmacother* **108**, 244-253, doi:10.1016/j.biopha.2018.09.023 (2018).

25 Zhao, P., Elks, C. M. & Stephens, J. M. The induction of lipocalin-2 protein expression in vivo and in vitro. *J Biol Chem* **289**, 5960-5969, doi:10.1074/jbc.M113.532234 (2014).

26 Zhang, Y. *et al.* Lipocalin 2 expression and secretion is highly regulated by metabolic stress, cytokines, and nutrients in adipocytes. *PLoS One* **9**, e96997, doi:10.1371/journal.pone.0096997 (2014).

27 Flo, T. H. *et al.* Lipocalin 2 mediates an innate immune response to bacterial infection by sequestrating iron. *Nature* **432**, 917-921, doi:10.1038/nature03104 (2004).

28 Goetz, D. H. *et al.* The neutrophil lipocalin NGAL is a bacteriostatic agent that interferes with siderophore-mediated iron acquisition. *Mol Cell* **10**, 1033-1043, doi:10.1016/s1097-2765(02)00708-6 (2002).

29 Schroll, A. *et al.* Lipocalin-2 ameliorates granulocyte functionality. *Eur J Immunol* **42**, 3346-3357, doi:10.1002/eji.201142351 (2012).

30 Devireddy, L. R., Gazin, C., Zhu, X. & Green, M. R. A cell-surface receptor for lipocalin 24p3 selectively mediates apoptosis and iron uptake. *Cell* **123**, 1293-1305, doi:10.1016/j.cell.2005.10.027 (2005).

31 Bong JJ, S. M., Kim HH, Han O, Back K, Baik M. . The 24p3 gene is induced during involution of the mammary gland and induces apoptosis of mammary epithelial cells. . *Mol Cells.* (2004).

32 Schmidt-Ott, K. M. *et al.* Dual action of neutrophil gelatinase-associated lipocalin. *J Am Soc Nephrol* **18**, 407-413, doi:10.1681/ASN.2006080882 (2007).

33 Xu, G. *et al.* Lipocalin-2 induces cardiomyocyte apoptosis by increasing intracellular iron accumulation. *J Biol Chem* **287**, 4808-4817, doi:10.1074/jbc.M111.275719 (2012).

34 Golonka, R., Yeoh, B. S. & Vijay-Kumar, M. The Iron Tug-of-War between Bacterial Siderophores and Innate Immunity. *J Innate Immun* **11**, 249-262, doi:10.1159/000494627 (2019).

35 Parikh, C. R. *et al.* Urine NGAL and IL-18 are predictive biomarkers for delayed graft function following kidney transplantation. *Am J Transplant* **6**, 1639-1645, doi:10.1111/j.1600-6143.2006.01352.x (2006).

36 Coca, S. G., Yalavarthy, R., Concato, J. & Parikh, C. R. Biomarkers for the diagnosis and risk stratification of acute kidney injury: a systematic review. *Kidney Int* **73**, 1008-1016, doi:10.1038/sj.ki.5002729 (2008).

37 Hall, I. E. *et al.* IL-18 and urinary NGAL predict dialysis and graft recovery after kidney transplantation. *J Am Soc Nephrol* **21**, 189-197, doi:10.1681/ASN.2009030264 (2010).

38 Mishra, J. *et al.* Amelioration of ischemic acute renal injury by neutrophil gelatinase-associated lipocalin. *J Am Soc Nephrol* **15**, 3073-3082, doi:10.1097/01.ASN.0000145013.44578.45 (2004).

39 Ma, Q., Devarajan, S. R. & Devarajan, P. Amelioration of cisplatin-induced acute kidney injury by recombinant neutrophil gelatinase-associated lipocalin. *Ren Fail* **38**, 1476-1482, doi:10.1080/0886022X.2016.1227917 (2016).

40 Zhang, W., Yang, S., Cui, L. & Zhang, J. Neutrophil gelatinase-associated lipocalin worsens ischemia/reperfusion damage of kidney cells by autophagy. *Ren Fail* **38**, 1136-1140, doi:10.3109/0886022X.2016.1158041 (2016).

41 Li, D., Yan Sun, W., Fu, B., Xu, A. & Wang, Y. Lipocalin-2-The myth of its expression and function. *Basic Clin Pharmacol Toxicol* **127**, 142-151, doi:10.1111/bcpt.13332 (2020).

42 Heyne, N. *et al.* Urinary neutrophil gelatinase-associated lipocalin accurately detects acute allograft rejection among other causes of acute kidney injury in renal allograft recipients. *Transplantation* **93**, 1252-1257, doi:10.1097/TP.0b013e31824fd892 (2012).

43 Maier, H. T. *et al.* Prediction of delayed graft function and long-term graft survival by serum and urinary neutrophil gelatinase-associated lipocalin during the early postoperative phase after kidney transplantation. *PLoS One* **13**, e0189932, doi:10.1371/journal.pone.0189932 (2018).

44 Kriz, W. & Bankir, L. A standard nomenclature for structures of the kidney. The Renal Commission of the International Union of Physiological Sciences (IUPS). *Kidney Int* **33**, 1-7, doi:10.1038/ki.1988.1 (1988).

45 Seldin, D., and Griebisch, G. in *Physiology and Pathophysiology* (ed Orson W. Moe and Michael Caplan Robert J. Alpern) (Elsevier, 2013).

46 Curthoys, N. P. & Moe, O. W. Proximal tubule function and response to acidosis. *Clin J Am Soc Nephrol* **9**, 1627-1638, doi:10.2215/CJN.10391012 (2014).

47 Chan, C. H., Wu, S. N., Bao, B. Y., Li, H. W. & Lu, T. L. MST3 Involvement in Na(+) and K(+) Homeostasis with Increasing Dietary Potassium Intake. *Int J Mol Sci* **22**, doi:10.3390/ijms22030999 (2021).

48 Pfaller, W. & Gstraunthaler, G. Nephrotoxicity testing in vitro--what we know and what we need to know. *Environ Health Perspect* **106 Suppl 2**, 559-569, doi:10.1289/ehp.98106559 (1998).

49 Wilmes, A. *et al.* Identification and dissection of the Nrf2 mediated oxidative stress pathway in human renal proximal tubule toxicity. *Toxicol In Vitro* **25**, 613-622, doi:10.1016/j.tiv.2010.12.009 (2011).

50 Matzinger, P. Tolerance, danger, and the extended family. *Annu Rev Immunol* **12**, 991-1045, doi:10.1146/annurev.iy.12.040194.005015 (1994).

51 Pradeu, T. & Cooper, E. L. The danger theory: 20 years later. *Front Immunol* **3**, 287, doi:10.3389/fimmu.2012.00287 (2012).

52 DeWolf, S. E. *et al.* DAMPs Released From Injured Renal Tubular Epithelial Cells Activate Innate Immune Signals in Healthy Renal Tubular Epithelial Cells. *Transplantation* **106**, 1589-1599, doi:10.1097/TP.0000000000004038 (2022).

53 Nakhoul, N. & Batuman, V. Role of proximal tubules in the pathogenesis of kidney disease. *Contrib Nephrol* **169**, 37-50, doi:10.1159/000313944 (2011).

54 Aschauer, L. *et al.* Delineation of the key aspects in the regulation of epithelial monolayer formation. *Mol Cell Biol* **33**, 2535-2550, doi:10.1128/MCB.01435-12 (2013).

55 Zhuo, J. L. & Li, X. C. Proximal nephron. *Compr Physiol* **3**, 1079-1123, doi:10.1002/cphy.c110061 (2013).

56 Muto, S. *et al.* Claudin-2-deficient mice are defective in the leaky and cation-selective paracellular permeability properties of renal proximal tubules. *Proc Natl Acad Sci U S A* **107**, 8011-8016, doi:10.1073/pnas.0912901107 (2010).

57 Gstraunthaler, G., Pfaller, W. & Kotanko, P. Interrelation between oxygen consumption and Na-K-ATPase activity in rat renal proximal tubule suspension. *Ren Physiol* **8**, 38-44, doi:10.1159/000173032 (1985).

58 Elsakka, E. G. E., Mokhtar, M. M., Hegazy, M., Ismail, A. & Doghish, A. S. Megalin, a multi-ligand endocytic receptor, and its participation in renal function and diseases: A review. *Life Sci* **308**, 120923, doi:10.1016/j.lfs.2022.120923 (2022).

59 Nielsen, R., Christensen, E. I. & Birn, H. Megalin and cubilin in proximal tubule protein reabsorption: from experimental models to human disease. *Kidney Int* **89**, 58-67, doi:10.1016/j.kint.2015.11.007 (2016).

60 Hummelgaard, S. & Weyer, K. Megalin-Mediated Endocytosis in the Kidney Proximal Tubule: Relevance to Regulation of the Renal Renin-Angiotensin System. *Nephron* **147**, 244-249, doi:10.1159/000526369 (2023).

61 Bao, G. *et al.* Iron traffics in circulation bound to a siderocalin (Ngal)-catechol complex. *Nat Chem Biol* **6**, 602-609, doi:10.1038/nchembio.402 (2010).

62 Hvidberg, V. *et al.* The endocytic receptor megalin binds the iron transporting neutrophil-gelatinase-associated lipocalin with high affinity and mediates its cellular uptake. *FEBS Lett* **579**, 773-777, doi:10.1016/j.febslet.2004.12.031 (2005).

63 Devireddy, L. R., Teodoro, J. G., Richard, F. A. & Green, M. R. Induction of apoptosis by a secreted lipocalin that is transcriptionally regulated by IL-3 deprivation. *Science* **293**, 829-834, doi:10.1126/science.1061075 (2001).

64 Langelueddecke, C. *et al.* Lipocalin-2 (24p3/neutrophil gelatinase-associated lipocalin (NGAL)) receptor is expressed in distal nephron and mediates protein endocytosis. *J Biol Chem* **287**, 159-169, doi:10.1074/jbc.M111.308296 (2012).

65 Wang, X. *et al.* Molecular and functional profiling of apical versus basolateral small extracellular vesicles derived from primary human proximal tubular epithelial cells under inflammatory conditions. *J Extracell Vesicles* **10**, e12064, doi:10.1002/jev2.12064 (2021).

66 Gould, S. E., Day, M., Jones, S. S. & Dorai, H. BMP-7 regulates chemokine, cytokine, and hemodynamic gene expression in proximal tubule cells. *Kidney Int* **61**, 51-60, doi:10.1046/j.1523-1755.2002.00103.x (2002).

67 Wilkinson, R., Wang, X., Roper, K. E. & Healy, H. Activated human renal tubular cells inhibit autologous immune responses. *Nephrol Dial Transplant* **26**, 1483-1492, doi:10.1093/ndt/gfq677 (2011).

68 Linke, A. *et al.* Antigen Cross-Presentation by Murine Proximal Tubular Epithelial Cells Induces Cytotoxic and Inflammatory CD8(+) T Cells. *Cells* **11**, doi:10.3390/cells11091510 (2022).

69 Rong, S., Lewis, A. G., Kunter, U., Haller, H. & Gueler, F. A knotless technique for kidney transplantation in the mouse. *J Transplant* **2012**, 127215, doi:10.1155/2012/127215 (2012).

70 Livak, K. J. & Schmittgen, T. D. Analysis of relative gene expression data using real-time quantitative PCR and the 2(-Delta Delta C(T)) Method. *Methods* **25**, 402-408, doi:10.1006/meth.2001.1262 (2001).

71 Sieckmann, T. (FU Berlin, Refubium FU Berlin, 2023).

72 Butler, A., Hoffman, P., Smibert, P., Papalexi, E. & Satija, R. Integrating single-cell transcriptomic data across different conditions, technologies, and species. *Nat Biotechnol* **36**, 411-420, doi:10.1038/nbt.4096 (2018).

73 McGinnis, C. S., Murrow, L. M. & Gartner, Z. J. DoubletFinder: Doublet Detection in Single-Cell RNA Sequencing Data Using Artificial Nearest Neighbors. *Cell Syst* **8**, 329-337 e324, doi:10.1016/j.cels.2019.03.003 (2019).

74 Lake, B. B. *et al.* An atlas of healthy and injured cell states and niches in the human kidney. *Nature* **619**, 585-594, doi:10.1038/s41586-023-05769-3 (2023).

75 Wolf, F. A., Angerer, P. & Theis, F. J. SCANPY: large-scale single-cell gene expression data analysis. *Genome Biol* **19**, 15, doi:10.1186/s13059-017-1382-0 (2018).

76 Leiz, J. *et al.* Nuclei Isolation from Adult Mouse Kidney for Single-Nucleus RNA-Sequencing. *J Vis Exp*, doi:10.3791/62901 (2021).

77 Leiz, J. (Lebenswissenschaftliche Fakultät, HU Berlin, 2023).

78 Stuart, T. *et al.* Comprehensive Integration of Single-Cell Data. *Cell* **177**, 1888-1902 e1821, doi:10.1016/j.cell.2019.05.031 (2019).

79 Ransick, A. *et al.* Single-Cell Profiling Reveals Sex, Lineage, and Regional Diversity in the Mouse Kidney. *Dev Cell* **51**, 399-413 e397, doi:10.1016/j.devcel.2019.10.005 (2019).

80 Chen, L. *et al.* Transcriptomes of major renal collecting duct cell types in mouse identified by single-cell RNA-seq. *Proc Natl Acad Sci U S A* **114**, E9989-E9998, doi:10.1073/pnas.1710964114 (2017).

81 Young, M. D. *et al.* Single-cell transcriptomes from human kidneys reveal the cellular identity of renal tumors. *Science* **361**, 594-599, doi:10.1126/science.aat1699 (2018).

82 Neuwirth, E. *RColorBrewer: ColorBrewer Palettes. R package version 1.1-3*, <https://CRAN.R-project.org/package=RColorBrewer > (2022-04-03).

83 Gerhardt, L. M. S., Liu, J., Koppitch, K., Cippa, P. E. & McMahon, A. P. Single-nuclear transcriptomics reveals diversity of proximal tubule cell states in a dynamic response to acute kidney injury. *Proc Natl Acad Sci U S A* **118**, doi:10.1073/pnas.2026684118 (2021).

84 Cippa, P. E. & McMahon, A. P. Proximal tubule responses to injury: interrogation by single-cell transcriptomics. *Curr Opin Nephrol Hypertens* **32**, 352-358, doi:10.1097/MNH.0000000000000893 (2023).

85 Hinze, C. *et al.* Single-cell transcriptomics reveals common epithelial response patterns in human acute kidney injury. *Genome Med* **14**, 103, doi:10.1186/s13073-022-01108-9 (2022).

86 R&D Systems, I. Cell Marker Interactive Resource Tool.

87 Zhang, X. *et al.* CellMarker: a manually curated resource of cell markers in human and mouse. *Nucleic Acids Res* **47**, D721-D728, doi:10.1093/nar/gky900 (2019).

88 Shen, Q. *et al.* Single-Cell RNA Sequencing Reveals the Immunological Profiles of Renal Allograft Rejection in Mice. *Front Immunol* **12**, 693608, doi:10.3389/fimmu.2021.693608 (2021).

89 Lund, F. E. & Randall, T. D. Effector and regulatory B cells: modulators of CD4+ T cell immunity. *Nat Rev Immunol* **10**, 236-247, doi:10.1038/nri2729 (2010).

90 Chaplin, D. D. Overview of the immune response. *J Allergy Clin Immunol* **125**, S3-23, doi:10.1016/j.jaci.2009.12.980 (2010).

91 Vivier, E., Tomasello, E., Baratin, M., Walzer, T. & Ugolini, S. Functions of natural killer cells. *Nat Immunol* **9**, 503-510, doi:10.1038/ni1582 (2008).

92 Etxebarria, A., Díez-Martín, E., Astigarraga, E. & Barreda-Gómez, G. Role of the Immune System in Renal Transplantation, Types of Response, Technical Approaches and Current Challenges. *Immuno* **2**, 548-570, doi:10.3390/immuno2040035 (2022).

93 Ashraf, M. I. *et al.* Natural Killer Cells Promote Kidney Graft Rejection Independently of Cyclosporine A Therapy. *Front Immunol* **10**, 2279, doi:10.3389/fimmu.2019.02279 (2019).

94 Yazdani, S. *et al.* Natural killer cell infiltration is discriminative for antibody-mediated rejection and predicts outcome after kidney transplantation. *Kidney Int* **95**, 188-198, doi:10.1016/j.kint.2018.08.027 (2019).

95 Karimi, M. A. *et al.* NKG2D expression by CD8+ T cells contributes to GVHD and GVT effects in a murine model of allogeneic HSCT. *Blood* **125**, 3655-3663, doi:10.1182/blood-2015-02-629006 (2015).

96 Ivanova, O. K. *et al.* CD3(+) CD8(+) NKG2D(+) T Lymphocytes Induce Apoptosis and Necroptosis in HLA-Negative Cells via FasL-Fas Interaction. *J Cell Biochem* **118**, 3359-3366, doi:10.1002/jcb.25990 (2017).

97 Prajapati, K., Perez, C., Rojas, L. B. P., Burke, B. & Guevara-Patino, J. A. Functions of NKG2D in CD8(+) T cells: an opportunity for immunotherapy. *Cell Mol Immunol* **15**, 470-479, doi:10.1038/cmi.2017.161 (2018).

98 Macian, F. *et al.* Transcriptional mechanisms underlying lymphocyte tolerance. *Cell* **109**, 719-731, doi:10.1016/s0092-8674(02)00767-5 (2002).

99 Ai, W., Li, H., Song, N., Li, L. & Chen, H. Optimal method to stimulate cytokine production and its use in immunotoxicity assessment. *Int J Environ Res Public Health* **10**, 3834-3842, doi:10.3390/ijerph10093834 (2013).

100 Ross, S. H. & Cantrell, D. A. Signaling and Function of Interleukin-2 in T Lymphocytes. *Annu Rev Immunol* **36**, 411-433, doi:10.1146/annurev-immunol-042617-053352 (2018).

101 Nissen, M. H., Jeppesen, M. & Claesson, M. H. Splenocytes cultured in low concentrations of IL-2 generate NK cell specificities toward syngenic and allogenic targets. *Cell Immunol* **203**, 47-54, doi:10.1006/cimm.2000.1670 (2000).

102 De, S., Kuwahara, S. & Saito, A. The endocytic receptor megalin and its associated proteins in proximal tubule epithelial cells. *Membranes (Basel)* **4**, 333-355, doi:10.3390/membranes4030333 (2014).

103 Alpern, R. J., Caplan, M. J. & Moe, O. W. *Seldin and Giebisch's The Kidney: Physiology and Pathophysiology*. (Elsevier Science, 2012).

104 Taal, M. W. *et al. Brenner and Rector's The Kidney E-Book*. (Elsevier Health Sciences, 2011).

105 Kamiyama, M., Garner, M. K., Farragut, K. M. & Kobori, H. The establishment of a primary culture system of proximal tubule segments using specific markers from normal mouse kidneys. *Int J Mol Sci* **13**, 5098-5111, doi:10.3390/ijms13045098 (2012).

106 Legouis, D. *et al.* Ex vivo analysis of renal proximal tubular cells. *BMC Cell Biol* **16**, 12, doi:10.1186/s12860-015-0058-4 (2015).

107 Weigmann, A., Corbeil, D., Hellwig, A. & Huttner, W. B. Prominin, a novel microvilli-specific polytopic membrane protein of the apical surface of epithelial cells, is targeted to plasmalemmal protrusions of non-epithelial cells. *Proc Natl Acad Sci U S A* **94**, 12425-12430, doi:10.1073/pnas.94.23.12425 (1997).

108 Balzer, M. S., Rohacs, T. & Susztak, K. How Many Cell Types Are in the Kidney and What Do They Do? *Annu Rev Physiol* **84**, 507-531, doi:10.1146/annurev-physiol-052521-121841 (2022).

109 Oikawa, T. *et al.* Necessity of p53-binding to the CDH1 locus for its expression defines two epithelial cell types differing in their integrity. *Sci Rep* **8**, 1595, doi:10.1038/s41598-018-20043-7 (2018).

110 Kirita, Y., Wu, H., Uchimura, K., Wilson, P. C. & Humphreys, B. D. Cell profiling of mouse acute kidney injury reveals conserved cellular responses to injury. *Proc Natl Acad Sci U S A* **117**, 15874-15883, doi:10.1073/pnas.2005477117 (2020).

111 Beenken, A. *et al.* Structures of LRP2 reveal a molecular machine for endocytosis. *Cell* **186**, 821-836 e813, doi:10.1016/j.cell.2023.01.016 (2023).

112 Zheng, G. *et al.* Organ distribution in rats of two members of the low-density lipoprotein receptor gene family, gp330 and LRP/alpha 2MR, and the receptor-associated protein (RAP). *J Histochem Cytochem* **42**, 531-542, doi:10.1177/42.4.7510321 (1994).

113 Chi, Y. *et al.* Cancer cells deploy lipocalin-2 to collect limiting iron in leptomeningeal metastasis. *Science* **369**, 276-282, doi:10.1126/science.aaz2193 (2020).

114 Huang, Y. *et al.* Lipocalin-2 in neutrophils induces ferroptosis in septic cardiac dysfunction via increasing labile iron pool of cardiomyocytes. *Front Cardiovasc Med* **9**, 922534, doi:10.3389/fcvm.2022.922534 (2022).

115 Kristina Kuhbandner, J. H., Theresa Pohlkamp. Biochemistry of Lipids, Lipoproteins and Membranes (Seventh Edition): Chapter 18 - Lipoprotein receptors. *Elsevier*, 583-622, doi:https://doi.org/10.1016/B978-0-12-824048-9.00018-3 (2021).

116 Schaub, J. A., Venkatachalam, M. A. & Weinberg, J. M. Proximal Tubular Oxidative Metabolism in Acute Kidney Injury and the Transition to CKD. *Kidney360* **2**, 355-364, doi:10.34067/KID.0004772020 (2021).

117 Faivre, A., Verissimo, T., Auwerx, H., Legouis, D. & de Seigneux, S. Tubular Cell Glucose Metabolism Shift During Acute and Chronic Injuries. *Front Med (Lausanne)* **8**, 742072, doi:10.3389/fmed.2021.742072 (2021).

118 Gewin, L. S. Sugar or Fat? Renal Tubular Metabolism Reviewed in Health and Disease. *Nutrients* **13**, doi:10.3390/nu13051580 (2021).

119 Hall, A. M. & de Seigneux, S. Metabolic mechanisms of acute proximal tubular injury. *Pflugers Arch* **474**, 813-827, doi:10.1007/s00424-022-02701-y (2022).

120 Lu, Y. A. *et al.* Single-Nucleus RNA Sequencing Identifies New Classes of Proximal Tubular Epithelial Cells in Kidney Fibrosis. *J Am Soc Nephrol* **32**, 2501-2516, doi:10.1681/ASN.2020081143 (2021).

121 Park, J. *et al.* Single-cell transcriptomics of the mouse kidney reveals potential cellular targets of kidney disease. *Science* **360**, 758-763, doi:10.1126/science.aar2131 (2018).

122 Xu, J. *et al.* Transcriptional and functional motifs defining renal function revealed by single-nucleus RNA sequencing. *Proc Natl Acad Sci U S A* **119**, e2203179119, doi:10.1073/pnas.2203179119 (2022).

123 Meseguer, A. & Catterall, J. F. Cell-specific expression of kidney androgen-regulated protein messenger RNA is under multihormonal control. *Mol Endocrinol* **4**, 1240-1248, doi:10.1210/mend-4-8-1240 (1990).

124 Janosevic, D. *et al.* miRNA and mRNA Signatures in Human Acute Kidney Injury Tissue. *bioRxiv*, doi:10.1101/2023.09.11.557054 (2023).

125 Gauer, S. *et al.* Kidney Injury Molecule-1 Is Specifically Expressed in Cystically-Transformed Proximal Tubules of the PKD/Mhm (cy/+) Rat Model of Polycystic Kidney Disease. *Int J Mol Sci* **17**, doi:10.3390/ijms17060802 (2016).
126 Dhillon, P. *et al.* The Nuclear Receptor ESRRA Protects from Kidney Disease by Coupling Metabolism and Differentiation. *Cell Metab* **33**, 379-394 e378, doi:10.1016/j.cmet.2020.11.011 (2021).
127 Gong, Y. & Hou, J. Claudins in barrier and transport function-the kidney. *Pflugers Arch* **469**, 105-113, doi:10.1007/s00424-016-1906-6 (2017).
128 Novella-Rausell, C., Grudniewska, M., Peters, D. J. M. & Mahfouz, A. A comprehensive mouse kidney atlas enables rare cell population characterization and robust marker discovery. *iScience* **26**, 106877, doi:10.1016/j.isci.2023.106877 (2023).
129 Brekken, R. A. & Sage, E. H. SPARC, a matricellular protein: at the crossroads of cell-matrix. *Matrix Biol* **19**, 569-580, doi:10.1016/s0945-053x(00)00105-0 (2000).
130 Bradshaw, A. D. & Sage, E. H. SPARC, a matricellular protein that functions in cellular differentiation and tissue response to injury. *J Clin Invest* **107**, 1049-1054, doi:10.1172/JCI12939 (2001).
131 Mihevc, M., Petreski, T., Maver, U. & Bevc, S. Renal proximal tubular epithelial cells: review of isolation, characterization, and culturing techniques. *Mol Biol Rep* **47**, 9865-9882, doi:10.1007/s11033-020-05977-4 (2020).
132 Trzpis, M. *et al.* Expression of EpCAM is up-regulated during regeneration of renal epithelia. *J Pathol* **216**, 201-208, doi:10.1002/path.2396 (2008).
133 Zeisberg, M. & Neilson, E. G. Biomarkers for epithelial-mesenchymal transitions. *J Clin Invest* **119**, 1429-1437, doi:10.1172/JCI36183 (2009).
134 Serrano-Gomez, S. J., Maziveyi, M. & Alahari, S. K. Regulation of epithelial-mesenchymal transition through epigenetic and post-translational modifications. *Mol Cancer* **15**, 18, doi:10.1186/s12943-016-0502-x (2016).
135 Djudjaj, S. *et al.* Keratins are novel markers of renal epithelial cell injury. *Kidney Int* **89**, 792-808, doi:10.1016/j.kint.2015.10.015 (2016).
136 Snider, N. T. Kidney keratins: cytoskeletal stress responders with biomarker potential. *Kidney Int* **89**, 738-740, doi:10.1016/j.kint.2015.12.040 (2016).
137 Scholzen, T. & Gerdes, J. The Ki-67 protein: From the known and the unknown. *Journal of Cellular Physiology* **182**, 311-322, doi:10.1002/(sici)1097-4652(200003)182:3<311::Aid-jcp1>3.0.Co;2-9 (2000).
138 Zhang, Y. *et al.* Identification of resident progenitors labeled with Top2a responsible for proximal tubular regeneration in ischemia reperfusion-induced acute kidney injury. *Cell Signal* **101**, 110506, doi:10.1016/j.cellsig.2022.110506 (2023).
139 Ascension, A. M., Arauzo-Bravo, M. J. & Izeta, A. The need to reassess single-cell RNA sequencing datasets: the importance of biological sample processing. *F1000Res* **10**, 767, doi:10.12688/f1000research.54864.2 (2021).
140 Juran, C. M., Zvirblyte, J., Cheng-Campbell, M., Blaber, E. A. & Almeida, E. A. C. Cdkn1a deletion or suppression by cyclic stretch enhance the osteogenic potential of bone marrow mesenchymal stem cell-derived cultures. *Stem Cell Res* **56**, 102513, doi:10.1016/j.scr.2021.102513 (2021).
141 Cazzalini, O., Scovassi, A. I., Savio, M., Stivala, L. A. & Prosperi, E. Multiple roles of the cell cycle inhibitor p21(CDKN1A) in the DNA damage response. *Mutat Res* **704**, 12-20, doi:10.1016/j.mrrev.2010.01.009 (2010).

142 Karimian, A., Ahmadi, Y. & Yousefi, B. Multiple functions of p21 in cell cycle, apoptosis and transcriptional regulation after DNA damage. *DNA Repair (Amst)* **42**, 63-71, doi:10.1016/j.dnarep.2016.04.008 (2016).

143 Trzpis, M. *et al.* Spatial and temporal expression patterns of the epithelial cell adhesion molecule (EpCAM/EGP-2) in developing and adult kidneys. *Nephron Exp Nephrol* **107**, e119-131, doi:10.1159/000111039 (2007).

144 Simon, N. & Hertig, A. Alteration of Fatty Acid Oxidation in Tubular Epithelial Cells: From Acute Kidney Injury to Renal Fibrogenesis. *Front Med (Lausanne)* **2**, 52, doi:10.3389/fmed.2015.00052 (2015).

145 Madine, M. A., Khoo, C. Y., Mills, A. D. & Laskey, R. A. MCM3 complex required for cell cycle regulation of DNA replication in vertebrate cells. *Nature* **375**, 421-424, doi:10.1038/375421a0 (1995).

146 Nojima, H. *et al.* IQGAP3 regulates cell proliferation through the Ras/ERK signalling cascade. *Nat Cell Biol* **10**, 971-978, doi:10.1038/ncb1757 (2008).

147 Mallipattu, S. K., Estrada, C. C. & He, J. C. The critical role of Kruppel-like factors in kidney disease. *Am J Physiol Renal Physiol* **312**, F259-F265, doi:10.1152/ajprenal.00550.2016 (2017).

148 Ke, B., Zhang, A., Wu, X. & Fang, X. The Role of Kruppel-like Factor 4 in Renal Fibrosis. *Front Physiol* **6**, 327, doi:10.3389/fphys.2015.00327 (2015).

149 Gong, J. *et al.* Kruppel-like factor 4 ameliorates diabetic kidney disease by activating autophagy via the mTOR pathway. *Mol Med Rep* **20**, 3240-3248, doi:10.3892/mmr.2019.10585 (2019).

150 Tan, R. J. & Liu, Y. Matrix metalloproteinases in kidney homeostasis and diseases. *Am J Physiol Renal Physiol* **302**, F1351-1361, doi:10.1152/ajprenal.00037.2012 (2012).

151 Bengatta, S. *et al.* MMP9 and SCF protect from apoptosis in acute kidney injury. *J Am Soc Nephrol* **20**, 787-797, doi:10.1681/ASN.2008050515 (2009).

152 Liu, T. *et al.* Hypoxia-induced PLOD2 promotes clear cell renal cell carcinoma progression via modulating EGFR-dependent AKT pathway activation. *Cell Death Dis* **14**, 774, doi:10.1038/s41419-023-06298-7 (2023).

153 Faria, D. *et al.* The calcium-activated chloride channel Anoctamin 1 contributes to the regulation of renal function. *Kidney Int* **85**, 1369-1381, doi:10.1038/ki.2013.535 (2014).

154 Mehta, N., Gava, A. L., Zhang, D., Gao, B. & Krepinsky, J. C. Follistatin Protects Against Glomerular Mesangial Cell Apoptosis and Oxidative Stress to Ameliorate Chronic Kidney Disease. *Antioxid Redox Signal* **31**, 551-571, doi:10.1089/ars.2018.7684 (2019).

155 Antonioli, L., Pacher, P., Vizi, E. S. & Hasko, G. CD39 and CD73 in immunity and inflammation. *Trends Mol Med* **19**, 355-367, doi:10.1016/j.molmed.2013.03.005 (2013).

156 Barry, F., Boynton, R., Murphy, M. & Zaia, J. The SH-3 and SH-4 Antibodies Recognize Distinct Epitopes on CD73 from Human Mesenchymal Stem Cells. *Biochemical and Biophysical Research Communications* **290**, doi:10.1006/bbrc.2002.6381 (2002).

157 Staff, P. O. Correction: NT5E mutations that cause human disease are associated with intracellular mistrafficking of NT5E protein. *PLoS One* **10**, e0118252, doi:10.1371/journal.pone.0118252 (2015).

158 Adriana Ramírez-Cosmes, E. R.-J., Cecilia Zertuche-Martínez, Carlos A, Hernández-Hernández, R. G.-R., Roberto I Romero-Díaz, Adán E Manuel-Martínez, Jesús & Elizarrarás-Rivas, V. R. V.-G. The implications of ABCC3 in cancer drug resistance: can we use it as a therapeutic target? *Am J Cancer Re* **2021;11(9):4127-4140** (2021).

159 Zhang, G. & Li, Q. Inflammation Induces Lipid Deposition in Kidneys by Downregulating Renal PCSK9 in Mice with Adriamycin-Induced Nephropathy. *Med Sci Monit* **25**, 5327-5335, doi:10.12659/MSM.917312 (2019).

160 Lee, R. G. *et al.* ACAT2 contributes cholesteryl esters to newly secreted VLDL, whereas LCAT adds cholesteryl ester to LDL in mice. *J Lipid Res* **46**, 1205-1212, doi:10.1194/jlr.M500018-JLR200 (2005).

161 Lee, R. G., Willingham, M. C., Davis, M. A., Skinner, K. A. & Rudel, L. L. Differential expression of ACAT1 and ACAT2 among cells within liver, intestine, kidney, and adrenal of nonhuman primates. *Journal of Lipid Research* **41**, 1991-2001, doi:10.1016/s0022-2275(20)32360-9 (2000).

162 Rossi, E., Bernabeu, C. & Smadja, D. M. Endoglin as an Adhesion Molecule in Mature and Progenitor Endothelial Cells: A Function Beyond TGF-beta. *Front Med (Lausanne)* **6**, 10, doi:10.3389/fmed.2019.00010 (2019).

163 Selbi, W. *et al.* Overexpression of hyaluronan synthase 2 alters hyaluronan distribution and function in proximal tubular epithelial cells. *J Am Soc Nephrol* **17**, 1553-1567, doi:10.1681/ASN.2005080879 (2006).

164 Wells, A. *et al.* Increased hyaluronan in acutely rejecting human kidney grafts. *Transplantation* **55**, 1346-1349, doi:10.1097/00007890-199306000-00025 (1993).

165 Hains, D. S. *et al.* Carbonic anhydrase 2 deficiency leads to increased pyelonephritis susceptibility. *Am J Physiol Renal Physiol* **307**, F869-880, doi:10.1152/ajprenal.00344.2014 (2014).

166 Catania, J. M., Chen, G. & Parrish, A. R. Role of matrix metalloproteinases in renal pathophysiologies. *Am J Physiol Renal Physiol* **292**, F905-911, doi:10.1152/ajprenal.00421.2006 (2007).

167 Kassiri, Z. *et al.* Loss of TIMP3 enhances interstitial nephritis and fibrosis. *J Am Soc Nephrol* **20**, 1223-1235, doi:10.1681/ASN.2008050492 (2009).

168 Nechemia-Arbely, Y. *et al.* IL-6/IL-6R axis plays a critical role in acute kidney injury. *J Am Soc Nephrol* **19**, 1106-1115, doi:10.1681/ASN.2007070744 (2008).

169 Shalaby, M. R., Waage, A. & Espevik, T. Cytokine regulation of interleukin 6 production by human endothelial cells. *Cell Immunol* **121**, 372-382, doi:10.1016/0008-8749(89)90036-1 (1989).

170 Yan, S. F. *et al.* Induction of interleukin 6 (IL-6) by hypoxia in vascular cells. Central role of the binding site for nuclear factor-IL-6. *J Biol Chem* **270**, 11463-11471, doi:10.1074/jbc.270.19.11463 (1995).

171 Tornavaca, O. *et al.* Kidney androgen-regulated protein transgenic mice show hypertension and renal alterations mediated by oxidative stress. *Circulation* **119**, 1908-1917, doi:10.1161/CIRCULATIONAHA.108.808543 (2009).

172 Fang, W. K. *et al.* A novel alternative spliced variant of neutrophil gelatinase-associated lipocalin receptor in oesophageal carcinoma cells. *Biochem J* **403**, 297-303, doi:10.1042/BJ20060836 (2007).

173 Ichimura, T. *et al.* Kidney injury molecule-1 (KIM-1), a putative epithelial cell adhesion molecule containing a novel immunoglobulin domain, is up-regulated in renal cells after injury. *J Biol Chem* **273**, 4135-4142, doi:10.1074/jbc.273.7.4135 (1998).

174 Kuehn, E. W., Park, K. M., Somlo, S. & Bonventre, J. V. Kidney injury molecule-1 expression in murine polycystic kidney disease. *Am J Physiol Renal Physiol* **283**, F1326-1336, doi:10.1152/ajprenal.00166.2002 (2002).

175 Alberts B, J. A., Lewis J, et al. in *Molecular Biology of the Cell. 4th edition. New York: Garland Science* (2002).

176 Short, S., Lewik, G. & Issa, F. An Immune Atlas of T Cells in Transplant Rejection: Pathways and Therapeutic Opportunities. *Transplantation* **107**, 2341-2352, doi:10.1097/TP.0000000000004572 (2023).
177 Gaughan, A. *et al.* Key role for CD4 T cells during mixed antibody-mediated rejection of renal allografts. *Am J Transplant* **14**, 284-294, doi:10.1111/ajt.12596 (2014).
178 Zhang, N. & Bevan, M. J. CD8(+) T cells: foot soldiers of the immune system. *Immunity* **35**, 161-168, doi:10.1016/j.immuni.2011.07.010 (2011).
179 Gueler, F., Gwinner, W., Schwarz, A. & Haller, H. Long-term effects of acute ischemia and reperfusion injury. *Kidney Int* **66**, 523-527, doi:10.1111/j.1523-1755.2004.761_11.x (2004).
180 Zuidema, M. Y. & Zhang, C. Ischemia/reperfusion injury: The role of immune cells. *World J Cardiol* **2**, 325-332, doi:10.4330/wjc.v2.i10.325 (2010).
181 Nicosia, M., Fairchild, R. L. & Valujskikh, A. Memory T Cells in Transplantation: Old Challenges Define New Directions. *Transplantation* **104**, 2024-2034, doi:10.1097/TP.0000000000003169 (2020).
182 Espinosa, J. R., Samy, K. P. & Kirk, A. D. Memory T cells in organ transplantation: progress and challenges. *Nat Rev Nephrol* **12**, 339-347, doi:10.1038/nrneph.2016.9 (2016).
183 Scozzi, D. *et al.* The Role of Neutrophils in Transplanted Organs. *Am J Transplant* **17**, 328-335, doi:10.1111/ajt.13940 (2017).
184 Qu, J., Jin, J., Zhang, M. & Ng, L. G. Neutrophil diversity and plasticity: Implications for organ transplantation. *Cell Mol Immunol* **20**, 993-1001, doi:10.1038/s41423-023-01058-1 (2023).
185 Panzer, S. E. Macrophages in Transplantation: A Matter of Plasticity, Polarization, and Diversity. *Transplantation* **106**, 257-267, doi:10.1097/TP.0000000000003804 (2022).
186 Medzhitov, R. & Janeway, C. A., Jr. Decoding the patterns of self and nonself by the innate immune system. *Science* **296**, 298-300, doi:10.1126/science.1068883 (2002).
187 Malone, A. F. Monocytes and Macrophages in Kidney Transplantation and Insights from Single Cell RNA-Seq Studies. *Kidney360* **2**, 1654-1659, doi:10.34067/KID.0003842021 (2021).
188 Yang, J., Zhang, L., Yu, C., Yang, X. F. & Wang, H. Monocyte and macrophage differentiation: circulation inflammatory monocyte as biomarker for inflammatory diseases. *Biomark Res* **2**, 1, doi:10.1186/2050-7771-2-1 (2014).
189 Clements, M. *et al.* Differential Ly6C Expression after Renal Ischemia-Reperfusion Identifies Unique Macrophage Populations. *J Am Soc Nephrol* **27**, 159-170, doi:10.1681/ASN.2014111138 (2016).
190 Chiossone, L. *et al.* Maturation of mouse NK cells is a 4-stage developmental program. *Blood* **113**, 5488-5496, doi:10.1182/blood-2008-10-187179 (2009).
191 Hayakawa, Y., Huntington, N. D., Nutt, S. L. & Smyth, M. J. Functional subsets of mouse natural killer cells. *Immunol Rev* **214**, 47-55, doi:10.1111/j.1600-065X.2006.00454.x (2006).
192 Alter, G., Malenfant, J. M. & Altfeld, M. CD107a as a functional marker for the identification of natural killer cell activity. *J Immunol Methods* **294**, 15-22, doi:10.1016/j.jim.2004.08.008 (2004).
193 Aktas, E., Kucuksezer, U. C., Bilgic, S., Erten, G. & Deniz, G. Relationship between CD107a expression and cytotoxic activity. *Cell Immunol* **254**, 149-154, doi:10.1016/j.cellimm.2008.08.007 (2009).

194 Ivashkiv, L. B. IFNgamma: signalling, epigenetics and roles in immunity, metabolism, disease and cancer immunotherapy. *Nat Rev Immunol* **18**, 545-558, doi:10.1038/s41577-018-0029-z (2018).

195 Schroder, K., Hertzog, P. J., Ravasi, T. & Hume, D. A. Interferon-gamma: an overview of signals, mechanisms and functions. *J Leukoc Biol* **75**, 163-189, doi:10.1189/jlb.0603252 (2004).

196 Ramirez-Labrada, A. *et al.* All About (NK Cell-Mediated) Death in Two Acts and an Unexpected Encore: Initiation, Execution and Activation of Adaptive Immunity. *Front Immunol* **13**, 896228, doi:10.3389/fimmu.2022.896228 (2022).

197 Osinska, I., Popko, K. & Demkow, U. Perforin: an important player in immune response. *Cent Eur J Immunol* **39**, 109-115, doi:10.5114/ceji.2014.42135 (2014).

198 Pasatu-Cornea, A. M., Ciciu, E. & Tuta, L. A. Perforin: An intriguing protein in allograft rejection immunology (Review). *Exp Ther Med* **24**, 519, doi:10.3892/etm.2022.11446 (2022).

199 Suarez-Alvarez, B. *et al.* NKG2D and its ligands: active factors in the outcome of solid organ transplantation? *Kidney Int Suppl (2011)* **1**, 52-57, doi:10.1038/kisup.2011.13 (2011).

200 Suarez-Alvarez, B., Lopez-Vazquez, A., Baltar, J. M., Ortega, F. & Lopez-Larrea, C. Potential role of NKG2D and its ligands in organ transplantation: new target for immunointervention. *Am J Transplant* **9**, 251-257, doi:10.1111/j.1600-6143.2008.02526.x (2009).

201 Zhu, L. *et al.* Circulating NKG2A-NKG2D+ CD56dimCD16+ Natural Killer (NK) Cells as Mediators of Functional Immunosurveillance in Kidney Transplant Recipients. *Ann Transplant* **25**, e925162, doi:10.12659/AOT.925162 (2020).

202 Eteghadi, A. *et al.* Th1, Th2, Th17 cell subsets in two different immunosuppressive protocols in renal allograft recipients (Sirolimus vs mycophenolate mofetil): A cohort study. *Int Immunopharmacol* **67**, 319-325, doi:10.1016/j.intimp.2018.12.033 (2019).

203 Hricik, D. E. Transplant immunology and immunosuppression: core curriculum 2015. *Am J Kidney Dis* **65**, 956-966, doi:10.1053/j.ajkd.2015.01.026 (2015).

204 Van der Hauwaert, C. *et al.* Isolation and characterization of a primary proximal tubular epithelial cell model from human kidney by CD10/CD13 double labeling. *PLoS One* **8**, e66750, doi:10.1371/journal.pone.0066750 (2013).

205 Baer, P. C., Bereiter-Hahn, J., Schubert, R. & Geiger, H. Differentiation status of human renal proximal and distal tubular epithelial cells in vitro: Differential expression of characteristic markers. *Cells Tissues Organs* **184**, 16-22, doi:10.1159/000096947 (2006).

206 Bonventre, J. V. Dedifferentiation and proliferation of surviving epithelial cells in acute renal failure. *J Am Soc Nephrol* **14 Suppl 1**, S55-61, doi:10.1097/01.asn.0000067652.51441.21 (2003).

207 Petreski, T., Varda, L., Gradisnik, L., Maver, U. & Bevc, S. Renal Proximal Tubular Epithelial Cells: From Harvesting to Use in Studies. *Nephron* **147**, 650-654, doi:10.1159/000531291 (2023).

208 Wagner, C. A. *et al.* A rapid enzymatic method for the isolation of defined kidney tubule fragments from mouse. *Pflugers Arch* **446**, 623-632, doi:10.1007/s00424-003-1082-3 (2003).

209 Tang, M. J., Cheng, Y. R. & Lin, H. H. Role of apoptosis in growth and differentiation of proximal tubule cells in primary cultures. *Biochem Biophys Res Commun* **218**, 658-664, doi:10.1006/bbrc.1996.0118 (1996).

210 Terryn, S. *et al.* A primary culture of mouse proximal tubular cells, established on collagen-coated membranes. *Am J Physiol Renal Physiol* **293**, F476-485, doi:10.1152/ajprenal.00363.2006 (2007).

211 Detrisac, C. J., Sens, M. A., Garvin, A. J., Spicer, S. S. & Sens, D. A. Tissue culture of human kidney epithelial cells of proximal tubule origin. *Kidney Int* **25**, 383-390, doi:10.1038/ki.1984.28 (1984).

212 Tang, M. J. & Tannen, R. L. Relationship between proliferation and glucose metabolism in primary cultures of rabbit proximal tubules. *Am J Physiol* **259**, C455-461, doi:10.1152/ajpcell.1990.259.3.C455 (1990).

213 Sharpe, C. C. & Dockrell, M. E. Primary culture of human renal proximal tubule epithelial cells and interstitial fibroblasts. *Methods Mol Biol* **806**, 175-185, doi:10.1007/978-1-61779-367-7_12 (2012).

214 Vesey, D. A., Qi, W., Chen, X., Pollock, C. A. & Johnson, D. W. Isolation and primary culture of human proximal tubule cells. *Methods Mol Biol* **466**, 19-24, doi:10.1007/978-1-59745-352-3_2 (2009).

215 Vormann, M. K. *et al.* Implementation of a Human Renal Proximal Tubule on a Chip for Nephrotoxicity and Drug Interaction Studies. *J Pharm Sci* **110**, 1601-1614, doi:10.1016/j.xphs.2021.01.028 (2021).

216 Witzgall, R., Brown, D., Schwarz, C. & Bonventre, J. V. Localization of proliferating cell nuclear antigen, vimentin, c-Fos, and clusterin in the postischemic kidney. Evidence for a heterogenous genetic response among nephron segments, and a large pool of mitotically active and dedifferentiated cells. *J Clin Invest* **93**, 2175-2188, doi:10.1172/JCI117214 (1994).

217 Kriz, W., Kaissling, B. & Le Hir, M. Epithelial-mesenchymal transition (EMT) in kidney fibrosis: fact or fantasy? *J Clin Invest* **121**, 468-474, doi:10.1172/jci44595 (2011).

218 Schroder, S. K., Gasterich, N., Weiskirchen, S. & Weiskirchen, R. Lipocalin 2 receptors: facts, fictions, and myths. *Front Immunol* **14**, 1229885, doi:10.3389/fimmu.2023.1229885 (2023).

219 Xia, S. *et al.* Long Term Culture of Human Kidney Proximal Tubule Epithelial Cells Maintains Lineage Functions and Serves as an Ex vivo Model for Coronavirus Associated Kidney Injury. *Virol Sin* **35**, 311-320, doi:10.1007/s12250-020-00253-y (2020).

220 Secker, P. F., Luks, L., Schlichenmaier, N. & Dietrich, D. R. RPTEC/TERT1 cells form highly differentiated tubules when cultured in a 3D matrix. *ALTEX* **35**, 223-234, doi:10.14573/altex.1710181 (2018).

221 Taub, M. L. Primary culture of proximal tubule cells in defined medium. *Journal of Tissue Culture Methods* **9**, 67-71, doi:10.1007/bf01797777 (1985).

222 Garmaa, G., Manzeger, A., Haghighi, S. & Kokeny, G. HK-2 cell response to TGF-beta highly depends on cell culture medium formulations. *Histochem Cell Biol* **161**, 69-79, doi:10.1007/s00418-023-02237-x (2024).

223 Guo, C. *et al.* Claudin-2 Mediates the Proximal Tubular Epithelial Cell-Fibroblast Crosstalk via Paracrine CTGF. *Diabetes Metab Syndr Obes* **17**, 55-73, doi:10.2147/DMSO.S432173 (2024).

224 Linas, S. L. & Repine, J. E. Endothelial cells regulate proximal tubule epithelial cell sodium transport. *Kidney Int* **55**, 1251-1258, doi:10.1046/j.1523-1755.1999.00360.x (1999).

225 Carracedo, M. *et al.* 3D vascularised proximal tubules-on-a-multiplexed chip model for enhanced cell phenotypes. *Lab Chip* **23**, 3226-3237, doi:10.1039/d2lc00723a (2023).

226 Jang, H. S. *et al.* Activation of ERK accelerates repair of renal tubular epithelial cells, whereas it inhibits progression of fibrosis following ischemia/reperfusion injury. *Biochim Biophys Acta* **1832**, 1998-2008, doi:10.1016/j.bbadis.2013.07.001 (2013).

227 Sinha, D., Bannergee, S., Schwartz, J. H., Lieberthal, W. & Levine, J. S. Inhibition of ligand-independent ERK1/2 activity in kidney proximal tubular cells deprived of soluble survival factors up-regulates Akt and prevents apoptosis. *J Biol Chem* **279**, 10962-10972, doi:10.1074/jbc.M312048200 (2004).

228 Wortzel, I. & Seger, R. The ERK Cascade: Distinct Functions within Various Subcellular Organelles. *Genes Cancer* **2**, 195-209, doi:10.1177/1947601911407328 (2011).

229 Capolongo, G. *et al.* ERK1,2 Signalling Pathway along the Nephron and Its Role in Acid-base and Electrolytes Balance. *Int J Mol Sci* **20**, doi:10.3390/ijms20174153 (2019).

230 Kwon, D. S. *et al.* Signal transduction of MEK/ERK and PI3K/Akt activation by hypoxia/reoxygenation in renal epithelial cells. *Eur J Cell Biol* **85**, 1189-1199, doi:10.1016/j.ejcb.2006.06.001 (2006).

231 Hui, Z. *et al.* Increased expression of LCN2 formed a positive feedback loop with activation of the ERK pathway in human kidney cells during kidney stone formation. *Sci Rep* **10**, 21287, doi:10.1038/s41598-020-75670-w (2020).

232 Tao, M. *et al.* Blockade of ERK1/2 by U0126 alleviates uric acid-induced EMT and tubular cell injury in rats with hyperuricemic nephropathy. *Am J Physiol Renal Physiol* **316**, F660-F673, doi:10.1152/ajprenal.00480.2018 (2019).

233 Nowak, G., Clifton, G. L., Godwin, M. L. & Bakajsova, D. Activation of ERK1/2 pathway mediates oxidant-induced decreases in mitochondrial function in renal cells. *Am J Physiol Renal Physiol* **291**, F840-855, doi:10.1152/ajprenal.00219.2005 (2006).

234 Lu, Z. & Xu, S. ERK1/2 MAP kinases in cell survival and apoptosis. *IUBMB Life* **58**, 621-631, doi:10.1080/15216540600957438 (2006).

235 Ding, G. *et al.* Over-expression of lipocalin 2 promotes cell migration and invasion through activating ERK signaling to increase SLUG expression in prostate cancer. *Prostate* **75**, 957-968, doi:10.1002/pros.22978 (2015).

236 Preiser, J. C. Oxidative stress. *JPEN J Parenter Enteral Nutr* **36**, 147-154, doi:10.1177/0148607111434963 (2012).

237 Tomsa, A. M., Alexa, A. L., Junie, M. L., Rachisan, A. L. & Ciumarnean, L. Oxidative stress as a potential target in acute kidney injury. *PeerJ* **7**, e8046, doi:10.7717/peerj.8046 (2019).

238 Viau, A. *et al.* Lipocalin 2 is essential for chronic kidney disease progression in mice and humans. *J Clin Invest* **120**, 4065-4076, doi:10.1172/JCI42004 (2010).

239 Yammine, L., Zablocki, A., Baron, W., Terzi, F. & Gallazzini, M. Lipocalin-2 Regulates Epidermal Growth Factor Receptor Intracellular Trafficking. *Cell Rep* **29**, 2067-2077 e2066, doi:10.1016/j.celrep.2019.10.015 (2019).

240 Hallman, M. A., Zhuang, S. & Schnellmann, R. G. Regulation of dedifferentiation and redifferentiation in renal proximal tubular cells by the epidermal growth factor receptor. *J Pharmacol Exp Ther* **325**, 520-528, doi:10.1124/jpet.107.134031 (2008).

241 Hinze, C. *et al.* Kidney Single-cell Transcriptomes Predict Spatial Corticomedullary Gene Expression and Tissue Osmolality Gradients. *J Am Soc Nephrol* **32**, 291-306, doi:10.1681/ASN.2020070930 (2021).

242 Liberzon, A. *et al.* The Molecular Signatures Database (MSigDB) hallmark gene set collection. *Cell Syst* **1**, 417-425, doi:10.1016/j.cels.2015.12.004 (2015).

243 Subramanian, A. *et al.* Gene set enrichment analysis: a knowledge-based approach for interpreting genome-wide expression profiles. *Proc Natl Acad Sci U S A* **102**, 15545-15550, doi:10.1073/pnas.0506580102 (2005).

244 Su, H., Lei, C. T. & Zhang, C. Interleukin-6 Signaling Pathway and Its Role in Kidney Disease: An Update. *Front Immunol* **8**, 405, doi:10.3389/fimmu.2017.00405 (2017).

245 Warvariv V, I. S., Esquivel CO. . Transplantation immunology. *Surg Technol Int.* **Oct;2:147-53** (1993).

246 Hueper, K. *et al.* Longitudinal evaluation of perfusion changes in acute and chronic renal allograft rejection using arterial spin labeling in translational mouse models. *J Magn Reson Imaging* **46**, 1664-1672, doi:10.1002/jmri.25713 (2017).

247 Haase-Fielitz, A. *et al.* The predictive performance of plasma neutrophil gelatinase-associated lipocalin (NGAL) increases with grade of acute kidney injury. *Nephrol Dial Transplant* **24**, 3349-3354, doi:10.1093/ndt/gfp234 (2009).

248 Chevalier, R. L. The proximal tubule is the primary target of injury and progression of kidney disease: role of the glomerulotubular junction. *Am J Physiol Renal Physiol* **311**, F145-161, doi:10.1152/ajprenal.00164.2016 (2016).

249 Sekine, M. *et al.* Selective depletion of mouse kidney proximal straight tubule cells causes acute kidney injury. *Transgenic Res* **21**, 51-62, doi:10.1007/s11248-011-9504-z (2012).

250 P. F. Shanley, M. D. R., M. Brezis, P. Silva, F. H. Epstein, and S. Rosen. Topography of focal proximal tubular necrosis after ischemia with reflow in the rat kidney. *Am J Pathol.* (1986).

251 Venkatachalam, M. A., Bernard, D. B., Donohoe, J. F. & Levinsky, N. G. Ischemic damage and repair in the rat proximal tubule: differences among the S1, S2, and S3 segments. *Kidney Int* **14**, 31-49, doi:10.1038/ki.1978.87 (1978).

6 SUPPLEMENT

6.1 SUPPLEMENTARY FIGURES

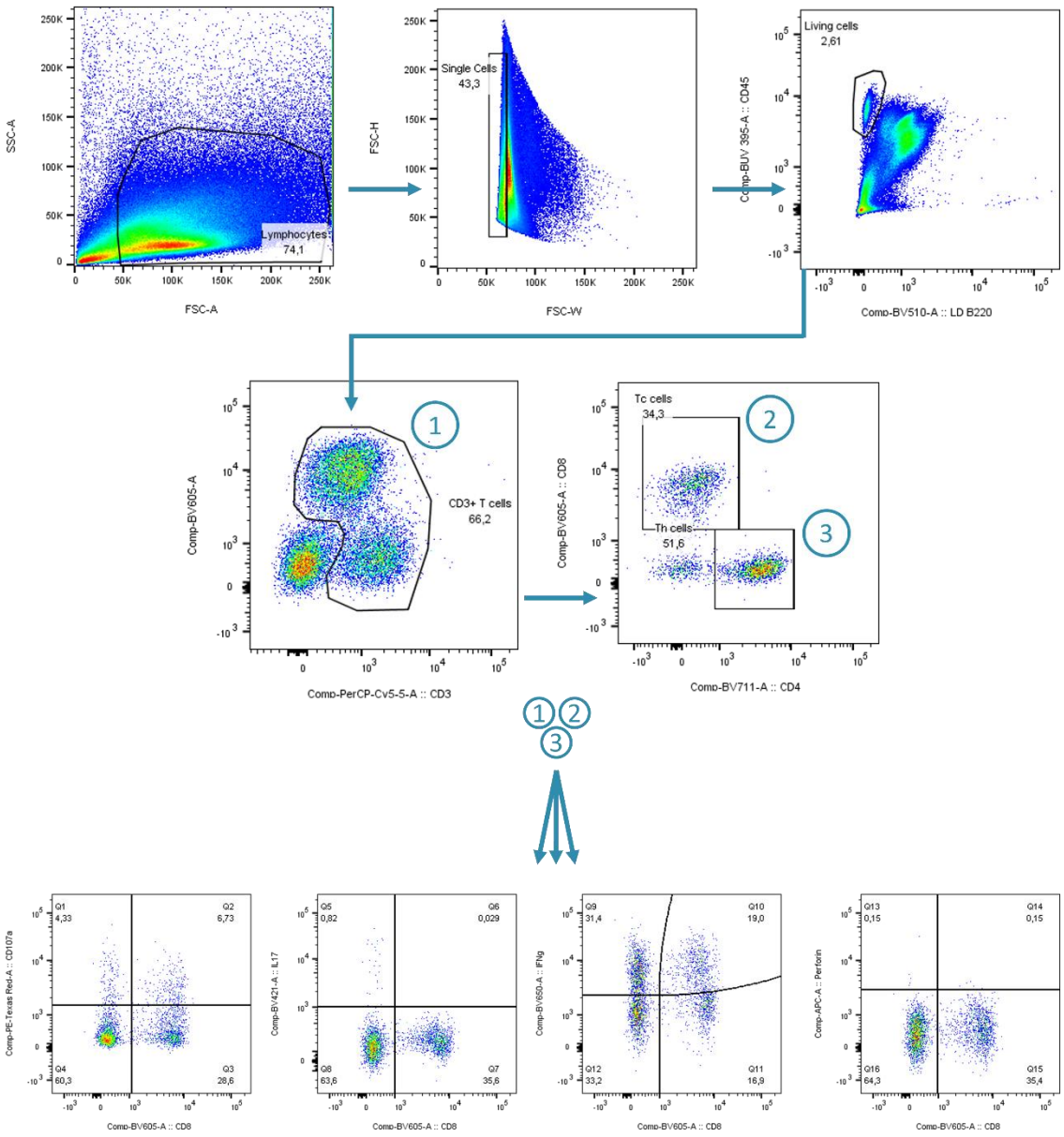

Figure S1: Gating strategy Functional-Panel.

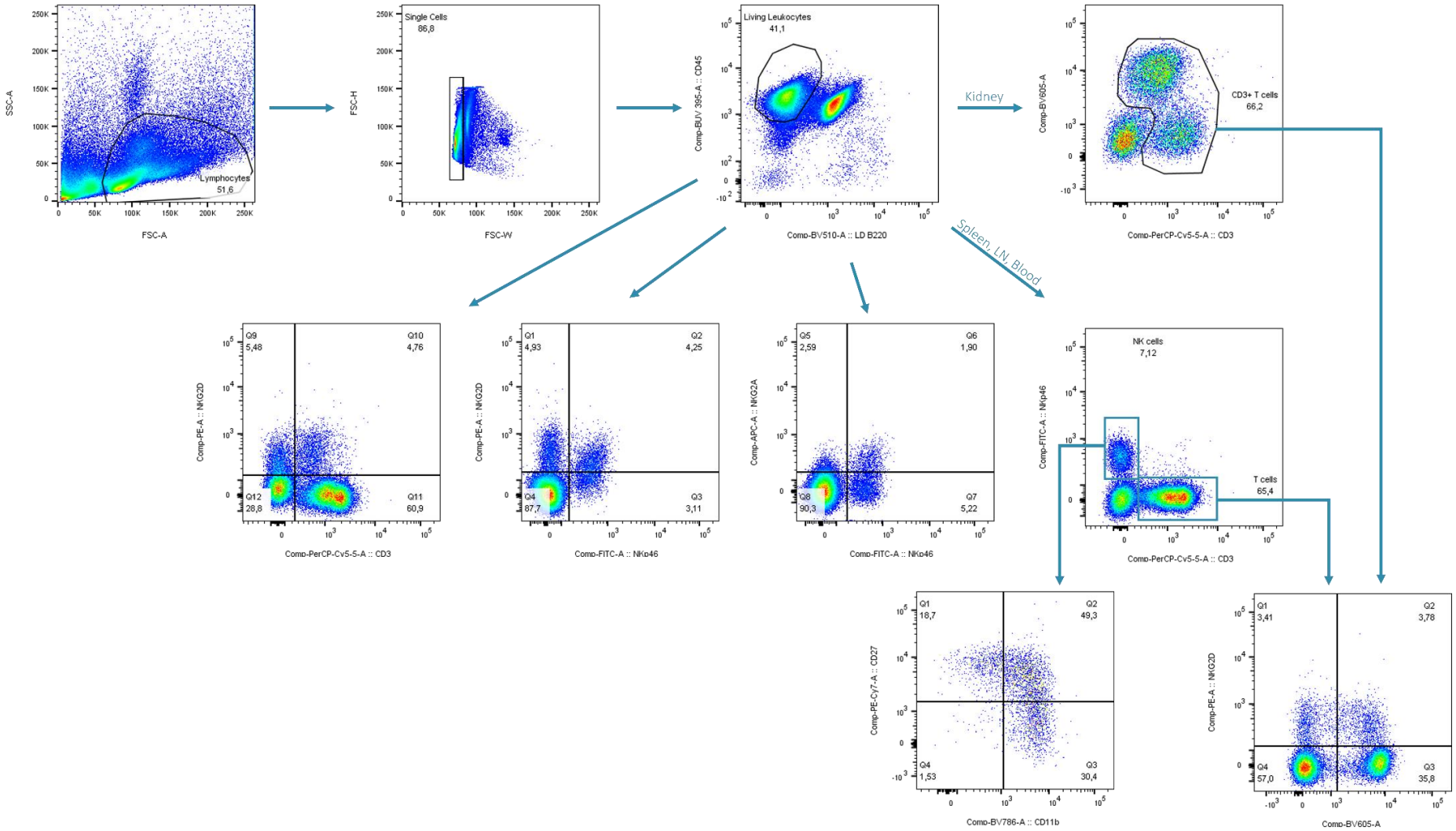

Figure S2: Gating strategy for NK-Panel.

To distinguish T-cells from non-T-cells in the kidney graft, CD8 was plotted against CD3 and from that gate NKG2D was plotted against CD8. To determine the other cell populations, the gating strategy remained the same. LN = lymph node

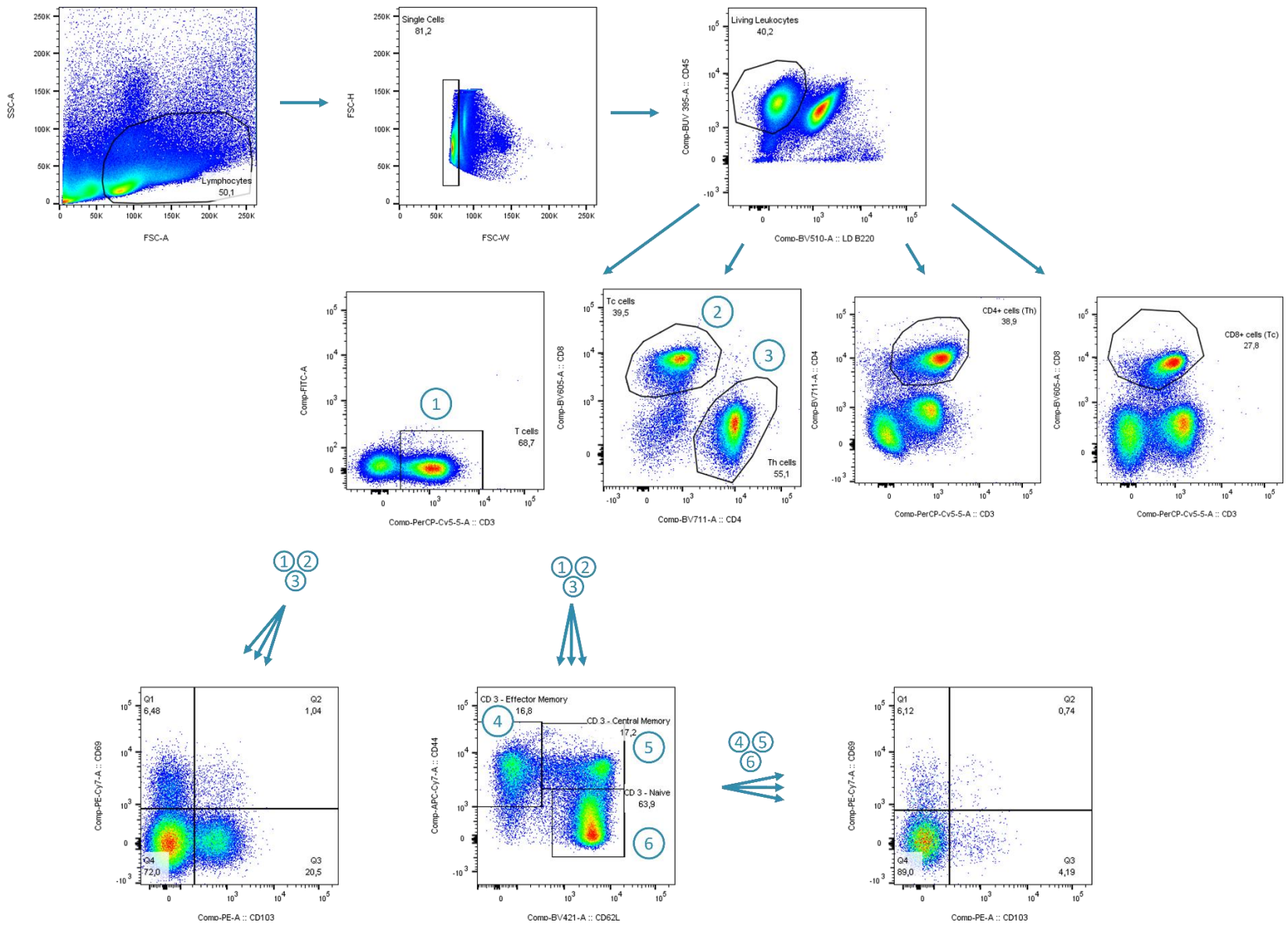

Figure S3: Gating strategy T-Panel.

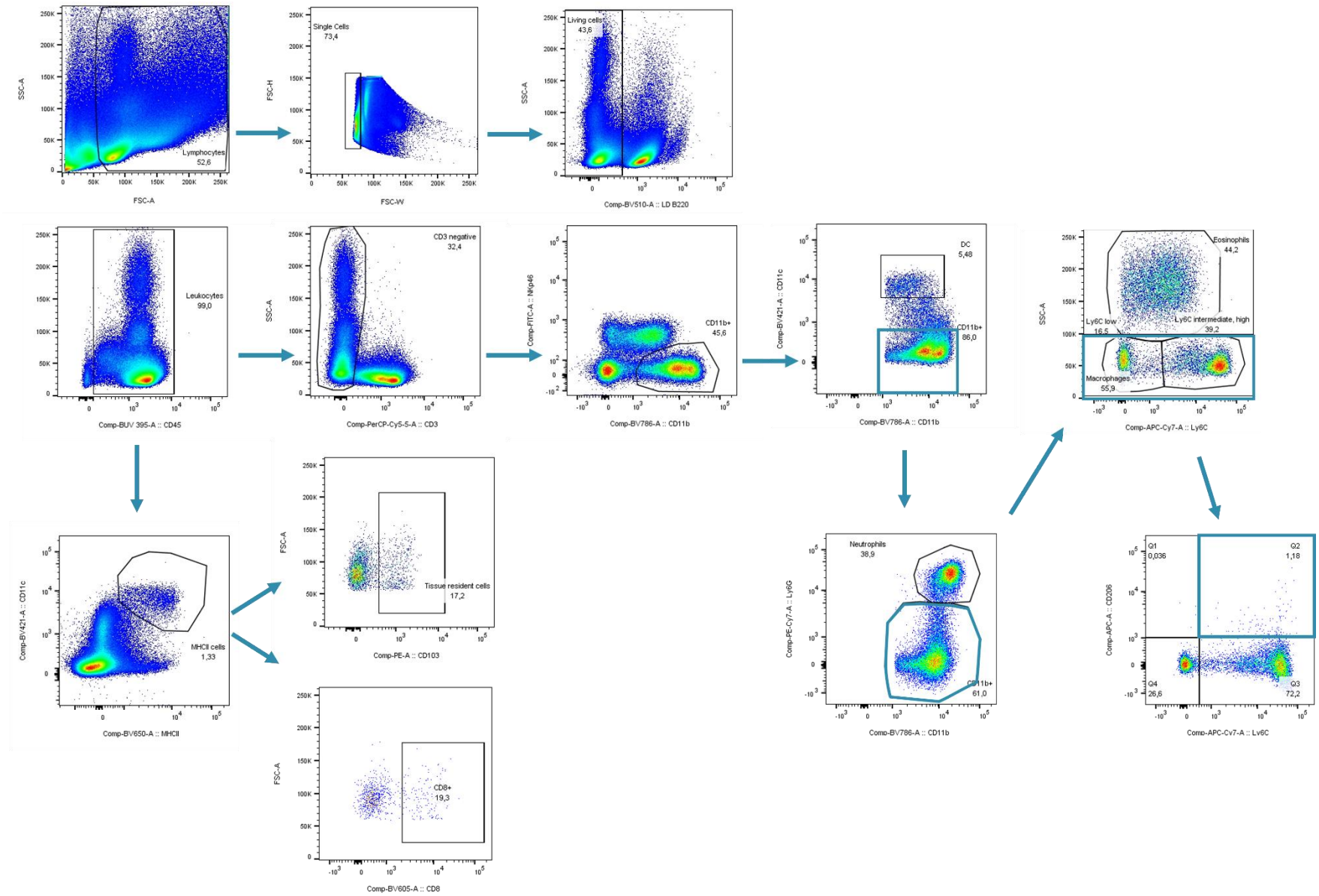

Figure S4: Gating strategy Innate-Panel.

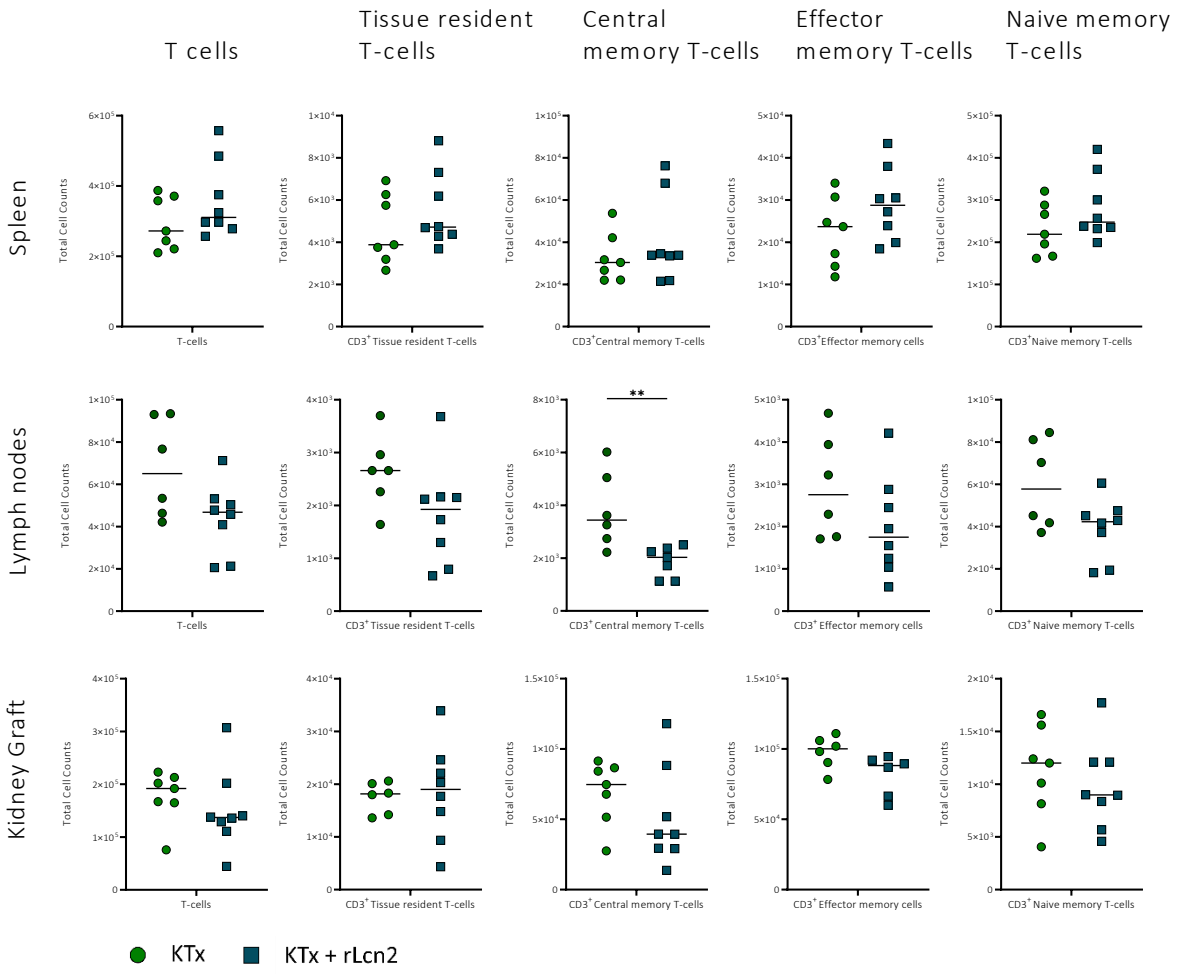

Figure S5: Treatment with rLcn2 significantly lowers total cell counts of central memory T-cells in lymph nodes at pod-3 after allogenic mKTx.

Immune cells were isolated from spleens, lymph nodes, kidney grafts, and blood after allogenic murine kidney transplantations from Balb/c to C57Bl/6 mice (n = 7-8) on pod-3 and pod-7. Immune cells were stained with a cocktail of monoclonal antibodies (*T-Panel*, **Table 10**). Total cell counts of T-cell and T-cell subpopulations were acquired on a BD LSRFortessa™ Cell Analyzer using Precision count™ beads for reference. Analysis and calculations were done using FlowJo™ and GraphPad Prism software. Horizontal lines represent the respective mean. Statistical analysis: Mann-Whitney t-test; * $p < 0.05$, ** $p \leq 0.01$.

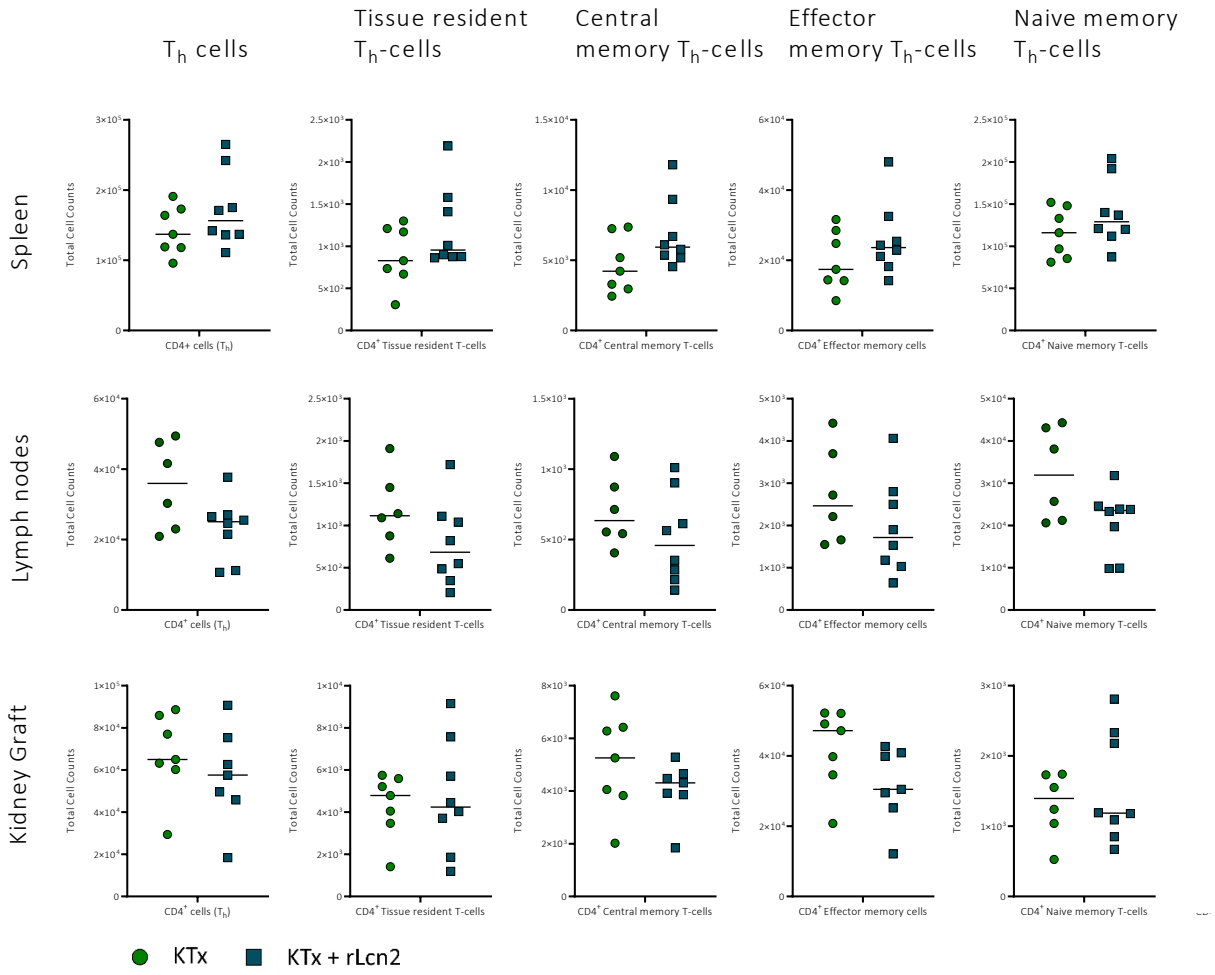

Figure S6: Treatment with rLcn2 does not affect total cell counts of T$_h$-cells at pod-3 after allogenic mKTx.
Immune cells were isolated from spleens, lymph nodes, kidney grafts, and blood after allogenic murine kidney transplantations from Balb/c to C57Bl/6 mice (n = 7-8) on pod-3 and pod-7. Immune cells were stained and analysed as stated in **Figure S5** (*T-Panel*, **Table 10**). Horizontal lines represent the respective mean. Statistical analysis: Mann-Whitney t-test; * $p < 0.05$, ** $p \leq 0.01$

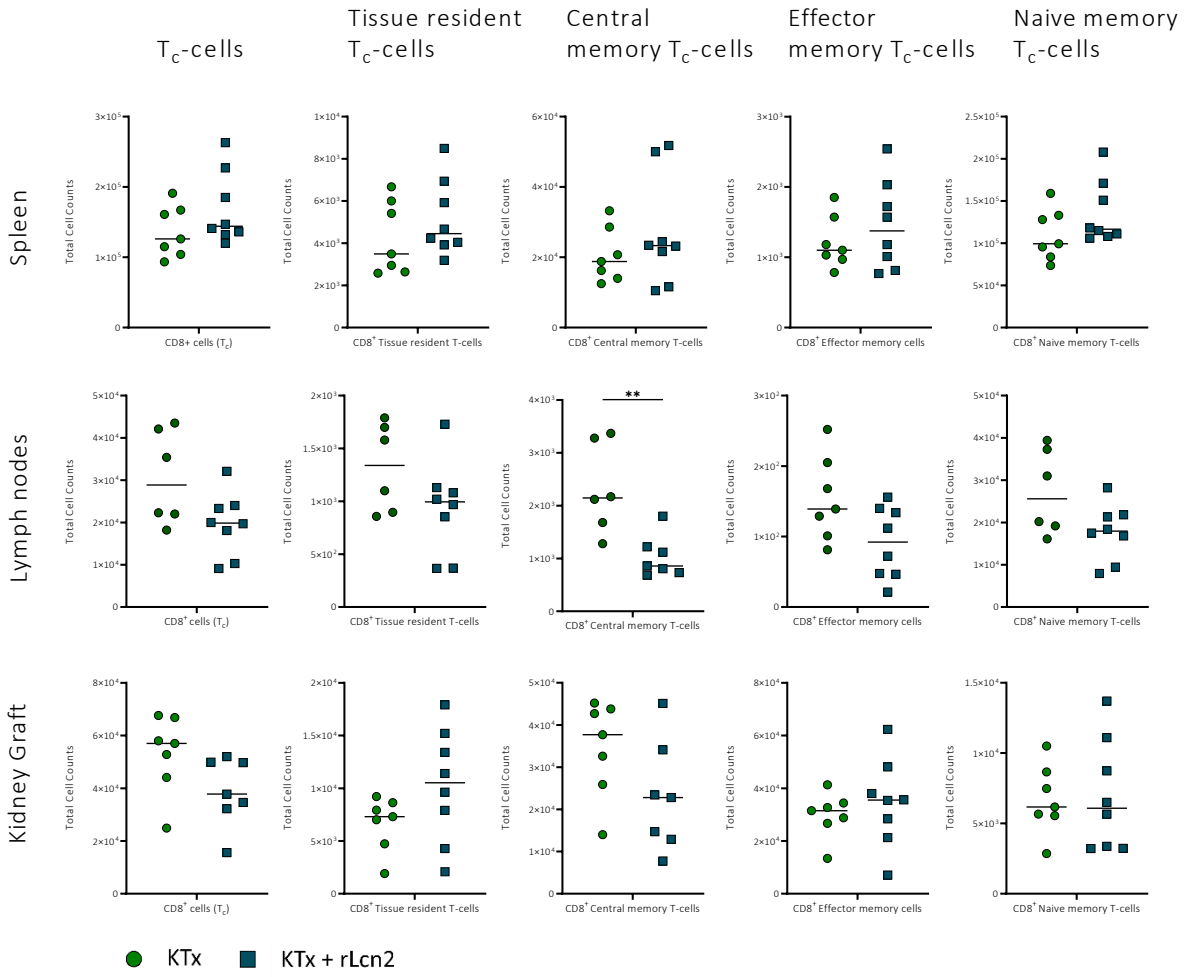

Figure S7: Total cell counts of central memory cytotoxic T-cells were significantly reduced in lymph nodes due to treatment with rLcn2 at pod-3 after allogenic mKTx.

Immune cells were isolated from spleens, lymph nodes, kidney grafts, and blood after allogenic murine kidney transplantations from Balb/c to C57Bl/6 mice (n = 7-8) on pod-3 and pod-7. Immune cells were stained and analysed as stated in **Figure S5** (*T-Panel*, **Table 10**). Horizontal lines represent the respective mean. Statistical analysis: Mann-Whitney t-test; * $p < 0.05$, ** $p \leq 0.01$.

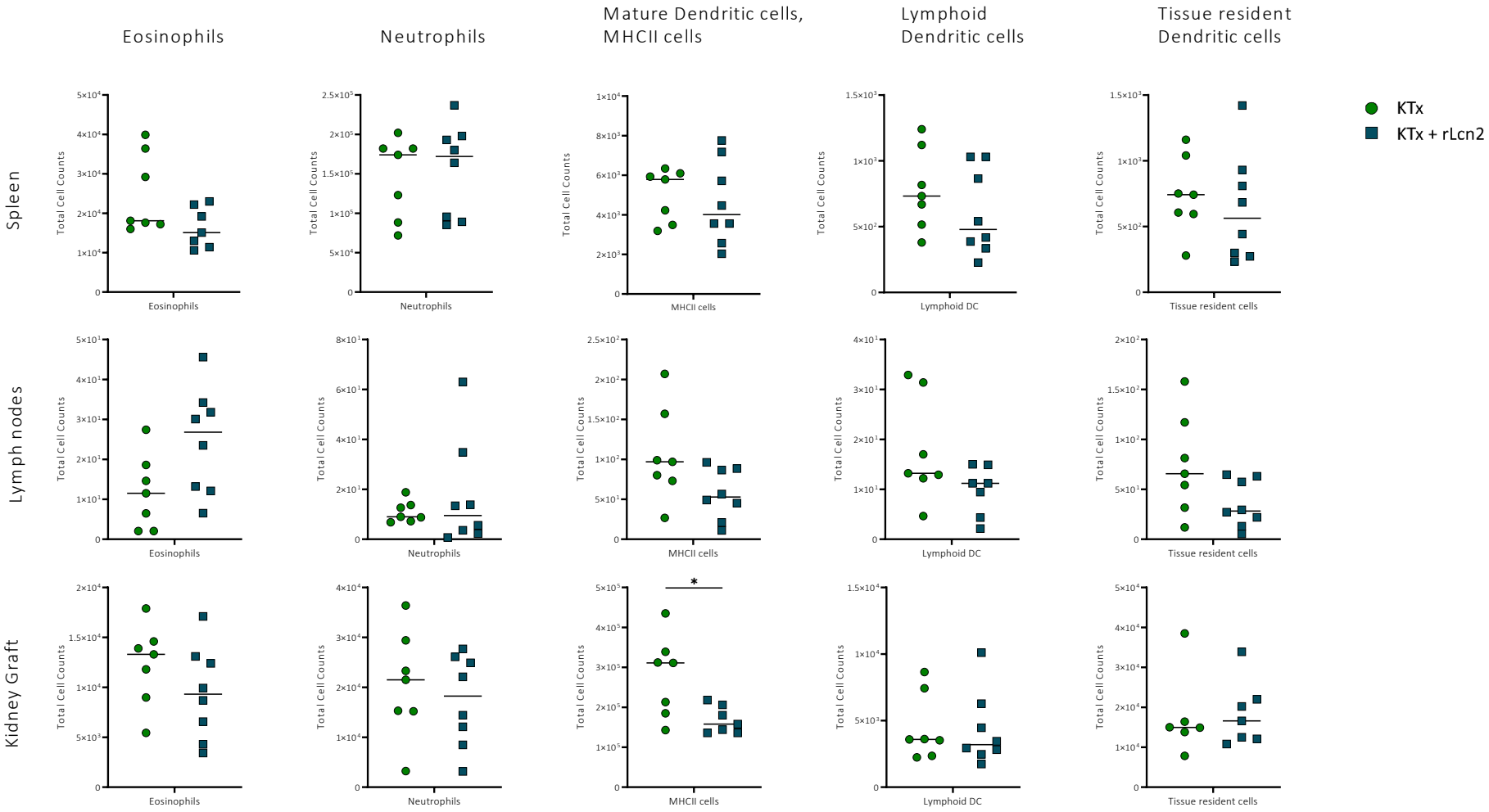

Figure S8: rLcn2-treatment significantly reduces the amount of mature dendritic cells in kidney grafts at pod-3 after allogeneic mKTx.
Immune cells were isolated from spleens, lymph nodes, kidney grafts, and blood after allogenic murine kidney transplantations from Balb/c to C57Bl/6 mice (n = 7-8) on pod-3 and pod-7. The same staining protocol and analysis methods as described in **Figure S5** were employed to assess the impact of rLcn2-treatment on total cell counts of innate immune cells (*Innate-Panel*, **Table 10**). Horizontal lines represent the respective mean. Statistical analysis: Mann-Whitney t-test; * $p < 0.05$, ** $p \leq 0.01$

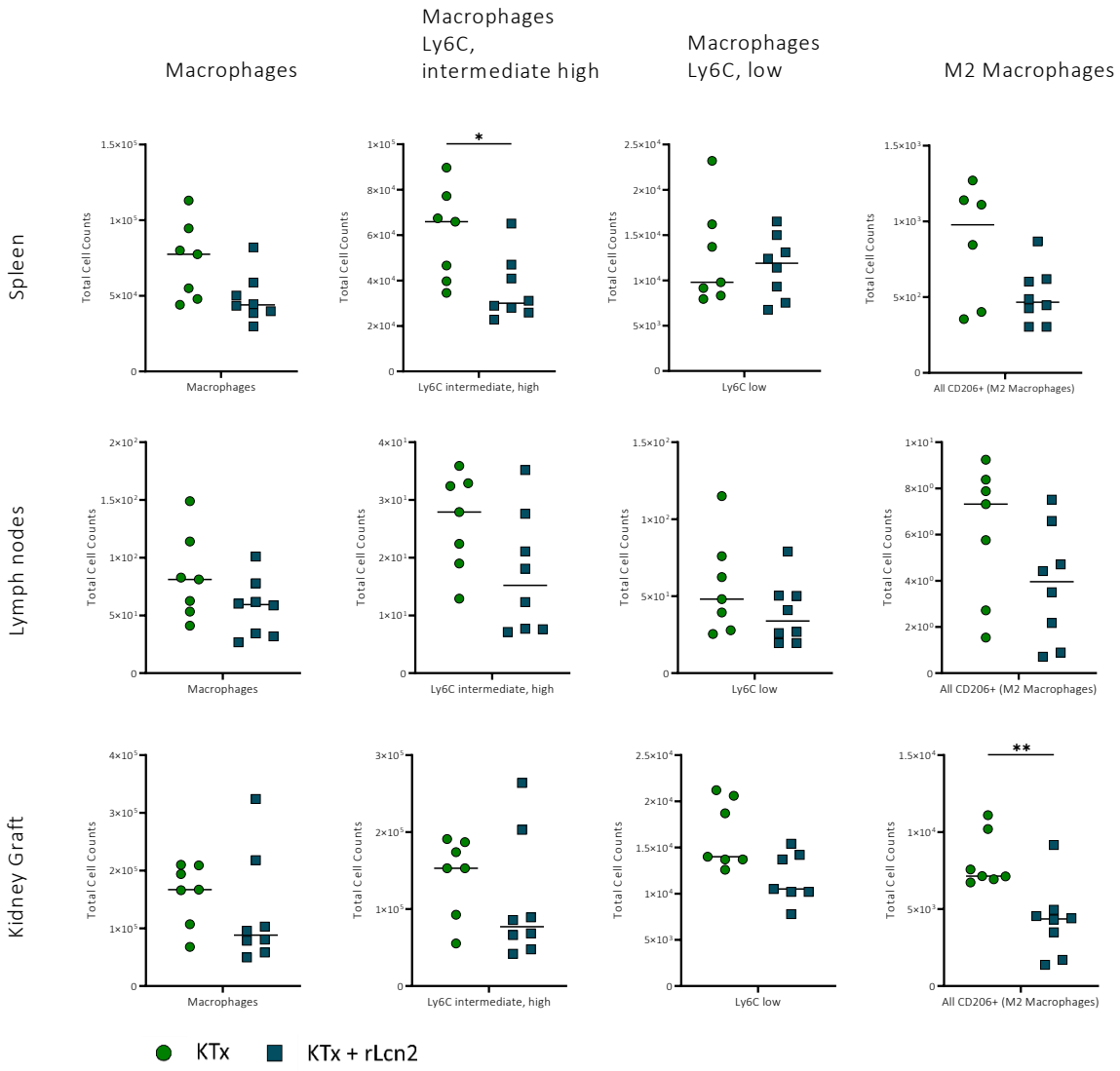

Figure S9: Treatment with rLcn2 significantly reduces the amount distinct macrophage populations at pod-3 after allogeneic mKTx.

Immune cells were isolated from spleens, lymph nodes, kidney grafts, and blood after allogenic murine kidney transplantations from Balb/c to C57Bl/6 mice (n = 7-8) on pod-3 and pod-7. The same staining protocol and analysis methods as described in **Figure S5** were employed to assess the impact of rLcn2-treatment on total cell counts of innate immune cells (*Innate-Panel*, **Table 10**). Horizontal lines represent the respective mean. Statistical analysis: Mann-Whitney t-test; * $p < 0.05$, ** $p \leq 0.01$.

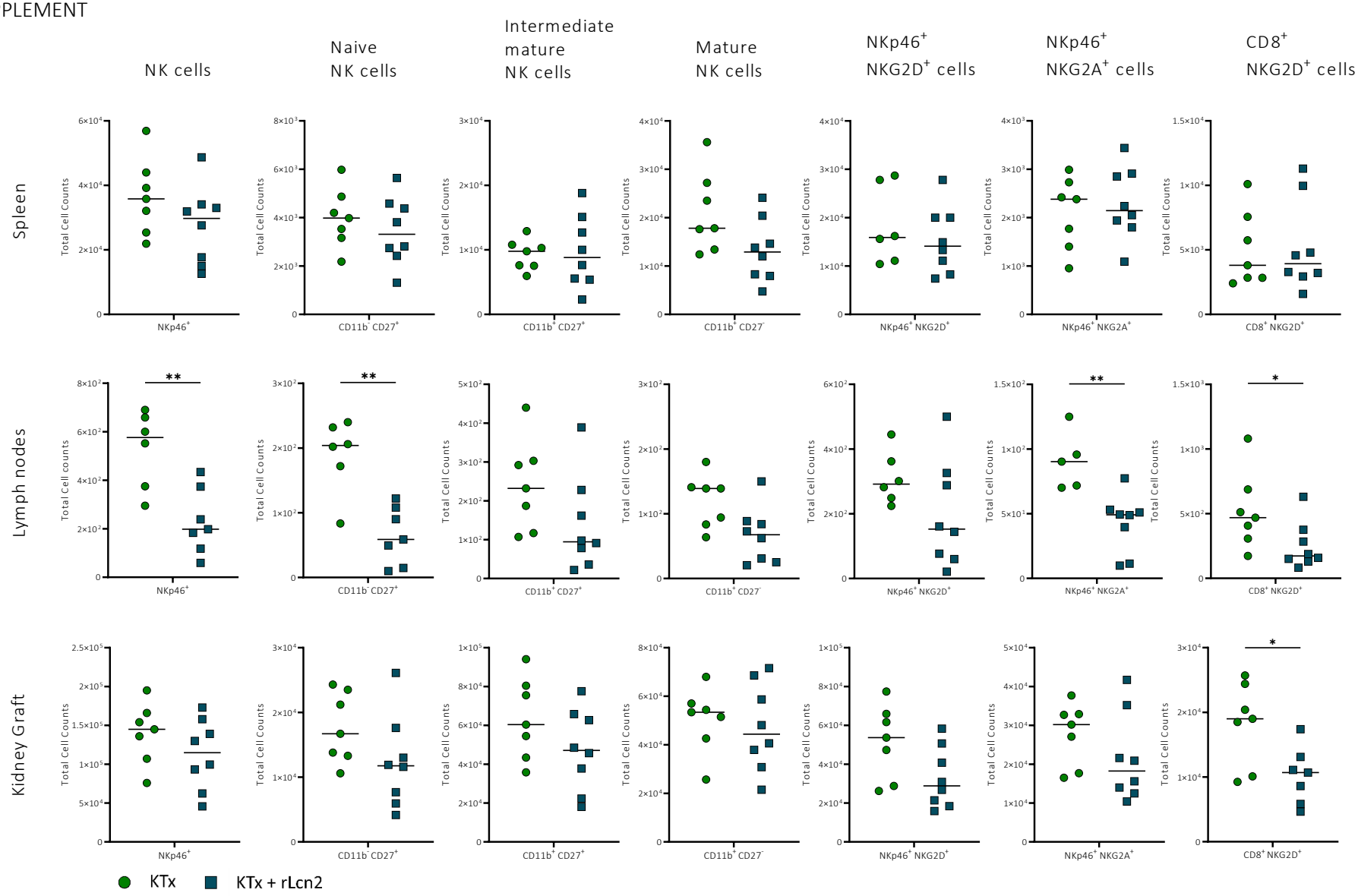

Figure S10: Total cell counts of distinctive NK cell populations in lymph nodes are affected by rLcn2-treatment at pod-3 after allogenic mKTx.
Immune cells were isolated from spleens, lymph nodes, kidney grafts, and blood after allogenic murine kidney transplantations from Balb/c to C57Bl/6 mice (n = 7-8) on pod-3 and pod-7. The same staining protocol and analysis methods as described in **Figure S5** were employed to assess the impact of rLcn2-treatment on total cell counts of NK cells and subgroups (*NK-Panel*, **Table 10**). Horizontal lines represent the respective mean. Statistical analysis: Mann-Whitney t-test; * $p < 0.05$, ** $p \leq 0.01$.

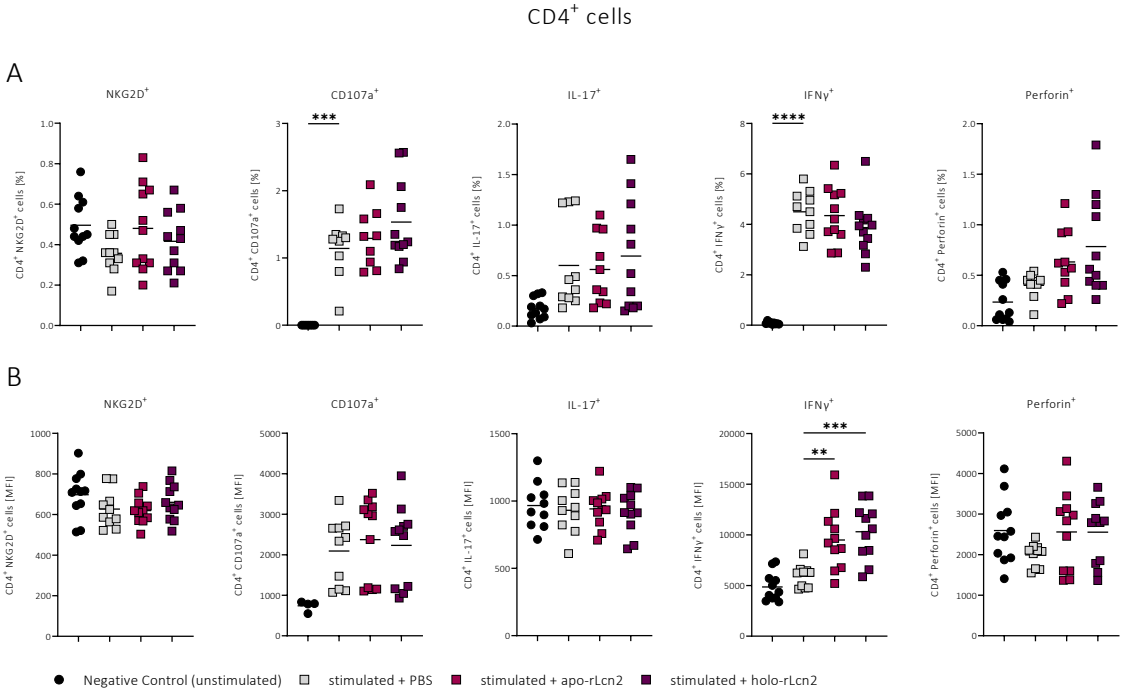

Figure S11: No effects of rLcn2 on CD4+ cells from *ex vivo* stimulated T cells.

Ex vivo activated lymphocytes isolated from spleens of C57Bl/6 mice were either treated with apo-rLcn2 or holo-rLcn2 and harvested after 48 hours of cell culture. T cells were stained with a cocktail of monoclonal antibodies with a marker for NKG2D additionally included (*Functional-Panel*, **Table 10**). Relative frequencies and MFI of immune cells were acquired on a BD LSRFortessa™ Cell Analyzer and analysed using FlowJo™ and GraphPad Prism software. Horizontal lines represent the respective mean. N = 10. Statistical analysis: Ordinary one-way ANOVA; * $p < 0.05$, ** $p \leq 0.01$, *** $p \leq 0.001$, **** $p \leq 0.0001$.

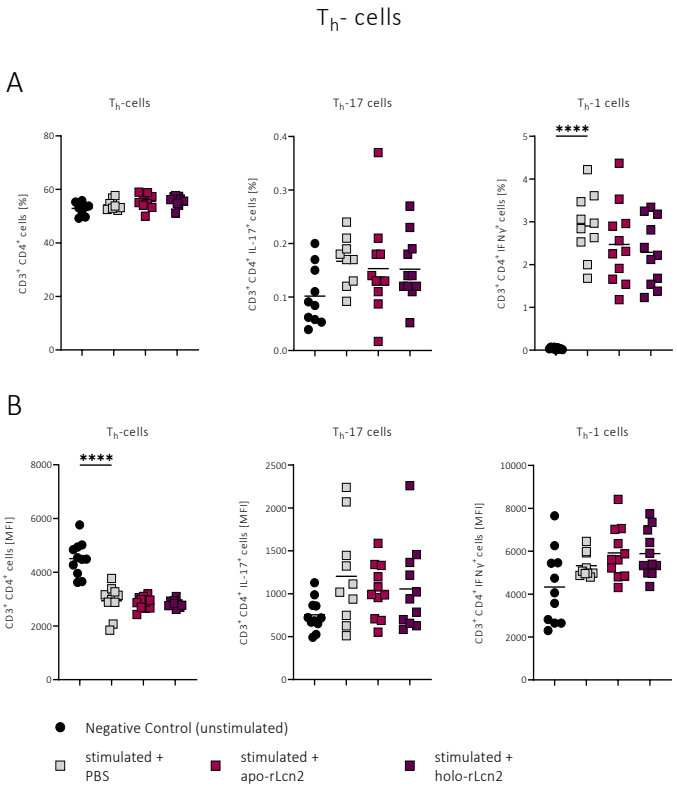

Figure S12: Treatment with rLcn2 had no effect on *ex vivo* stimulated T_h cells.

Ex vivo activated lymphocytes isolated from spleens of C57Bl/6 mice were either treated with apo-rLcn2 or holo-rLcn2, harvested after 48 hours of cell culture, and analysed as described in **Figure S11** (*Functional-Panel*, **Table 10**). Horizontal lines represent the respective mean. n = 10. Statistical analysis: Ordinary one-way ANOVA; * $p < 0.05$, ** $p \leq 0.01$, *** $p \leq 0.001$, **** $p \leq 0.0001$.

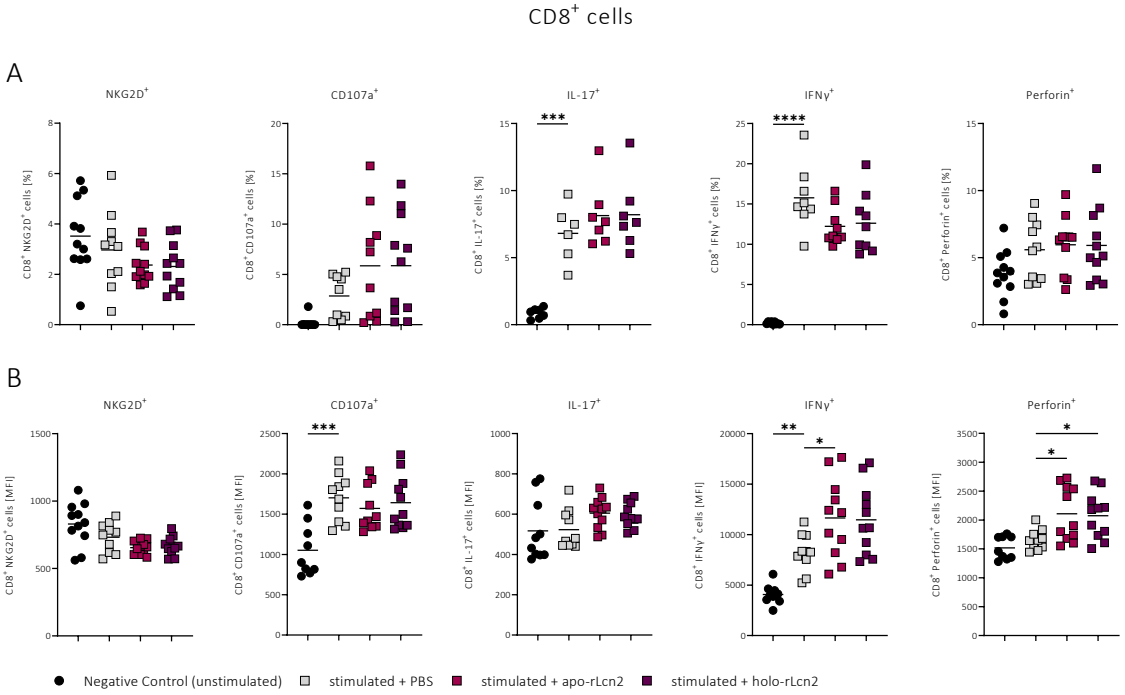

Figure S13: rLcn2-treatment exerted no effects on *ex vivo* stimulated CD8⁺ cells.
Ex vivo activated lymphocytes isolated from spleens of C57Bl/6 mice were either treated with apo-rLcn2 or holo-rLcn2, harvested after 48 hours of cell culture, and analysed as described in **Figure S11** (*Functional-Panel*, **Table 10**). Horizontal lines represent the respective mean. n = 10. Statistical analysis: Ordinary one-way ANOVA; * $p < 0.05$, ** $p \leq 0.01$, *** $p \leq 0.001$, **** $p \leq 0.0001$.

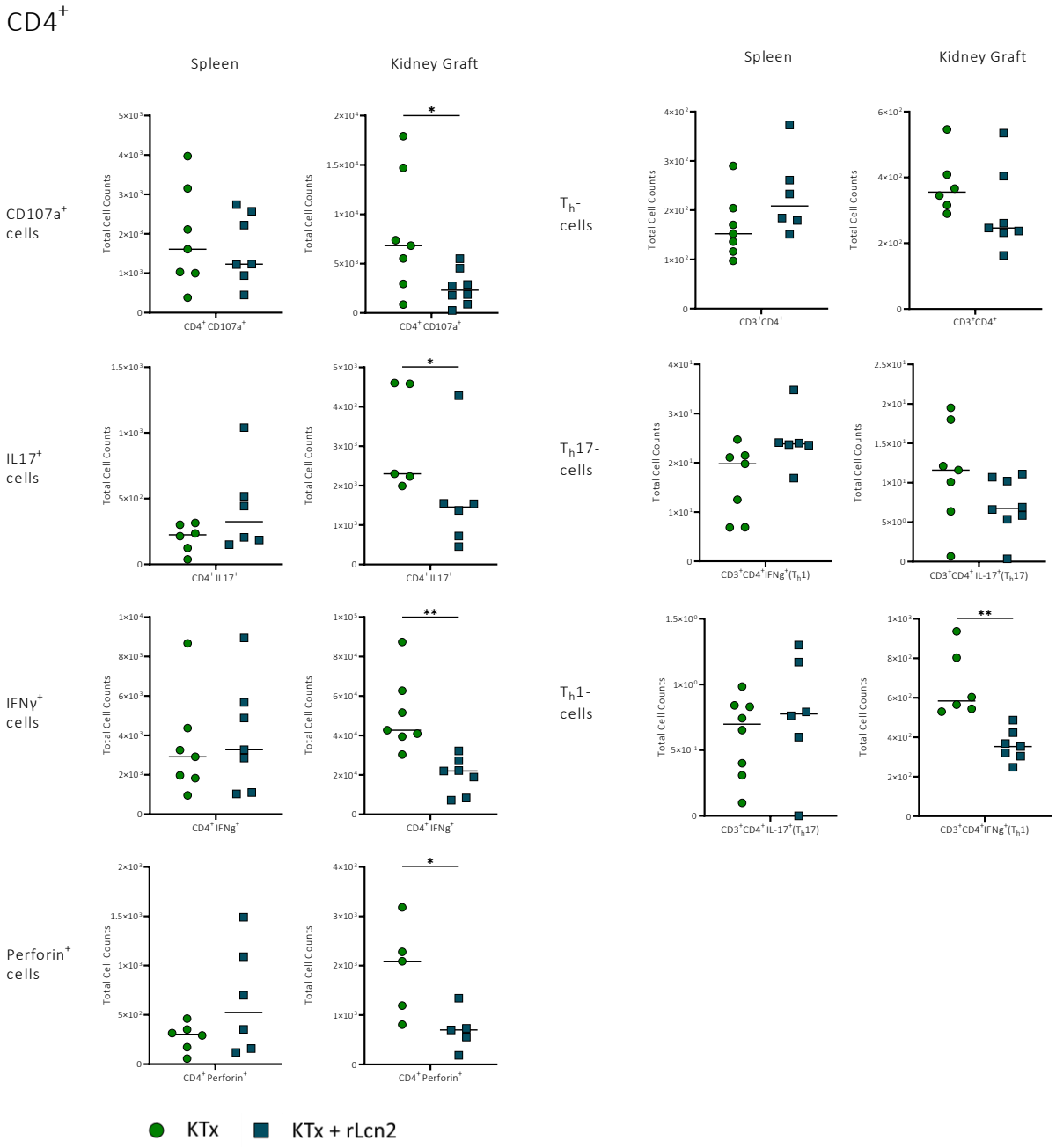

Figure S14: Treatment with rLcn2 significantly lowers total cell counts of *ex vivo* stimulated CD4⁺ immune cells in kidney grafts at pod-3 after allogenic mKTx.

Immune cells were isolated from spleens, lymph nodes, kidney grafts, and blood after allogenic murine kidney transplantations from Balb/c to C57Bl/6 mice (n = 7-8) on pod-3 and pod-7 and polyclonally stimulated *ex vivo* with PMA and ionomycin. Extracellular and intracellular staining was performed with a cocktail of monoclonal antibodies (*Functional-Panel*, **Table 10**).). Total cell counts of activated T- cells and subgroups were acquired on a BD LSRFortessa™ Cell Analyzer using Precision count™ beads for reference. Analysis and calculations were done using FlowJo™ and GraphPad Prism software. Horizontal lines represent the respective mean. Statistical analysis: Mann-Whitney t-test; * $p < 0.05$, ** $p \leq 0.01$.

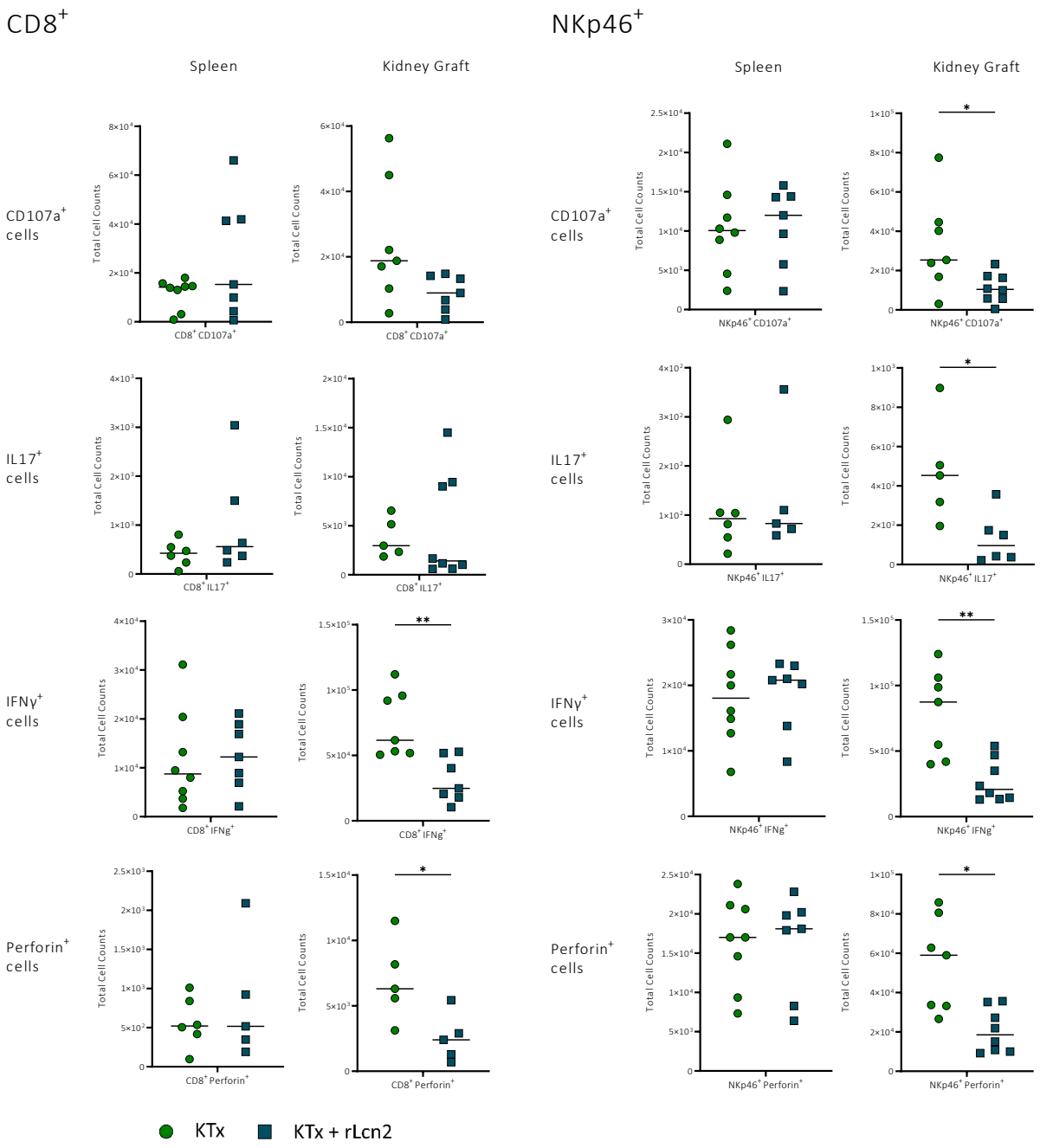

Figure S15: rLcn2-treatment-reduced total cell counts of *ex vivo* stimulated CD8⁺ and NKp46⁺ immune cells in kidney grafts at pod-3 after allogenic mKTx.

Immune cells were isolated from spleens, lymph nodes, kidney grafts, and blood after allogenic murine kidney transplantations from Balb/c to C57Bl/6 mice (n = 7-8) on pod-3 and pod-7 and polyclonally stimulated *ex vivo* with PMA and ionomycin. Extracellular and intracellular staining was performed with a cocktail of monoclonal antibodies (*Functional-Panel*, **Table 10**). Total cell counts of activated T-, NK cells, and respective subgroups were acquired on a BD LSRFortessa™ Cell Analyzer using Precision count™ beads for reference. Analysis and calculations were done using FlowJo™ and GraphPad Prism software. Horizontal lines represent the respective mean. Statistical analysis: Mann-Whitney t-test; * $p < 0.05$, ** $p \leq 0.01$.

A.

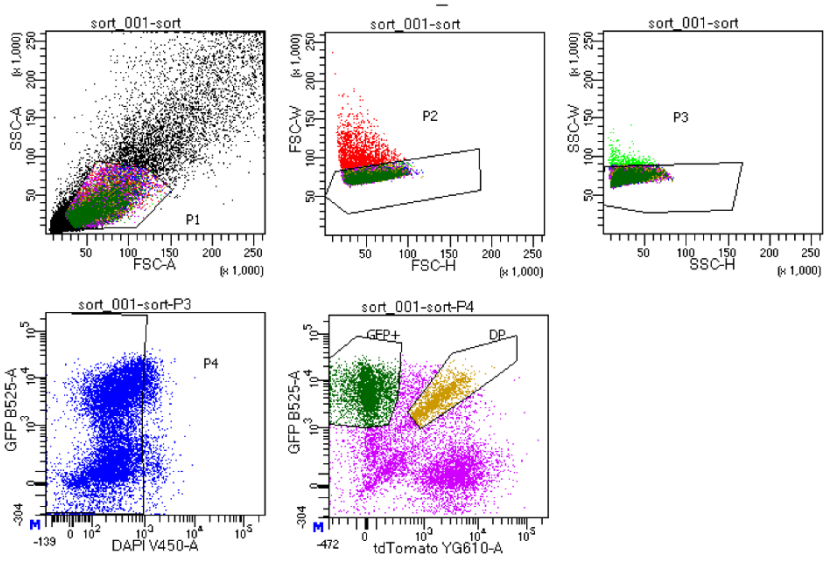

Tube: sort

Population	#Events	%Parent	%Total
All Events	50,000	####	100.0
P1	14,333	28.7	28.7
P2	12,497	87.2	25.0
P3	12,108	96.9	24.2
P4	10,888	89.9	21.8
GFP+	3,198	29.4	6.4
DP	1,511	13.9	3.0

B.

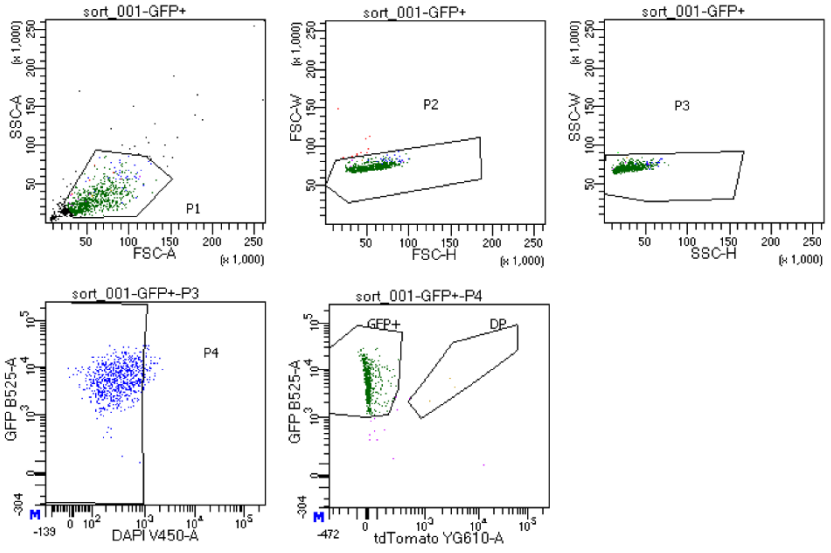

Tube: GFP+

Population	#Events	%Parent	%Total
All Events	1,000	####	100.0
P1	767	76.7	76.7
P2	757	98.7	75.7
P3	756	99.9	75.6
P4	715	94.6	71.5
GFP+	699	97.8	69.9
DP	3	0.4	0.3

Figure S16: Fluorescence activated cell sorting with a BD Aria II Calliope cytometer of primary proximal tubular epithelial cells isolated from mT/mG*PEPCK-Cre.

(A) Gating strategy used for separation of GFP$^+$, tdTomato$^+$ and double positive cells. During this representative run, the sample contained of 29.4 % GFP$^+$ cells and 13.9 % double positive cells. **(B)** Final assessment of the sorted sample in this representative run showed an almost pure PTEC population comprising of 97.8 % GFP$^+$ cells.

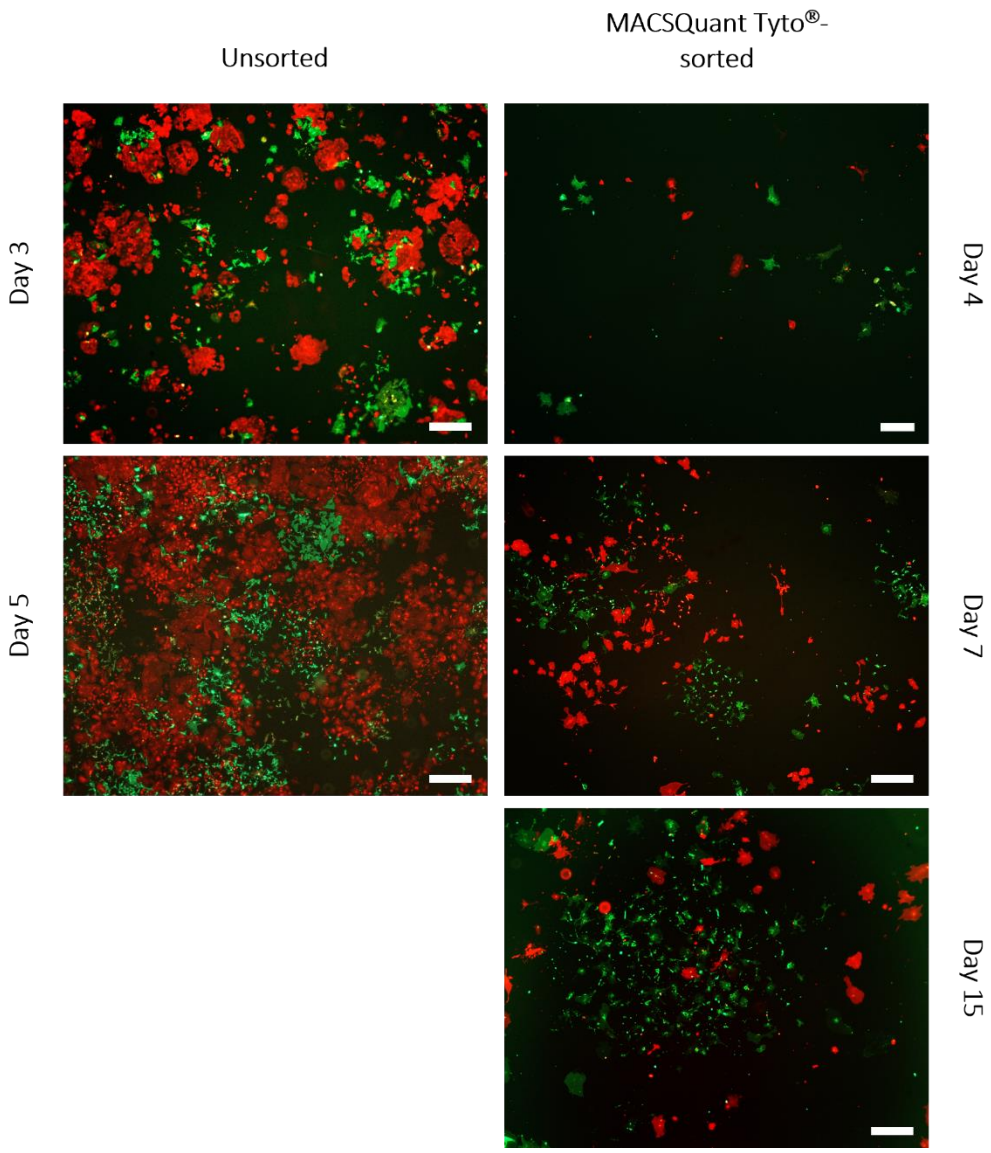

Figure S17: MACSQuant® Tyto® sorted primary PTEC (GFP⁺) from mT/mG*PEPCK-Cre do not survive the first 24 h of cell culture.

Representative fluorescence microscopy images over the course of cell culture are shown, comparing unsorted and MACSQuant® Tyto® sorted samples. Scale bar = 500 µm.

In comparison to unsorted cells, most of the sorted cells did not survive the first 24 h after sorting. The surviving cells formed small colonies that grew very slowly. After seven days of culture cultures of sorted cells grew to approximately 20 % confluency, compared to unsorted cells that reached confluency already after five days of culture. Sorted cells moreover exhibited an unhealthy phenotype with a flattened, elongated, and irregular morphology and did not reach confluency until 15 days of culture.

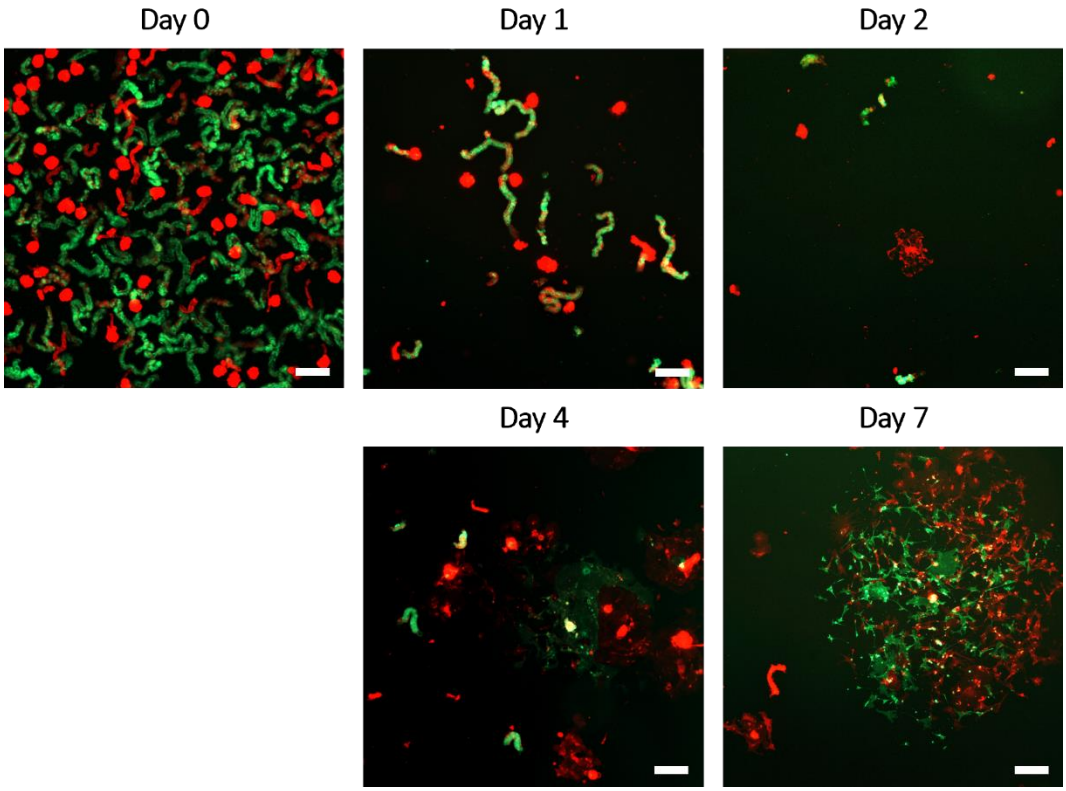

Figure S18: Most isolated proximal tubules from mT/mG*PEPCK-Cre using ultracentrifugation do not attach to the surface.

Representative fluorescence microscopy images over the course of cell culture. Scale bar = 500 µm. Proximal tubules exhibiting GFP fluorescence, are still attached to glomeruli, exhibiting tdTomato red fluorescence, after ultracentrifugation (day 0). At day 1 of culturing, a majority of proximal tubules were washed out during the medium change, and only a few of proximal tubule attached to the surface. Until day 7 of cell culture, only small and morphological irregular colonies of PTEC have formed. Most colonies comprised of green and red fluorescent cells growing either in proximity or were interwoven.

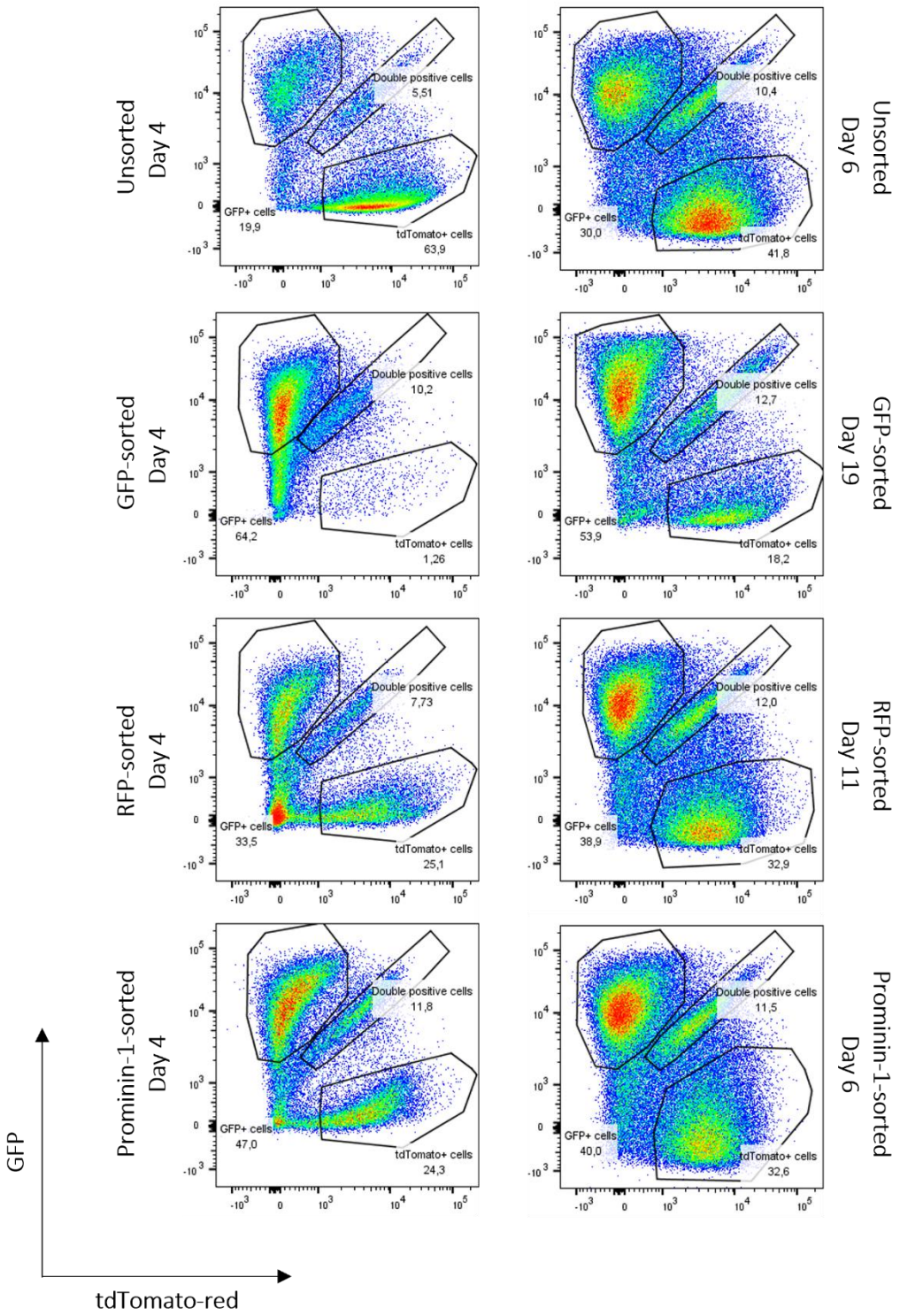

Figure S19: Representative scatter plots measuring isolated primary proximal tubular epithelial cells during flow cytometrical analysis.

Applied gating strategies to distinguish GFP⁺ cells from tdTomato⁺ and double positive cells ultimately allowed comparing the effectiveness of sorting procedures with anti-µMACS-GFP microbeads, RFP-antibody in addition to microbeads, as well as anti-prominin-1 microbeads in relation to isolated, but unsorted cell populations.

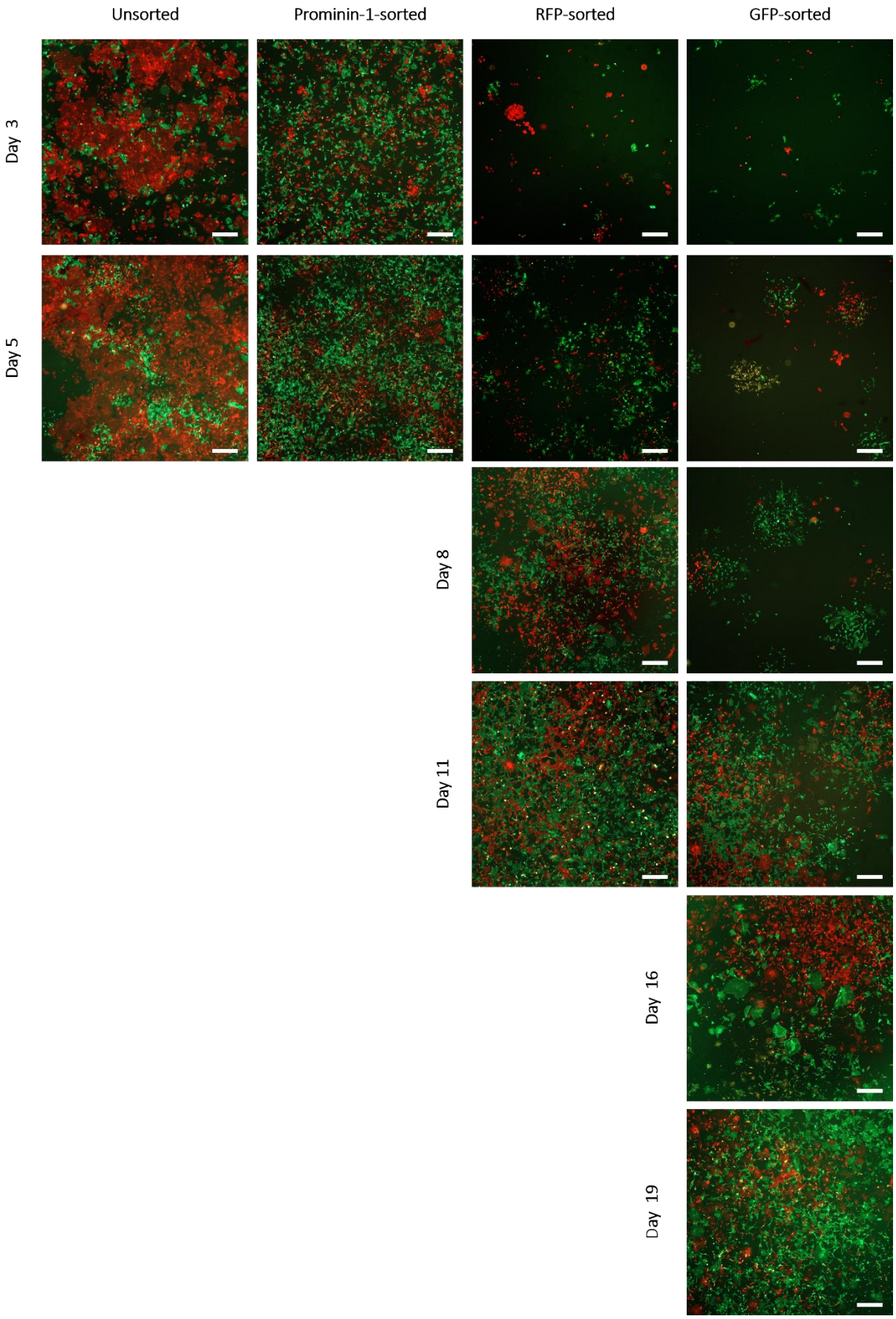

Figure S20: Overview of growing patterns of primary PTEC over time according to sorting procedures.
Primary PTEC were isolated from C57Bl/6 kidney cortexes applying validated gentleMACS™ dissociation protocols, followed by sorting via anti-µMACS-GFP microbeads, anti-prominin-1 microbeads, or RFP-antibody and microbeads.

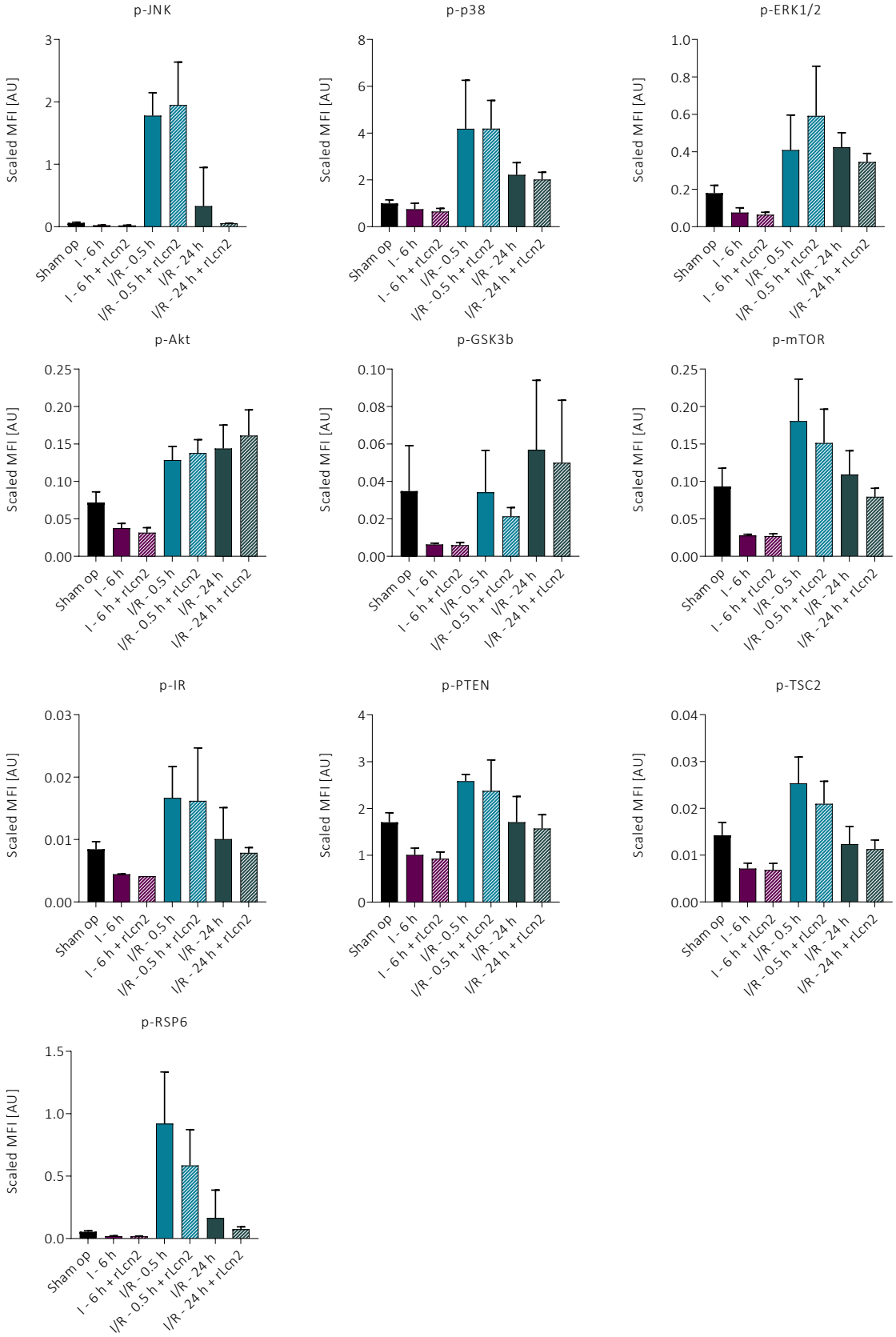

Figure S21: Intracellular signalling pathway analysis *in vivo* after kidney transplantation.
Mean and standard deviation of scaled mean fluorescent intensity (MFI) from selected growth, survival, and apoptotic pathways was measured under different ischemia and reperfusion conditions in sham operated (sham op) and rLcn2-treated tissues isolated from kidney grafts. AU—Arbitrary units. Statistical analysis: Student's t-test; * $p < 0.05$.

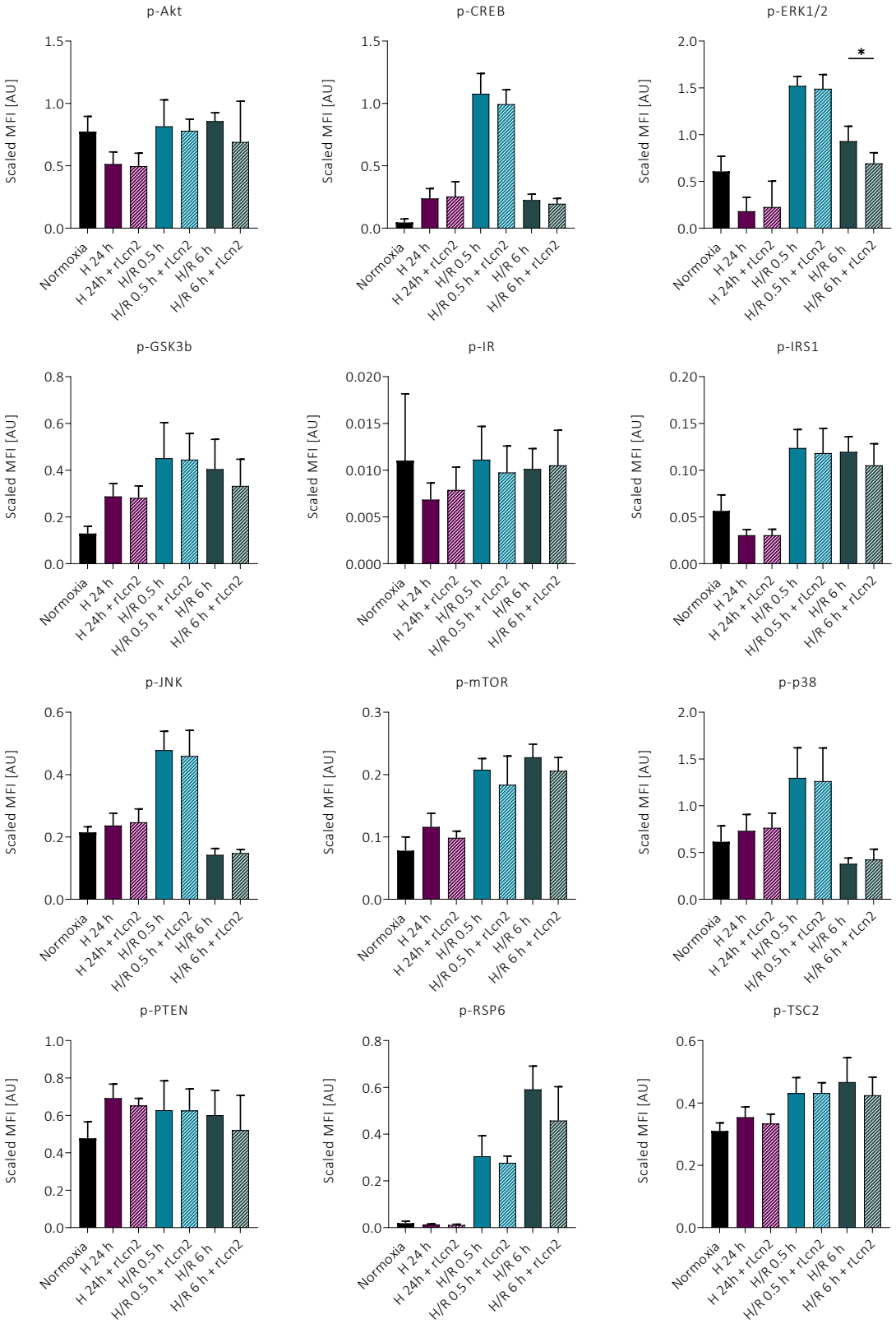

Figure S22: Intracellular signalling pathway analysis *in vitro* after isolation of primary PTEC from C57Bl/6 kidney cortexes followed by anti-prominin-1 microbeads-based MACS sorting.

Mean and standard deviation of scaled mean fluorescent intensity (MFI) from selected growth, survival, and apoptotic pathways was measured under different hypoxia and reoxygenation conditions under normoxic and different reoxygenation conditions comparing untreated cells to cells treated with rLcn2 in cell culture. AU—Arbitrary units. Statistical analysis: Student's t-test; * $p < 0.05$.

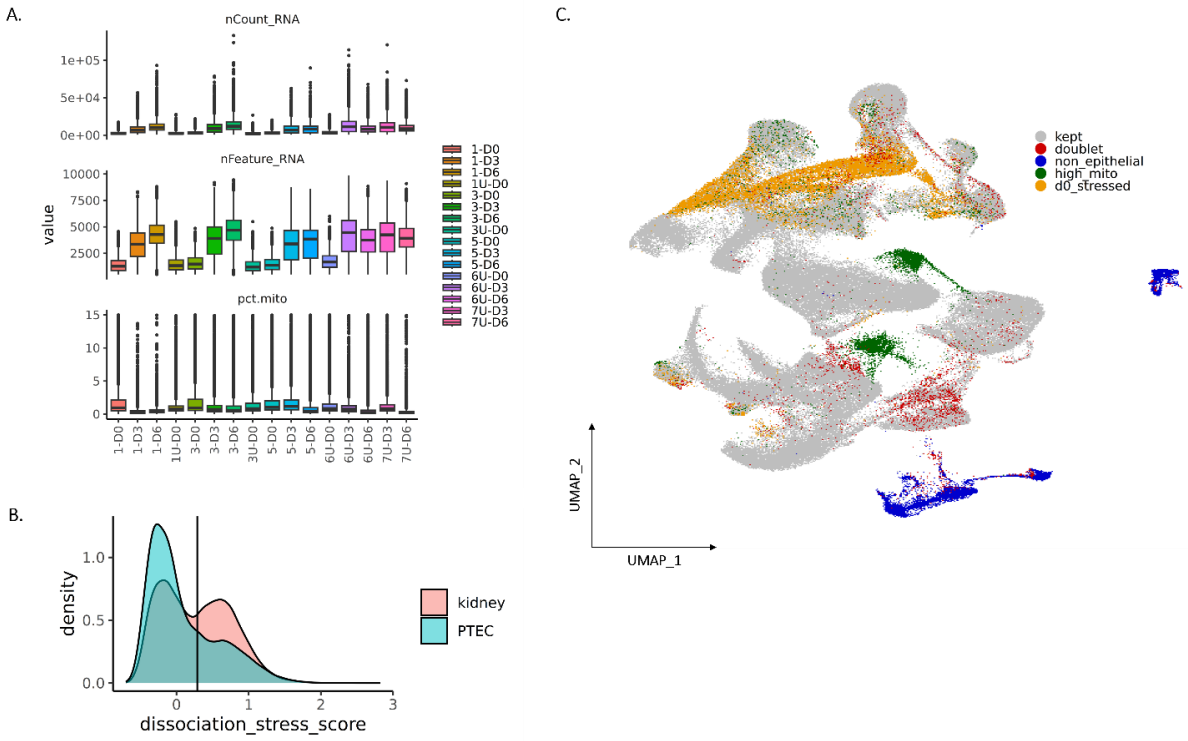

Figure S23: Single-cell RNA-sequencing of isolated PTEC from cell culture.
(A) Quality assessment of the total number of transcripts, the number of unique transcripts, and the percentage of mitochondrial RNA per single cell in pooled samples of unsorted and prominin-1 sorted PTEC from three different timepoints (day 0, day3, and day 6; 173,928 cells, n = 16). Cells with more than 15 % of mitochondrial RNA were excluded from the analysis. A total of 16 samples were analysed. **(B)** Distribution of dissociation stress score on the day of isolation comparing sorted (PTEC) and unsorted (kidney) cells. Cells above the threshold (0.25; black vertical line) were removed from analysis. **(C)** Initial UMAP displaying doublets, non-epithelial, high-mitochondrial, and dissociation stressed cells that were excluded from the dataset to reduce batch effects.

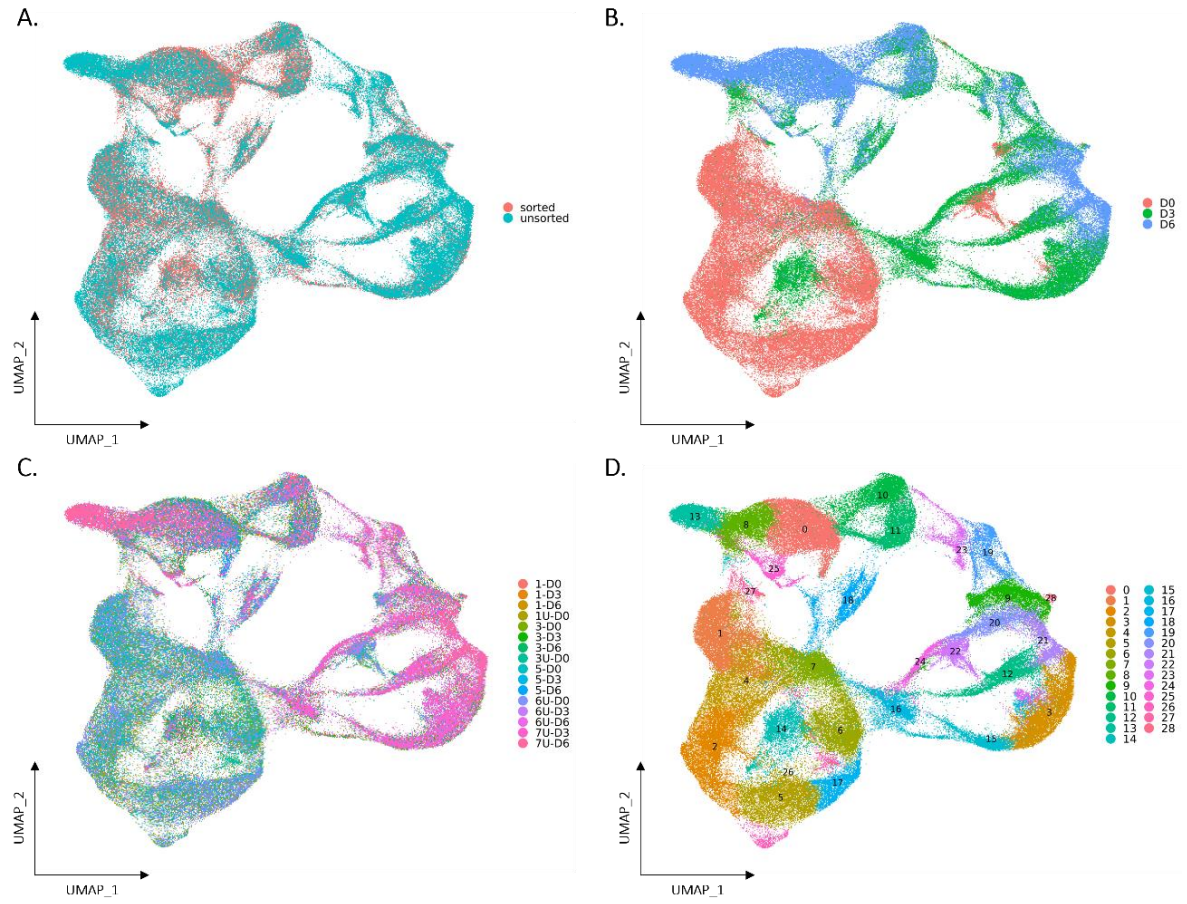

Figure S24: Follow-up analysis of cleaned scRNAseq data from isolated PTEC from cell culture.
(A) UMAP showing the distribution cells from anti-prominin-1 sorted and unsorted cells and **(B)** their distribution according to the timepoints they were isolated. **(C)** UMAP depicting cell distribution colour-coded by sample. **(D)** UMAP displaying 29 distinct cluster (154,351 cells, n = 16) after reapplication of analysis after batch effect removal (**Figure S23**). Clustering was based on highly variable genes.

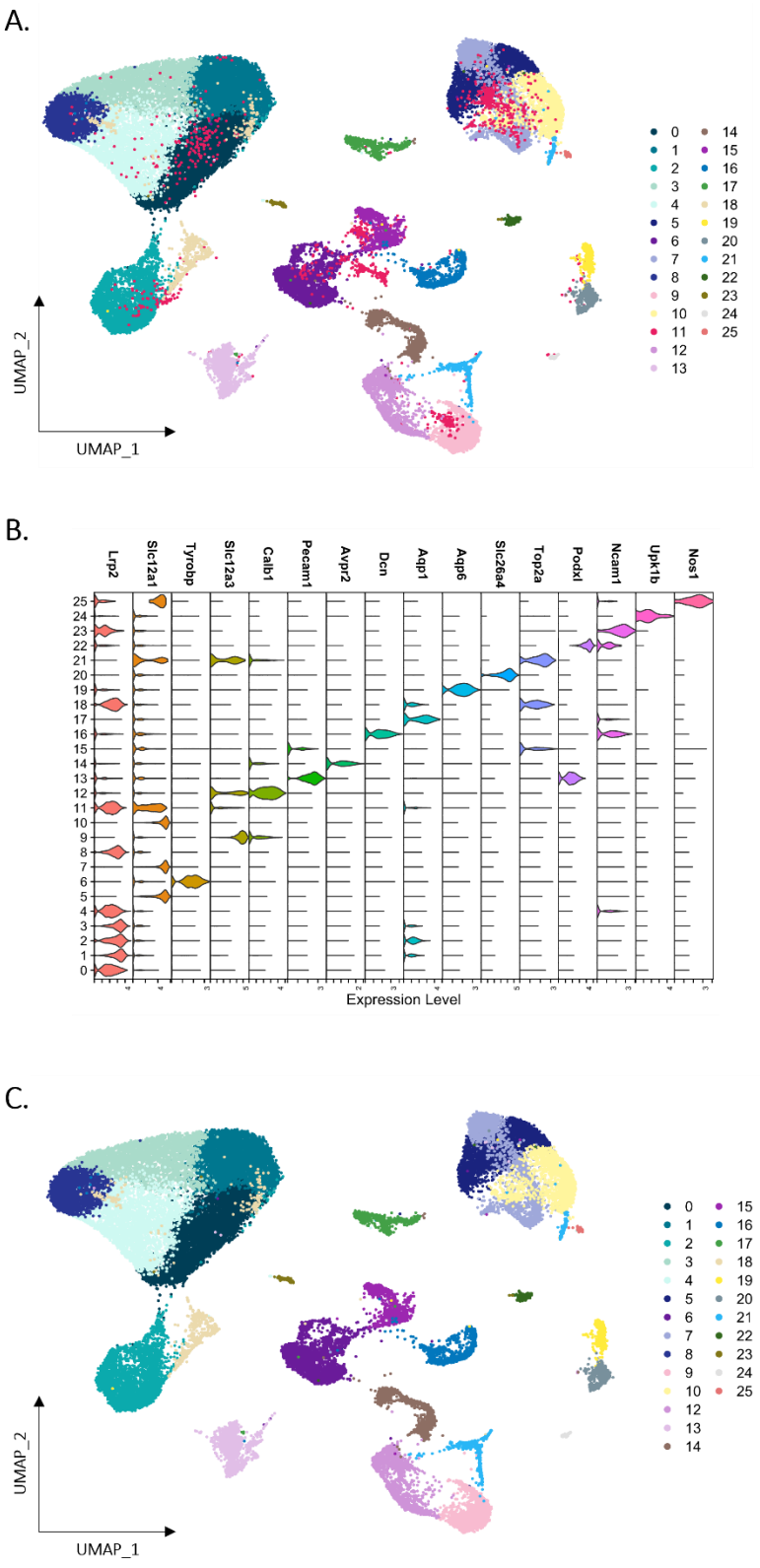

Figure S25: Initial analysis of snRNAseq data.
(A) UMAP plot displaying 26 distinct clusters after initial analysis. Clustering was based on highly variable genes. **(B)** Violin plot showing the expression of candidate marker genes to identify cell types in each cluster. As depicted in (A), cluster 11 is distributed over the whole UMAP, additionally contained more ambient RNA as other clusters, and was thus not clearly assignable to a certain cell type, hence being excluded from further analysis. **(C)** UMAP after removal of cluster 11.

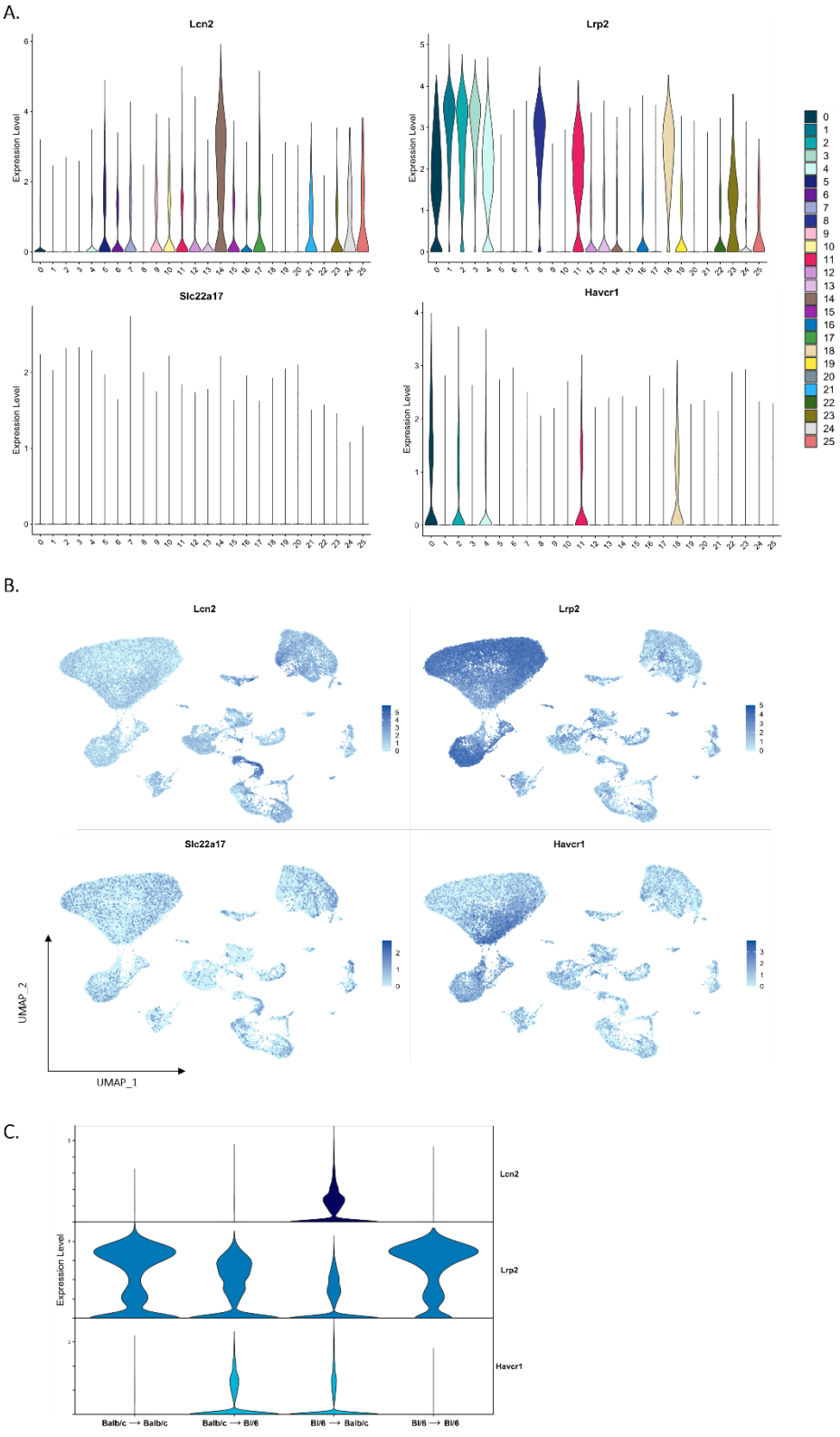

Figure S26: Gene expression analysis in clusters from initial analysis.

(A) Expression of Lcn2 was highest in cluster 14. Clusters 0, 1,2,3,4, 8, 11, 18, and 23 had the highest expression of *Lrp2*. Some expression of Havcr1 was detected in clusters 0, 2, 4, 11, and 18. *Slc22a17* was not detected in any cluster. n = 1-3, depending on the transplantation group. **(B)** Feature plot displaying expression distribution of Lcn2, *Lrp2*, *Slc22a17*, and Havcr1. Grey – no expression, dark blue – highest expression. **(C)** Violin plot depicting the overall expression of Lcn2, Lrp2 and Havcr1 separated according to transplantation groups. Lcn2 expression was only detectable in C57Bl/6 to Balb/c transplantation groups, while *Lrp2* expression occurred in every transplantation setting. Havcr1 expression was only observed in allogenic transplantation settings.

6.2 SUPPLEMENTARY TABLES

Table S1: Counts of NK⁺ cells, CD4⁺,and CD8⁺ cells including their subsets calculated with t-SNE analysis using FlowJo.

Compensated data from kidney grafts and spleens at pod-3 and pod-7 was used (n = 7-8). A total of 50,000 lymphocytes per group (either KTx or KTx + rLcn2) with 1,000 iterations and a perplexity of 30 were used for t-SNE calculation.

Kidney graft pod-3.

Subset name	KTx count	KTx + rLcn2 count
NK⁺ cells	12428	12142
NK⁺ CD107a⁺	3709	3581
NK⁺ IFNγ⁺	10880	8245
NK⁺ IL17⁺	2131	1075
NK⁺ Perforin⁺	7099	5458
CD4⁺ cells	9868	9814
CD4⁺ CD107a⁺	723	655
CD4⁺ IFNγ⁺	5247	5160
CD4⁺ IL17⁺	1284	496
CD4⁺ Perforin⁺	1245	397
CD8⁺ cells	11457	13672
CD8⁺ CD107a⁺	2253	2551
CD8⁺ IFNγ⁺	8755	8596
CD8⁺ IL17⁺	1309	600
CD8⁺ Perforin⁺	1949	1282

Kidney graft pod-7.

Subset name	KTx count	KTx + rLcn2 count
NK⁺ cells	2600	3835
NK⁺ CD107a⁺	397	1013
NK⁺ IFNγ⁺	1577	1491
NK⁺ IL17⁺	19	129
NK⁺ Perforin⁺	1168	2200
CD4⁺ cells	14623	15057
CD4⁺ CD107a⁺	1532	1732
CD4⁺ IFNγ⁺	7368	1946
CD4⁺ IL17⁺	528	256
CD4⁺ Perforin⁺	775	500
CD8⁺ cells	25661	20208
CD8⁺ CD107a⁺	5011	1256
CD8⁺ IFNγ⁺	18464	7386
CD8⁺ IL17⁺	2060	861
CD8⁺ Perforin⁺	9008	4541

Spleen pod-3.

Subset name	KTx count	KTx + rLcn2 count
NK⁺ cells	7803	12237
NK⁺ CD107a⁺	4608	6816
NK⁺ IFNγ⁺	6221	8932
NK⁺ IL17⁺	79	73
NK⁺ Perforin⁺	6345	9116
CD4⁺ cells	22438	19945
CD4⁺ CD107a⁺	734	464
CD4⁺ IFNγ⁺	1196	1041
CD4⁺ IL17⁺	168	118
CD4⁺ Perforin⁺	353	428
CD8⁺ cells	28575	26700
CD8⁺ CD107a⁺	7700	4060
CD8⁺ IFNγ⁺	3242	4632
CD8⁺ IL17⁺	102	120
CD8⁺ Perforin⁺	860	1433

Spleen pod-7.

Subset name	KTx count	KTx + rLcn2 count
NK⁺ cells	5933	4248
NK⁺ CD107a⁺	2031	234
NK⁺ IFNγ⁺	4517	3357
NK⁺ IL17⁺	839	835
NK⁺ Perforin⁺	5095	4155
CD4⁺ cells	38961	39317
CD4⁺ CD107a⁺	746	511
CD4⁺ IFNγ⁺	2723	1021
CD4⁺ IL17⁺	552	358
CD4⁺ Perforin⁺	5095	325
CD8⁺ cells	44074	46422
CD8⁺ CD107a⁺	7481	618
CD8⁺ IFNγ⁺	9362	5451
CD8⁺ IL17⁺	2945	2345
CD8⁺ Perforin⁺	4604	3715

Table S2: Relative standard deviations (RSD) of the analytes' mean fluorescence intensities (MFI) in the quality controls after multiplex analysis.

Milliplex MAP 9-Plex Multi-Pathway and 11-Plex Akt/mTOR signalling kits were used for multiplex assays, analysing various stress, inflammation, apoptotic, and survival signalling pathways of *in vivo* and *in vitro* samples. To show technical variations of the instrument, pooled quality controls from all analysed samples were included. For the samples, the background was subtracted, and all samples were scaled to the internal standard β-tubulin. Due to being below the background, NFκB, p70S6K, STAT3, IGF1R, P70S6K, and GSK3a could not be analysed. For STAT5, four values below the background were removed for further data analysis. The RSD for ß-Tubulin in all samples was 14 %.

Analytes	RSD of Quality Controls [%]
9Plex	
CREB	10
JNK	7
beta-Tubulin	5
NFκB	10
p38	5
ERK1/2	3
AKT	6
p70S6K	10
STAT3	7
STAT5	7

Analytes	RSD of Quality Controls [%]
11Plex	
beta-Tubulin	3
GSK3b (Ser9)	5
IGF1R (Tyr1135_1136)	11
IRS1 (Ser636)	11
Akt (Ser473)	11
mTOR (Ser2448)	8
P70S6K (Thr412)	5
IR (Tyr1162_1163)	9
PTEN (Ser380)	4
GSK3a (Ser21)	8
TSC2 (Ser939)	8
RPS6 (Ser235_236)	7
beta-Tubulin	3
GSK3b (Ser9)	5
TSC2 (Ser939)	8
RPS6 (Ser235_236)	7

Table S3: Annotation of the 19 distinct clusters from anti-prominin-1 microbeads-sorted and unsorted primary proximal tubular epithelial cells (PTEC) on isolation day (day 0).

PT–proximal tubule, PST–proximal straight tubule, PCT–proximal convoluted tubule, DCT–distal convoluted tubule, act. PT–immunoactive proximal tubule, CD–collecting duct. n = 3 sorted and 3 unsorted.

Cluster No.	Annotation Day 0 (sorted + unsorted PTEC)
0	PST
1	PCT
2	PCT
3	PCT
4	PST
5	PST
6	PCT
7	PST
8	PST
9	PCT
10	PCT
11	DCT
12	CD-transitional cells
13	TAL
14	Act. PT
15	CD-transitional cells
16	PST
17	PST
18	proliferating PT

Table S4: Samples for single-nucleus RNA-sequencing from kidneys of 12-week-old, male mice.
Isolation of nuclei is described in method section **2.10.3**. Samples with less than 1,000 counted nuclei were excluded (marked in red). UMI – unique molecular identifier. C57Bl/6 = Bl/6.

mKTx samples	Ambient RNA	Number of nuclei	Mean UMIs/ nucleus	Median genes/ nucleus	Number of genes
Balb/c → Balb/c (sample 1)	29,2	5.217	42.092	2.746	20988
Balb/c → Balb/c (sample 2)	33,6	5.093	72.287	2.329	21387
Balb/c → Bl/6 (sample 1)	29,1	3.948	54.052	3.258	21111
Balb/c → Bl/6 (sample 2)	48,8	23.162	17.149	848	21676
Balb/c → Bl/6 (sample 3)	32,5	23.740	10.519	1.135	22040
Bl/6 → Balb/c (sample 1)	29,2	3.796	57.490	3.468	20677
Bl/6 → Balb/c (sample 2)	27,8	4.260	87.122	2.898	21565
Bl/6 → Balb/c (sample 3)	39,6	16.109	14.332	1.727	21569
Bl/6 → Bl/6 (sample 1)	35,1	5.186	44.807	2.711	20425
Bl/6 → Bl/6 (sample2)	29,3	12.389	24.043	924	20248

Table S5: Marker genes to identify cell types in the distinct 27 clusters from initial snRNAseq analysis.

Marker genes	Cell type	References
Podxl	Podocytes	[79-81]
Ncam1	Parietal epithelial cells (PEC)	[79-81]
Lrp2	Proximal tubules (PT)	[79-81]
Aqp1	Thin limb (tL)	[79-81]
Slc12a1	Thick ascending limb (TAL)	[79-81]
Nos1	Macula densa	[79-81]
Slc12a3	Distal convoluted tubule (DCT)	[79-81]
Calb1	Connecting tubule (CNT)	[79-81]
Avpr2	Collecting duct-principal cell (CD-PC)	[79-81]
Upk1b	Deep medullary epithelial of pelvis (DMEP)	[79-81]
Aqp6	Intercalated cell type a (CD-IC-A)	[79-81]
Slc26a4	Intercalated cell type b (CD-IC-B)	[79-81]
Pecam1	Endothelial cells	[79-81]
Dcn, Col1a2, Acta2	Interstitial cells	[79-81]
Tyrobp	Immune cells	[79-81]
Top2a, Stmn1	Proliferation	[79-81]

Table S6: Initial clustering based on marker gene expression.

Percent expression per cluster and syngeneic and allogeneic murine kidney transplantation settings. C57Bl/6 = Bl/6.

Cluster No.	Annotation	Balb/c → Balb/c (n = 2)	Balb/c → Bl/6 (n = 2)	Bl/6 → Balb/c (n = 3)	Bl/6 → Bl/6 (n = 1)
0	PT Injury-1	6,85	15,15	15,89	3,25
1	PT-1	16,60	6,75	4,85	19,69
2	PT Injury-2	8,68	6,78	7,19	14,30
3	PT-2	12,40	4,89	4,37	16,49
4	PT Injury-3	3,45	8,37	9,17	3,13
5	TAL-1	7,82	6,32	6,97	4,62
6	Immune-1	0,13	5,22	9,86	0,07
7	TAL-2	6,12	4,48	5,13	6,36
8	PT-3	7,62	3,29	3,17	11,94
9	DCT	3,59	3,15	4,51	4,52
10	TAL-3	4,61	3,24	3,53	4,22
11	Unclear	1,32	6,25	2,54	1,63
12	CNT	3,71	2,90	3,25	2,87
13	EC	3,51	2,95	3,52	0,80
14	CD-PC	4,06	3,15	1,93	1,22
15	Immune-2	0,01	4,07	3,33	0,00
16	Interstital cells	1,58	3,08	2,20	0,49
17	tL	2,28	2,11	1,90	0,38
18	PT Injury-4	0,31	2,79	1,14	0,33
19	CD-IC-A	1,61	1,30	1,18	0,87
20	CD-IC-B	1,56	0,99	1,17	1,51
21	Proliferation	0,94	1,15	1,17	0,21
22	Podocytes	0,53	0,75	0,86	0,64
23	PEC	0,39	0,44	0,45	0,07
24	DMEP	0,13	0,26	0,52	0,19
25	Macula densa	0,20	0,18	0,19	0,19

Table S7: Initial cluster summarized to broad cell types.
Percent expression per cluster and syngeneic and allogeneic murine kidney transplantations settings. C57Bl/6 = Bl/6.

Cluster No., summarized	Annotation	Balb/c → Balb/c (n = 2)	Balb/c → Bl/6 (n = 2)	Bl/6 → Balb/c (n = 3)	Bl/6 → Bl/6 (n = 1)
0,1,2,3,4,8,18	PT	55,90	48,02	45,79	69,14
5,7,10	TAL	18,55	14,05	15,63	15,19
6,15	Immune Cells	0,14	9,29	13,19	0,07
9	DCT	3,59	3,15	4,51	4,52
11	Unclear	1,32	6,25	2,54	1,63
12	CNT	3,71	2,90	3,25	2,87
13	Endothelial Cells	3,51	2,95	3,52	0,80
14	CD-PC	4,06	3,15	1,93	1,22
16	Interstitial cells	1,58	3,08	2,20	0,49
17	tL	2,28	2,11	1,90	0,38
19	CD-IC-A	1,61	1,30	1,18	0,87
20	CD-IC-B	1,56	0,99	1,17	1,51
21	Proliferation	0,94	1,15	1,17	0,21
22	Podocytes	0,53	0,75	0,86	0,64
23	PEC	0,39	0,44	0,45	0,07
24	DMEP	0,13	0,26	0,52	0,19
25	Macula densa	0,20	0,18	0,19	0,19

Table S8: Percent expression of selected genes from the initial clustering in syngeneic and allogeneic murine kidney transplantation groups.

Gene expression Initial Clustering	Balb/c → Balb/c (n = 2)	Balb/c → Bl/6 (n = 2)	Bl/6 → Balb/c (n = 3)	Bl/6 → Bl/6 (n = 1)
Lcn2				
Average Expression [%]	0,12	1,23	3,29	0,14
Expressed [%]	4,04	21,82	51,76	2,26
avg.exp.scaled	-0,72	0,02	1,41	-0,71
Lrp2				
Average Expression [%]	17,34	8,50	2,72	22,73
Expressed [%]	72,78	64,63	43,95	86,69
avg.exp.scaled	0,51	-0,48	-1,13	1,11
Slc22a17				
Average Expression [%]	0,26	0,17	0,14	0,15
Expressed [%]	14,09	8,36	7,24	10,06
avg.exp.scaled	1,47	-0,21	-0,70	-0,56
Havcr1				
Average Expression [%]	0,21	1,21	1,35	0,03
Expressed [%]	8,11	31,75	28,07	1,11
avg.exp.scaled	-0,72	0,76	0,96	-0,99

Table S9: Proximal tubule clustering based on validated marker gene expression.
Percent expression of cluster per syngeneic and allogeneic transplantation groups. C57Bl/6 = Bl/6.

PT-subcluster	Balb/c → Balb/c (n = 2)	Balb/c → Bl/6 (n = 2)	Bl/6 → Balb/c (n = 3)	Bl/6 → Bl/6 (n = 1)
0	12,23	4,94	29,42	28,19
1	26,52	27,73	12,18	12,30
2	28,07	28,01	12,32	8,16
3	4,79	1,64	18,68	26,21
4	9,67	11,65	6,23	4,81
5	9,60	12,10	5,17	4,68
6	4,81	8,59	3,49	3,87
7	0,91	0,31	3,83	7,05
8	2,88	4,60	2,99	2,38
9	0,51	0,44	5,70	2,35

Table S10: Proximal tubule cluster summarized to broad cell types.
Percent expression of broad cell types per syngeneic and allogeneic transplantation groups.

PT-subcluster broad cell types	Balb/c → Balb/c (n = 2)	Balb/c → Bl/6 (n = 2)	Bl/6 → Balb/c (n = 3)	Bl/6 → Bl/6 (n = 1)
PCT	39,01	20,34	19,36	44,43
PST	42,55	22,03	16,84	48,25
PST-Injury	17,94	51,93	61,45	6,88
PST-Proliferation	0,51	5,70	2,35	0,44

Table S11: Percent expression of selected genes from the proximal tubule clustering in syngeneic and allogeneic murine kidney transplantation groups.

Gene expression PT-subcluster	Balb/c → Balb/c (n = 2)	Balb/c → Bl/6 (n = 2)	Bl/6 → Balb/c (n = 3)	Bl/6 → Bl/6 (n = 1)
Lcn2				
Average Expression [%]	0,03	0,31	1,05	0,02
Expressed [%]	1,72	12,76	40,02	1,12
avg.exp.scaled	5,00	9,00	20,00	4,00
Lrp2				
Average Expression [%]	29,71	15,37	5,36	31,68
Expressed [%]	99,51	96,15	78,74	99,86
avg.exp.scaled	15,00	7,00	1,00	16,00
Slc22a17				
Average Expression [%]	0,28	0,20	0,11	0,13
Expressed [%]	15,75	9,96	6,25	9,47
avg.exp.scaled	20,00	11,00	3,00	4,00
Havcr1				
Average Expression [%]	0,35	1,90	2,38	0,04
Expressed [%]	12,76	45,55	41,87	1,40
avg.exp.scaled	4,00	14,00	18,00	2,00

Table S12: Clustering of immune cells based on *Find.Markers* function from the Seurat package.
Percent expression of cluster per syngeneic and allogeneic transplantation groups. C57Bl/6 = Bl/6.

Immune-subcluster	Balb/c → Balb/c (n = 2)	Balb/c → Bl/6 (n = 2)	Bl/6 → Balb/c (n = 3)	Bl/6 → Bl/6 (n = 1)
0	75,00	19,54	37,08	66,67
1	0,00	25,91	13,31	0,00
2	0,00	9,28	12,63	0,00
3	0,00	11,67	7,94	0,00
4	0,00	9,81	7,71	0,00
5	8,33	5,04	6,90	0,00
6	8,33	5,31	5,05	0,00
7	0,00	4,33	2,53	0,00
8	0,00	3,27	3,02	0,00
9	0,00	2,21	1,98	33,33
10	8,33	1,86	1,22	0,00
11	0,00	1,77	0,63	0,00

Table S13: Immune cell cluster summarized to broad cell types.
Percent expression of broad cell types per syngeneic and allogeneic transplantation groups. C57Bl/6 = Bl/6.

Immune cells - broad cell types	Balb/c → Balb/c (n = 2)	Balb/c → Bl/6 (n = 2)	Bl/6 → Balb/c (n = 3)	Bl/6 → Bl/6 (n = 1)
Polarizing M1/M2-Macrophages	75,00	28,82	49,71	66,67
Macrophages-Proliferation	8,33	5,04	6,90	0,00
M2-Macrophages	0,00	15,30	12,72	33,33
Intermediate State DC/Macrophages, stressed	8,33	5,31	5,05	0,00
T-cells	0,00	25,91	13,31	0,00
T-cells-Proliferation	0,00	11,67	7,94	0,00
Dendritic-cells	0,00	4,33	2,53	0,00
NK-cells	8,33	1,86	1,22	0,00
B-cells	0,00	1,77	0,63	0,00

Table S14: Percent expression of selected genes from the immune cells clustering in syngeneic and allogeneic murine kidney transplantation groups.

Gene expression Immune-subcluster	Balb/c → Balb/c (n = 2)	Balb/c → Bl/6 (n = 2)	Bl/6 → Balb/c (n = 3)	Bl/6 → Bl/6 (n = 1)
Lcn2				
Average Expression [%]	0,00	0,47	1,76	0,00
Expressed [%]	0,00	15,47	44,70	0,00
avg.exp.scaled	2,00	7,00	20,00	2,00
Lrp2				
Average Expression [%]	3,23	1,69	0,60	9,23
Expressed [%]	66,67	34,22	16,28	66,67
avg.exp.scaled	7,00	3,00	1,00	20,00
Slc22a17				
Average Expression [%]	0,60	0,04	0,04	0,89
Expressed [%]	25,00	1,86	1,76	33,33
avg.exp.scaled	12,00	1,00	1,00	18,00
Havcr1				
Average Expression [%]	0,00	0,55	0,53	0,00
Expressed [%]	0,00	18,74	16,55	0,00
avg.exp.scaled	1,00	16,00	15,00	1,00